Moving and changing: using cold gas and spatially resolved spectroscopy to understand galaxies as evolving dynamic systems

Stephanie Campbell

A thesis submitted for the degree of PhD
at the
University of St Andrews

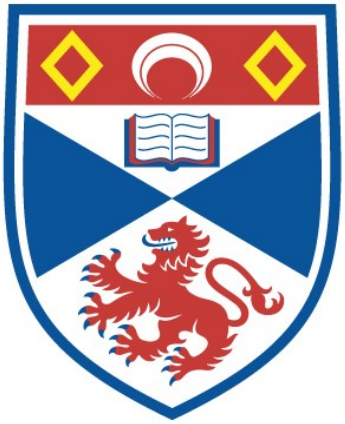

2024

Declaration

Candidate's declaration

I, Stephanie Campbell, do hereby certify that this thesis, submitted for the degree of PhD, which is approximately 32,000 words in length, has been written by me, and that it is the record of work carried out by me, or principally by myself in collaboration with others as acknowledged, and that it has not been submitted in any previous application for any degree. I confirm that any appendices included in my thesis contain only material permitted by the 'Assessment of Postgraduate Research Students' policy.

I was admitted as a research student at the University of St Andrews in September 2019.

I received funding from an organisation or institution and have acknowledged the funder(s) in the full text of my thesis.

Date 28/2/24 Signature of candidate

Supervisor's declaration

I hereby certify that the candidate has fulfilled the conditions of the Resolution and Regulations appropriate for the degree of PhD in the University of St Andrews and that the candidate is qualified to submit this thesis in application for that degree. I confirm that any appendices included in the thesis contain only material permitted by the 'Assessment of Postgraduate Research Students' policy.

Date Signature of supervisor

Permission for publication

In submitting this thesis to the University of St Andrews we understand that we are giving permission for it to be made available for use in accordance with the regulations of the University Library for the time being in force, subject to any copyright vested in the work not being affected thereby. We also understand, unless exempt by an award of an embargo as requested below, that the title and the abstract will be published, and that a copy of the work may be made and supplied to any bona fide library or research worker, that this thesis will be electronically accessible for personal or research use and that the library has the right to migrate this thesis into new electronic forms as required to ensure continued access to the thesis.

I, Stephanie Campbell, confirm that my thesis does not contain any third-party material that requires copyright clearance.

The following is an agreed request by candidate and supervisor regarding the publication of this thesis:

Printed copy

No embargo on print copy.

Electronic copy

No embargo on electronic copy.

Date 28/2/24 Signature of candidate

Date Signature of supervisor

Underpinning Research Data or Digital Outputs

Candidate's declaration

I, Stephanie Campbell, understand that by declaring that I have original research data or digital outputs, I should make every effort in meeting the University's and research funders' requirements on the deposit and sharing of research data or research digital outputs.

Date 28/2/24 Signature of candidate

Permission for publication of underpinning research data or digital outputs

We understand that for any original research data or digital outputs which are deposited, we are giving permission for them to be made available for use in accordance with the requirements of the University and research funders, for the time being in force.

We also understand that the title and the description will be published, and that the underpinning research data or digital outputs will be electronically accessible for use in accordance with the license specified at the point of deposit, unless exempt by award of an embargo as requested below.

The following is an agreed request by candidate and supervisor regarding the publication of underpinning research data or digital outputs: No embargo on underpinning research data or digital outputs.

Date 28/2/24 Signature of candidate

Date Signature of supervisor

Abstract

Galaxies are vast systems which contain stars, gas, and dust, spiralling under the influence of gravity. On human timescales they appear constant and fixed, however these systems are in motion – moving internally at vast speeds, and evolving through life stages. This work considers how the combination of multiwavelength observations can be used to understand these dynamic systems.

For decades, our observations of the motions of stars in these systems have not matched those expected based on the visible matter which is seen to be present. This has necessitated the inclusion of a dark matter component in our theory of galactic structure. This component cannot be directly observed, however dynamical modelling offers an avenue through which the properties of this can be derived. In this work, I use dynamical modelling to aid in the study of a population of galaxies known as red geysers. These galaxies may offer direct signatures of large scale outflows in galaxies which are needed in our theoretical framework to explain how galaxies stop forming new stars. Through this, more evidence was produced which points towards these galaxies exhibiting large scale outflows. Further, I then use dynamical modelling to explore the dark matter content of galaxies, and develop a novel method which incorporates cold gas observations into the process in order to better constrain the dark matter parameters. This method is shown to improve the modelling outcomes, and is an important proof-of-concept test to highlight the potential for future work using cold gas kinematics in dynamical models.

Galaxies are composed of their stellar populations contained within, and the evolutionary processes we see hinge on how these populations are affected. Some of the most extreme evolution processes are seen in so-called jellyfish galaxies, which are experiencing external environmental pressure as they fall into dense cluster environments. The final section of this work presents evidence of ongoing quenching taking place asymmetrically in a sample of these galaxies, demonstrated by spectral signatures of post-starburst formation histories on their leading edges. Using multiple data sources, I make the argument that this effect is being caused by the progressive compression and stripping of gas due to the external pressure.

Acknowledgements

General acknowledgements

Completing a PhD at any time is a great feat, however it must be said that doing so in the years 2019-2023 was really something extra special. In this time we all learned how interconnected we are with the people around us (sometimes due to a lengthy period without being able to feel those connections). I have no idea how these words will stand up to the test of time – again, as the past few years have shown, massive events can be right around the corner – but this is how life, our universe, and science works: sometimes things are eclipsed in a moment. However, reaching this moment would not have been possible without the support of many people around me. I aim to thank as many as possible here, but this list can never be complete – from family, to friends, to strangers I've met on the train, nothing anyone achieves is in isolation.

My greatest thanks goes to the incredible Dr Anne-Marie Weijmans who has been there to support, encourage, and "strongly advise" me every step of the way. Coming into this PhD, I had pictured the traditional hierarchical model of academic supervision – the supervisor knows all, and I am here to follow – however I couldn't have hoped for a better working relationship over the course of some very difficult years for everyone. My time studying would have been very different if it weren't for having a supervisor who trusted in me, was a calming influence, made me feel everything was manageable with her positivity, and most importantly was **human**. Anne-Marie was always available to talk through any of my research problems, discuss exciting ideas, have a cup of tea and talk about anything else, and also to reign me in when I got too carried away down any specific rabbit hole.

I'm incredibly grateful to my flatmates over the past four years (all of them!), but especially to the two constants since 2019 – Juan and James. They have truly seen the best and worst of me, from PhD stress and the depths of lockdown, to incredible dinners, films, gardening and the pub. There have been so many challenges over the past 4 years (both personal and global) which I couldn't imagine having navigated my way through with anyone else.

While I am renowned for the scarcity of my presence in the office, I owe a lot to the wonderful people in there. In no particular order, I give special thanks to Hin for entertaining

and abetting my jellyfish plans, and for answering Teams messages from me at all kinds of hours. To Zoe for giving me Scottish company and helping clear up any myths. To Lewis for giving me someone to be the butt of every joke. To Kat for the opportunity to gossip, and all the baked goods. To Alfie for making lots of whatsapp stickers on demand, and giving me a window into the MOND world. To Michael for indulging my dinosaur interest. To Elliott for keeping me up to date with everything going on, even when he wasn't in the office. To Sahyadri for always bringing the best comedic timing. To Clara for teaching me how to use git much later than I should have learnt this. To Suinan for blazing the trail to submission in front of me, and answering all the questions I had as I followed. And to everyone else I may have forgotten (maybe it was ambitious to try and remember everyone as I write this at the end of the thesis-writing period). I can think of no other office which has such a nice environment as ours, and I hope this continues at St Andrews for many years.

Professionally, I would like to thank the staff in St Andrews. I thank Professor Vivienne Wild for her discussions on post starburst galaxies and galaxies in general. I thank Professor Ian Bonnell and Professor Moira Jardine as my PGR assessors for their annual conversations and guidance throughout my PhD. I thank Dr Rita Tojeiro for always being happy to drop in for a coffee and a chat about anything – research related or otherwise. I also give thanks to the admin staff in the department – Dimali, Lesley, Linda, Poppy and Leah – who have always been on hand to help with whatever ridiculous requests or questions I may have. I also give special thanks to Ian Taylor for his help with the IT side of things, and especially for his last minute emergency intervention to keep Vela online for a few more hours so I could run some last minute code. Beyond St Andrews, I thank Professor Karen Masters and Dr Dave Stark for their collaboration on dynamical modelling and providing the H I -MaNGA data. I also would like to thank the whole MaNGA kinematics group for their important input on discussing the project throughout its development. A special mention goes to Dr Tim Davis for our discussions about MCMC methods. Somewhere between a colleague and a personal friend, I would also like to thank Robina Boehnke who has been my counsellor through student services throughout my PhD years. More than anyone else, she has seen the full spectrum of my highs and lows throughout this journey, and as much as she would argue otherwise I don't think I could have made it without her undying support.

I am grateful to everyone in my life outside the PhD world who has been there to adventure with me, chat with me, listen to me complain, and been patient with me throughout the past 4 years. I cannot possibly name everyone, but some special mentions to Viki and Doska who are always happy to have a drink and a swim and some unhinged laughter wherever we go, to Jac and Luna who have been there to support me and give me an escape to Glasgow or to the garden when needed, and to Lara who kept pushing me to climb even when I was being lazy, and to Felix for endless cups of tea and bird chat.

A special mention goes to Nikki who was there with me through the hardest parts of this process – the depths of lockdown. In the face of all those challenges, they were there to force me out into nature, to make me try new things, and to help me find my own way to do a PhD. I hope their PhD has also benefitted from me in turn.

I also extend an extra big, soppy, un-punk thank you to Nico. They came into my life at the least fun time, just as I disappeared into thesis-writing hibernation, and have been endlessly supportive and patient with me – there to cheer me on when I feel ready to give up, and to pull me away to the pub when I need a break. They offered up their office in Glasgow for me to work in for a much-needed change of scene, and helped remind me of all the fun adventures waiting once I'm finished and free. I can't wait to enjoy them all.

My final thanks goes to my family, who have supported me not just for the past 4 years, but for the full 26 (I guess 23 in Andrew's case – but he makes up for it). Mum is always there for a chat on the phone or to go on a walk with the dogs when I visit, Dad extends his taxi driving into giving me a lift when I need it (when I get stuck in St Andrews for example) and to call me to tell me all the goings on and give me advice. Andrew has put up with being sent a picture of my face every single day for the past 2,075 (!!), and always knows how to make me laugh more than anyone else. I thank my cousins, my Aunts, my Uncles, and everyone else.

Finally, I dedicate this thesis to my Gran. Granny Fisher was always my biggest cheerleader throughout my life – whether it be completing high school, completing my masters degree, or singing my praises for how well I had used the space on the wall behind her couch to draw a dragon in pencil while my Mum was livid. While she isn't here to see this one to the end, I know how proud of me she is, and that she knows how grateful I am to her for everything she taught me in my life.

Funding

This work was supported by the UK Reasearch and Innovation Science and Technology Funding Council (UKRI STFC) [Grant code: ST/T506448/1].

Research Data/Digital Outputs access statement

- The MaNGA data (used in all Chapters), alongside the H I -MaNGA data value-added catalogue, are available at: https://dr17.sdss.org/
- The LoTSS data, used in Chapter 5 are available through Roberts et al. (2021) and references therein.
- The DESI Legacy SUrvey Data are available at https://www.legacysurvey.org/dr10/description/

Contents

List of Figures

List of Tables

1

Galaxies in a Dynamical Context

Suggested listening: I'm Having A Good Time by Skip Church

1.1 Galaxies

Galaxies are some of the most beautiful structures known to us, and shine out as islands of light and matter in the vast dark emptiness of the Universe. From afar they appear serene, and on

Chapter image: Andromeda, NASA/Robert Gendler

human timescales, permanent and unchanging. However galaxies are dynamic environments on astronomical timescales. Their structure, formation and evolution are long studied topics, but still a field which throws up problems large enough to challenge our current understanding of the whole Universe and the physics therein.

Being prominent in the night sky, our own galaxy, the Milky Way, has been the subject of study since ancient times, across many cultures (Danezis et al., 2010; Carolina Sparavigna, 2013). In the southern hemisphere, the dark night sky is dominated by the Milky Way and the Small and Large Magellanic Clouds (SMC, LMC), and this is reflected in the traditional sky-lore of the indigenous peoples there. In South Africa, among some peoples, the LMC and SMC are named "Famine" and "Plenty" in their languages, reflecting their use to predict rainfall – during times of drought, the SMC would be obscured by dust while the LMC would remain visible due to its greater brightness (Medupe, 2015). In Australia, where Aboriginal people discovered variable stars thousands of years prior to western science discovering them only 200 years ago (Hamacher, 2018), the LMC and SMC are told by some to be the camps of an elderly man and woman, called Jukara, who are too old to gather their own food, but have support from other "star people" who catch fish from the river of the Milky Way, and bring them to be cooked on their campfires (Filipovic et al., 1996). In other Australian sky cultures, such as that of the Yaraldi people of the Lower Murray region, the LMC and SMC are identified as emus – ancestors of the great emu which is seen as a dark patch across the western part of the milky way (see Figure 1.1; Clarke, 2016). Descriptions, stories, and guidance from extragalactic sources like the LMC and SMC are countless across human history, and central to many cultures, but cannot be covered in this work. I direct the reader to the sources above, and further reading within. As far back as the 10th century, there are recorded observations from Persian astronomer al-Ṣūfī noting and describing Andromeda and the Large Magellanic Cloud (Kunitzsch, 1987; Hafez et al., 2011). It would be centuries however before the significance of these observations were realised – that Andromeda was the same type of object as the

Figure 1.1: The Milky Way is prominent in the southern night sky, and the dark patches caused by dust obscuration within the disk have their own places in sky lore of other cultures, including the Great Emu of aboriginal peoples' skylore. Image credit: Wikimedia Commons / Barnaby Norris, 2007.

Milky Way simply viewed externally, and the implication that we exist in one galaxy among trillions of others (Conselice et al., 2016).

Now, over 1000 years later, with almost unrecognisably advanced observational equipment, powerful computational simulations and the advancement in our understanding of fundamental physics, we have a much clearer picture of what galaxies are, how they form, how they change, and how they interact with the wider Universe. In order to understand galaxies fully, we have to call upon advancements in knowledge of astrophysical processes at all scales. Galaxies act as a crossroads for physics and astronomy, their existence and evolution depending on the interplay between the smallest scales (stellar physics and the nuclear processes therein), and the grandest (the cosmic structure of the Universe). While much of our knowledge in these areas is built up independently, galaxies offer an ideal testing ground for our theories, as they depend so much on such a wide range of physics. Indicative of this, despite extremely precise predictions in many of these areas, we still encounter problems when we bring them together on galactic scales. There are still many unanswered questions and troubling misalignments between the way we expect things to behave and what we observe.

When we look at the demographics of galaxies, it has been well established from early in the history of modern extragalactic astronomy (Hubble, 1926) that they exist in a largely bimodal population. When distributed in colour-stellar mass (or colour-luminosity) space, a clear separation becomes apparent between what is known as the "red sequence" and the so-called "blue cloud" (Brammer et al., 2009). This is illustrated schematically in Figure 1.2 (taken from Schawinski et al., 2014), alongside the area in between which is known as the "green valley". The galaxies inhabiting these distinct regions differ in many key ways.

Morphologically, the blue cloud is the home of spiral (late-type) galaxies. These exhibit structured spiral shapes, and have distinct dynamical structures, with an extended flat disk of stars orbiting circularly in the same plane, and a more bulging structure nearer the centre where more elliptical, dynamically-hot orbits dominate. They shine bluer due to populations of young massive stars from recent/ongoing star formation. This star formation is fuelled by vast amounts of cold hydrogen gas which exist in a flat rotating thin disk extending beyond the region occupied by stars (Bland-Hawthorn, 1997).
Meanwhile the red sequence is generally populated by early-type galaxies (elliptical and S0 type) which lack the disky spiral structure, appearing disordered and kinematically hot with

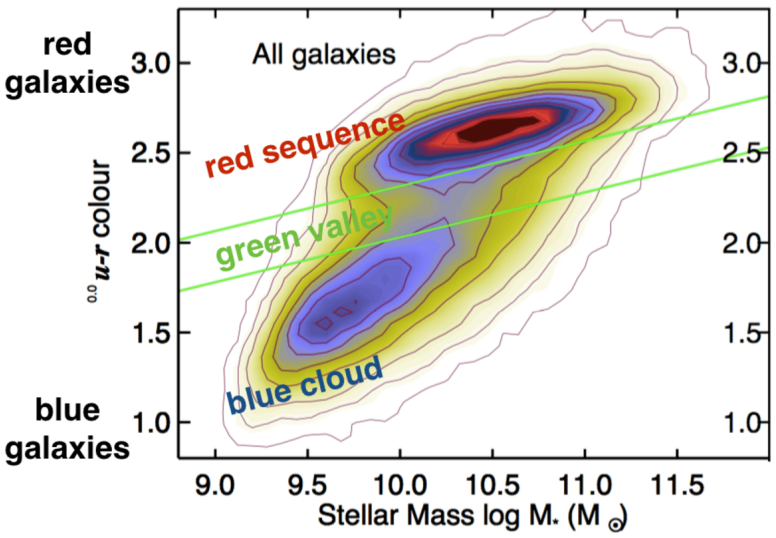

Figure 1.2: Schematic from Schawinski et al. (2014) illustrating the distribution of galaxies in the colour-stellar mass space, and showing the distinct regions inhabited by the "red sequence", the "blue cloud" and the "green valley".

elliptical orbits dominating throughout. The redder appearance of these galaxies is due to the absence of ongoing star formation, leaving only older stellar populations as the short-lived blue population dies and is not replenished. This was traditionally attributed to elliptical galaxies being completely bereft of gas, however recent radio studies have shown that this is not the case (Demoulin-Ulrich et al., 1984; Binette et al., 1994; Morganti et al., 2006a; Serra et al., 2012). Nonetheless, the fraction and surface density of gas in elliptical galaxies is still below that found in spiral galaxies and so it is generally accepted that the differences in star formation are due in part to the variation in gas content between the two populations (Grossi et al., 2009), alongside the essential impact of processes which prevent the gas present from cooling (Ciotti & Ostriker, 1997; Benson et al., 2003; Rafferty et al., 2008; Conroy et al., 2015).

The existence of green valley galaxies which inhabit the region between the two other populations has been understood in the context of a time sequence between spiral galaxies and elliptical galaxies (Coenda et al., 2018). The star formation in spiral galaxies ends, causing the youngest blue stars to cease to be present as they die off and are not replaced, and this starts the transition to the red sequence. Following this scenario, the galaxies in the green valley represent galaxies in the process of this transition. Generally, it is believed that a hierarchical evolution occurs with spirals merging together; disrupting their structure, turning them into

elliptical galaxies; and disrupting gas reservoirs causing them to undergo quenching during this process (Kauffmann et al., 2006; Gabor et al., 2010; Pontzen et al., 2017; Poggianti et al., 2020). However, the picture is not so simple. Evidence has also shown that the green valley population is best fit by not one but two gaussians (Jin et al., 2014), which would suggest there is more than one physical process at play (Schawinski et al., 2014; Nogueira-Cavalcante et al., 2019). The existence of red spirals (Masters et al., 2010) highlights the importance of secular processes in the cessation of star formation, as this population has stopped star formation but not lost their disk structures through merging. Equally, populations of blue ellipticals (Schawinski et al., 2009) illustrate that star formation can continue despite morphological disruption. It has also been shown that the transition from the blue cloud to the red sequence is not necessarily a unidirectional process, with some galaxies moving from the red sequence back into the green valley as star formation is rekindled (Salim, 2014). The processes determining the evolution of a galaxy through its lifetime are complex and multifaceted, and cannot be simply explained through external appearances alone.

While we began to classify galaxies and explain the demographics of the galaxy population on a global scale through an evolutionary sequence, the study of the internal properties of galaxies also brought to light questions about wider physics. As our ability to observe the kinematics of the Milky Way and nearby galaxies grew, evidence began to accumulate which pointed towards a key missing ingredient in what we knew of galaxies.

1.2 Dark Matter

In the 1920s, kinematic studies of the local stars in the Milky Way showed that their motion was not directly in agreement with the mass which could be accounted for by observations (Kapteyn, 1922; Jeans, 1922). This led to the coining of the phrase "dark matter" to refer to mass which is inferred to be present by motion, but cannot be directly detected by any observations.

For decades the idea that there was a vast fraction of the mass in the Universe which we could not account for in any way was not generally accepted (not least because the implications of this were inherently uncomfortable for many), however evidence slowly accumulated from many independent sources.

Studies of motions in galaxy clusters in the 1930s revealed that the orbital velocities were

ten times higher than could be accounted for by the visible matter in the cluster (Zwicky, 1933; Andernach, 2017, for English translation). Without the presence of a large quantity of dark matter, these clusters would be torn apart.

In the 1960s, 21cm observations of the Andromeda galaxy (M31) showed that the neutral hydrogen continued far beyond the edge of the optical component of the galaxy, and crucially the rotation curve at these large radii was flat, instead of decreasing as implied by the distribution of visible matter and our understanding of gravity. This pointed to a mass to light ratio of ~ 20 in M31 overall, with the region beyond the edge of the stars being dominated by this invisible mass (Roberts, 1966).

In the 1970s, Vera Rubin produced strong evidence from galactic dynamics for dark matter. The data on the rotation curve of M31 was improved further as it was derived for both optical data and radio data out to 30 kpc (Rubin & Ford, 1970) and rotation curves were derived for diverse samples of spiral galaxies (Rubin et al., 1978, 1980; Rubin, 1983). Throughout, the mismatch between the distribution of light from optical images and the distribution of mass inferred from the rotation persisted, and the rotation curves were all found to be flat in the outermost regions.

Simultaneously, the first redshift surveys began to map the distribution of nearby galaxies. At the time, contemporary cosmology predicted that galaxies were distributed randomly. The early results from the Centre for Astrophysics (CfA) redshift survey showed that galaxies follow a structured distribution which traces overlapping filamentary lines in a web-like structure, with vast empty voids in between (de Lapparent et al., 1986, see Figure 1.3). This could not be accounted for by the gravitational clustering of matter as it was understood at the time, and required the Universe to be dominated by non-baryonic matter which allowed the clustering to happen faster than baryonic matter.

As these independent sources of evidence piled up, all converged and pointed to the irrefutable conclusion that there was a significant fraction of the mass in the Universe which we could not account for with matter as we knew it.

Our current understanding of the Universe, the standard ΛCDM cosmological model, incorporates dynamically cold dark matter as a key component (Blumenthal et al., 1982). In this model, dark matter is hypothesised to be a weakly interacting non-baryonic particle. After the Big Bang, the Universe expanded and large scale structure began to form through gravitational

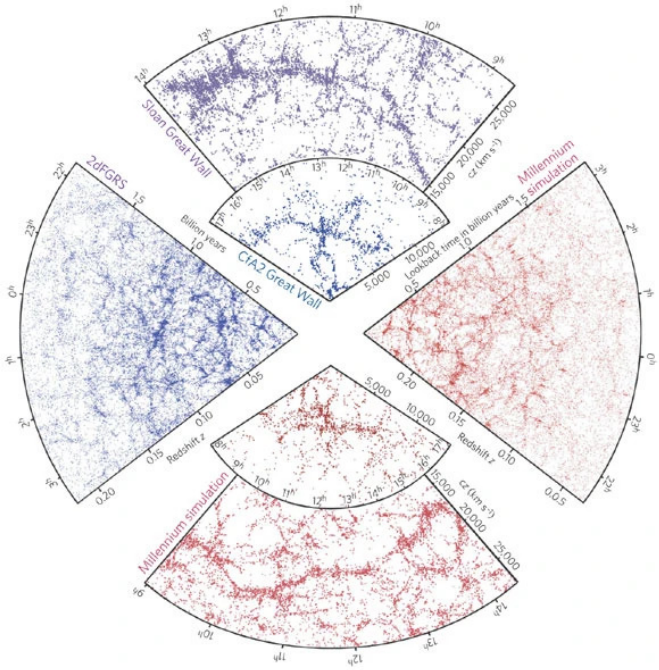

Figure 1.3: Summary plot from Springel et al. (2006) which shows large scale structure generated from simulation in the right and lower quadrants in red, compared with the observed large scale structure from two different surveys in the left and upper quadrants in blue and purple.

clustering around small perturbations in the matter density. As cold dark matter (CDM) is non-baryonic and doesn't interact dynamically, the underlying dark matter structure could evolve and collapse more quickly than the baryonic matter into filaments and knots and concentrated haloes of dark matter. As such, dark matter forms a sort of scaffolding for the Universe in the form of the Cosmic Web. It was this interconnected tangle of filaments which was seen to be traced by the distribution of galaxies in the redshift surveys. Due to the deeper potential wells generated by the dark matter concentrated in the knots and haloes where the filaments overlap, baryonic matter then fell into these regions, and it is here that galaxies begin to form (Einasto, 2009).

By running dark matter only simulations of the formation and evolution of the large scale structure, the exact cosmological parameters required to reproduce observations were pinned down (Davis et al., 1985) and the current paradigm of ΛCDM cosmology began to be widely accepted.

These dark matter haloes offered a solution to the problems seen in galactic dynamics. As stated in White & Rees (1978), it is now understood that "every galaxy thus forms as a concentrated luminous core embedded in an extensive dark halo". When simulated with dark matter alone, the structure of the haloes follow a universal radial density profile known as an NFW

profile (Navarro et al., 1996). As these haloes extend far beyond the luminous components, they offered an explanation of the flat rotation curves seen in the outskirts of galaxies where the dark matter would become most dominant. Simulations however are only as valuable as their ability to be tested against observations, this is crucial to establishing their accuracy and validity of the underlying physics. In this case, the form of these curves would depend on the structure of the haloes and behaviour of the dark matter, and so galactic dynamics allow observational tests of the simulated dark matter physics.

The ΛCDM model has been one of the most rigorously tested theories in scientific history, and on cosmological scales has proven to be extremely accurate (Bull et al., 2016). This is perhaps epitomised by the 2015 results from the Planck Collaboration which measured the parameters of the cosmological model describing the Universe to unprecedented accuracy, and found them to remain concurrent with theory (Ade et al., 2016). However the picture is still far from complete.

Despite the irrefutable evidence, we still do not know the nature of dark matter. The search for candidate particles has not yet succeeded. Alternative theories such as modified gravity (which posits that dark matter does not exist but accounts for the observational evidence through changes to how we understand gravity to work) still persist, though equally cannot fully explain all observed phenomena. On galactic scales we still encounter observational problems (Weinberg et al., 2015). One of the most striking of these is the apparent divergence from NFW profiles in the centre of dwarf galaxies, known as the cusp-core problem (de Blok, 2010). While simulations predict the halo density to peak sharply in the centre, observations have indicated a region in the centre of constant density (a core). Further, the so-called "missing satellite problem" describes the issue of simulations predicting hundreds of small subhaloes in the structure of haloes, whereas observationally we can only account for a dozen around the Milky Way (Klypin et al., 1999). These problems present a great challenge to our understanding of dark matter and the cosmological model. Attempts have been made to explain them through baryonic feedback affecting the dark matter distribution and gas accretion (Pontzen & Governato, 2012), or the problems could indicate more complex new physics relating to the behaviour of the dark matter itself (Egana-Ugrinovic et al., 2021; Paduroiu et al., 2015; Iwanus et al., 2017). As hydrodynamic simulations attempt to replicate these effects through changes to baryonic feedback physics or changes to dark matter physics, precise and accurate observations are essential. One key measurement is the dark matter (DM)

fraction of a galaxy, and ideally the spatially-resolved equivalent: the DM distribution. These quantities can be recovered through dynamical modelling.

1.3 Dynamical Modelling

Dynamical modelling is an incredibly useful tool for understanding the structure of a galaxy. In essence, the technique takes the distribution of light in a galaxy and uses this to infer the distribution of mass, and then predicts the motions which would be expected for this distribution, conditional on some other parameters. As galaxies contain a dark component, this prediction directly from the luminous mass fails to match the observed motions, and hence theoretical distributions of dark matter are often included in the "other parameters" part of the model in order to measure a dark matter distribution.

Within this general description, there are many types of dynamical modelling methods, each with their own advantages and disadvantages, in general they are grouped into two camps – one which handles Jeans equations and deals with the integrals of motion in bulk, and one which treats the system as a superposition of different orbits. Made to measure (M2M) and Schwarzschild methods belong to the second camp. These methods work to build detailed models of the gravitational potential of the system based on the mass distribution, tied to the light distribution and a dark component added. Then, in the case of the Schwarzschild method, generate a library of possible orbits in this potential; or, in the M2M method, create an n-body simulation of particles in the potential. These are then weighted and matched to reproduce the observed surface brightness distribution and the kinematics (Schwarzschild, 1979; Thomas, 2010). These models offer great accuracy and can model more realistic systems with triaxial potentials (van de Ven et al., 2008; van den Bosch et al., 2008), however are expensive and require deep observations of the kinematics of the system. This limits the number of systems to which this can be applied, however exhibit great successes where they are applicable (Cappellari et al., 2007; Kormendy & Ho, 2013; Yang et al., 2019; Santucci et al., 2022). In contrast to this, Jeans modelling requires only the lower order kinematic moments – the line of sight velocity and velocity dispersions – and so can be applied more widely to systems where this is available. Jeans modelling uses the equations of stellar hydrodynamics introduced in Jeans (1915), and directly integrates these for a given distribution function. However in order to make the integrals involved solveable, the potentials modelled require some restrictive assumptions such as axisymmetry, which limit the systems which can be modelled. This method

is described in detail in Section 2.6, as it is the method expanded upon in this thesis.

Dynamical modelling methods have been used successfully for decades to expand our understanding of galactic structure and mass content (Cappellari, 2015), and have been expanded upon by the inclusion of different tracers to allow more deep exploration into the dark matter potentials. For example the use of stellar kinematics combined with discrete tracers like globular clusters (Napolitano et al., 2014; Zhu et al., 2014, 2016) and/or planetary nebulae (Tremblay et al., 1995; Zhu et al., 2016), or continuous tracers like cold molecular gas (Tsukui et al., 2020) or neutral hydrogen (Yang et al., 2019). In the case of the use of continuous tracers, these have required resolved observations of the kinematic maps for these components, which are not available for a wide sample of galaxies. Unresolved observations of neutral hydrogen in galaxies are widely available (Haynes et al., 2011, 2018; Koribalski et al., 2020), and still contain information about the global cold hydrogen kinematics which can help in informing dynamical models. This could allow constraints on the dark matter halo of galaxies through tracing the potential at greater radii, while still being applicable to a statistically significant sample of galaxies. The potential information available in unresolved observations of cold gas in galaxies is detailed in Section 2.3, and in Chapter 4 I introduce and apply a method which combines Jeans modelling with unresolved neutral hydrogen observations.

Dynamical models deal with the dynamics of a galaxy in the moment that we observe them, which remain constant in the human timescales on which we view them, but by their very nature on longer timescales galaxies are evolving and changing.

1.4 Galaxies as Ever-Changing Dynamic Systems

If we consider a finite box in the Universe containing a finite amount of gas, and a finite amount of dark matter, we can give an overview of how a galaxy would move through its life stages if it were in complete isolation.

Under the influence of gravity, the material present would begin to cluster and collapse. As dark matter interacts only through gravity and doesn't collide or experience pressure, this component is able to condense and collapse more quickly than the gas which heats through pressure and and collisions as it collapses. The collapse of the dark matter component deepens the gravitational potential well, and allows the collapse of the baryonic gas component to occur more quickly than if the gas was present alone. We see evidence for this when we

look at how quickly structure is able to form in the history of the Universe – without a dark matter component, the material to create galaxies would not be able to cluster as quickly as we observe (Frenk & White, 2012). As the gas falls into a deepening potential well, it heats up, which slows the collapse process and prevents the gas from reaching the temperatures and densities required to form stars – this occurs through equilibrium between the gravitational forces encouraging collapse, and the thermal pressure resisting collapse. Further, as the gas is collisional, these collisions in the vertical plane leads to the gas collapsing into one plane as a thin rotating disk (Binney & Tremaine, 2008). As this accretion process continues, instabilities in the gas (Toomre instabilities, Parker instabilities, Kelvin-Helmholtz instabilities, etc: Toomre, 1964; Parker, 1966; Murray et al., 1993) cause the breakdown of equilibrium, and allow cooling through shocks, and the formation of dense clumps in the gas medium. These clumps can condense enough to collapse on themselves and form molecular gas clouds (HII regions), finally reaching densities required for stars to form – seeing the central core heat up enough through pressure that fusion can begin. Stars form in the medium according to an initial mass function which is set by the fragmentation process of the clouds (still a topic of research; Padoan & Nordlund, 2002; Larson, 2003). Depending on their mass, stars evolve through different life stages according to stellar evolution (beyond the scope of this thesis, see: Bodenheimer, 2003; Beccari & Carraro, 2015). Lower mass stars generate lower temperatures and appear more red due to their blackbody spectrum, and have long lifespans; while high mass stars generate higher temperatures and appear more blue, living considerably shorter lifespans. During their lifetimes, stars generate new nuclear elements through nucleosynthesis, ejecting some of these in stellar winds, and changing the interstellar medium (ISM) from just hydrogen into a mix of elements (Hensler, 2014). Further, the radiation generated by stars heats and ionises the ISM, creating a complex multiphase ISM (McKee, 1995). Massive stars reach their end through supernovae explosions which release vast amounts of energy into the surrounding ISM, heating and removing gas from the nearby regions through feedback. This feedback acts to slow star formation due to the injection of energy which acts against further cooling. Further feedback effects would impact our galaxy from AGN activity in the central regions (Bourne et al., 2014). Here, the density of material has become so high that there is a supermassive black hole present. When this object accretes material, it radiates vast amounts of thermal energy which heats the surrounding area, and can launch large scale jets which mechanically removes material from the system (Fabian, 2012a). In our idealised

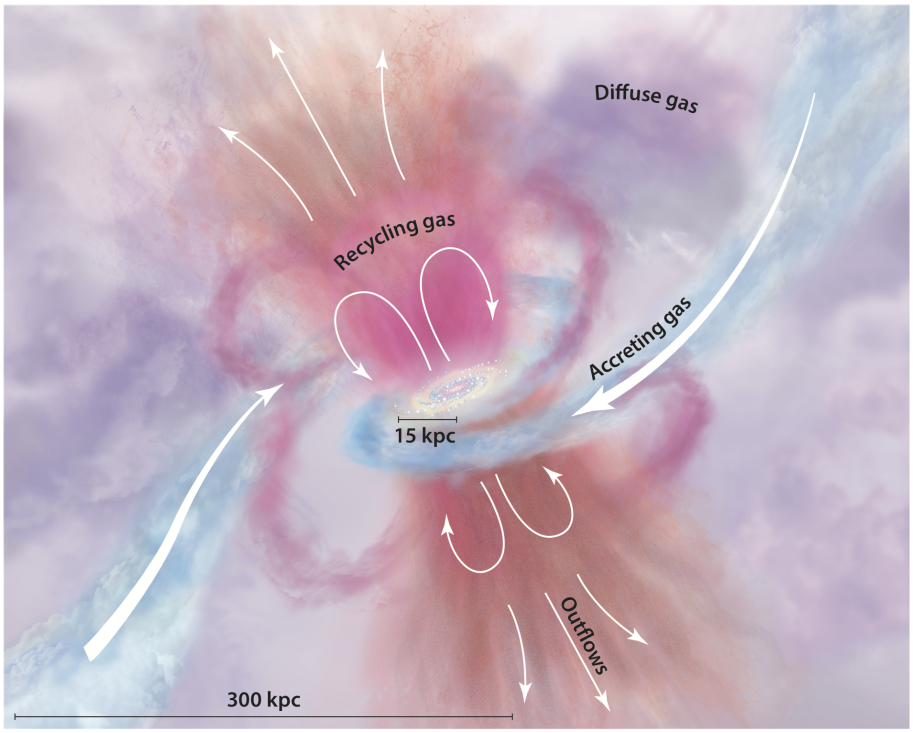

Figure 1.4: From Tumlinson et al. (2017). An illustrative schematic of the gas cycle in galaxies through the circumgalactic medium (CGM). A galaxy is fed by filamentary accretion of fresh gas from the intergalactic medium (blue), while outflows remove gas from the disk in pink and orange, and pink gas shows ejected gas being re-accreted. The purple background tones represent the diffuse gas halo, which is a mixed contribution of all these sources.

finite box with finite material, this "galaxy" would continue to evolve through generations of massive stars living and dying, injecting their material and energy into the ISM, before this material cooled again and cycled into more stars. Star formation would also be impacted by periodic eruptions of feedback from the AGN. These effects together create the gas cycle we see in galaxies (see Figure 1.4), where gas is recycled. Gas would be cycled from existing in the ISM, to being used in stars, to being ejected into the circumgalactic medium (CGM) by feedback processes, before cooling again back to the ISM – becoming more metal-rich each time through nucleosynthesis. Eventually, in the absence of new gas being accreted, the system would run out of hydrogen gas to fuel new generations of stars, and the underlying population of long-lived low-mass red stars would remain. Without further injection of fresh hydrogen gas into the system, this would leave a "red dead" galaxy as we see in the galactic demographics.

However galaxies in the real universe do not exist in isolated finite boxes, and as such can be considered to have fresh gas available to accrete. This allows galaxies to continue to form stars past the depletion of their original reserves, but is also balanced by gas which is not recycled but is fully removed from the potential well and lost to the surroundings. This

raises the question of how galaxies remain quenched when there is still gas available – this is addressed, in part, in Chapter 3. Also, there is the question of morphological evolution – ie. the change from spiral disks to spheroidal ellipticals. This is difficult to address for a galaxy in isolation, though there are some secular processes such as bar formation which thicken the disk and lead to more elliptical morphologies (Gadotti, 2009, 2011; Kormendy, 2013, 2016).

1.5 Environmental Effects

In the real Universe, galaxies exist as part of a full ecosystem, with their environment – the local Universe around them – varying greatly from galaxy to galaxy. Some exist in dense clusters, interacting with many other galaxies; some are in smaller group environments; while others are isolated in the field. Many features of galaxies are seen to correlate with their environmental density, which is why we observe environment to be one of the leading factors in determining the evolutionary path of a galaxy, and how they quench, as galaxies interact with their surrounding structures (or lack thereof).

Galaxies in low density environments, which lack sources for new gas (Aragon Calvo et al., 2019), suffer from starvation. This is the closest to our idealised finite box situation described above. With the absence of a supply of fresh gas, these galaxies simply deplete their gas reservoirs until no new stars can form. Further, with no nearby galaxies to interact with, these galaxies avoid any external evolutionary factors such as merging and harassment, and evolve secularly. These are often distinct from those affected by other quenching mechanisms, such as interactions, as their disk structures are preserved Masters et al. (2010).

Galaxies existing in more dense environments where new gas is available either through cold streams or through interactions with other galaxies, are replenished with fresh gas. The effects in these regions are multifaceted. While there is more gas being fed to galaxies here which can fuel further star formation and avoid starvation Darvish et al. (2014), the newly accreted gas can shock as it enters the galaxies and feed directly to the central SMBH (Dubois et al., 2013). This triggers AGN feedback which can quench star formation through heating and ejecting gas. Further, the motion of the galaxies relative to any gas in the nearby environment has been shown in simulations to be able to cause stripping of the gas due to the Kelvin-Helmholtz effect at the edge of gas disks, and ram pressure stripping effects removing gas from the system (Winkel et al., 2021). In these more dense environments galaxies also interact more

often with other galaxies – whether through glancing blows defined as "harassment", which perturbs the distribution of material in a pair of galaxies, affecting star formation, adding non-axisymmetric structures, and disrupting disks (Moore et al., 1996; Bialas et al., 2015); or through major mergers, which have the effect of providing new gas to fuel star formation, but also heating and removing gas reservoirs, and catastrophically disrupting disk morphologies (Struck, 1999; Lambas et al., 2012; Ellison, 2019). Indeed, we see observationally that galaxies with closer proximity to denser filaments tend to be more likely to be quenched than those further away (Chen et al., 2017; Kraljic et al., 2018), though some studies show that galaxies become more massive nearer filament centres while remaining bluer than those in denser cluster environments (Lee et al., 2021).

The trend of denser environments hosting a higher fraction of quenched galaxies extends to the densest of environments – clusters. In these environments, galaxies suffer not only the harassment and merging seen at intermediate densities, but the intracluster medium (ICM) hosts hot dense gas which has heated due to collapse into the cluster potential, and has also been heated due to the processes which have expelled this gas from galaxies in the cluster – high metallicities in the ICM are a consequence of the gas being ejected from galaxies. This gas is hot enough to emit in the x-ray regime, allowing us to observe its high density (Sarazin, 1986). A consequence of the density and velocity dispersion of this gas is the effect of ram pressure stripping (RPS) on galaxies which are infalling into the cluster environment. These galaxies are not in virial equilibrium with the cluster, so often have extremely high velocities relative to the cluster – this, combined with the density of the medium, generates a pressure force on the material in the infalling galaxy. This force is proportional to the density of the medium and the relative velocity and causes the heating and removal of material from the galaxy, most strongly affecting the most diffuse elements, pushing the material out of the system and into a trail behind the galaxy. Sometimes this effect is so extreme that the material left in the tails is dense enough to be observed, and even so dense as to host star formation outside the galaxy (Kenney & Koopmann, 1999; Roediger, 2009; Poggianti et al., 2017, 2019a; Gullieuszik et al., 2023; Giunchi et al., 2023; Waldron et al., 2023). These systems are known as "jellyfish" galaxies, and the study of the quenching process in these is the subject of Chapter 5. This, along with the other consequences of existing in a cluster environment, leads to a much higher rate of quenching for galaxies in these environments.

1.6 Spatially Resolved Evolution

Based upon the presence or lack of certain emission lines, absorption lines, and other spectral features, we can determine the evolution stage of a galaxy – and with resolved observations, we can do this for spatially resolved parts of a galaxy (Wilkinson et al., 2015). As more massive, hotter, bluer stars have a shorter lifetime than less massive, redder stars, their presence is an indicator of recent star formation – with the signatures of the most massive stars being signs of current ongoing star formation. This is the most simple inference we can make, however this technique expands to full spectral modelling of the spectral energy distribution (SED) for a spaxel of a galaxy. This uses a library of possible template spectra from different masses, ages, and metallicities of stars, and fits the observed spectrum with different weights of these templates in order to infer the underlying stellar population which has produced the SED. This allows a determination of the age of the population, the metallicity, and the star formation history (SFH) of the region (Conroy, 2013). This is an invaluable tool which allows studies of how quenching takes place in galaxies spatially, and how this varies for galaxies in different environments with different histories – helping understand which different processes cause quenching.

Beyond just classifying spaxels as star forming or quenched, this also allows the speed at which the quenching has occurred to be taken into account – this leads to a specific classification known as "post-starburst" (PSB Tran et al., 2004; Quintero et al., 2004; Le Borgne et al., 2006; Kaviraj et al., 2007). These regions have spectral signatures which show that they have undergone a recent burst in star formation before rapidly quenching, and are of particular interest to understanding processes which could cause rapid shutdown of star formation (Dressler & Gunn, 1983; Wild et al., 2009; Chen et al., 2019a) – often indicating environmental processes (Li et al., 2023). There have been studies which have noted that jellyfish galaxies and other galaxies in clusters show signatures which suggest post-starburst star formation histories (Poggianti et al., 2019a), and have looked at global spectra to indicate this. Others have seen post-starburst signatures in the outer parts of disks as gas is stripped away. This suggests that post-starburst classifications of spaxels in resolved observations of jellyfish galaxies could illuminate the processes taking place. This is explored in a sample of jellyfish galaxies introduced in Chapter 5 which exhibit PSB signatures in regions consistent with their motion through a cluster.

1.7 This Thesis

This thesis will describe and present the results of the work I have completed. This work focuses widely on understanding the structure and evolution of galaxies as dynamical systems, through combining observational data of the stars in a galaxy with observations of other components – for example, the gas.

In Chapter 2 I describe some methods which are used across the following Chapters, including the basis for observations that are used, dynamical modelling methods, statistical methods and spectral analysis. In Chapter 3, I use dynamical models to constrain the inclination of Red Geyser galaxies in order to predict the shape of their spectral lines depending on whether the observations we see are due to outflows or due to a rotating disk. In Chapter 4, I build upon the use of dynamical models, this time adding a dark matter component, and showing proof of concept for a novel method which incorporates cold gas observations in order to improve the measurement of the dark matter content in a large sample of galaxies. In Chapter 5, I expand into considering the stellar populations and evolution of galaxies in cosmic time through the study of post-starburst signatures in a sample of jellyfish galaxies – galaxies which are experiencing extreme environmental effects due to infall into a dense environment. Finally, I summarise the results of Chapters 3 - 5 in Chapter 6, discuss their implications, and set out my vision for how these concepts can be built upon in future with the observations we have currently and the observations we will have in the future.

2

Observations, Methods, and Data

Suggested listening: O-o-h Child by Nina Simone

This chapter will set out the theory behind modelling methods, spectroscopic methods, and tools which are used across multiple further chapters in this thesis. Sections 2.1, 2.2, 2.3 and 2.4 will describe the observational methods which generate the imaging data, optical integral field spectroscopic (IFS) data, 21cm radio, and low frequency data used across the

Chapter image: Sloan 2.5m Telescope, SDSS

following chapters, and introduce the data used. Section 2.5 describes the multi-Gaussian expansion (MGE) method of parameterising surface brightness distributions which is central to mass modelling techniques. The Jeans Anisotropic Modelling technique is described in Section 2.6, and the numerical fitting methods used to fit these models to data are described in Section 2.7. Section 5.3.1 describes how spectral indices are used to identify signatures of post-starburst star formation histories in galaxies. These methods are essential to the following chapters, and so are explained here as they are threaded through the following work.

2.1 Astronomical Images

The most simple, and oldest, means of studying the night sky is through the use of our eyes. Our eyes work by collecting photons, and focusing them on a focal plane so we end up with a spatial map of surface brightness. Optical telescopes also act as photon collectors to enhance what can be seen of the night sky by collecting more photons, and focus these images into the focal plane to allow 2D projected distributions of surface brightness to be realised. In the focal plane, these images can be recorded on photographic plates, or digitally recorded by (charge coupled devices) CCDs which convert the photons collected into an electronic signal. For extended objects such as galaxies, this is important to understand their morphologies. Further, use of wavelength filters allow imaging to localise where certain energies of light are coming from in a 2D image of an object.

2.1.1 DESI Legacy Survey

The DESI Legacy Imaging Survey (hereafter The Legacy Survey; Dey et al., 2019) is an optical wide-field imaging survey, which was motivated by the need to provide targets for the Dark Energy Spectroscopic Instrument Survey (DESI survey; Aghamousa et al., 2016). As the DESI survey aims to spectroscopically measure redshifts of 35 million galaxies and quasars in order to map large scale structure, many of the desired targets require greater imaging depths for selection than previous wide-field surveys have provided (eg. SDSS and Pan-STARRS; Abazajian et al., 2009; Chambers et al., 2016). The data generated by such a deep wide-field survey also has wide-reaching secondary benefits and applications. In this instance, the provision of deep imaging data for a large sample of galaxies which are also present in IFU surveys such as MaNGA (see Section 2.2.1) is extremely useful for dynamical modelling, as we see in Chapters 3 and 4. As the modelling process relies on optical imaging to ascertain the surface brightness

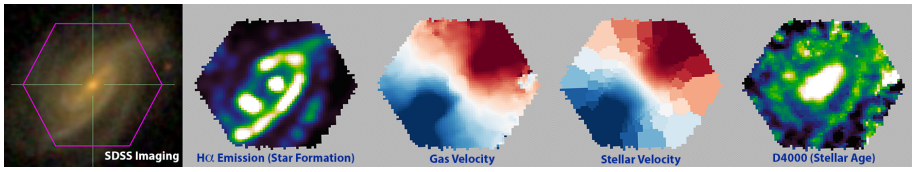

Figure 2.1: Diagram from SDSS MaNGA illustrating the data products produced by integral field spectroscopy for one galaxy.From left to right: colour imaging of the galaxy, with the pink hexagon highlighting the region covered by the MaNGA IFU; map of the Hα emission which traces star formation, this is seen to be stronger in the arms of the spiral galaxy; map of ionised gas velocity map showing rotation; stellar velocity map showing rotation aligned with that of the gas; map of the spectral index D4000 which quantifies the ratio of two parts of the spectrum, a proxy for stellar age as a higher D4000 value indicates an older stellar population.

of the galaxy, which is then used to approximate the stellar potential, deeper imaging is crucial to ensure this element is accurate. Deep imaging is also key to capturing any diffuse disturbed optical components in the outskirts of galaxies which are undergoing tidal disruption or ram pressure stripping, such as jellyfish galaxies (as seen in Chapter 5).

The Legacy Survey is comprised of three imaging surveys conducted across three different telescopes, providing *g*-, *r*-, and *z*-band optical images for use in target selection for the DESI spectroscopic survey. These are the Beijing-Arizona Sky Survey (BASS; Zou et al., 2017), the Dark Energy Camera Legacy Survey (DECaLS; Flaugher et al., 2015) and the Mayall *z*-band Legacy Survey (MzLS; Dey et al., 2016). In this thesis, the work was conducted when Data Release 9 (DR9) was the most current release of the survey, so all imaging used is from this release. The images have a pixelscale of 0.27 arcseconds/pixel, and the point spread function full width half maximum (PSF FWHM) is obtained manually for each image by fitting a 2D gaussian to point sources in the field around the galaxy (on average 3.32 pixels, or ~ 1 arcsecond). DR9 also includes a catalog for objects in the survey, with photometric quantities such as fluxes and magnitudes. These quantities are used for verification checks in some of the analysis performed in Chapter 4.

2.2 Integral Field Spectroscopy and Derived Quantities

One of the greatest advances in astronomy was the switch from simply "taking pictures" with telescopes, to using spectroscopy to study derived quantities from the light emitted. This has been taken even further through the use of Integral Field Units (IFUs) which allows a galaxy to be split into multiple pixels in the field of view, with a spectrum produced for each pixel (known as a "spaxel"). Each spectrum can then be used to derive physical quantities for each spaxel (for example, the emission at certain wavelengths, the gas or stellar velocities, different

emission line indices, etc – see Figure 2.1 for examples), in essence mapping a chosen quantity spatially across a galaxy. This has revolutionised studies of galaxies.

Optical telescopes can be considered as "photon collectors", and observations started from this point. If a telescope is pointed at an astronomical object, photons can be collected and used to infer a brightness or luminosity of the object. A step further than this used photographic film or CCD detectors to collect photons from different points in the focal plane, and produce a 2D distribution of photon counts – an image. This reveals the spatial distribution of surface brightness in extended objects such as galaxies, and allows the morphology of these objects to be studied. Many surveys have been conducted to image objects across the sky and were revolutionary to our understanding of astronomy at their time (Lund & Dixon, 1973; Skrutskie et al., 2006; Abazajian et al., 2009; Blanc et al., 2010; Cuillandre et al., 2012; Chambers et al., 2016; Dey et al., 2019). Still, imaging is bringing key developments in our understanding of galaxy evolution as we extend our imaging capabilities to high redshifts and the early universe (Eisenstein et al., 2023; Williams et al., 2023). By pairing this technique with filters which only allow certain wavelengths of light to pass through to the detector, different elements of galaxies could be studied. For example, a narrow-band filter can be used to collect photons of the wavelength corresponding to emission from ionised hydrogen, and this can be seen to coincide with brighter areas of star formation (O'Dell, 2001). Building upon this, spectroscopy takes the light collected from an observation and splits it finely by wavelength in order to produce the spectrum of light collected. The spectrum of a star or galaxy shows the distribution of energy emitted by the object as a function of wavelength, and allows access to quantities which are not available from imaging alone – however, prior to integral field spectroscopy (IFS), these observations lacked spatial resolution and would simply give the spectrum of the whole object – or at least the central regions covered by the aperture of a single fibre – and not how it changes over the object. Nonetheless, this still allows essential quantities to be measured, such as redshift which is encoded in the shift of emission and absorption lines, or velocity dispersion (i.e. the spread of velocities around the mean velocity) which is encoded in the width of emission lines. Redshift surveys (Huchra et al., 1983; Huchra & Geller, 1991; Hahn et al., 2023) revolutionised our understanding of large scale structure in the Universe as they allowed the distribution of galaxies in 3D space to be fully realised for the first time. Spectroscopy also allows information about the stellar populations of a galaxy to be derived, such as star formation rates, through comparison of the spectrum to libraries of stellar spectra

(Maraston, 2013).

Integral field spectroscopy combines these two strengths to allow spectroscopic information to be recovered with spatial resolution. This has been implemented across many galaxy surveys to produce detailed derived information for thousands of galaxies (de Zeeuw et al., 2002; Bacon et al., 2010; Cappellari et al., 2011; Sánchez et al., 2012; Bryant et al., 2015). In terms of dynamics, while unresolved spectroscopy allowed measurement of the line-of-sight velocity dispersion, IFS dramatically increased the information available as we now have access to the 2D internal kinematics of the systems, for stellar and gaseous components.

2.2.1 The MaNGA Survey

Particular to this thesis, the SDSS-IV survey Mapping Nearby Galaxies at APO (MaNGA; Bundy et al., 2015) implements IFS technology using optical fibre bundles and a plate in the focal plane of the 2.5m Sloan Telescope (Gunn et al., 2006). The system has 17 bundles which can be used to observe multiple objects in the field of view in one pointing. The plates are uniquely drilled with holes to cover targets in the field of view, and each hole is then fed a hexagonal bundle of between 19 to 127 optical fibres (Drory et al., 2015) which cover the galaxy from the centre out to 1.5 to 2.5 effective radii (Wake et al., 2017). Each spaxel placed across the galaxy gives a spatial sampling of 1-2kpc, and observes a spectrum from 3600 Å to 10000 Å with a spectral resolution of around 60km/s (Smee et al., 2013). With the final MaNGA data release, the survey successfully observed 10,010 galaxies (Abdurro'uf et al., 2022), providing an extremely significant sample for understanding galaxy evolution and dynamical modelling.

The spectra obtained from IFS observations must be analysed in order to derive physical properties. In general terms, this is done using spectral fitting, and varies by survey. For the purposes of this thesis, as I use MaNGA survey data for IFS data, I outline here how this is done for this survey. MaNGA has its own data analysis pipeline (DAP; Westfall et al., 2019) which generates the derived quantities. The DAP calculates the signal to noise ratio (SNR) and other quality assurance quantities for the spectra, before spatially binning the data, measuring the stellar kinematics, and fitting models to the emission lines to derive emission line properties. In order to create accurate measurements of stellar kinematics, high SNR is required, and so an adaptive binning scheme is used which combines spectra from nearby spaxels in order to reach a chosen SNR of 10. This is the voronoi binning scheme, described in Cappellari & Copin (2003). In order to fit the stellar kinematics and emission lines, the DAP uses the penalised

pixel fitting (pPXF; Cappellari & Emsellem, 2004; Cappellari, 2017) method, which considers the galaxy spectrum to be a superposition of different individual stellar spectra contained in a library (in this case, the MILES stellar-template library; Sánchez-Blázquez et al., 2006; Falcón-Barroso et al., 2011). These are convolved with kinematics and then fit to the observed spectrum to give derived DAP quantities, which include 2D maps of kinematics (line-of-sight velocity, and velocity dispersion), alongside equivalent widths and fluxes of different emission lines. MaNGA IFU data are used in Chapters 3, 4, and 5, with the specific data products used in each case described within.

2.3 Observing Hydrogen and Deriving Quantities

Hydrogen is the most abundant chemical element in the Universe, and is essential to galaxies as it is the reservoir from which stars are formed. In its simplest form, neutral atomic hydrogen (H I) consists of a single proton and a single electron, and this exists in many galaxies in a thin, regularly rotating disk (Morganti et al., 2006b; Oosterloo et al., 2010). H I does not emit light in optical wavelengths so cannot be observed with optical telescopes, however the electron present in the atom can inhabit two energy states defined by the alignment of the electron spin with that of the proton. When this electron changes spin (known as a spin-flip transition), a photon is emitted with a wavelength of 21cm (see Figure 2.2). This wavelength is in the radio regime and detectable by radio telescopes, and has played a large role in our understanding of galaxies and the Universe more widely (Dutta, 2019; Ouchi et al., 2020; Moazzenzadeh & Firouzjaee, 2021; McClure-Griffiths et al., 2023). As the angular resolution of a telescope is given by $R = \lambda/D$, (where R is the angular resolution in radians, λ is the wavelength of the light, and D is the diameter of the telescope), radio observations are inherently limited in their spatial resolution, and a single radio telescope on the scale we can currently engineer does not achieve meaningful angular resolution to map quantities across a galaxy, and is considered spatially unresolved.

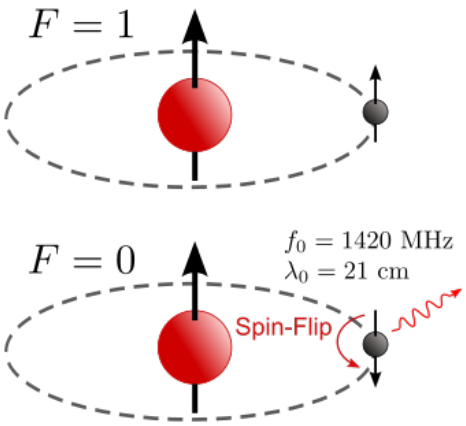

Figure 2.2: Schematic showing the set up of a neutral hydrogen atom with one proton and one electron, and the mechanics of the spin-flip transition which allows it to emit at 21cm. Source: Wikimedia Commons

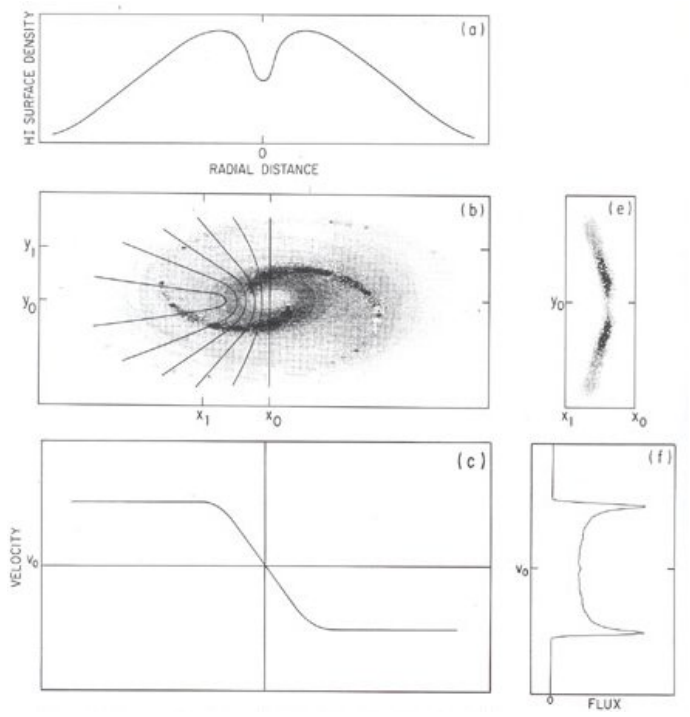

Figure 2.3: Schematic from Giovanelli & Haynes (1988) showing how a rotating disk of H I in a galaxy produces a double-horned profile in a 21cm spectrum. **Panel b**: the gas density in an idealised rotating spiral galaxy, with contours on the left half showing lines of equal velocity. **Panel a**: gas surface density along the major axis of the galaxy. **Panel c**: the rotational velocity of the galaxy along the major axis. **Panel e**: the gas surface density seen in one narrow channel of the spectrum, this selects only gas which is moving within the velocities in this channel, and so echoes the form of the lines of equal velocity. **Panel f**: the full spectrum of the galaxy, highlighting the double-horned form created by the rotation.

This means the data produced by observing a galaxy at 21cm is often a single spectrum for the whole system, as the resolution is on the order of multiple arcminutes.

Despite offering different information than resolved optical astronomy, the data collected by single-dish radio astronomy contains a wealth of information about the hydrogen in galaxies, encoded in the shape of the 21cm emission line (Giovanelli & Haynes, 1988). For a galaxy with its neutral hydrogen distributed in a perfectly thin, uniform, regularly rotating disk, an observed 21cm spectrum will exhibit a characteristic double-horned profile due to the geometry and kinematics (see Figure 2.3). In the outer regions of a galaxy where the hydrogen extends to, the rotation curve flattens and so large amounts of the H I gas will be moving at the same velocity, and so we see two distinct peaks in H I flux which is redshifted and blueshifted away from the 21cm line as per the Doppler effect. As the rotation and distribution is symmetric, theoretically this profile should also be symmetric. Deviations from the symmetry of the line profile can be attributed to asymmetries in the spatial distribution of the gas in the disk, or disturbances in the rotation, and work has been done to extract as much information

from modelling these profiles as possible (Richter & Sancisi, 1994; Haynes et al., 1998; Laine & Gottesman, 1998; Saintonge, 2007; Nelson, 2009; Stewart et al., 2014). Contained in the profile is the mass of H I present, which is proportional to the flux integrated under the profile (F_{H_I}), and is recovered as per Springob et al. (2005), by the equation (Masters et al., 2014):

$$\left(\frac{M_{H_I}}{M_\odot}\right) = 2.356 \times 10^5 \left(\frac{D}{Mpc}\right)^2 \left(\frac{F^c_{H_I}}{Jykms^{-1}}\right) \tag{2.1}$$

where $F^c_{H_I} = cF_{H_I}$ and $c = (a/b)^{0.12}$, where a/b is the axial ratio of the galaxy.

As the peaks of the double horned profile correspond to the maximum velocity then the full linewidth corresponds to twice the rotational velocity (Roberts, 1978). There are multiple methods to measure this width in the literature (see Masters et al., 2014), however W_{F50} (the width measured between polynomial fits to the sides of the profile at 50% of the peak minus the root mean squared (rms) noise) is considered most robust to noise and so is used in this work (Giovanelli et al., 1997; Springob et al., 2005). The error on the width is found as:

$$\epsilon_{W_{F50}} = \sqrt{\left(\frac{rms}{a_l}\right)^2 + \left(\frac{rms}{a_r}\right)^2} \tag{2.2}$$

where a_l and a_r are the slopes of the polynomial fits to the left and right sides of the profile, and rms is the root mean squared noise in each channel in the signal-free part of the spectrum.

In order to recover the rotational velocity from W_{F50}, the value must be corrected for multiple effects, as outlined in Springob et al. (2005). The signal must be smoothed (see Springob et al., 2005, for details), and the measured width corrected for instrumental and noise effects, corrected for redshift stretch and corrected for turbulence. This means the corrected width (W_c) is given by:

$$W_c = (W_{F50} - 2\Delta v\lambda)/(1+z) - W_t \tag{2.3}$$

where Δv is the channel width in kms^{-1}, z is the redshift, W_t is a linear correction for turbulence which is given as $6.5kms^{-1}$, and λ is a value which depends on the signal to noise ratio:

$$\lambda = \lambda_1(\Delta v) \quad \text{for } \log(SNR) < 0.6, \tag{2.4}$$

$$\lambda = \lambda_2(\Delta v) + \lambda_2^{'}(\Delta v)\log SNR \quad \text{for } 0.6 < \log SNR < 1.1, \tag{2.5}$$

$$\lambda = \lambda_3(\Delta v) \quad \text{for } \log SNR > 1.1. \tag{2.6}$$

The values for λ_1, λ_2, $\lambda_2^{'}$ and λ_3 are constant where $\Delta v < 5 kms^{-1}$ and $\Delta v > 11 kms^{-1}$, but depend on Δv at values in between these. λ_1, λ_2, $\lambda_2^{'}$ and λ_3 are given as follows: $\lambda_1 = 0.037\Delta v - 0.18$, $\lambda_2 = 0.0527\Delta v - 0.732$, $\lambda_2^{'} = -0.027\Delta v + 0.92$, and $\lambda_3 = 0.023\Delta v + 0.28$.

And finally to correct for viewing angle (i) and retrieve the intrinsic rotational velocity,

$$v_{rot} = W_c / \sin i. \tag{2.7}$$

As the H I data is unresolved, and the beam of the observation is on the order of arcminutes, the data does not directly specifiy the radius at which this rotational velocity measured. However, an estimation of the radius probed by this observation can be obtained by using the well-studied H I mass-size relation (Broeils & Rhee, 1997; Wang et al., 2016), given as:

$$\log D_{H_I} = 0.51 \times \log M_{H_I} - 3.32 \tag{2.8}$$

where D_{H_I} is defined as the diameter, in kpc, at which the surface density of the gas reaches 1 $M_\odot pc^{-2}$, with M_{H_I} in units of $M_\odot pc^{-2}$, and the radius R_{H_I} simply being half of this diameter.

To acquire radio data with spatial resolution, radio arrays are required as these offer the benefits of interferometry – exploiting the fact that the angular resolution equation can also be presented as $R = \lambda/B$ where B is the length of the baseline of an array of radio telescopes. By spreading individual radio telescopes out in an array over large distances, smaller angular resolution and spatially resolved data can be produced. This can be used to produce images of the H I distribution in the sky (van Haarlem et al., 2013; Koribalski et al., 2020; Shimwell et al., 2022), or 2D distribution and kinematic maps for individual galaxies (Franx et al., 1994; Schoenmakers et al., 1997; Wong et al., 2004; Thean et al., 1997; Duffy et al., 2012; Yang et al., 2019; Eibensteiner et al., 2023) similar to those produced by IFU data for stellar kinematics (see Section 2.2). The details of how interferometric data is reduced and how physical quantities are derived from their datacubes is beyond the scope of this thesis, the

reader is directed to Chapter 7 of Bradt (2004).

H I surveys specific to this thesis are outlined below as the dataproducts are used in the following chapters.

2.3.1 H I -MaNGA

Given the importance of neutral hydrogen in galaxies as the reservoir of fuel for star formation, a major component of the interstellar medium, an extended dynamical tracer, and a signal for environmental disturbance, the combination of stellar IFU observations with H I observations can offer incredible synergy in many fields of study (star formation, quenching processes, environmental interactions, dynamics, etc). As such, followup surveys which aim to provide deep H I observations for samples of galaxies which already have optical IFU observations are of great value. This is seen in the SAMI-H I survey in the southern hemisphere (Catinella et al., 2023), and in the H I -MaNGA survey in the northern hemisphere (Masters et al., 2019; Stark et al., 2021).

H I -MaNGA is a follow-up programme dedicated to providing 21cm H I radio observations and upper limits for as many of the galaxies observed in the MaNGA survey as can be targeted (see description in Section 2.2). This is done through a combination of matching existing H I observations from the ALFALFA survey (Arecibo Legacy Fast Arecibo L-band Feed Array; Haynes et al., 2011, 2018), and performing new observations using the Robert C. Byrd Green Bank Telescope (GBT; under project code AGBT16A_095). The GBT observations provide single dish data with a beam full width half maximum of 8.8 arcminutes, and a spectral resolution of 1.2 km/s which is reduced to an effective spectral resolution of 10km/s after smoothing. The reduced and calibrated spectra are produced using the `GBTIDL` package, and global properties such as H I mass and WF50 are derived as per the methods mentioned above in this section. These are then published. As of DR3 (released as part of MaNGA DR17; Abdurro'uf et al., 2022), data is publicly available for 6358 unique galaxies in the MaNGA survey. This data is used in Chapter 4.

2.4 Low Frequency Observations

The LOFAR Two Metre Sky Survey (LoTSS; Shimwell et al., 2017) is using the Low Frequency Array (LOFAR; van Haarlem et al., 2013) to image the whole northern sky at frequencies of

120-168 MHz, to a resolution of 6 arcseconds. This is achieved by using LOFAR to tile the sky, with beam of full width half maximum $\sim 4°$, with pointings using 8hr observing times in order to achieve a depth of $\sim 100\mu$Jy/beam. This is important for studying the radio properties of galaxies, as 144MHz frequencies trace thermal emission from plasma in H II regions of star forming galaxies, but are dominated by non-thermal synchrotron emission from relativistic cosmic ray electrons (CRe) accelerated by supernovae Condon (1992). CRe can be moved within the galaxy before emission can take place through synchrotron interaction with magnetic fields, and so can result in extended emission. In the case of galaxies in clusters which are experiencing ram pressure, CRe are transported by advection from the ram pressure wind (Murphy et al., 2009; Vollmer et al., 2013), and so these galaxies exhibit extended tails in 144MHz images (Roberts et al., 2021; Poggianti et al., 2016a) (and in other tracers, including ionised and molecular gas, UV stellar light, and X-ray emission; see Poggianti et al., 2019b; Cramer et al., 2019). This allows LoTSS to be used to identify galaxies being stripped in clusters. This data is used in Chapter 5 for this purpose.

2.5 Multi-Gaussian Expansion

To understand and model the motions in a galaxy, the gravitational field has to be described mathematically, which follows from the mass distribution. Galaxies are, for all practical purposes, infinitely complex systems with structure at every scale. This doesn't lend itself well to creating mathematical models, so as in many fields of physics we must use approximations. We first assume that in regions where galaxies are luminous enough to be detected, the mass distribution is dominated by luminous mass (i.e. stars), and so assume that the mass distribution and light distribution are one and the same. This allows simply an image of a galaxy showing the surface brightness distribution to be converted via a mass-to-light ratio (which is assumed to be constant) into a mass distribution and therefore infer the gravitation potential. In our method, we leave this mass-to-light ratio to be fitted based on the data, however note that another option would be to fix this to values derived from stellar population analysis. This doesn't resolve the issue of describing the distribution. The method of using a Multi-Gaussian Expansion (MGE) in order to approximate the distribution in a way which lends itself to analytical mathematics has been used widely since it was introduced in Monnet et al. (1992) (and streamlined for use in galactic kinematics in Emsellem et al., 1994; Cappellari, 2002). This method involves parameterising the observed surface brightness distribution of a galaxy as a

set of 2D concentric elliptical Gaussians, with a constant position angle. The use of Gaussians means convolving the result with a PSF to take seeing into account, and deprojecting the result from an observed distribution into an intrinsic distribution, can be done analytically which is more efficient. Further, the potential can be obtained with a single integration, while more are required for other parameterisations, and velocity moments from Jeans equations can be found with a double integration instead of triple.

As this thesis restricts its use of dynamical modelling to the Jeans Anisotropic Modelling (JAM) method, this section sets out the theory of MGE models for the axisymmetric case only – bypassing the more complex cases of triaxial distributions (for this, see; Cappellari, 2002).

First we define a coordinate system which is projected on the sky, $(x^{'}, y^{'}, z^{'})$, with $z^{'}$ pointing along the line of sight towards the observer, and $(0,0,0)$ being the centre of the galaxy. In this system, the projected surface brightness can be expressed as a sum of Gaussian components:

$$\Sigma(R',\theta') = \sum_{j=1}^{N} \frac{L_j}{2\pi\sigma_j^2 q_j'} \exp\left[-\frac{1}{2\sigma_j^2}\left(x_j'^2 + \frac{y_j'^2}{q_j'^2}\right)\right] \tag{2.9}$$

Here, N is the number of Gaussian components added in superposition to create the MGE, L_j is the total luminosity of each Gaussian, q_j' is the observed axial ratio of each Gaussian (ranging between 0 and 1), σ_j is the width of the major axis of the Gaussian, and ψ_j is the position angle of the major axis counterclockwise from y' axis. (R',θ') are the polar coordinates on the plane of the sky, so that:

$$\begin{aligned} x_j' &= R'\sin(\theta' - \psi_j) \\ y_j' &= R'\cos(\theta' - \psi_j) \end{aligned} \tag{2.10}$$

This surface brightness is then deprojected to recover the intrinsic surface brightness distribution. Assuming oblate axisymmetric geometry, the intrinsic luminosity density of a single Gaussian component of the MGE (the sum is omitted but implied), can be written as:

$$\rho(x,y,z) = \frac{L}{(\sigma\sqrt{2\pi})^3 q} \exp\left[-\frac{1}{2\sigma^2}\left(x^2 + y^2 + \frac{z^2}{q^2}\right)\right] \tag{2.11}$$

where the (x,y,z) coordinate system used here are such that the x-axis is aligned with the long axis of the Gaussian and z-axis is aligned with short axis, σ is the observed major axis

width, and q is the intrinsic axial ratio. The intrinsic axial ratio is obtained from the observed axial ratio in the oblate axisymmetric case by:

$$q^2 = \frac{q'^2 - \cos^2 i}{\sin^2 i} \tag{2.12}$$

for a galaxy viewed at inclination i, where $i = 90°$ is edge on.

As such, by iteratively fitting stacks of Gaussians to photometry from imagery, the intrinsic surface brightness distribution can be described by 3 N-dimensional vectors (where N is the number of Gaussians), the luminosity of the Gaussian components, the width of the Gaussian components, and the axial ratio of the Gaussian components.

In order to correctly compare this model to the observations, the model must be convolved with the instrumental PSF of the observation, and the PSF caused by the atmospheric seeing. We assume the PSF to be a circular Gaussian which is defined by a width σ_{PSF}. The luminosity of the MGE is unaffected by the PSF, but the width (σ_j) and the axial ratio (q_j) are altered, to their convolved values ($\tilde{\sigma}_j$, $\tilde{q}_j$), so that:

$$\begin{aligned} \tilde{\sigma}_j^2 &= \sigma_j^2 + \sigma_{PSF}^2 \\ \tilde{\sigma}_j^2 \tilde{q'}_j^2 &= \sigma_j^2 q_j'^2 + \sigma_{PSF}^2 \end{aligned} \tag{2.13}$$

Leaving the convolved surface brightness model as:

$$\tilde{\Sigma}(R', \theta') = \Sigma(R', \theta') * PSF = \sum_{j=1}^{N} \frac{L_j}{2\pi\tilde{\sigma}_j^2 \tilde{q}'_j} \exp\left[-\frac{1}{2\tilde{\sigma}_j^2} \left(x_j'^2 + \frac{y_j'^2}{\tilde{q}_j'^2} \right) \right] \tag{2.14}$$

The python package `MgeFit`, described in Cappellari (2002), introduces an efficient fitting algorithm for the MGE method which uses least-squared fitting to create an MGE parameterisation of surface brightness distribution from imaging. This is used in Chapters 3 and 4 to represent the light distribution used in dynamical models.

2.5.1 Minimum Inclination Restrictions

It is noted in Cappellari (2002); Scott et al. (2013), and many other papers using MGE parameterisations that Equation 2.12 is undefined unless the criteria $\cos^2 i < q_j'^2$ is satisfied for all Gaussians in the MGE. This creates a non-physical restriction on the minimum inclination

which can be modelled in a JAM model, defined by the flattest Gaussian component. In order to allow the JAM model to explore the full parameter space in inclination in order to find the best fit parameter for the model, this limitation should be worked around. This is done by iteratively placing higher and higher limits on the minimum axial ratio (q') allowed for any single component in the MGE fit, until the mean average deviation of the fit becomes 10% higher than the unrestricted model (this signifies the point where the model has been restricted too far and can no longer reproduce the distribution). The value of 10% is used due to the precedent set in the Scott et al. (2013) paper, which is shown to be robust. This method is used in all MGE models created throughout this thesis.

2.6 JAM Models

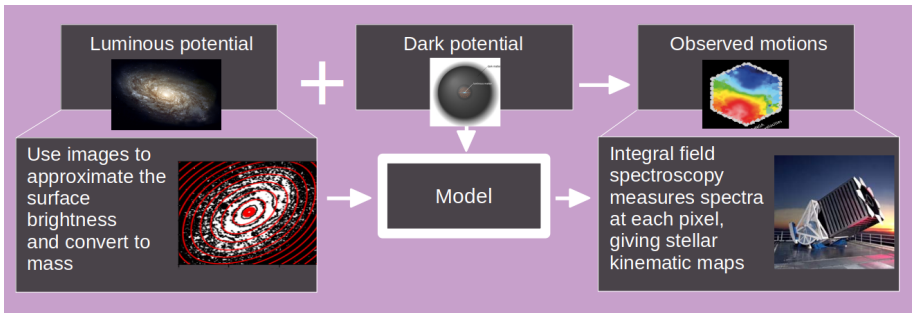

Figure 2.4: A schematic showing an overview of how dynamical models work. The observed motions are dictated fully by the luminous potential and the dark potential, and if these could be perfectly described then the motion predicted would match those observed. The luminous potential can be described using the luminous matter distribution (though not perfectly), but the dark potential has no observable. Generating predicted motions from the luminous mass distribution alone, and comparing to observations, allows a theoretical dark potential to be added which causes the predicted motions to match those observed.

As detailed in Section 1.3, dynamical modelling is an essential tool which allows recovery of intrinsic quantities from galaxies which cannot be determined from imaging or spectroscopy alone. There are many types of dynamical models which are used to measure these quantities, however the key underlying principle is the same. The observed motions of the stars and gas in galaxies must be generated by a gravitational potential. This gravitational potential in turn must be generated by the distribution of matter, including the dark matter. As such, by comparing the observed motions to the motions expected based on some modelled potential, we can constrain the shape of the potential and hence the underlying matter distribution. Through observation, we can estimate the potential due to the baryonic matter, then allowing models to be constructed with varying dark distributions in order to find the best fit (see Figure

2.4 for an outline of this). It is in the method used to predict observables from input that the model types vary.

The work in this thesis uses the Jeans Anisotropic Modelling (JAM) technique, introduced in Cappellari (2008). This method solves Jeans' Equations (Jeans, 1915) in order to generate a velocity field for a galaxy in a given potential. A galaxy may contain hundreds of billions of stars, and modelling the individual positions and velocities of each one is not feasible, so Jeans' equations rely on a distribution function which describes the densities of stars in position, velocity and time. These equations are adapted from the collisionless Boltzmann equations (Binney & Tremaine, 2008, equation 4–13b) – hence relying on the assumption that galaxies are collisionless systems – to apply to the 6D phase space distribution of stars in a gravitational potential. They take the form:

$$\frac{\partial n}{\partial t} + \sum_i \frac{\partial (n\langle v_i \rangle)}{\partial x_i} = 0, \tag{2.15}$$

$$\frac{\partial (n\langle v_j \rangle)}{\partial t} + n\frac{\partial \Phi}{\partial x_j} + \sum_i \frac{\partial (n\langle v_i v_j \rangle)}{\partial x_i} = 0 \quad (j = 1, 2, 3) \tag{2.16}$$

where Φ is the gravitational potential, n is the spatial density of stars at a time t and position $x = (x_1, x_2, x_3)$, and v is the velocity vector (v_1, v_2, v_3). In these equations, $\langle ... \rangle$ denotes an average in space and time.

In general, these cannot be uniquely solved except in special cases, as they are not closed. The JAM method introduces assumptions and parameterisations which allow a solution to be found. The method assumes axisymmetry in the system in a framework of cylindrical coordinates (R, ψ, z), and defines the anisotropy parameter β in terms of the velocity dispersions in the z and R directions ($\beta = 1 - \sigma_z^2/\sigma_R^2$), in order to describe the motions in the system. This anisotropy is assumed to be constant across the system. Further, a choice is made to assume the shape and orientation of what is known as the velocity ellipsoid. This can be chosen to be spherically aligned – i.e. if one were to plot the velocities of the stars in spherical coordinates (v_r, v_θ, v_ψ), and fit an ellipsoid to the distribution, then this would be aligned with the axis – or cylindrically aligned – i.e. the same is true if the velocities were plotted in cylindrical coordinates (v_R, v_ψ, v_z). Studies which have used the cylindrically and spherically aligned JAM method on different systems confirm that the cylindrically-aligned method is valid for fast rotating elliptical galaxies (Cappellari et al., 2007), and also disk galaxies (Noordermeer

et al., 2008; Kalinova et al., 2017; Li et al., 2017). This thesis focuses on these galaxies and so uses the cylindrically-aligned version. Combining these assumptions with the assumption that mass follows light (so that the mass distribution is recovered by scaling the surface brightness distribution), and parameterising the surface brightness distribution and any dark components as an MGE (as described in Section 2.5), the equations become solvable, reducing to:

$$\frac{b\mu\overline{v_z^2} - \mu\overline{v_\psi^2}}{R} + \frac{\partial(b\mu\overline{v_z^2})}{\partial R} = -\mu\frac{\partial\Phi}{\partial R} \tag{2.17}$$

$$\frac{\partial(\mu\overline{v_z^2})}{\partial z} = -\mu\frac{\partial\Phi}{\partial z} \tag{2.18}$$

where μ represents the luminosity density, Φ is the gravitational potential, v is the velocity with subscript in the cylindrical coordinates (R, ϕ, z), b is a variation of the orbital anisotropy given by $b = \overline{v_R^2}/\overline{v_z^2}$. This is assumed to be constant. Here the notation used is:

$$\mu\overline{v_k v_j} \equiv \int v_k v_j f \, d^3\mathbf{v} \tag{2.19}$$

In this case, we use the implementation of the JAM method released in the Python package `jampy`. We direct the reader to Cappellari (2008) for a full description of the method, and use this section to describe the practical considerations required.

Input into the model are the observations that are used to determine the best fit:

- MGE parameters (total counts, width, and axial ratio for each Gaussian) describing the surface brightness of the galaxy, obtained from observation.
- A 2D kinematic map of the root mean squared velocity, V_{RMS}, is needed to evaluate the model. In this case, we use the first and second kinematic moments (V, σ) observed by MaNGA (described in Section 2.2) which are combined into a 2D map of $V_{RMS} = \sqrt{V^2 + \sigma^2}$, and a 2D map of accompanying propagated errors is also input. This map is in the voronoi binning scheme which amalgamates spatial bins to reach an SNR > 10 in each. JAM also performs a convolution of the predicted kinematic maps with the PSF of the MaNGA observations in order to allow for comparison to the observations.

And free parameters which are fitted by the model:

- A mass-to-light ratio (M/L) is provided as a free parameter which multiplies the luminous MGE to convert from a luminosity distribution to a mass distribution. This could have been fixed to values derived from stellar population modelling, but is left as a free variable to reduce uncertainty introduced from these models.

- If a dark component is included in the model (true for Chapter 4), this is also required in MGE form, and is provided as per the specific method used in that chapter, with the parameters of the halo left free to be fitted. In the model, JAM takes an input of the luminous MGE and the potential MGE, and the inclusion of the dark component is reflected in the difference between the two (i.e. the luminous MGE contains that from the surface brightness, and the potential MGE contains both that from the surface brightness scaled by the mass-to-light-ratio and that from the dark component).

- The orbital anisotropy, β is also a free parameter.

- The inclination is also required, and in this case we leave this as a free parameter in models which do not contain a dark matter halo, and then take the best fit inclination from dark matter-free models and input this fixed value for the models which do include dark matter (this is considered valid as the dark matter haloes are close to spherical due to the lack of collisions, so the inclusion or omission should not affect the inclination).

Within JAM, the modelled kinematic map is generated and is then compared to the observed kinematics in order to evaluate the model. This is what is then used to quantify the likelihood values for the fitting process (described in Section 2.7) in order to determine the best fit values for the free parameters in our models, given priors.

2.7 MCMC Fitting

Markov-Chain-Monte-Carlo (MCMC) techniques are now an essential component of an Astronomer's science "toolkit". In essence, these methods repeatedly vary some input parameters, as per our understanding of how these inputs may be distributed, and compare the output with an observation in order to obtain a distribution of the input parameters based on the probability that these were the conditions that allowed the observation to happen. For example, JAM models as described in the previous section take a set of input parameters (some observed and fixed, others allowed to vary so as to find the best fit values), to produce a prediction of

the kinematics of a system given those input conditions. In order to find the values that are most likely to lead to the kinematics observed, the free input parameters are varied in value until the kinematics are most similar to the observation – measured by a maximisation of the likelihood. MCMC methods are a statistical tool which rely on Bayesian statistics. Bayesian statistics deal with probability distributions. These differ from classical frequentist statistics, in that they describe the likelihood of an observation based on the probability distribution of parameters, instead of simply values.

These methods are based on Bayes' Theorem which describes the probability of an outcome based on the knowledge of the probability distribution of factors affecting this (Jeffreys, 1939). The theorem relates three probability distributions – a prior, a likelihood, and a posterior – as:

$$P(\theta|D) = \frac{P(D|\theta)P(\theta)}{P(D)} \tag{2.20}$$

where θ is the input parameters of a model, and D is the observed data. So $P(\theta)$ is the probability distribution of the input parameters based on the knowledge available without the data – i.e. the prior distribution, $P(D|\theta)$ evaluates how likely the data we observe is based on the prior distributions of the parameters – i.e. the likelihood distribution, multiplying the prior and the likelihood functions gives the probability of the input parameters based on the data we have observed – i.e. the posterior distribution. The term $P(D)$ is known as the evidence and simply normalises the function. The parameter values, θ, are varied within their prior distributions until a set is found which maximises the likelihood of the observed data.

MCMC methods are algorithms which dictate how the parameters are varied at each step through the creation of Markov chains which explore the multidimensional parameter space. An algorithm is used to explore this space in a way which efficiently finds the maximum likelihood in the multidimensional parameter space. The details of the differences between these parameter exploration methods are beyond the scope of this thesis, and we direct the reader to Sharma (2017) for a detailed description of many algorithms used. However we note that in Chapter 3 we use the Python package `emcee` (Foreman-Mackey et al., 2013) which uses a novel algorithm to implement the Affine Invariant MCMC Ensemble Sampler (Goodman & Weare, 2010). This was chosen as it is easy to implement and well-tested on relatively simple posterior distributions with low dimensionality. In Chapter 4, we choose instead to use a Gibbs' sampling algorithm (see Section 3.3 of Sharma, 2017), which is efficient and able to explore

posterior distributions with many local minima in order to find the global minimum. This is implemented in the `GAStimator` Python package (built by T. Davis, and publicly available).

2.8 PSB Selection

As noted in Section 1.6, PSB signatures are indicative of a unique quenching situation which sees rapid quenching after a period of enhanced star formation. The means by which these regions are identified is important when considering the interpretation of the results seen. There are multiple ways in which PSB signatures are classified. In general, these spectra are characterised by strong Balmer absorption (Hδ) – indicative of intermediate-age A-type stars, but an absence of emission lines (like Hα and [OIII])which would be generated by hot young O-type and B-type stars (Dressler & Gunn, 1983). These conditions occur when there has been star formation followed by a rapid quenching which has taken place in the last 1 Gyr Poggianti et al. (1999); Dressler et al. (2004). Quantitatively, there are a few different methods for selecting PSB spectra. In this thesis we focus primarily on the method introduced in Chen et al. (2019a), which selects a region in the plane defined by Hα equivalent width and Hδ absorption (hereafter referred to as the Chen method). We also mention and discuss a method using principal component analysis (PCA) introduced in Wild et al. (2007), which ignores the information of emission lines, and so may contain regions which still experience some star formation, and may probe a slightly later quenching timescale (hereafter referred to as the PCA method). As is noted in French (2021), there are many different methods and definitions for PSB signatures, and as such any method will not individually be able to completely identify all spaxels which are PSB alone, and these methods by virtue will disagree. This feature may allow specific identification of individual quenching mechanisms by considering differences, overlaps, and distinctions between regions identified by each method.

2.8.1 Chen et al Method

This method is the one primarily relied upon in Chapter 5. Introduced in Chen et al. (2019a), it relies upon measurements of the Hα emission line equivalent width and the Hδ absorption. These quantities are both measure by IFU surveys , and in particular are included in the analysis of MaNGA data (see Section 2.2.1). Following this method, a spaxel is classified as PSB if it meets the following criteria:

- The signal to noise ratio must be greater than 8
- Hδ absorption, $H\delta_A > 3$ Å
- Hα equivalent width, $EW(H\alpha) < 10$ Å
- $\log EW(H\alpha) < 0.23 H\delta_A - 0.46$

We also use an alternative classification scheme which relaxes the SNR requirement to SNR > 3, in order to investigate lower brightness outer regions. Where this is done, we check against a control sample to mitigate against simply gaining a PSB classification through noise.

Looking at the $EW(H\alpha)$ - $H\delta_A$ plane, this selects the region shown in Figure 2.5, which finds spaxels where the SFH features an initial burst of star formation, followed by a second burst at $t = 6.5Gyr$, and then an exponential decline in star formation with the e-folding times between 50 and 300 Myr as shown in the legend.

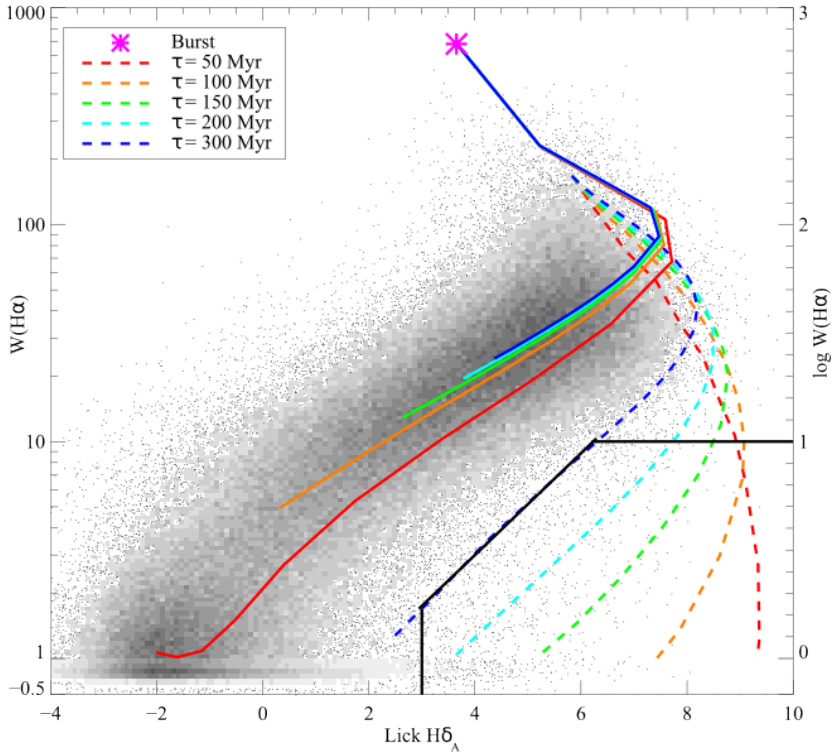

Figure 2.5: From Chen et al. (2019a), showing evolutionary tracks of galaxies with different rates of exponentially declining star formation (coloured lines) in the plane of Hα equivalent width versus Hδ absorption. Solid lines show those which decline exponentially from an initial burst, dashed lines show those which have an additional burst after 6.5Gyr before exponentially declining. The magenta star shows the initial burst for all model galaxies, and the greyscale scatter points show all galaxies in the SDSS DR7 catalogue. The black solid line indicates the region which is selected for PSB signatures.

2.8.2 PCA Method

In Wild et al. (2007), indices were defined using a principal component analysis (PCA) technique. This method works by considering the spectrum near the 4000 Å break (the region which contains the strongest features related to the content of young stars in a galaxy) as a vector in an N-dimensional space. Then principal component analysis works to define eigenvectors in the space which designate axes along which the maximum variance is found between different stellar spectra in a library. These are then defined as PCA1 and PCA2. The full method is set out in Wild et al. (2007), and Wild et al. (2009) applies this to a sample. PCA1 is equivalent to the D4000 index, while PC2 traces the excess Balmer absorption – and so PSB signatures are classified as those with high PC2 but not high PC1. In Rowlands et al. (2018), regions in the PCA1-PCA2 plane are used to classify different spaxels evolution stages as per Figure 2.6. The purple region shows the area in which spaxels of a galaxy are classified as PSB using this PCA method. These classifications are used in Chapter 5 in order to compare the selection of PSB regions in our jellyfish galaxies with the Chen method.

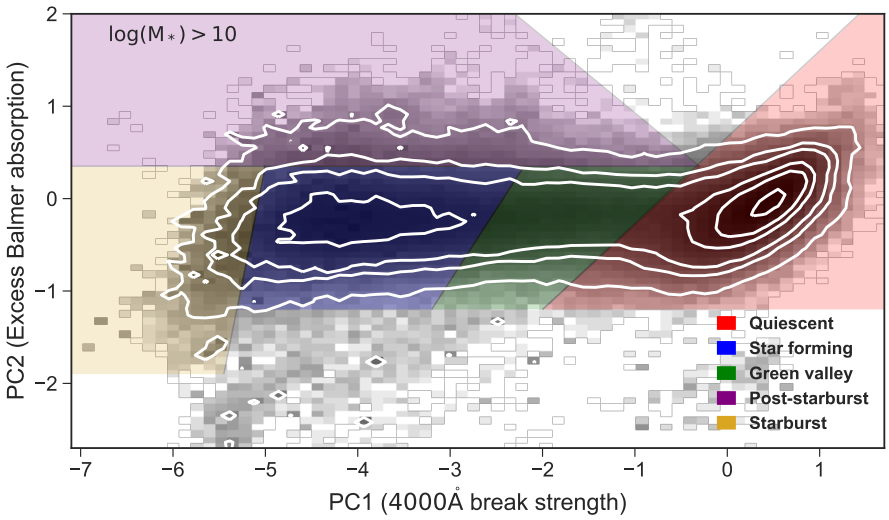

Figure 2.6: From Rowlands et al. (2018), showing classification regions in the PCA1-PCA2 plane (indices defined using principal component analysis), with colours indicating the classification regions as per the legend. Grey density plot and contours indicate the positions in the plane of spaxels in a sample of MaNGA galaxies with log stellar masses greater than 10. Purple region indicates the region defined as PSB.

3

Jeans Modelling for Red Geysers

Suggested listening: Kite by Kate Bush

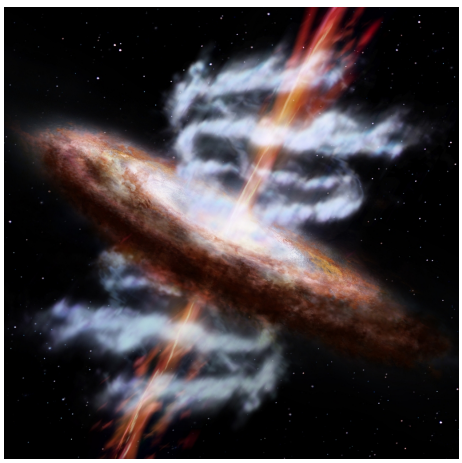

We exist on our planet which orbits our star, the Sun, at 30 kilometres per second (Levin et al., 2017). Similarly, our Sun exists amongst billions of other stars in our galaxy – the Milky

Chapter image: Artist's Impression of an Active Galaxy, ESA/AOES Medialab

Way. Our Sun (and many of the others) is in orbit around the galactic centre, moving at a blistering speed of 200 kilometres per second (Hunt et al., 2016). The cosmos is not at rest. Galaxies are not simply stationary discrete objects in space, but are dynamic systems in motion. Not only instantaneously in the motions of their constituents, but also in a grander scale as they evolve through different life stages. In some cases, the instantaneous dynamics of the system can be used as a tool to better understand the global evolution of the system. This Chapter explores how dynamical modelling and kinematic observations can be used to study processes taking place in galaxies which illuminate the mechanisms which cause a galaxy to evolve.

The work contained in this chapter is published in Roy et al. (2021). This work is led by Namrata Roy, and my specific contribution is the dynamical modelling of the galaxies involved in order to provide accurate constraints on their inclination. This chapter describes this modelling process and the impact of this work on the science problem detailed.

3.1 Background

In Section 1.1 we discussed how galaxies evolve from actively star forming to quiescent, and some of the mechanisms by which this transition could be driven. The trend for higher fractions of quiescent galaxies at present times (Bundy et al., 2006; Faber et al., 2007; Ilbert et al., 2010; Moustakas et al., 2013) indicates that the change must be at least semi-permanent, which indicates the removal of gas alone is not the only factor. If gas were simply removed in a single event, then star forming would cease; but new gas would begin to refuel the gas reservoir and allow star formation to begin again. Whether the gas was provided through minor mergers or through mass loss from older stars in the system (Mathews & Brighenti, 2003), without any other processes it would begin to condense and cool. Therefore, when considering how quenching can take place globally in a galaxy, we require a secondary ongoing process which prevents this gas from accumulating, cooling, condensing and forming stars.

Multiple processes have been suggested as candidates to explain this, including nuclear activity from central supermassive black holes (SMBHs). This relies on the understanding that active galactic nuclei (AGN) can cause feedback to their host galaxies through two different modes: "radiative-mode" usually seen in lower mass systems when the SMBH is accreting efficiently with the bulk of the energy output in radiation, and "jet-mode" which is primarily

seen in high-mass systems where the SMBH is accreting inefficiently, producing little energy in radiation and instead imparting energy through narrow bilateral outflows (jets) (Heckman & Best, 2014). This second mode is posited as the source of our "maintenance-mode" feedback, which recurrently accretes gas which begins to cool and in turn feeds just enough energy back into the surrounding gas – heating it and preventing the cooling required for star formation, but not so much as to remove it from the galaxy entirely. Evidence for this process has been seen in some central clusters (Fabian et al., 2006; Fabian, 2012b), however if this process is responsible for maintaining quiescence in the quiescent population we would expect to observe signatures in a significant proportion of the local quiescent population in the field.

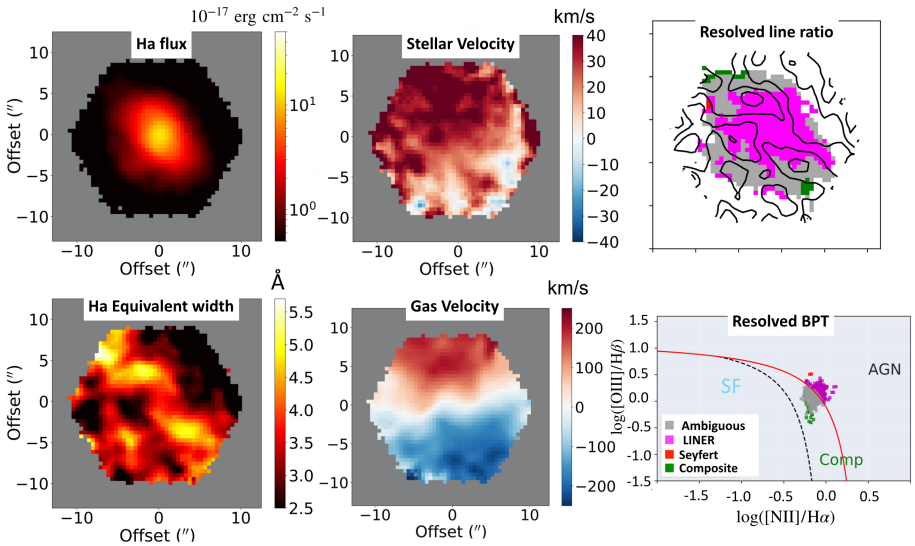

Figure 3.1: Reproduced from Roy et al. (2021). Spatially resolved emission line and kinematic maps of Target 1, the prototypical red geyser from MaNGA observations, demonstrating the characteristic features. **Upper left:** Hα flux; **lower left:** Hα equivalent width, showing bisymmetric ionised patterns aligned with ionised gas kinematic axis; **upper centre:** 2D stellar line of sight velocity map, showing rotation at much lower velocities than the ionised gas component; **lower centre:** ionised 2D gas velocity field, showing greater velocities than stellar component, and misaligned axis; **upper right:** spatial map of spaxels which are coloured according to BPT classification as per the lower right panel, showing AGN signatures in the central regions; **lower right:** spatially resolved BPT diagram indicating the BPT classification colours used above (for details of this, see: Roy et al., 2021).

In Cheung et al. (2016), a population of galaxies were introduced which were argued to exhibit these outflow signatures, and could make up as much as 10% of the population. These were dubbed "red geysers", and – in summary – are a population of quiescent spheroidal galaxies characterised by ionised gas which is kinematically misaligned from the stellar component, with ionised gas velocities which far exceed stellar velocities, and bilateral features in Hα equivalent width (EW, a measure of the strength of a spectral feature determined by the area of the feature against the continuum) which are aligned with the kinematic axis of the gas (see

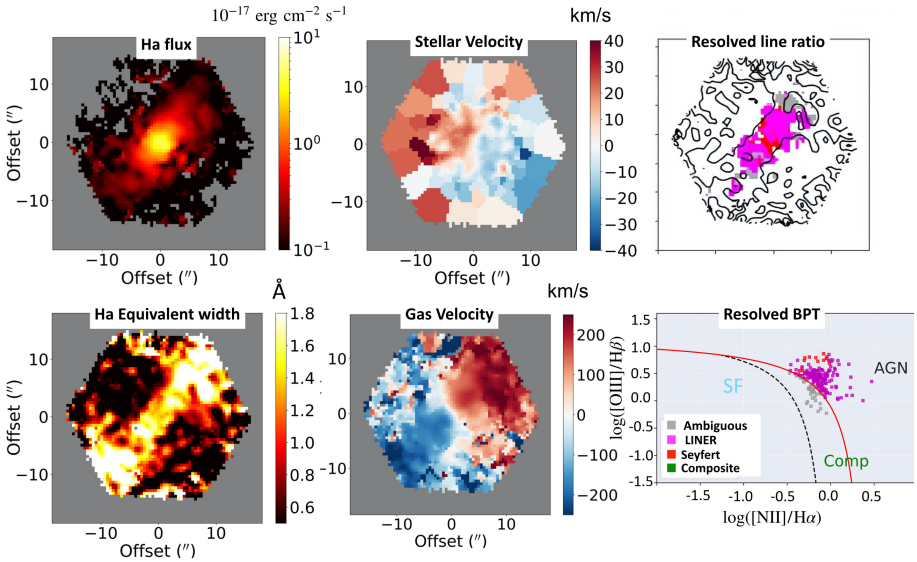

Figure 3.2: Reproduced from Roy et al. (2021). Spatially resolved emission line and kinematic maps of Target 2 from MaNGA observations. Panels the same as in Figure 3.1.

Figures 3.1 and 3.2). These types of galaxies had previously been observed (Sarzi et al., 2010; Kehrig et al., 2012; Allen et al., 2015; Gomes et al., 2016), but the features were attributed to the rotation of a misaligned gas accretion disk (Lagos et al., 2015). In the red geysers framework, the misaligned ionised gas kinematics are not in rotation, but are wide biconical outflows from the AGN which we are observing face on, and the Hα features are shocked regions in the centre of these outflows (see Figure 3.3). For the prototypical red geyser in Cheung et al. (2016), they supported this interpretation over the disk model by using Jeans modelling (see Section 2.6) to show the velocities of the gas are incompatible with rotation (being higher than the escape velocity). This interpretation was also supported by work in Roy et al. (2018), which showed enhanced nuclear radio emission in the red geyser population compared to a control sample matched in mass, redshift and axial ratio, hence suggesting the presence of AGN activity in this population.

In order to further exclude the possibility of a rotating disk explaining the observations, Roy et al. (2021) set out to compare the changing shape of emission lines along the gradient of the gas velocity map with those expected from a rotating disk model. For full details of the methods used for this, see Roy et al. (2021), however for the purposes of this Chapter I give a qualitative summary. The specific shape of the emission lines viewed at different lines of sight away from the centre of the galaxy would exhibit a characteristic asymmetric shape which would vary with position along the bisymmetric feature. Modelling shows that these would be different in the case of a rotating disk model compared to that expected from a wind

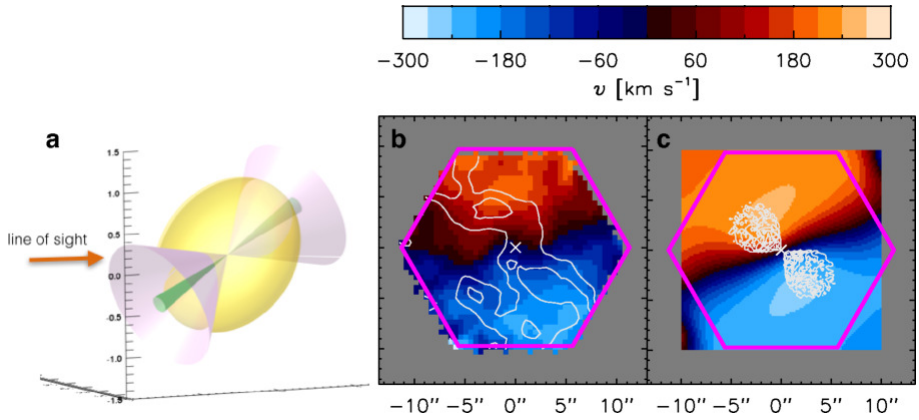

Figure 3.3: Reproduced from Cheung et al. (2016). **a.** A schematic diagram of the galaxy in gold, and the biconical wind in purple. The wind has an opening angle of 80°, and the inner 10°of the bicone is highlighted in green. The line of sight is indicated by the red arrow. **b.** The observed line of sight velocity of the ionised gas in the prototypical red geyser, with Hα equivalent width overplotted in white contours. **c.** The predicted observed ionised gas velocity derived from the wind model in **a.** (see Cheung et al. (2016) for method details) with the white contours outlining the central axis of the wind. model (see Figure 3.4).

For this to work, strong constraints are required on the inclination of the galaxies, which – due to their more spherical geometry – isn't straightforward to obtain for elliptical galaxies from imaging alone. Dynamical modelling allows this to be constrained.

This showcases the power of dynamical modelling as a tool to measure things which are otherwise not evident from imaging or unresolved spectroscopy alone.

3.2 Data

3.2.1 Sample Selection

A parent sample of red geysers in the MaNGA survey was introduced in Roy et al. (2018), which includes 84 galaxies. These were visually selected to exhibit the features outlined in Section 3.1. In this work, two galaxies were selected from this sample in order to be targeted for spectroscopic followup with Keck, to obtain spectroscopic measurements which are detailed enough to recover the change in asymmetric shapes of the emission lines due to Doppler effects along the outflow axis. The two galaxies were selected to cover a range in Hα fluxes, radio flux, and angle of kinematic misalignment in order to offer the best possible representation of the full parent sample. The first galaxy has MaNGA ID: 1-217022, and is the original prototype galaxy studied in detail in Cheung et al. (2016), and is known herein as "Target 1". In that paper, a Jeans model was already constructed for this galaxy, which constrained the inclination.

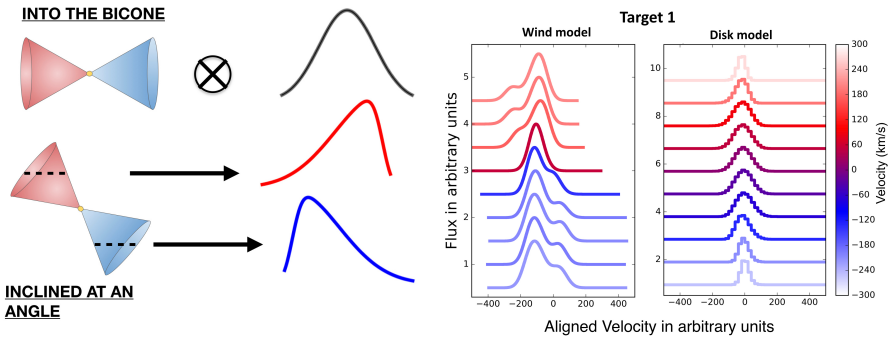

Figure 3.4: Reproduced from Roy et al. (2021). **Left:** A schematic diagram, showing how the shape of emission lines would be expected to change if viewed on the approaching or receding sides, with a characteristic wing to the blue side for the redshifted emission line, and wing on the red side for the blueshifted line; **Right:** Mock spectra produced for the first target galaxy in the case of a wind scenario (left), and disk scenario (right), highlighting the possibility to observationally distinguish between the two scenarios by observing emission line shapes and their variation at different points along the axis of the bisymmetric outflow.The difference arises from a biconical wind producing a range of inclinations at which the material moves, and thus a broad component/tail exists in the emission line profile which is not produced in the case of a rotating disk.

The second galaxy has MaNGA ID: 1-145922, and herein is referred to as "Target 2". This galaxy also exhibits the characteristic features of a red geyser, however differs from Target 1 in a few ways, as seen in comparing Figures 3.1 and 3.2. Target 2 exhibits lower Hα EW compared to Target 1, doesn't exhibit signs of systematic rotation in the stellar kinematics, is not radio detected, and LINER-type emission line ratios are present throughout much of the galaxy as diagnosed by a BPT diagram.

3.2.2 Keck Followup Observations

The Keck Echellette Spectrograph and Imager (ESI) performs spectroscopy through use of a single long slit, which spans 20 arcseconds. This gives spectra for an object which is spatially resolved in one dimension, into 10 spectra, along the slit length. This number is decided by the spatial resolution of 0.9 arcseconds, and the galaxy covering 9 arcseconds in the sky. The spectra provided by these observations have a spectral resolution of $\sim$ 37 km/s or R $\sim$ 8000, and a spatial seeing FWHM of 0.9 arcseconds. The wavelength range covered is from 0.39 to 1.1 micrometers, which includes the Hα and [NII]λ6584 emission lines. Comparing to MaNGA's (see 2.2.1) IFU observations, which provide spectral resolution R $\sim$ 2000 and spatial resolution of 2.4 arcseconds, we see why this analysis could not be performed using MaNGA data as the shape features of the emission lines would be lost. The targets are observed with the slits aligned with the axis of the ionised bisymmetric features, using the above set up of Keck ESI, with an exposure time of 1.5 - 2 hours each.

Figure 3.5: DESI Legacy Image in the r-band for Target 2, used to create MGE parameterisation of surface brightness distribution.

3.2.3 MaNGA Kinematics

In order to create a dynamical model as per the JAM method (see Section 2.6) to constrain the inclination of Target 2, IFU data is required for the galaxy in order to derive the line-of-sight stellar velocity and the stellar velocity dispersion. These are combined in order to produce a 2D map of the root mean squared velocity (V_{RMS}).

In this case, we use IFU data from the Sloan Digital Sky Survey (SDSS-IV; Blanton et al., 2017) programme Mapping Nearby Galaxies Using Apache Point Observatory (MaNGA; Bundy et al., 2015). This is described fully in Section 2.2.1.

3.2.4 Legacy Survey Imaging

To create a dynamical model, along with kinematics, we also require deep images of the galaxy in a single band. This gives a surface brightness distribution which can be used to approximate the gravitational potential in a mathematically convenient form, via the MGE method (see Section 2.5). As this is such an essential part of the model which has potential to greatly affect the results, we opt to use imaging from the DESI Legacy Survey (fully described in Section 2.1) which offers deep imaging. Further, we choose to use *r*-band imaging as this best corresponds to the stellar component, with minimum sacrifice to dust, and has been frequently chosen for previous JAM studies (see Scott et al., 2013). This is taken from DR9 of the survey.

3.3 Methods

This thesis focuses on the work personally performed by me during the course of my PhD. As such, the details of the methods used in this paper for work carried out which I was not

personally involved in (ie. the emission line fitting, asymmetry measurements, creation of the mock model spectra), are not covered in detail here. This section focuses on the creation of a dark matter-free dynamical JAM model to constrain the inclination of Target 2, which is central to the generation of the mock model spectra to which the observations are compared. If the reader wishes to know more about the methods applied in the rest of the paper, they are directed to Roy et al. (2021).

3.3.1 MGE

As discussed in Sections 2.5 and 2.6, to create a JAM model, the surface brightness is parameterised using the MGE method described in Section 2.5. In this case, the r-band DESI Legacy Survey accessed for Target 2 (see Figure 3.5) is used to construct the MGE approximation, via the Python implementation `MgeFit` (Cappellari, 2002). As seen in the image, Target 2 has a spheroidal morphology. The issue with an artificial restriction on the minimum inclination allowed by an MGE model, as discussed in Section 2.5.1, is avoided by using the method described therein.

The MGE parameters which best fit the observed surface brightness distribution are listed in Table 3.1, and the residuals of the fit are compared to the photometry in Figure 3.6. These residuals all remain within 20% of the observed values (majority lower than 10%), and so the fit is determined to be accurate, and is used in the following section to create a JAM model.

Total Counts	σ	q_{obs}
272.88	2.47	0.95
432.69	10.7	0.95
165.53	21.1	0.95
476.80	23.2	1.0
1109.95	58.3	1.0

Table 3.1: The parameters of the best fit MGE. Total Counts refer to the counts under each component, σ is the width of each component in pixels, and q_{obs} is the projected axial ratio of each component. We acknowledge the lack of errors and small significant figures produced, however this is following the accuracy obtained in Table 2 of Scott et al. (2013), where this method was developed.

3.3.2 JAM

JAM modelling allows the creation of modelled kinematic maps of a galaxy based on input parameters which include inclination. To achieve this we follow the method described in Sections 2.6, to create models with no dark matter component using the MGE surface brightness distribution of the galaxy. We decided that a simple JAM model neglecting dark matter is ade-

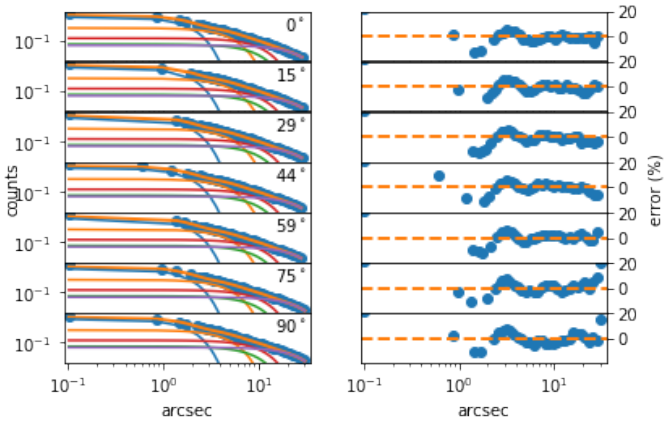

Figure 3.6: Plots displaying the evaluation of the MGE fit based on the photometry in sectors around the galaxy centre. **Left:** From top to bottom, the best fit MGE Gaussians (lines) are compared to the data (points) radially along sectors. **Right:** The residuals of the fit along sectors.

quate for measuring the inclination, as in Cappellari et al. (2013), since modelled dark matter haloes are spherical, and so the lack of inclusion does not affect the best fit inclination of the system.

This leaves only non-dark matter parameters to be input into the model.

We use an MCMC simulation, through the Python package `emcee` (described fully in Section 2.7), in order to determine the best fit parameters of the model based on the observed kinematics, and constrain the inclination.

Free parameters to the model, and their priors, are listed here:

- Inclination, as $\cos i$: flat prior between 0 and $\cos i_{min}$,
  where i_{min} is imposed by the axial ratio of the flattest component in the MGE as per :

$$\frac{\sqrt{q_{obs}^2 - \cos {i_{min}}^2}}{\sin i_{min}} > 0.05 \tag{3.1}$$

  where q_{obs} is the observed axial ratio of the flattest MGE component.

- Orbital anisotropy, β: flat prior between 0 and 0.75
  (Restricting $\beta > 0$ is required to break the known degeneracy between anisotropy and inclination, and is observationally motivated for fast rotators (see Section 3.1.1 of Cappellari et al., 2013) as the red geyser population are found to be).

- Mass-to-light ratio, M/L: flat prior between 0 and 10 in units of $M_\odot/L_\odot$.

(Note that M/L in this case is not a stellar M/L, but a dynamical M/L, so expresses discrepancies seen due to omission of the dark matter halo alongside a stellar M/L. This means the value should not be compared to stellar M/L values found through other means, such as stellar population modelling).

The MCMC was run until the parameters converged, and the first 1000 steps were discarded as burn-in. The best fit values of the parameters were taken as the mean of the distribution, with errors at the 16th and 84th percentile.

3.4 Results and Discussion

The best fit model is found with $\chi^2/DoF = 2.68$, and Figure 3.7 shows the predicted v_{RMS} from the model compared to the observed v_{RMS}, along with the residual map. The parameters corresponding to the best fit values are presented in Table 3.2.

Inclination (°)	β	M/L
$19.58^{+0.070}_{-0.057}$	$0.216^{+0.025}_{-0.029}$	$6.921^{+0.019}_{-0.021}$

Table 3.2: The parameters of the best fit JAM model.

We note the small errors reported in the above results. As discussed in Cappellari (2008), these errors only account for the statistical errors in the fitting process and do not account for systematic errors precipitating from the model used. I.e. the model we have used is fit very well, but whether this is the correct model to use is not reflected in these numbers. Cappellari (2008) explains that these systematic errors are often dominant but difficult to estimate. In their work, they compare many different models and find a systematic error in M/L consisted with 6%. As such, these errors should be considered artificially small. Further, recent work by Zhu et al. (2023) proposes the artificial inflation of errors on the kinematic observations obtained from MaNGA, which will also produce more accurate error estimation.

I now summarise the science results which were precipitated from the constraints on the inclination provided by my dynamical modelling, to situate the work in the context it was completed.

Using the inclination recovered above for Target 2, and the inclination previously constrained for Target 1 in Cheung et al. (2016), models were constructed to show the shape of emission lines expected for both the disk and the wind models for both the targets. Figures 3.8 and 3.9 show these alongside the observed emission line shapes of Hα and [NII] for the

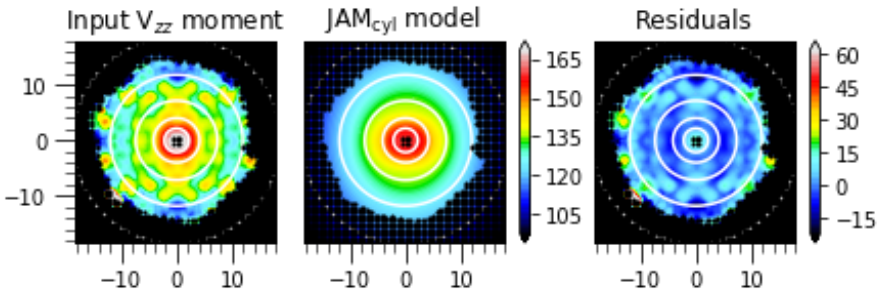

Figure 3.7: Left: The symmetrised v_{rms} field (denoted as v_{zz}) for the galaxy which is input to JAM, Centre: The output v_{rms} field from the best fit cylindrical JAM model, Right: The residuals of the model and data. The white contours on all trace the surface brightness of the MGE. Black dots denote masked pixels.

two galaxies from Keck.

These emission lines were fitted using a Gauss-Hermite polynomial (for details, see: Roy et al., 2021), which provides a value for the skewness parameter, k. A positive k value represents a wing on the emission line to the "red" side, a negative k value represents a wing to the "blue" side, and $k = 0$ represents a symmetrical profile. These wings are shown to be present for the case of the wind model due to the distribution of velocities of gas outflowing in the cone, but less present in a disk model as this would only have one component. Figure 3.10 shows the variation of the skewness parameter with spaxel number, which indicates position along the bisymmetric feature. The parameter is shown for the Keck data, the disk model, and the wind model, for both Targets. The greater amplitude of the variation in observed skewness with distance from the galaxy centre is more in line with those predicted for the wind model, and thus this paper concludes more support for the wind model.

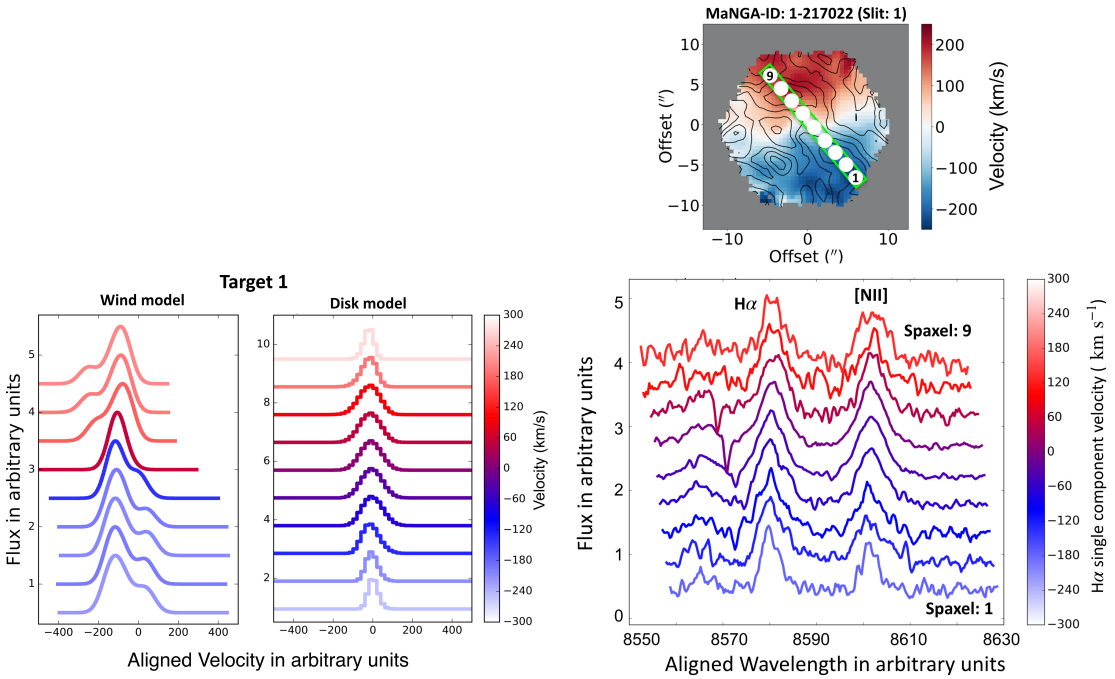

Figure 3.8: Reproduced from Roy et al. (2021). **Left:** Mock spectra produced for Target 1 in the case of a wind scenario (left), and disk scenario (right), highlighting the possibility to observationally distinguish between the two scenarios by observing emission line shapes and their variation at different points along the axis of the bisymmetric outflow.; **Right:** Observed spectra showing the Hα and [NII] emission lines across the 9 spaxels observed using the slit. **Top:** Ionised gas velocity map of the galaxy showing the position and alignment of the slit, and the nine spaxels for which spectra were produced.

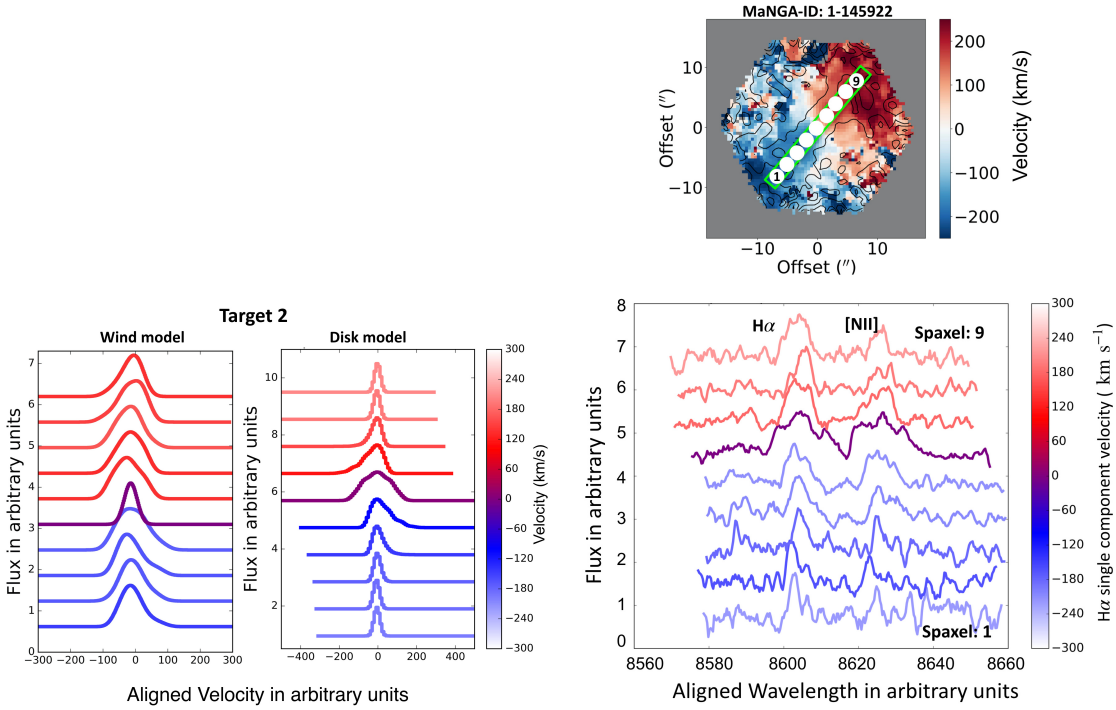

Figure 3.9: Reproduced from Roy et al. (2021). Same as in Figure 3.8, but for target 2.

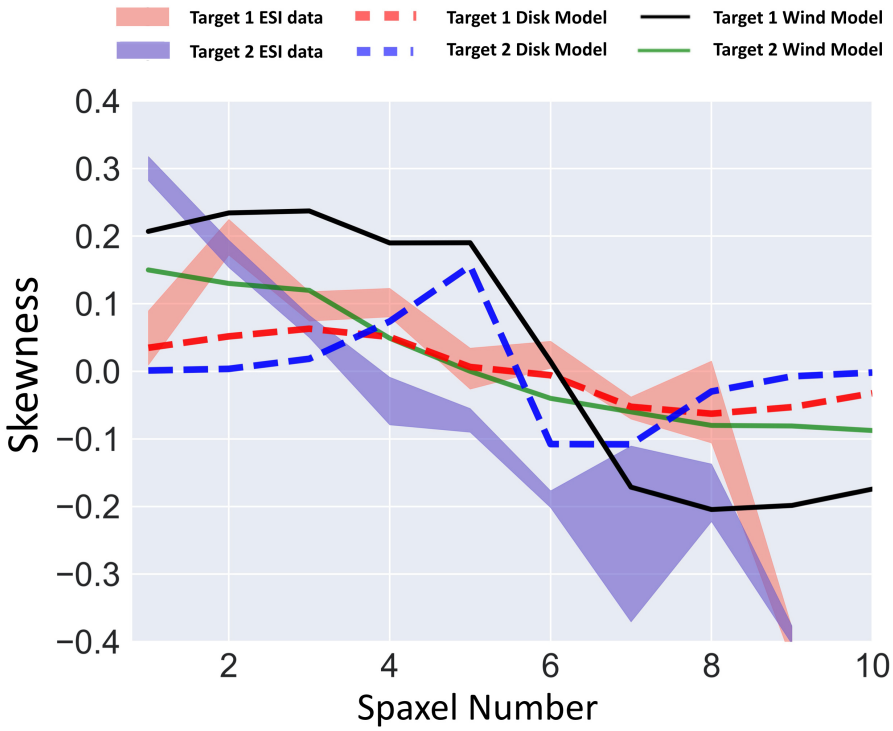

Figure 3.10: Reproduced from Roy et al. (2021). The spatial variation of the skew parameter obtained from fitting observed emission lines from Keck observations for the two targets, compared with the predictions of the wind and disk models. The red and blue shaded regions show the skew parameter averaged over the Hα and [NII] emission lines. The dashed lines show the predicted skew parameters along the same spatial axis predicted for the disk model, and the solid lines show this for the wind model.

3.5 Summary and Future Outlook

This Chapter has described the work I contributed towards the published work Roy et al. (2021), through building a JAM dynamical model in order to constrain the inclination of the galaxy, which was required in order to create models of the shape of emission lines for two different models. This allowed more certainty that the red geyser population is a population exhibiting large scale ionised gas outflows due to nuclear activity, which helps to advance our understanding of how galaxies remain quenched after their gas has been removed. Dynamical modelling can contribute further to the analysis of a greater sample of red geyser galaxies in the MaNGA sample, by constraining escape velocities for each system and comparing this to the observed gas velocities in order to ascertain if the gas is bound (i.e. in a rotating disk) or if it is outflowing (i.e. we are truly seeing red geyser phenomena). Situated in the context of our understanding of galaxy evolution, direct observation of large scale AGN outflows in "maintenance-mode" AGN is a big step in confirming the importance of these nuclear process in not just quenching galaxies, but keeping them quenched. This also showcases the power of IFS observations and dynamical models to illuminate features of galaxies which otherwise cannot be easily constrained from imaging or unresolved spectroscopy alone. Perhaps one of the most glaring examples of a feature of galaxies which cannot be explored using imaging is the dark matter component. This is the focus of the work in the next Chapter.

4

Jeans Modelling to Constrain the Dark Matter Halo

Suggested listening: Turn on the Dark by Nick Shoulders

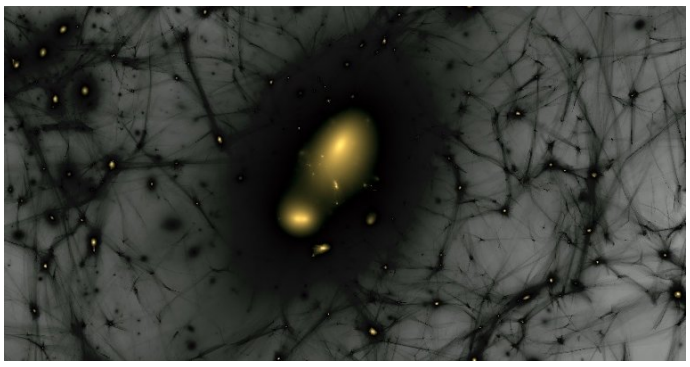

Our current understanding of the Universe still fails to fully explain what we observe. The problem of dark matter has challenged Physics since it was first suggested to explain the

Chapter image: Still from video showing dark matter simulation of the Milky Way, Ralf Kaehler/SLAC National Accelerator Laboratory

motions seen in galaxies in the 30s by Zwicky (1933). While in some ways, the invocation of a dark matter component in our cosmos was a step towards fully describing our Universe; in other ways it kicked the problem into the grass as it offered no explanation of what this dark matter was – other than stating it did not interact with electromagnetic radiation, and thus could not be directly observed by any means at our disposal. In order to understand this component more, we must use our observations of the gravitational effects it has on the observable matter around it in order to infer its presence, distribution, and behaviour. In this field, galactic dynamical models play an essential role.

This Chapter describes the work I have done which will contribute to a lead author paper (currently in preparation). The work looks at using JAM models (described in Section 1.3) to explore the dark matter content of galaxies, and introduces a novel method which includes observed unresolved cold gas kinematics in the modelling process to offer an improvement on the constraints of the dark matter halo parameters. In the Chapter, this is demonstrated in-depth for a small sample and then the results of applying the technique to a larger sample are presented and discussed. The properties of the dark matter haloes which are measured are then related to other galaxy properties in order to explore the link between the dark mass content and the evolution of galaxies.

4.1 Background

One of the most powerful uses of dynamical modelling is to determine the total mass present in a galaxy – independent of the mass we see. Historically, this has changed the view of our Universe through the discovery of a dark mass component which is unexplained by the standard model. As detailed in section 1.2, there are still problems present in our understanding in this field, and as such improvements on dynamical modelling techniques are extremely valuable. An ideal dynamical modelling method would be able to model each individual system in extreme detail using as much data as possible, while also being applicable to a large, statistically significant sample of galaxies. However, there is currently a trade-off between these priorities as detailed modelling requires more time-expensive observations and computationally expensive methods, while the models achievable with less expensive data and methods are applicable to many systems but are less accurate. This work aims to balance these priorities by using single dish hydrogen observations to improve the modelling for a large statistically significant sample. For more details on the current field of dynamical modelling, see Section

1.3.

As we are not able to directly observe dark matter, our best means of exploring its properties is through comparison of observation with simulations. By running cosmological simulations which model dark matter from first principles based on our theoretical assumptions of how it may behave, we create mock observations of what we would expect the Universe (and the galaxies within) to look like if that theory were correct. By creating simulations which include as much realistic physics as computationally possible, if we base these on the correct theories then we should be able to reproduce the Universe that we see. This involves an iterative process of creating simulations, generating mock observations, and comparing to real observed properties in order to fine tune the physics involved and create a more accurate simulation. However, essential to this process is the observations to which the simulations are compared – simulations are only as valuable as the observations that we compare them to. As we cannot detect the dark matter in the Universe directly, we must use dynamical models to measure the dark matter properties of galaxies around us, which can then be compared to the simulations. A simulation which contained all of the correct physics that act in the Universe would be able to reproduce not just the average galaxy properties of the population, but also the diversity in the population too. For this reason, we must have dynamical modelling methods which allow us to collect observations which test whether this is being achieved. As such, we need methods which are applicable to large, statistically significant, samples. The limitations on dynamical models for large samples are discussed in Section 1.3. This Chapter introduces a new method which allows improved dynamical modelling with the addition of single dish hydrogen data – and so is applicable to large samples.

As outlined in Section 2.2, integral field spectroscopy (IFS), and the resolved kinematics obtained from this has allowed massive progress in data available for dynamical modelling. However, as seen in Figure 4.1, the stellar component of a galaxy which is detectable by IFS techniques is contained in the very central region of an extended halo of dark matter (typically the half light radius of the galaxy's stellar component is only around 1-2% of the virial radius of the dark matter halo; Kravtsov, 2013; Somerville et al., 2018). In these regions, the stellar mass also generates a gravitational potential which dominates that of the

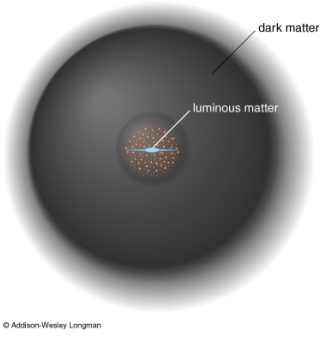

Figure 4.1: Schematic illustrating that the luminous component of a galaxy only inhabits the very central regions of an extended halo of dark matter. Credit: Addison-Wesley Longman

dark matter component. In order to study dark matter effectively, ideally we would want to probe regions where dark matter is the dominant component. This is not possible with optical data as the stellar component does not extend to these radii, however, as detailed in Section 1.3, dynamical models have used stellar kinematics combined with other tracers in the outer regions. As shown in Figure 4.2, neutral hydrogen (H I) exists in galaxies in a thin rotating disk which extends to far greater radii than the stellar component, and if the rotation is regular – as is the case in many elliptical galaxies (Morganti et al., 2006b; Oosterloo et al., 2010), and we assume to be true for spiral galaxies which in general exhibit less velocity dispersion (Beckman et al., 2004) – the dynamics can be treated as simple circular motion instead of more complex kinematic modelling (Yang et al., 2019).

Figure 4.2: NGC 6946 observed in the optical on the left (Digitized Sky Survey), and in H I on the right (Westerbork Synthesis Radio Telescope), on the same scale (from Boomsma et al., 2008)

As the nature of H I requires it to be dynamically cold, this gas can be assumed to be rotating close to circular velocity due to the low velocity dispersion and lack of asymmetric drift effect, with the velocity being dictated by the gravitational potential of the system. As such, this rotation would be an excellent tracer on the potential where the dark matter dominates in the outer regions, as the circular velocity, v_c, relates to the potential, Φ:

$$v_c = \sqrt{r \frac{\partial \Phi}{\partial r}} \tag{4.1}$$

Observing H I is intrinsically different from optical observations, and comes with its own limitations, as explained in Section 2.3, however the information which can be extracted from these observations is rich. Indeed, many studies (Weijmans et al., 2008; Martinsson et al., 2013; Yang et al., 2019) have exploited this extra information to create very detailed models of individual systems from resolved observations of H I kinematics. This highlights again the trade off between sample size and modelling detail – resolved H I observations require full radio array interferometric observations in order to give spatial information. These require deep time-intensive observations, and are only available for a few hundred galaxies (this is changing with the next generation of radio observatories; Apertif, MeerKAT, SKA, etc; Oosterloo et al.,

2009; Jonas & MeerKAT Team, 2016; Dewdney et al., 2009; McMullin et al., 2022). Unresolved radio observations are much more widely available, however these observations do not contain spatial information and just provide a single spectrum for the region covered by the beam, which is on the order of several arcminutes (for Green Bank Telescope, GBT, at 21cm; Masters et al., 2019).

With the radio data alone, some quantities can be constrained, including a dynamical mass inside the beam, which can be used to derive the dark matter fraction within the beam by comparing with the stellar mass measured optically. However, without the details of the stellar kinematics there is little to be done in terms of full dynamical modelling. As such, the need for large surveys of galaxies which provide both optical IFS data for the stellar component, alongside hydrogen kinematics has been identified, precipitating plans to create and conduct such surveys (Masters et al., 2019; Falcón-Barroso et al., 2019; Catinella et al., 2023). One such survey, H I -MaNGA, is providing unresolved single-dish H I kinematics for galaxies observed by an IFU in the MaNGA survey. The details of this survey are explained in Section 2.3, as these are the data exploited in this chapter.

4.2 Sample and Data

This section uses stellar kinematic data from the MaNGA survey DR17 (see Section 2.2), H I kinematic data from the H I -MaNGA survey DR3 (see section 2.3), and r-band imaging and photometry data from the DESI Legacy Survey DR9 (see Section 2.1).

From the 6632 galaxies which had been observed in all three surveys at the time of the data releases listed, a sample was constructed based on the following criteria:

- The galaxy has a positive detection in the H I -MaNGA survey
- The H I -MaNGA survey detection has signal-to-noise ratio $SNR > 5$
- The H I -MaNGA data is not flagged for any quality issues such as beam confusion (another galaxy detected in the beam), baseline structure (there is a detection in what should be the background baseline which has affected the baseline subtraction), etc.
- The galaxy inclination as measured in the SDSS survey through axial ratio is greater than 60°, where 90° is edge-on.

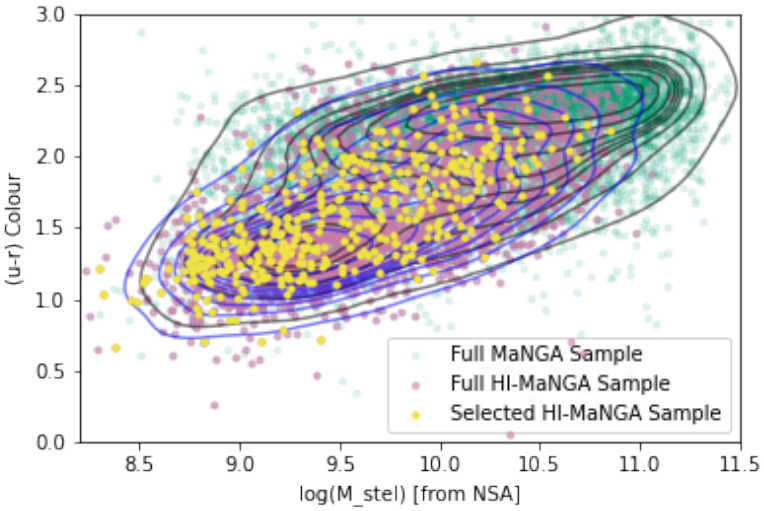

Figure 4.3: $(u-r)$ colour vs stellar mass for the sample used. Green points and black contours show the distribution of the full MaNGA DR17 sample, purple points and blue contours show the galaxies observed in the full DR3 sample of H I -MaNGA, and yellow points show the galaxies selected in the sample for this work based on the selection criteria described.

After the above criteria are applied this takes the sample size to 423. Figure 4.3 shows where these galaxies lie in the colour-luminosity plane, and shows that the sample observed by H I -MaNGA spans the full MaNGA sample but misses the most massive elliptical galaxies, while the sample selected by the criteria above preferentially selects bluer galaxies. These criteria do not actively address application of assumptions in the modelling process – for example, galaxies exhibiting bar structures which cause the position angle to vary with radius would not match the assumption of axisymmetry required for JAM modelling. These issues are dealt with during the process by applying goodness-of-fit criteria to quality of MGE parameterisation fits and JAM fits. This results in any galaxies which are not able to be adequately modelled by the assumptions in our modelling process being discarded.

In terms of biases introduced in our sample at this stage, we note that the requirement for a H I detection means we have, by design, selected galaxies which contain significant gas content, which preferentially selects bluer disk galaxies with ongoing star formation, as can be seen in Figure 4.3. While the MGE and JAM methods were originally designed for use on elliptical galaxies, we note that past studies have worked with "fast rotators", which are elliptical galaxies which contain a rotating disk component, and studies have applied the methods to the modelling of disk galaxies explicitly (Kalinova et al., 2017; Li et al., 2017). This is valid as these systems are rotationally dominated, and so can be modelled using these methods.

4.3 Modelling with MaNGA Data Alone, without Dark Matter

4.3.1 Methods

Initially, I created JAM models using only the IFU data, similarly to what has been done previously in Santucci et al. (2022); Cappellari et al. (2011), and Chapter 3. These models do not include any dark matter component, and are created to measure the inclination of the galaxies for later modelling, and to demonstrate that dark matter is required in our models. First, the gravitational potential must be approximated as per Section 2.5, which is then used to create our JAM models.

Luminous Mass Distribution

A multi-gaussian expansion (MGE) parameterisation of the surface brightness was created following the method explained in Section 2.5, again using r-band imaging from DR9 of the DESI Legacy Survey – described in Section 2.1. This was done by the exact same method as was applied in the previous Chapter in Section 3.3.1, including the process by which artifical limitations on inclination are avoided. This gives a 2-dimensional surface brightness distribution which can then be multiplied by a mass-to-light ratio to convert this into a stellar mass distribution and give the gravitational potential. We assume this mass-to-light ratio to be spatially constant across the galaxy, which has its limitations compared to the physical reality of a galaxy with diverse stellar populations. Galaxies are shown to have a spatially varying mass-to-light ratio, with decomposition into a bulge mass-to-light-ratio and a disk mass-to-light ratio often considered more accurate, however the assumption of a constant value has yielded valid results in past studies, with Cappellari et al. (2011) and Cappellari (2008) showing that masses can be recovered within 6% of true values using this method. These models are presented here in Figures 4.4, 4.5, 4.6, and 4.7 for four example galaxies. This shows that the MGE parameterisation fits the surface brightness distribution of the galaxies well, with residuals staying below 20% at all radii in each sector. A 20% residual for the light in an individual sector would translate to a mass error of just 0.1% for the full galaxy. Therefore, keeping the errors within 20% for each sector at each radial bin is sufficient (even given the cumulative effects of errors across the spatial extent of the MGE) to ensure our models are accurate. These example galaxies are used as a proof-of-concept sample in these sections, and results are shown for them in detail. These models are used throughout this Chapter when JAM models are created.

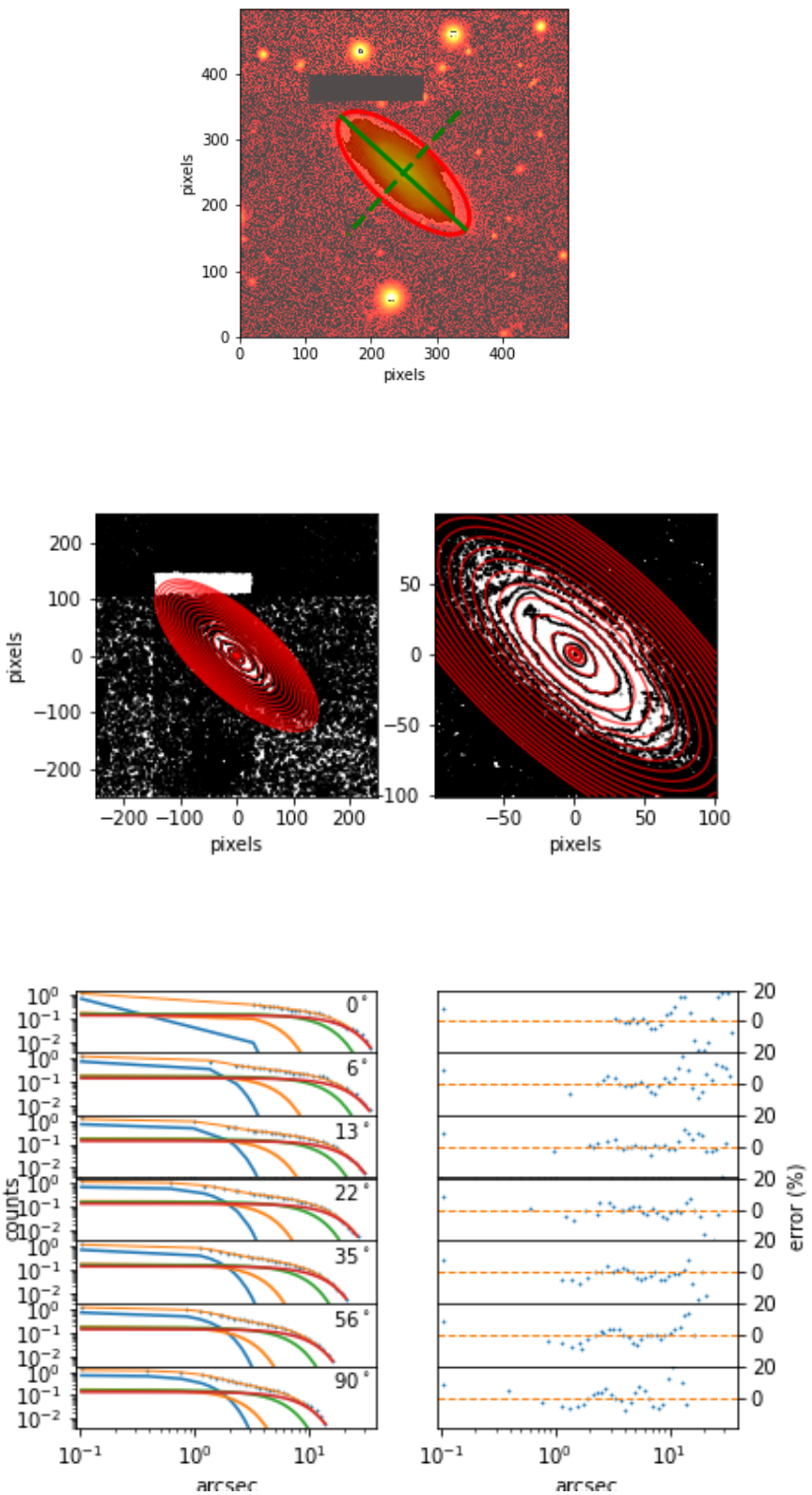

Figure 4.4: MGE evaluation for 9095-12704. **Top:** Identification of the galaxy centre and major/minor axes (green lines), and extent of surface brightness (red ellipse). **Middle:** MGE surface brightness contours (red) compared with the observed r-band surface brightness contours (black). **Bottom:** Left shows model photometry (lines) versus observed (dots) at different position angles, right shows residual photometry.

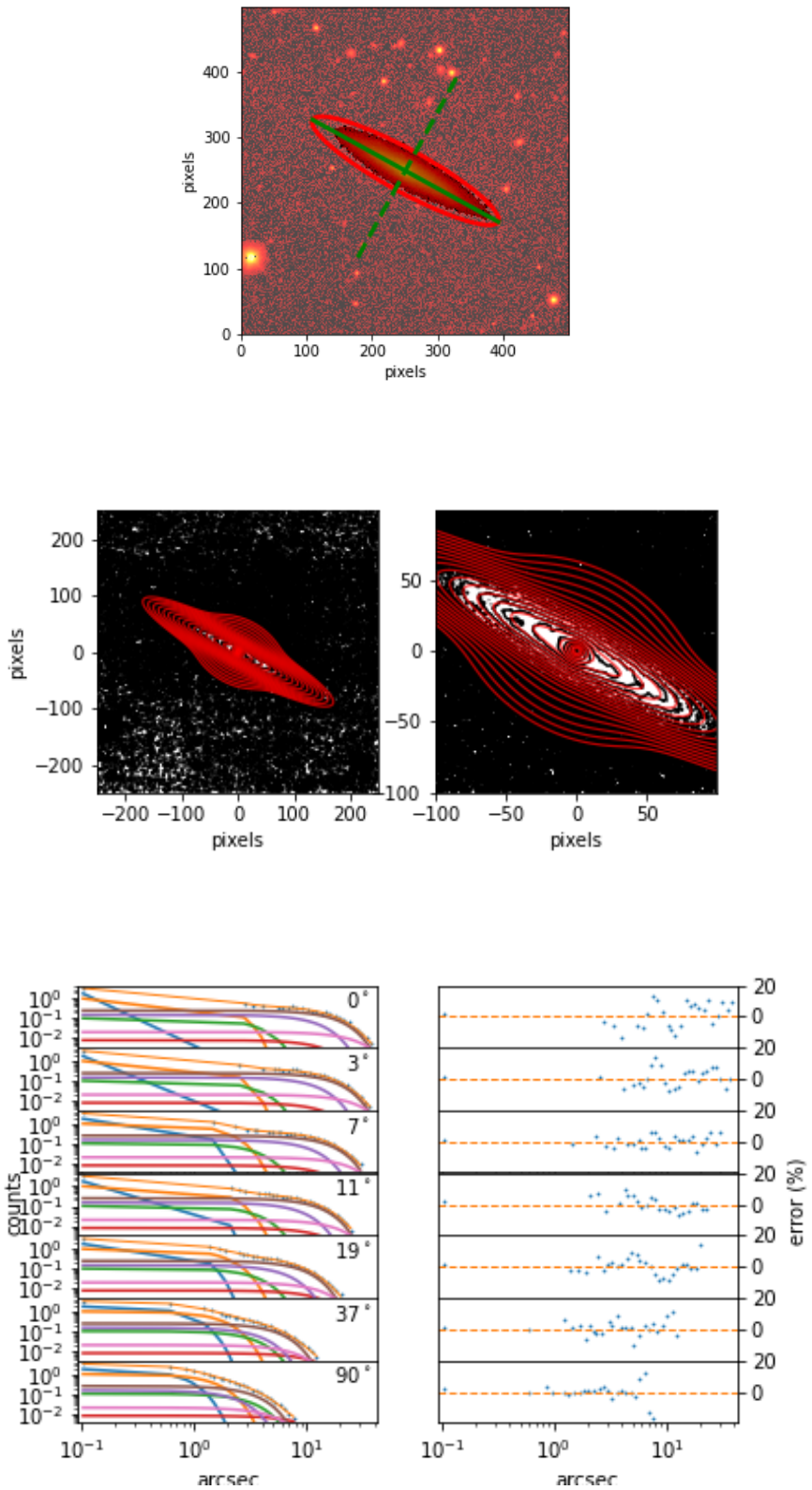

Figure 4.5: MGE evaluation for 8084-12705. Panels same as in Figure 4.4.

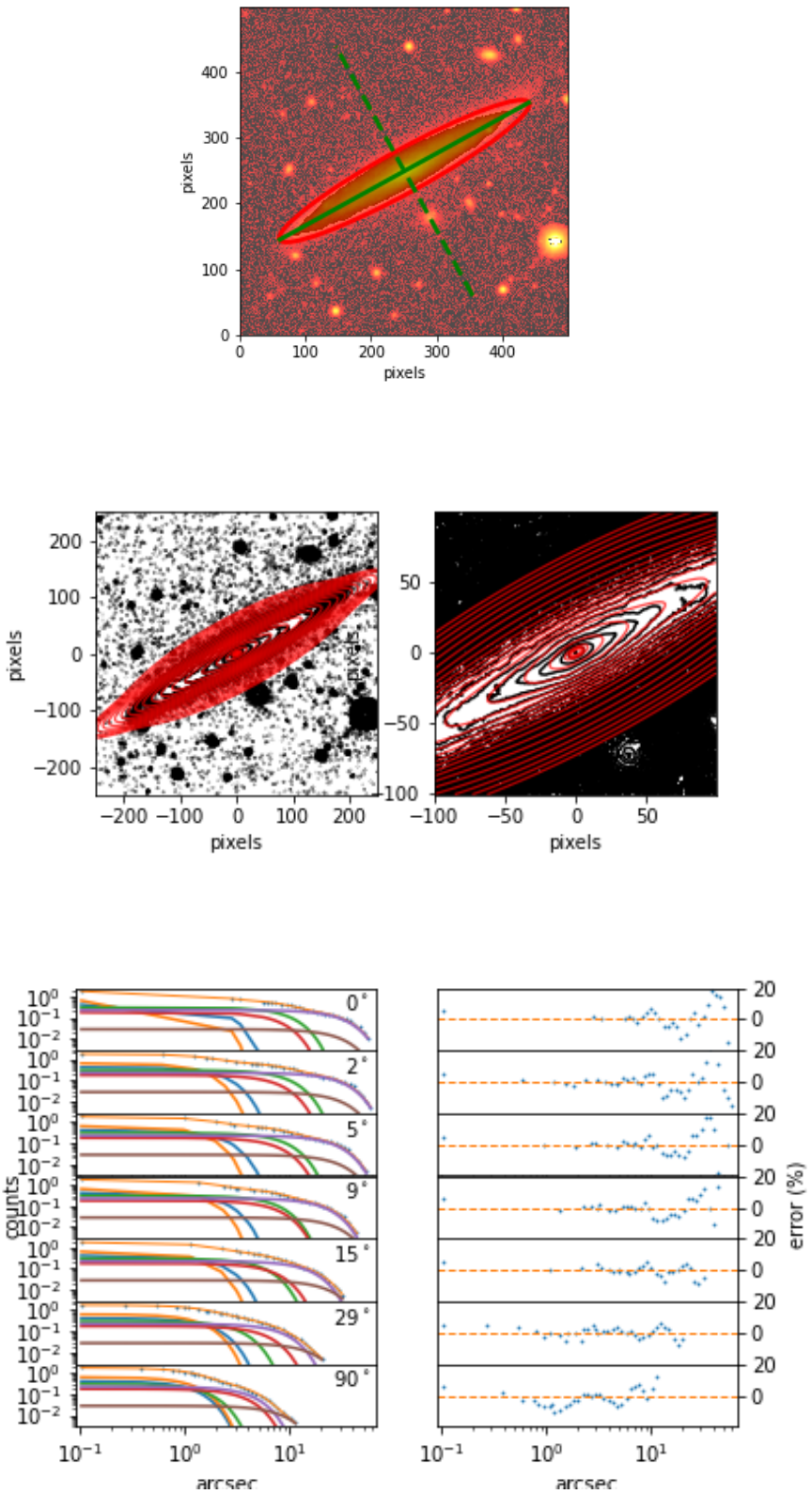

Figure 4.6: MGE evaluation for 9190-12702. Panels same as in Figure 4.4.

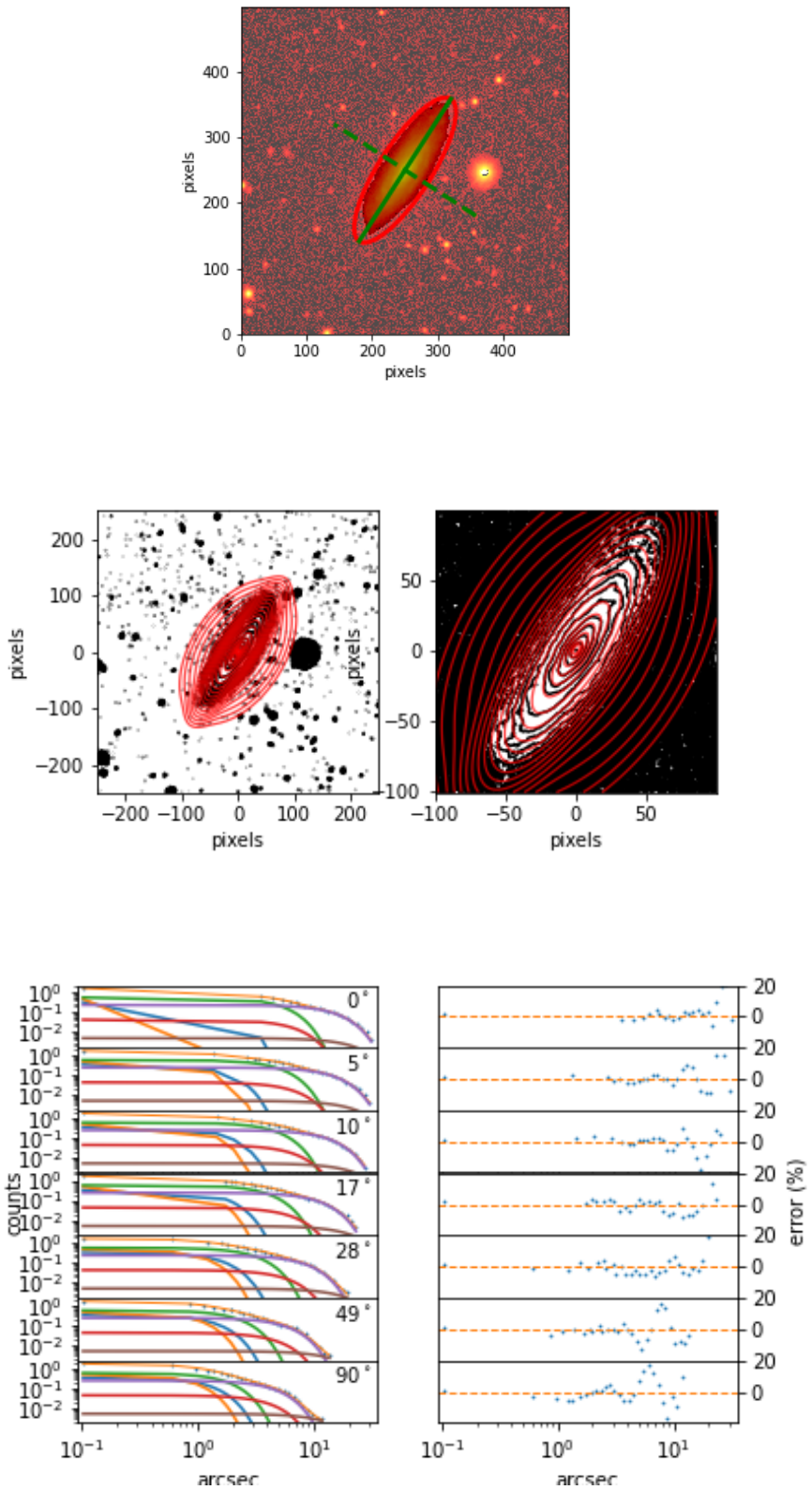

Figure 4.7: MGE evaluation for 12079-12702. Panels same as in Figure 4.4.

Rejected MGE Models

While for these examples the MGE fits have worked well, we ran our MGE fitting algorithm over all galaxies in the sample, with the same base parameters set. Of the 423 galaxies in our selected sample, many failed to produce adequate models. After visual inspection of the MGE models for the sample, we selected a limit of $\chi^2 < 6$, as this removed the failures from the sample upon visual inspection (note, this is not reduced χ^2). This value was calculated as the comparison between the observed counts from the legacy image in each sector at each radius, and the value found by the MGE model at this point. It is important to note that no errors are taken into account for the image, and therefore this chi2 will be conservative. This left a sample of 84 galaxies. This was a conservative estimate to exclude catastrophic failures, which we note may exclude many viable galaxies. We also note that the precise nature of the failures were diverse, ranging from failing to identify enough guide stars to calculate the PSF or misidentifying the galaxy centre in the frame, to being badly modelled by a constant proper angle or exhibiting strong non-axisymmetric structures like bars. See Figures 4.8 to 4.10 for examples. As JAM modelling relies on axisymmetry, we have to discard those which fail to be accurately fit by this model. Some of these could be salvaged by tailoring the fitting parameters to each galaxy or manually masking features in the images – however, as this is a proof-of-concept study on a relatively large sample, we elected to discard those which were not able to be fit without manual intervention, as this was beyond the scope of this project. This leaves our sample size at 84 galaxies which are put through the modelling process. We note that this biases our sample by removing those with barred structures, especially those with bars which have a varying position angle. This is discussed in further sections.

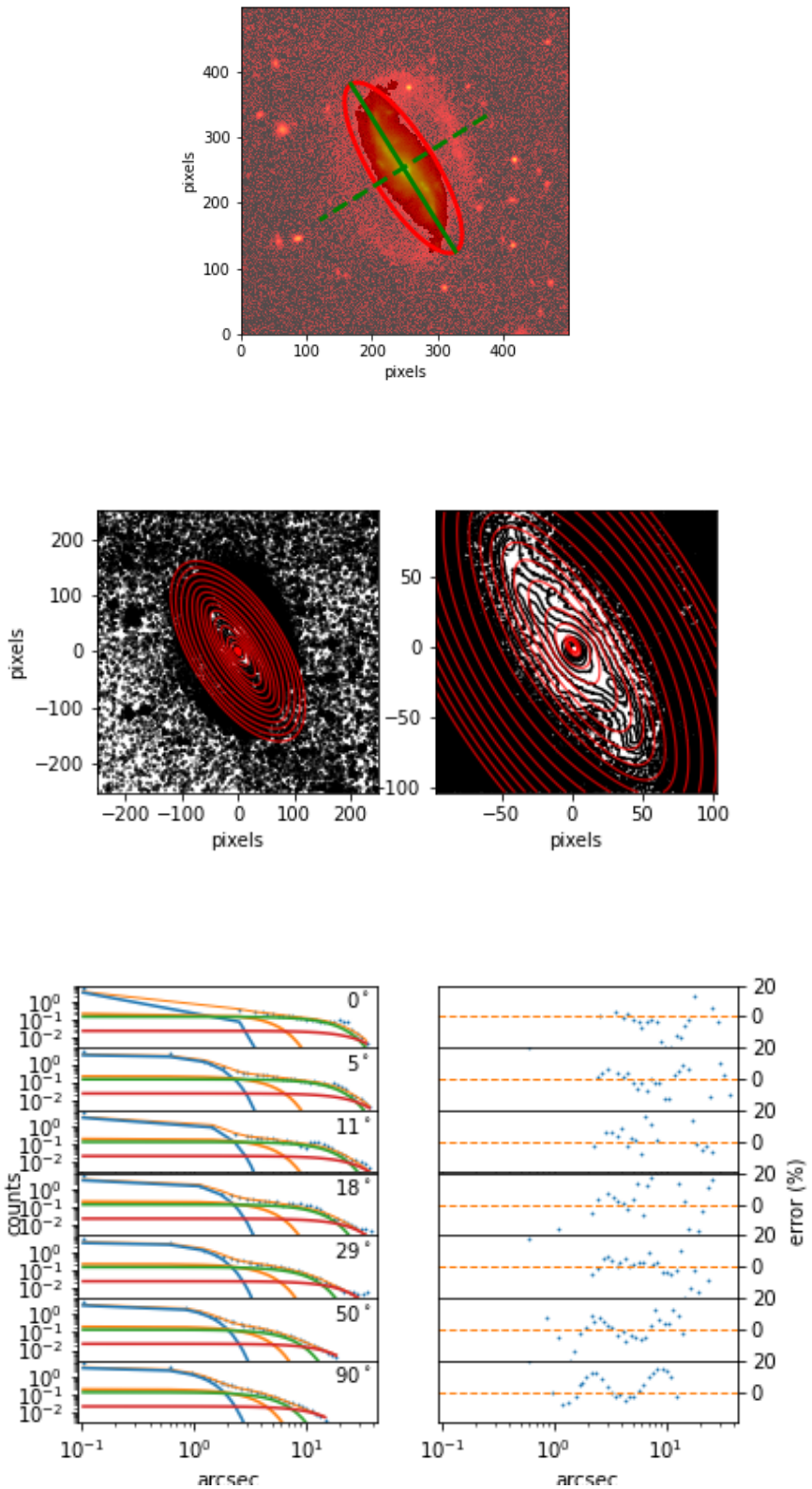

Figure 4.8: MGE evaluation for 8154-12705. This model failed, with chi2 value of 26. Panels same as in Figure 4.4

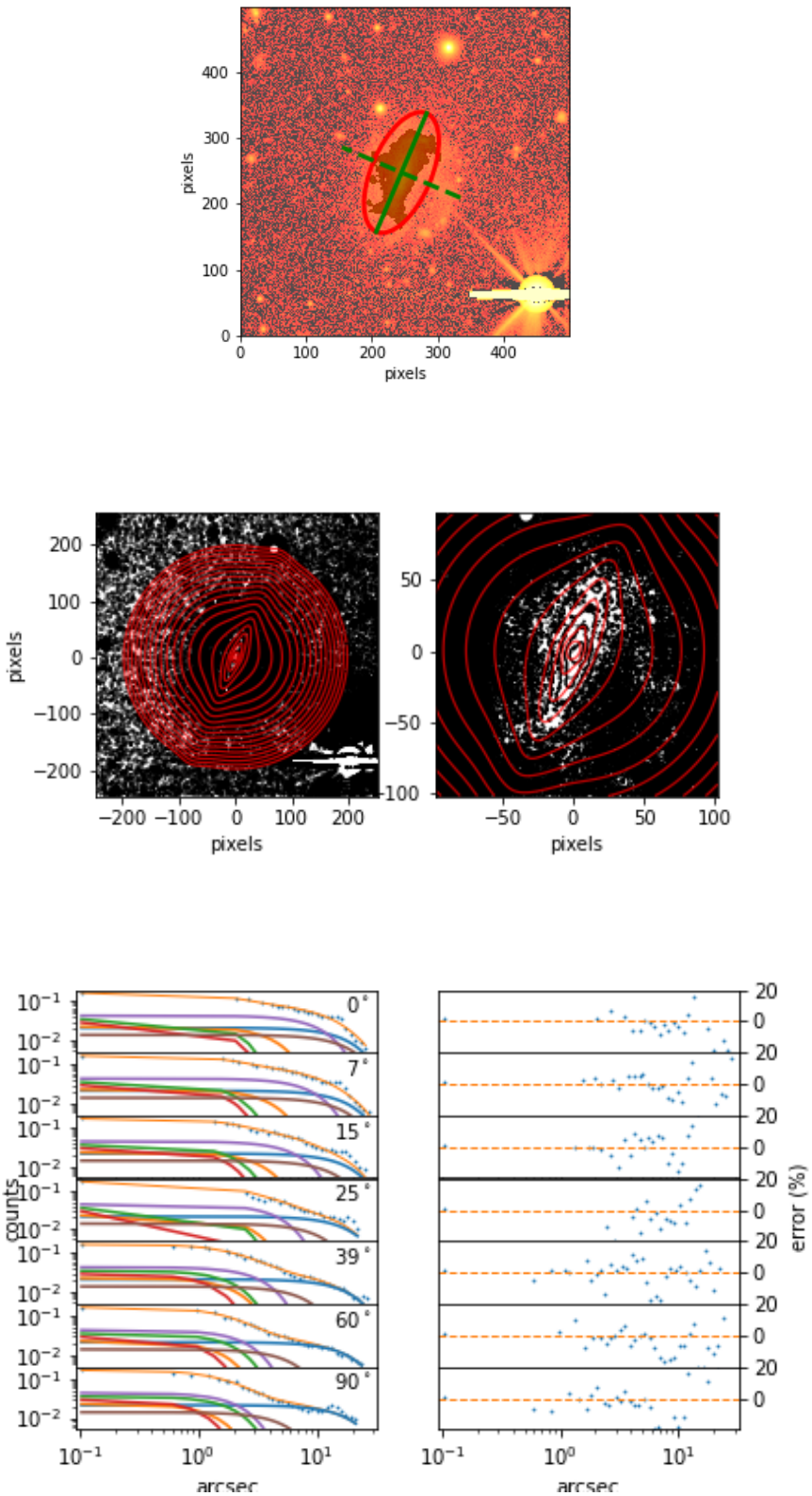

Figure 4.9: MGE evaluation for 10841-12702. This model failed, with chi2 value of 10. Panels same as in Figure 4.4

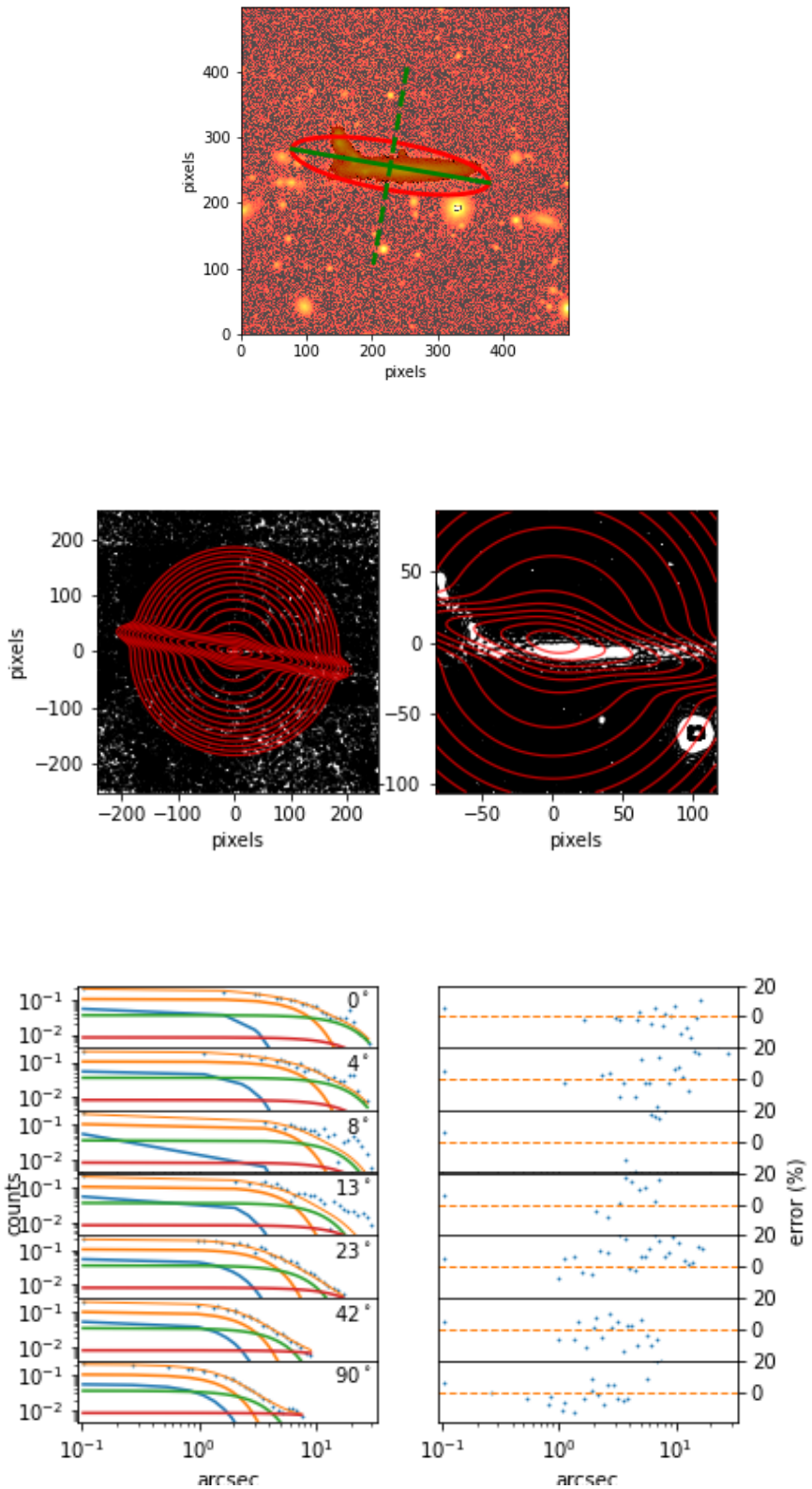

Figure 4.10: MGE evaluation for 11824-12702. This model failed, with chi2 value of 51. Panels same as in Figure 4.4

Gaseous Mass Distribution

Initially I create models with no dark matter, following the method used in Chapter 3. The mass components present are the luminous component already described, along with a gaseous component. The second component was included because the sample selection described in Section 4.2 selects galaxies which are detected in H I -MaNGA, which by design means the sample contains predominantly gas-rich galaxies and so the gas mass cannot be neglected. Indeed, the H I gas mass in the sample is found to be around 0.1-0.2 that of the stellar mass. In this case the gas is modelled as an exponential disk and parameterised based on the total gas mass (as per Bigiel & Blitz, 2012), which is determined by scaling relations from the observed H I mass from H I -MaNGA observations. Additional factors are added in order to account for gas mass in other phases, including a factor of 1.36 to account for helium (as per Weijmans et al., 2008), and a factor which depends on the stellar mass to derive the molecular H_2 mass (as per Table 3 of Catinella et al., 2018). As such, the gas mass is equal to:

$$M_{gas,total} = M_{H_I} + (0.36 \times M_{H_I}) + (A_{H_2} \times M_{H_I}) \tag{4.2}$$

where A_{H_2} is the (M_{H_2}/ M_{H_I}) value taken from Table 3 of Catinella et al. (2018), reproduced here in Table 4.1:

x	$\langle x \rangle$	Median log(M_{H_2}/ M_{H_I})
log $M_\star$	9.18	−1.044
	9.53	−1.003
	9.88	−0.704
	10.22	−0.691
	10.59	−0.659
	10.91	−0.521
	11.20	−0.559

Table 4.1: Molecular-to-atomic gas mass ratio scaling relations for xGASS-CO, reproduced from Catinella et al. (2018)

Using the $M_{gas,total}$ value from Equation 4.2, the density profile is then given (as per Bigiel & Blitz, 2012) as:

$$\Sigma_{gas}(r) = 2.1 \times \Sigma_{trans} \times e^{-1.65 \times r/r_{25}} \tag{4.3}$$

where Σ_{trans} is the surface density of the gas at the "transition radius" which is where the

density of molecular gas is equal to the density of atomic gas, and is given by:

$$\Sigma_{trans} = \frac{M_{gas,total}}{2\pi \times 2.1 \times 0.37 \times r_{25}^2} \tag{4.4}$$

where r_{25} is the radius at which a galaxy reaches a surface brightness of 25 magnitudes/ arcsec^2 in the B-band. Our galaxies do not have B-band surface photometry, but this is converted using $R_{25} = 2.5 \times R_{eff}$ (Trujillo et al., 2020), where R_{eff} is the half-light radius in the r-band, which is available for our galaxies from the SDSS NSA catalogue from elliptical petrosian fitting. This profile is then also parameterised in MGE form, and added to the JAM model.

JAM Model

JAM models without dark matter are constructed for our sample following the method described in Sections 2.6 and 3.3.2. As with Section 3.3.2, we use MCMC to find the best fit model. However, as these models are going to be developed to include more free parameters to describe the dark halo, we opt to use a Gibbs Adaptive sampler implemented through `GAStimator` (see Section 2.7). This is more robust to likelihood distributions with many local minima. For these models, the free parameters and their priors are the same as those used in Chapter 3.

The MCMC was run using a log likelihood function of:

$$\log L = -\frac{\chi^2}{2} = -\frac{1}{2}\sum_{i}^{N}\left(\frac{(v_{rms,i}^{obs} - v_{rms,i}^{model})^2}{(\sigma_{v_{rms,i}}^{obs})^2}\right) \tag{4.5}$$

where i indicates each data point in the 2D map, and N is the total number of valid data points in the IFU. This is the quantity which is maximised by the MCMC process, and is at its maximum when the IFU data is most closely reproduced by the model. We note that this form is only truly valid in the case of uncorrelated errors, however in Cappellari et al. (2011), the authors applied the method using both correlated and uncorrelated forms and state that in practice the values and errors did not disagree between the methods. The errors used are the inverse variance errors given by the MaNGA data. We also note that in Mitzkus et al. (2017), a case was made for using inflated errors to avoid the issue of small bins in the inner regions of the datacube. The authors were not aware of this method during the implementation of

the model, and so used the method from Cappellari et al. (2011). This accounts for why propagated errors of the model are artificially small.

As in Chapter 3, the MCMC was run until the parameters converged, and the first 1000 steps were discarded as burn-in. The best fit values of the parameters were taken as the mean of the distribution, with errors at the 16th and 84th percentile. For reference, running parallel on 30 cores, one galaxy model takes approximately just under an hour to run.

Comparison with Measured Cold Gas Velocity

As the M/L is now constrained for our models, this value can multiply the luminous MGE in order to give the mass distribution present in the galaxy. The rotation curve can be produced and extrapolated to greater radii based on the mass model, showing the circular velocity vs radius, as circular velocity (v_{circ}) at a given radius (R) in an axisymmetric potential (Φ) is determined by:

$$v_{circ} = \sqrt{R\frac{d\Phi}{dR}} \tag{4.6}$$

This can then be compared to the hydrogen velocity observed in order to see how well the model fits in the most dark matter dominated region. To do this, the velocity is extracted from the H I -MaNGA data as explained in Section 2.3, alongside the estimate of the radius probed. This is estimated using the H I mass-size relation, as described in Section 2.3. While the scatter in the relation means this is a rough estimate of the radius probed, this should correspond to the outer parts of the disk as this is where the maximum rotational velocities are reached, and further the velocity profile in the outer regions of disk galaxies is known to be largely constant so our models should not be too sensitive to this selection.

4.3.2 Results

As described in Section 4.3.1, JAM models were created to constrain the dynamical mass present in the galaxies, and this was used to extrapolate the velocity curves expected for this mass distribution out to large radii by constraining the mass to light ratio and using an MGE approximation out to greater radii than the images. Figures 4.11, 4.12, 4.13 and 4.14 show the results of the JAM modelling process for a selection of 4 example galaxies from our sample – with the observed v_{RMS} map shown alongside that generated by the best fit model, and a map

of the residuals between the model and the observations, showing good agreement; a corner plot shows the posterior distributions of the free parameters in the JAM model from the MCMC process, showing they are converged; and finally a plot of the projected circular velocity for the best fit model is shown, with the velocity of the H I plotted to show that the models without dark matter fail to fit the data in the outer regions. This highlights the importance of obtaining data for the kinematics in the outer regions of galaxies, as despite these models managing to correctly match the data in the inner regions covered by the IFU and dominated by the stellar potential, they do not match the system in the outer regions. Further, and most importantly, this shows very strikingly the requirement for an additional undetected (dark matter) mass component in galaxies to explain the motions we observe at large radii.

Given these results, the next section (Section 4.4) creates models which include a dark matter halo and constrain these parameters with only the IFU data, to see if these can match the kinematics in the outer regions.

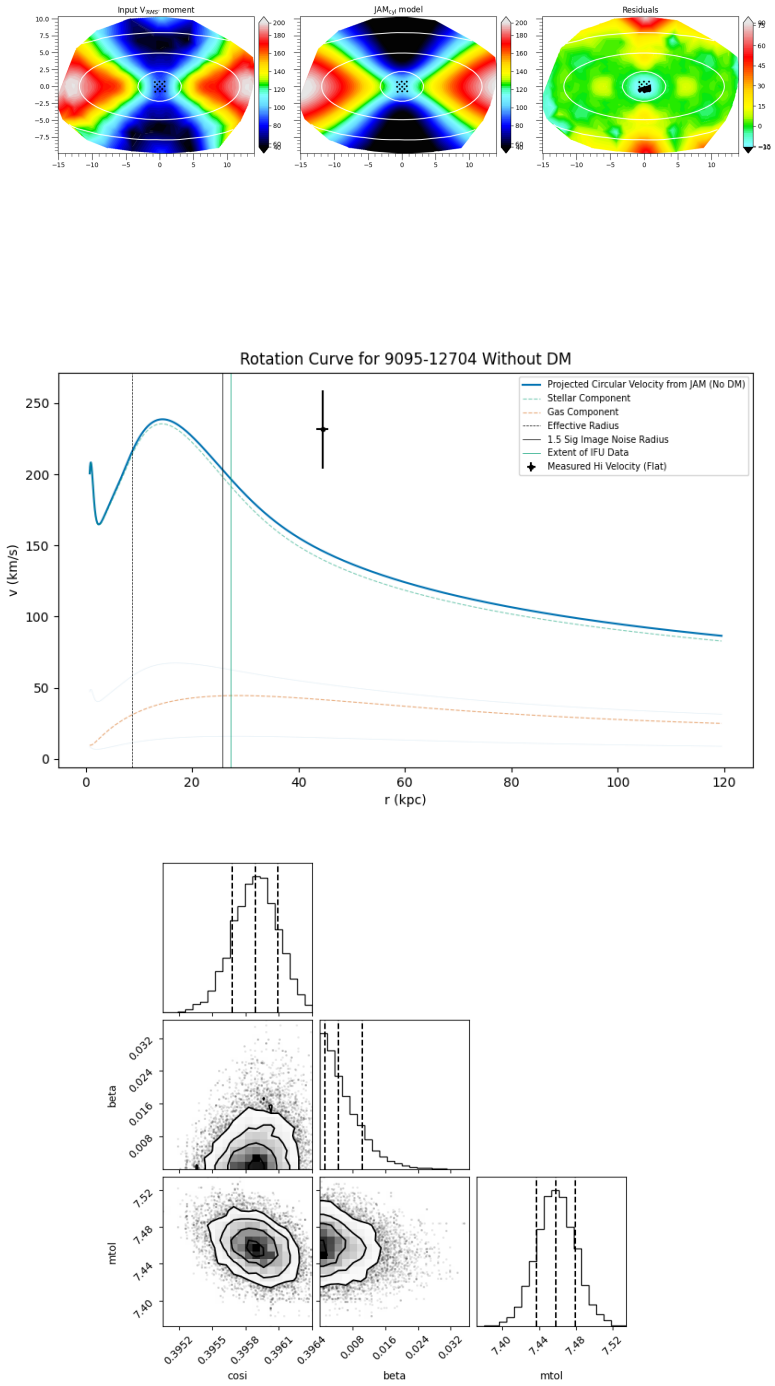

Figure 4.11: Evaluation of JAM model with no dark matter for 9095-12704. **Top:** From L-R, observed, modelled, and residual V_{RMS} maps. White contours show isophotes from the MGE model. **Middle:** Rotation curve generated by the model (blue), composed of the stellar component (dashed green curve) and gas component (dashed orange curve). Vertical dashed line indicates the effective radius of the galaxy, solid black line indicates the noise limit of the r-band image used to generate the MGE, and the green vertical line indicates the radius reached by the IFU data. The black point shows the measured H I velocity. **Bottom:** corner plot showing posterior distribution of variables from the JAM MCMC simulation.

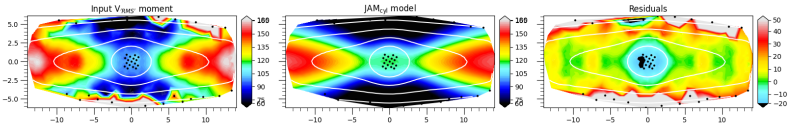

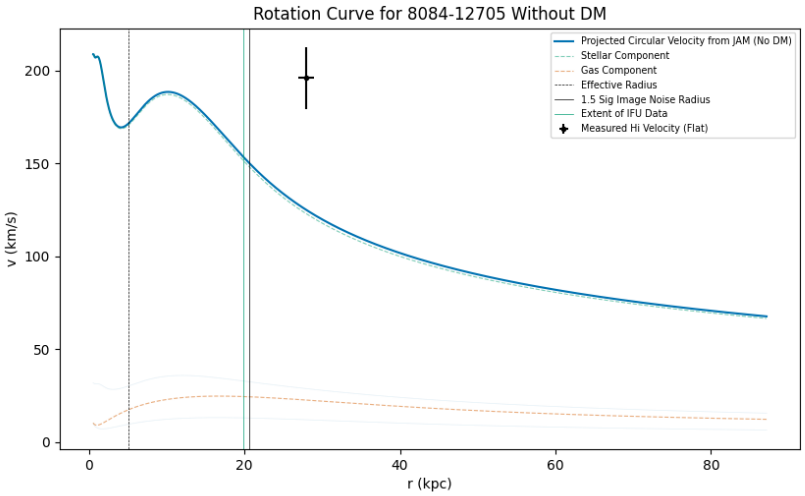

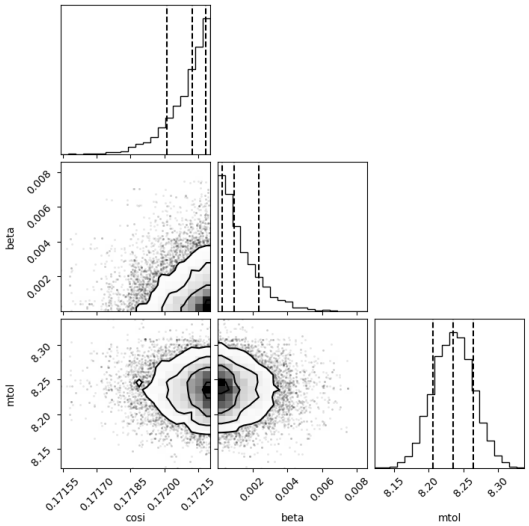

Figure 4.12: Evaluation of JAM model with no dark matter for 8084-12705. Panels same as in Figure 4.11.

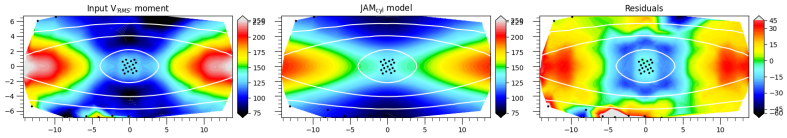

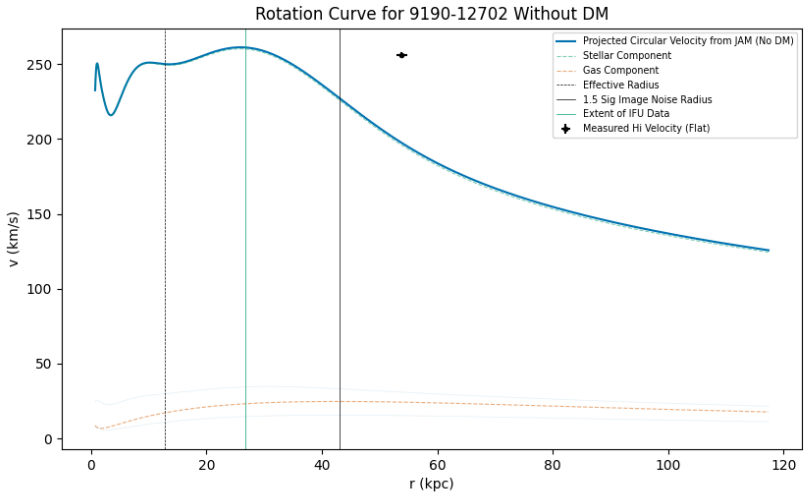

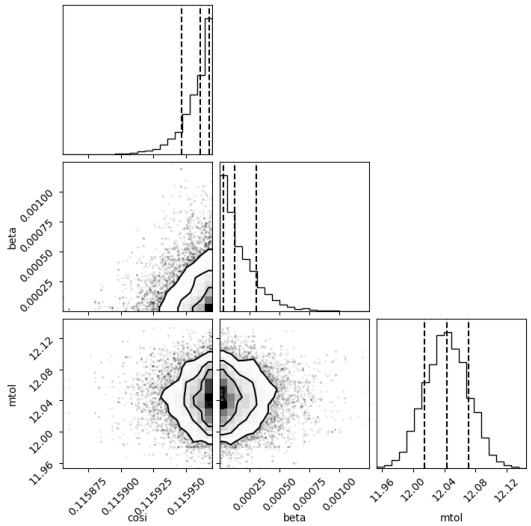

Figure 4.13: Evaluation of JAM model with no dark matter for 9190-12702. Panels same as in Figure 4.11.

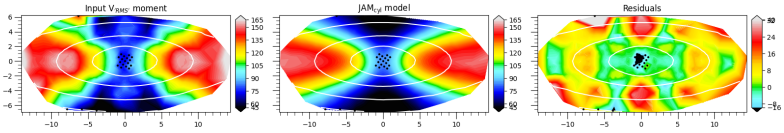

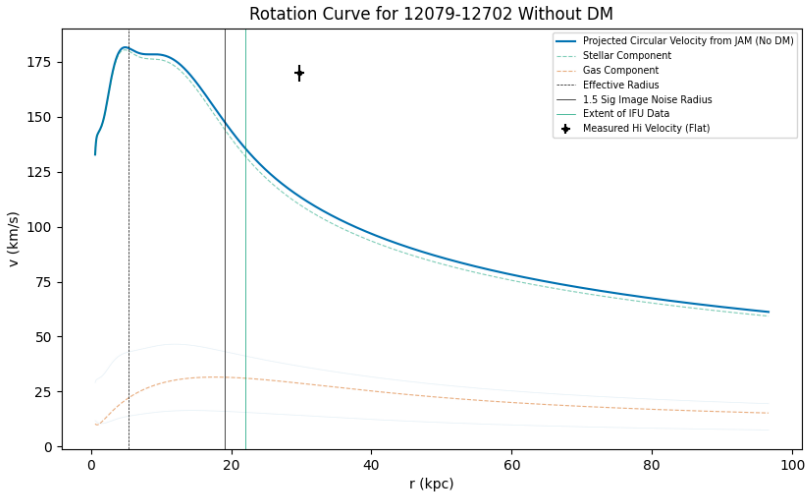

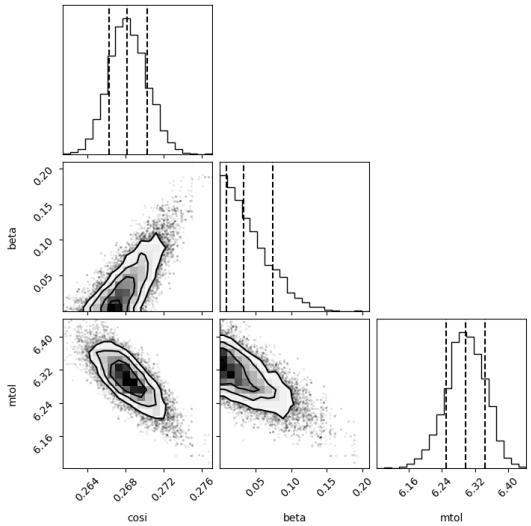

Figure 4.14: Evaluation of JAM model with no dark matter for 12079-12702. Panels same as in Figure 4.11.

4.4 Modelling with MaNGA Data Alone, including Dark Matter

In the previous section we saw that JAM models which omit dark matter are able to produce models which replicate the kinematics observed by IFS in the inner regions, but fail to produce high enough circular velocities in the outer regions to match our H I data. This section attempts to add a dark matter component into the models without the additional constraint of the H I data, to see if haloes can be correctly constrained by the IFU data alone.

4.4.1 Methods

These models follow the same method as those above in Section 4.3.1, except for the addition of a dark component to the mass distribution.

Dark Mass Distribution

To create a dark component, the `colossus` python package is used (COsmology, haLO and large-Scale StrUcture toolS; Diemer, 2018). Among many other features, this provides functions which generate radial density profiles for theoretical dark matter distributions, given defining parameters. Two options provided are an Einasto halo (Einasto, 1965) and an NFW halo (Navarro et al., 1996). A subsample of models were run using both of these forms, and the Einasto profile was seen to fit the data more reliably than the NFW halo. After some trials and comparison (and literature examples showing a better description than other halo distributions: Gao et al., 2008a), we select an Einasto halo (Einasto, 1965), which is defined as per the radial density profile:

$$\rho(r) = \rho_s \exp\left(-\frac{2}{\alpha}\left[\left(\frac{r}{r_s}\right)^{\alpha} - 1\right]\right) \tag{4.7}$$

where ρ is the density, r is the radius, and the halo is defined by a scale density ρ_s, a scale length r_s at which the scale density is reached, and a parameter α which determines how quickly the profile steepens with slope. This equation can be transformed within `colossus` to create Einasto haloes defined by α alongside the halo mass M_{200} (defined as the mass enclosed within the sphere bounded at the radius where the density reaches that of 200 times the background density) and concentration c, which are more widely used in the literature.

This adds further free parameters to our model. However, in order to minimise free pa-

rameters in an effort to give the models the best chance to converge, we fix the α parameter to ~ 0.16, which was the value found in Gao et al. (2008a) to best fit the distribution of present day haloes in the Millennium Simulation (Gao et al., 2008b).

JAM Model

JAM models including a dark matter halo are constructed for our sample following the method described in Section 4.3.1, but with the addition of an extra component in the form of a theoretical dark matter halo in MGE form, and a change to some priors. Further, the inclination is no longer treated as a free parameter, but is fixed to the value which was found from the model with no dark matter. This is valid as the dark matter halo added is spherically symmetrical, and so the inclination is not expected to change with the addition of the dark component.

During the MCMC process, as each set of free parameters are generated from the priors (including the additional parameters which define the halo), a dark matter profile is generated by `colossus` which is also then parameterised as an MGE (this time only one dimensional radial density profile is required as the dark matter halo is considered to be spherical) as per Section 2.5, and added to the JAM model as a dark potential for that iteration. As such, input into the JAM model are a luminous MGE which includes just the stellar MGE generated from the r-band imaging, and a potential MGE which includes all components from the stellar MGE, gas MGE, and dark MGE.

As with Section 3.3.2, we use MCMC to find the best fit model, and we opt again to use a Gibbs Adaptive sampler implemented through `GAStimator` (details in Section 2.7). For these models, the free parameters and their priors are listed here:

- Orbital anisotropy, β: flat prior between 0 and 0.75

- Stellar mass-to-light ratio, M/L: flat prior between 0.1 and the dynamical M/L fitted by the model with no dark matter.

- Halo mass, $\log M_{200}$: flat prior between 7 and 15. Note, M_{200} is close to, but not equivalent to, the virial mass.

- Halo concentration, c: Gaussian prior, centred on value set by the known mass-concentration

relation for redshift zero (from Klypin et al., 2011):

$$c(M_{200}) = 9.60\left(\frac{M_{200}}{10^{12}h^{-1}M_{\odot}}\right)^{-0.075} \tag{4.8}$$

with a 1σ width of 0.1, allowing scatter around this value. This relation is included as models with an uninformative flat prior on the concentration often failed to converge during the MCMC process.

The log likelihood function used, and the MCMC procedure are the same as in the previous models.

4.4.2 Results

As described above, JAM models were created for our sample which now include a dark matter halo (demonstrated to be needed in Section 4.3.2), and are fitted using only the IFU data. In Figures 4.15, 4.16, 4.17 ,and 4.18, our model results are presented, and compared to the H I data, for the same 4 example galaxies as in Section 4.3.2. We see that the inclusion of a dark matter halo improves the fit in the outer regions, while still fitting the data well in the inner regions, by increasing the circular velocity projected here, in some cases coming close to fitting the data. However, without the model "knowing" about the kinematics in these outer regions, it fails to match the measured velocities. Further, as in the case of 12079-12702, there is often a large spread of halo parameters allowed which creates a spread of possible rotation curves in the outer regions as the parameters are not as well constrained. We also see, as in the case of 9190-12702, that in some cases the halo parameters are able to fit the data in the inner regions well but then are massively failing to match the H I data in the outer regions.

We also note the impact of using the halo mass-concentration relation as a loose prior for the concentration values. Running these models with an uninformative flat prior on the concentration created models which often failed to converge during the MCMC process at all, whereas these models converge.

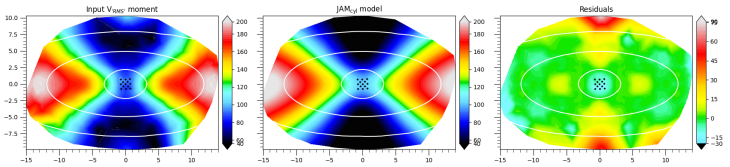

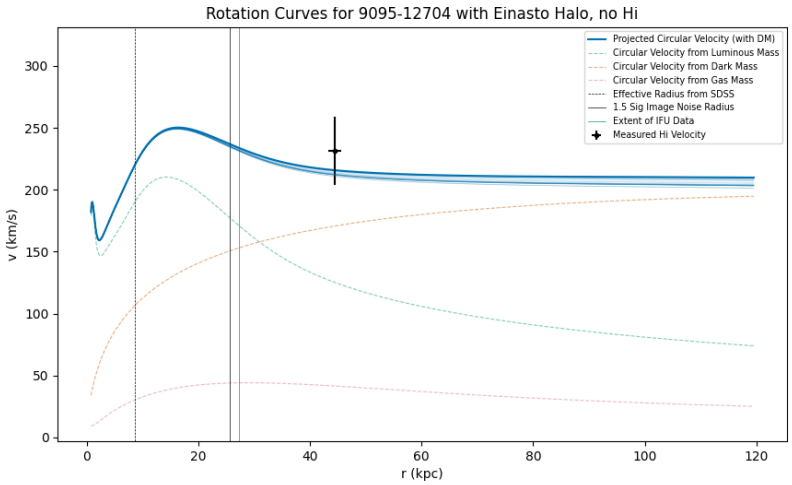

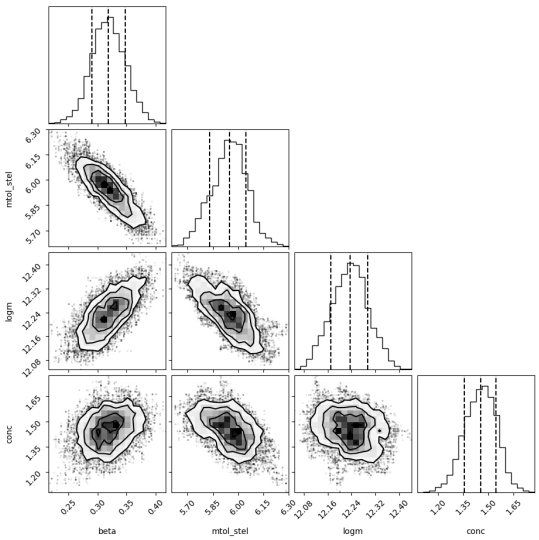

Figure 4.15: Evaluation of JAM model with dark matter, but no H I for 9095-12704. **Top:** From L-R, observed, modelled, and residual V_{RMS} maps. White contours show isophotes from the MGE model. **Middle:** Rotation curve generated by the model (blue), composed of the stellar component (dashed green curve), gas component (dashed pink curve), and dark component (dashed orange line). Vertical dashed line indicates the effective radius of the galaxy, solid black line indicates the noise limit of the r-band image used to generate the MGE, and the green vertical line indicates the radius reached by the IFU data. The black point shows the measured H I velocity. **Bottom:** corner plot showing posterior distribution of variables from the JAM MCMC simulation.

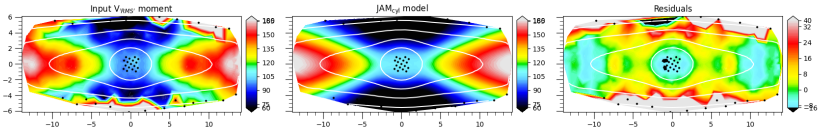

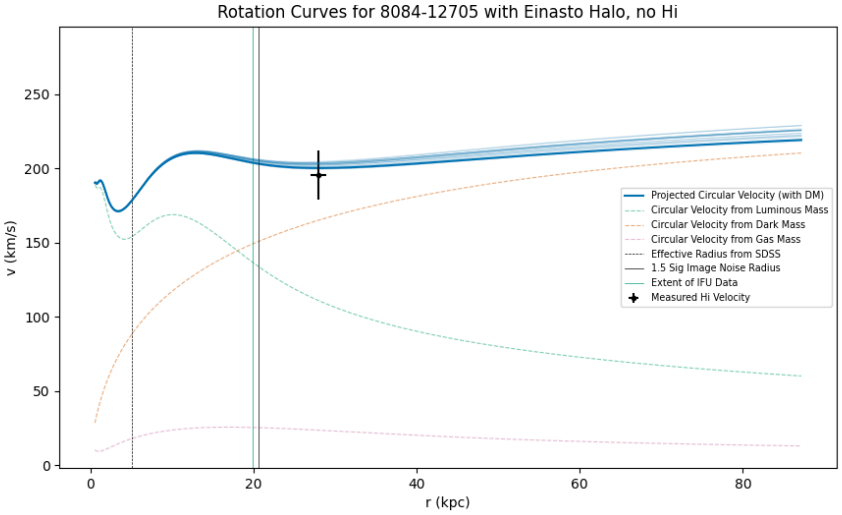

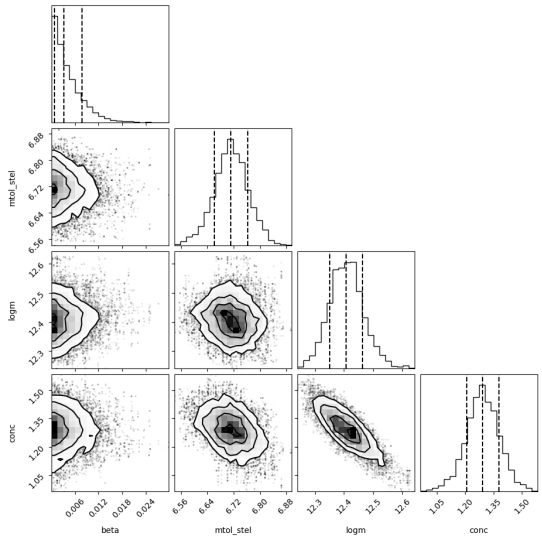

Figure 4.16: Evaluation of JAM model with dark matter, but no H I for 8084-12705. Panels same as in Figure 4.15.

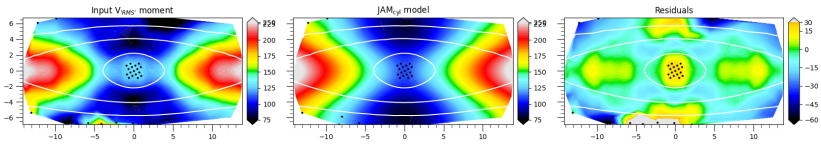

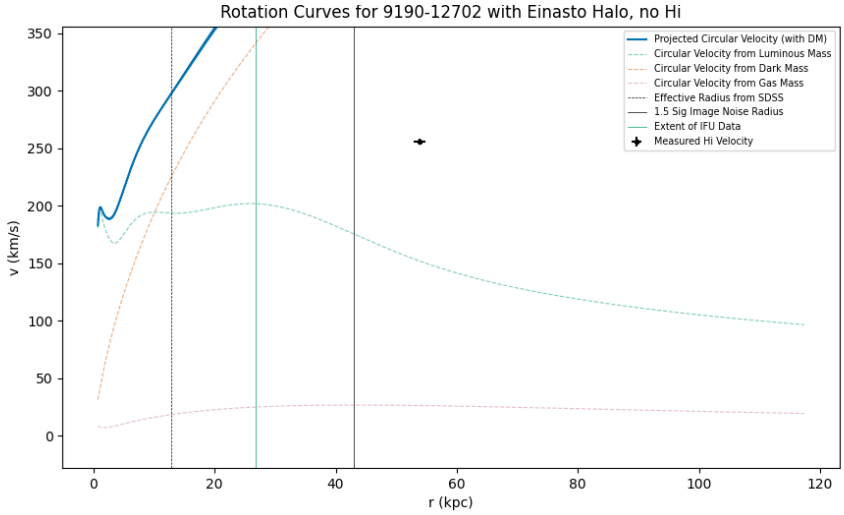

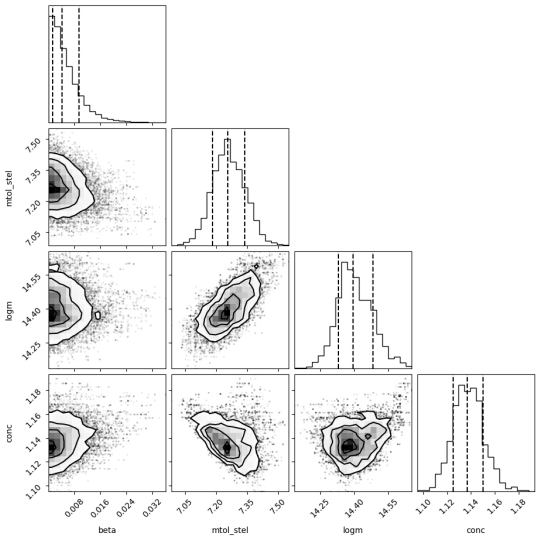

Figure 4.17: Evaluation of JAM model with dark matter, but no H I for 9190-12702. Panels same as in Figure 4.15.

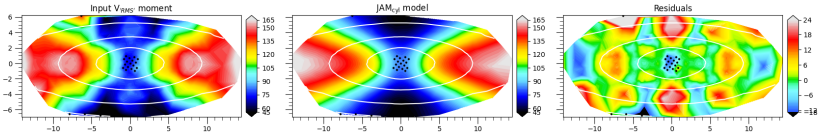

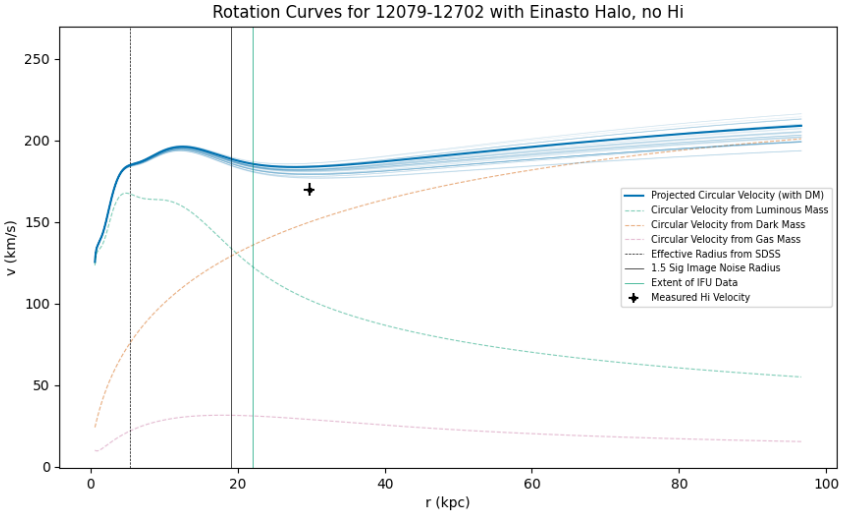

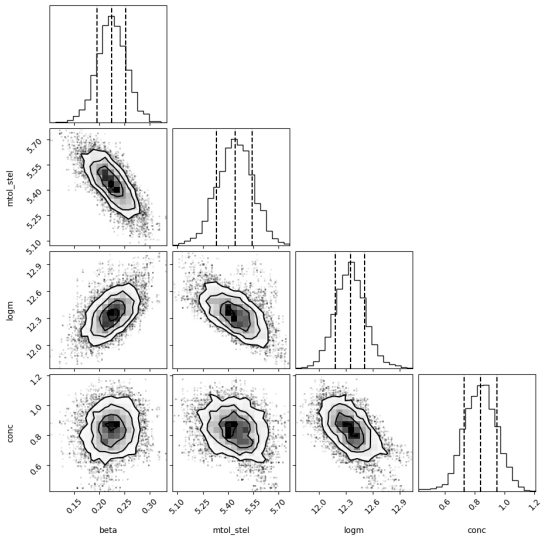

Figure 4.18: Evaluation of JAM model with dark matter, but no H I for 12079-12702. Panels same as in Figure 4.15.

4.5 Adding Single Dish Hydrogen Kinematics

In the previous two Sections, 4.3 and 4.4, through JAM modelling we have demonstrated the need for an additional dark matter component in our models in order to fit the kinematics measured in the outer regions, and further we have shown that simply adding this component and offering constraints from stellar IFU data alone is not enough to adequately constrain the model to reproduce the observations. In this Section we introduce a novel method to include the HI kinematic observations in the modelling process in order to offer an extra observational constraint on the data from the most dark matter-dominant regions. This builds upon the past techniques which have combined cold gas kinematics and other tracers with dynamical models (see Section 1.3, and Yang et al., 2019), however benefits from the widespread availability of single-dish HI data compared to resolved cold gas observations, allowing application to a large sample.

4.5.1 Methods

In this section, the models are created in the exact same way as in the previous section, except the fitting process is altered to include the HI observations in the likelihood function, thus making the model also attempt to fit that point. The models use the same luminous, gaseous, and dark MGE parameterisations as in Section 4.3.1. The rest of the method is detailed below.

JAM Model

JAM models including a dark matter halo are constructed for our sample following the method described in Section 4.4, with the same variables used and the same priors applied, except in this case the likelihood function also assesses how well the model matches the HI kinematics in the outer region. To do this, at each MCMC step the projected circular velocity at the HI radius (see Section 2.3) is calculated and compared to the measured observed velocity of the HI . This in effect acts to "tell" the model to also find the best fit taking this into account alongside the IFU data. This is added to the likelihood in combination with the IFU data through the amended log likelihood function below:

$$\log L_{H_I} = -\frac{(\chi^2_{IFU} + \mathscr{W}\chi^2_{H_I})}{2} = -\frac{1}{2}\left[\sum_i^N \left(\frac{(v^{obs}_{rms,i} - v^{model}_{rms,i})^2}{(\sigma^{obs}_{v_{rms,i}})^2}\right) + \mathscr{W}\frac{(v^{obs}_{H_I} - v^{model}_{H_I})^2}{(\sigma^{obs}_{H_I})^2}\right] \quad (4.9)$$

where i indicates each data point in the 2D map from the IFU, N is the number of data points in the IFU, and $\mathscr{W}$ is a weighting factor. This weighting factor is set so $\mathscr{W} = N$, in essence giving the H I point the same statistical weight as the whole IFU combined. This was tested at different values, and chosen as this was the highest weighting value that did not cause the fit to the central IFU data to become less good. $\log L_{H_I}$ is the quantity which is maximised by the MCMC process, and is at its maximum when the model is closest to fitting the data.

The MCMC simulation was run following the same procedure as previously.

4.5.2 Results

The results for models which use this novel method of combining the H I observation with the IFU observations in the modelling process are presented for the same 4 example galaxies as used previously in Figures 4.19, 4.20, 4.21, and 4.22.

For all of these galaxies, the best fit model now manages to correctly fit the H I point at the radius, while still fitting the IFU data in the centre (in some cases, the IFU data fit is even also improved upon from the previous model – eg. 9190-12702). The posterior distributions displayed in the corner plots show that the parameters in the model are well-constrained.

The H I points are fit very well by the models, which may suggest overfitting. Using lower values of the weighting parameter did not result in the inner data being fit less well, and so any fitting of the outer points are justified by the data. We note the extremely low errors on the modelled value. As noted previously, a new method described in Mitzkus et al. (2017) which was not known to the author at the time of modelling proposes an artificial inflation of the error values from the kinematic maps in order to more accurately estimate the true uncertainties in the data. This method will be tested in future to see if this accounts for the artificially small errors. We also note that these errors represent the ability of the model to fit the data using the MGE mass distribution, which itself did not account for any errors in the image data. As such, the errrors are expected to be underestimated.

This Section, and Sections 4.3 and 4.4, have demonstrated the improvements to JAM modelling provided by this method, featuring the addition of just one extra data point from unresolved 21cm hydrogen kinematics. These sections have demonstrated the results of this on four example galaxies, and in Section 4.6 we detail the application of this method to a large sample.

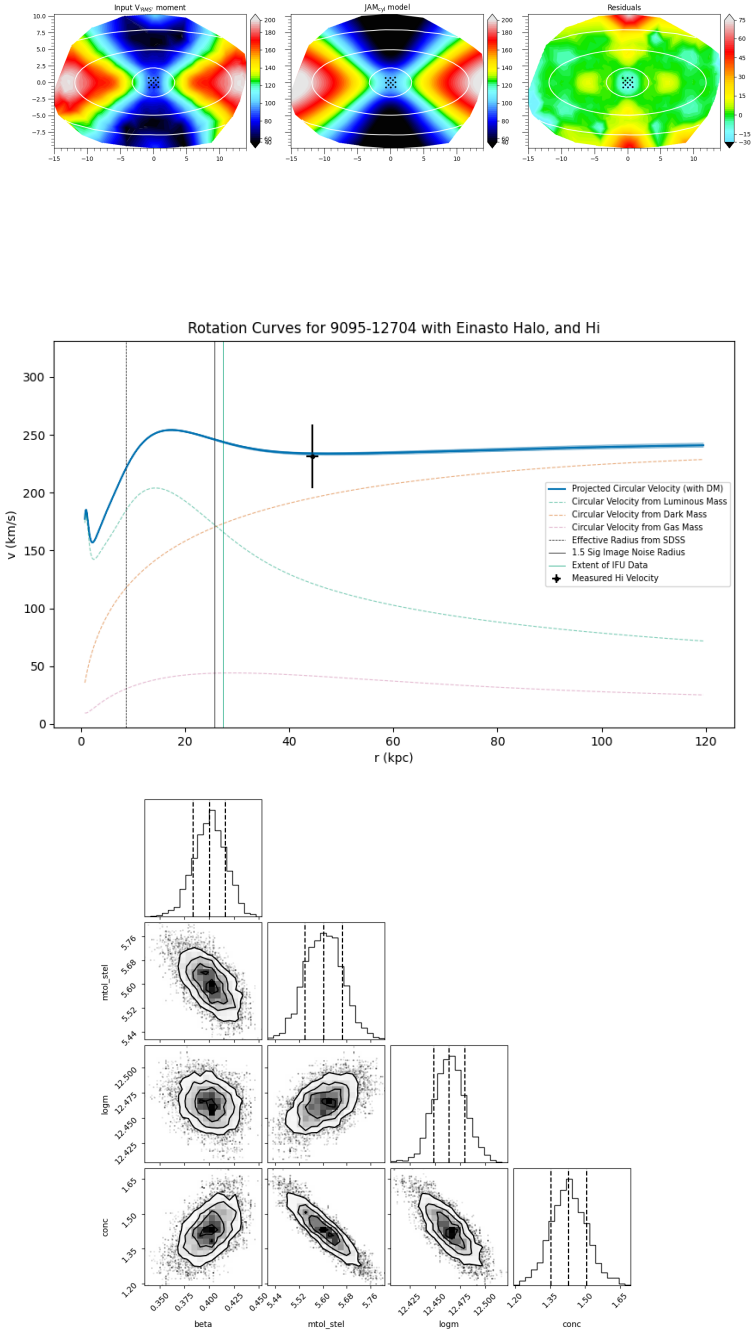

Figure 4.19: Evaluation of JAM model with dark matter and H I for 9095-12704. **Top:** From L-R, observed, modelled, and residual V_{RMS} maps. White contours show isophotes from the MGE model. **Middle:** Rotation curve generated by the model (blue), composed of the stellar component (dashed green curve), gas component (dashed pink curve), and dark component (dashed orange line). Vertical dashed line indicates the effective radius of the galaxy, solid black line indicates the noise limit of the r-band image used to generate the MGE, and the green vertical line indicates the radius reached by the IFU data. The black point shows the measured H I velocity. **Bottom:** corner plot showing posterior distribution of variables from the JAM MCMC simulation.

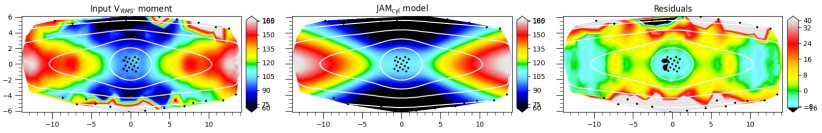

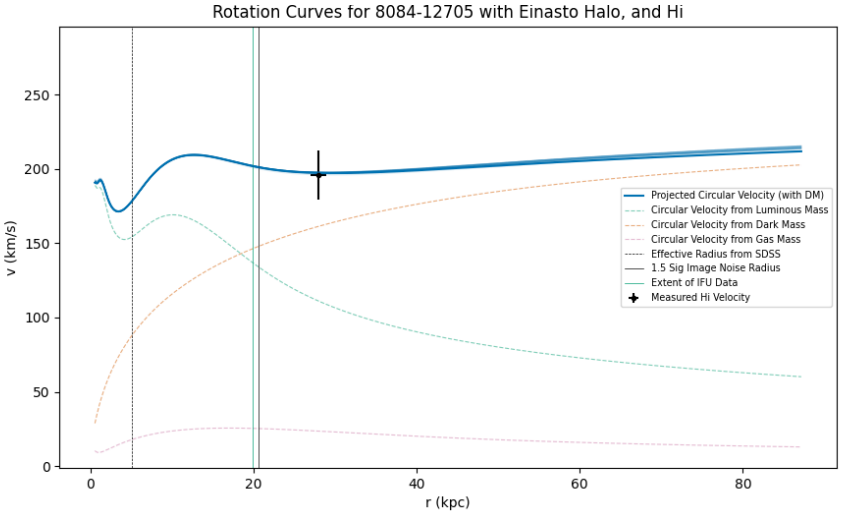

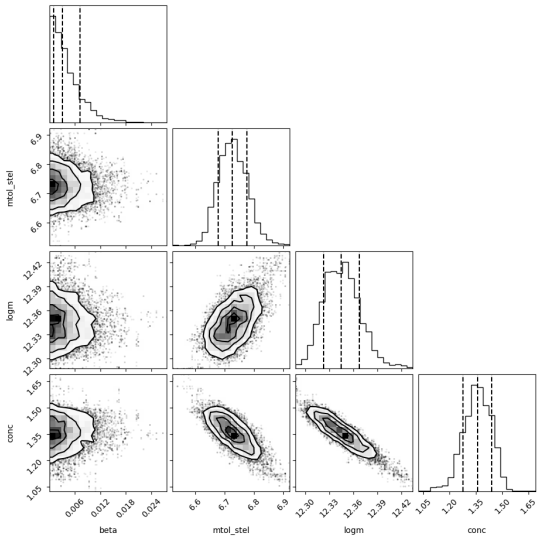

Figure 4.20: Evaluation of JAM model with dark matter and H I for 8084-12705. Panels same as in Figure 4.19.

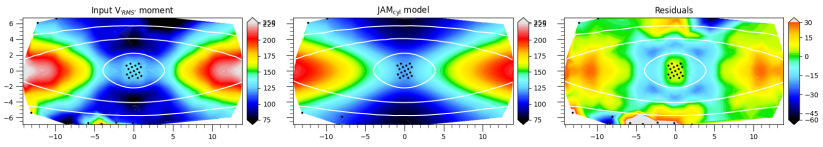

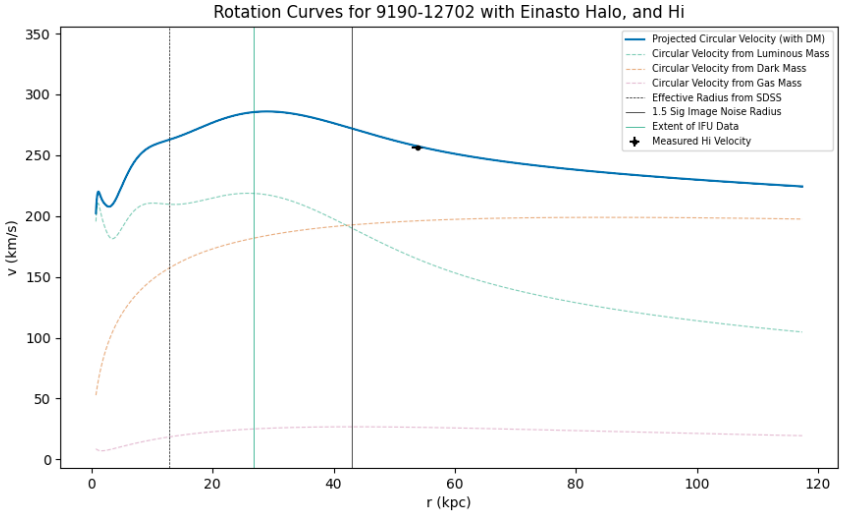

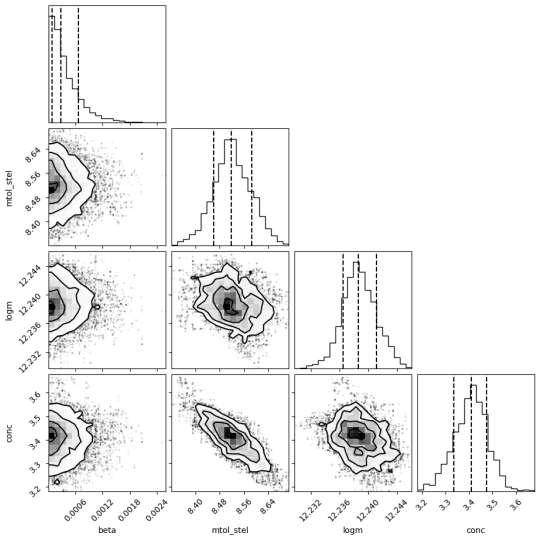

Figure 4.21: Evaluation of JAM model with dark matter and H I for 9190-12702. Panels same as in Figure 4.19.

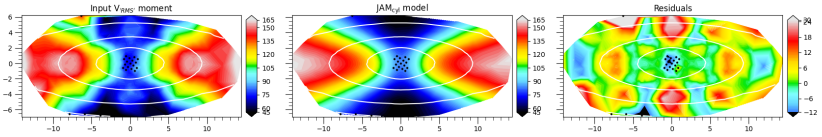

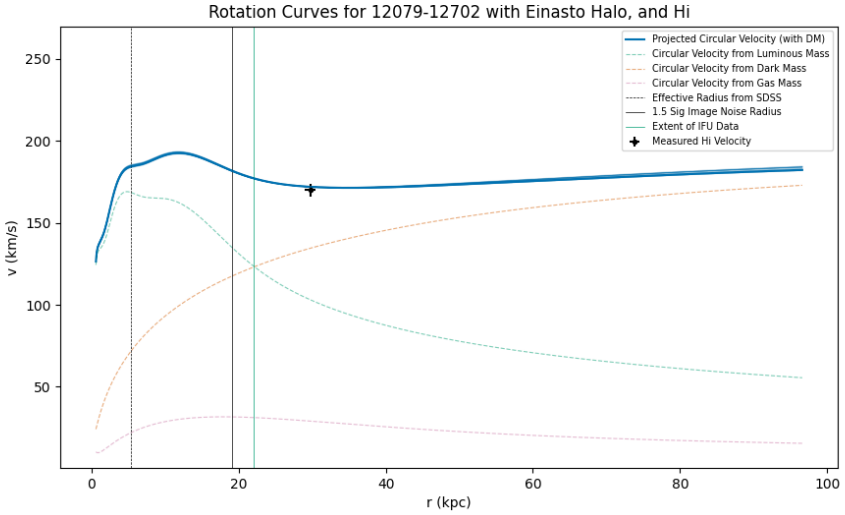

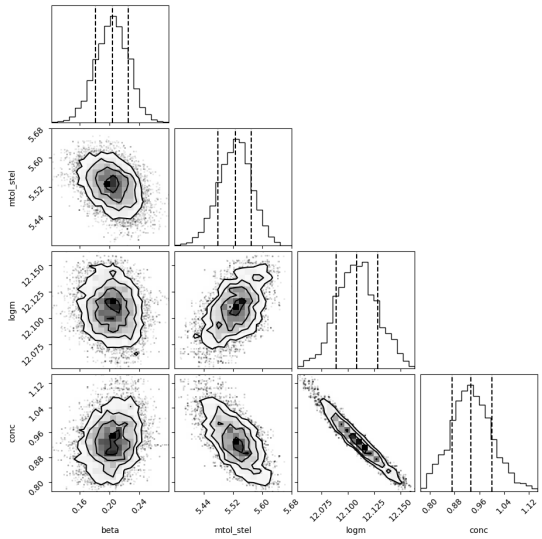

Figure 4.22: Evaluation of JAM model with dark matter and H I for 12079-12702. Panels same as in Figure 4.19.

4.6 Applying this Method to the Full Sample

In Sections 4.3, 4.4 and 4.5, it has been demonstrated that JAM models require a dark matter component in order to reproduce the observed kinematics in the outer regions, and also that these outer region kinematics must be included in the modelling process in order to appropriately constrain the model – single dish H I observations can achieve this. These sections presented the results of this process in detail for 4 example galaxies. However, in Section 4.1 we stressed the importance of being able to model statistically significant sample sizes, and in Section 4.2 we introduced a large sample of galaxies which had the prerequisite data available for this method to be applied to. This section documents the outcome of applying this modelling technique to the sample, details galaxies which are rejected from the sample, and evaluates the results of the modelling process. Further, we take the parameters measured by the modelling process and examine how these relate to other galaxy properties – comparing this to literature and our understanding of galaxy evolution.

4.6.1 Galaxies Discarded from Sample

The sample originally defined in Section 4.2 contained 423 galaxies. In Section 4.3.1, we note that a large proportion of this sample failed to produce adequate MGE fits using our automatic algorithm. This reduced our sample to 84 galaxies which could carry on to the modelling process. The results of these models are shown here.

4.6.2 Evaluating Fits

All 84 galaxies which we set out to model produced viable dynamical modelling results. The models produced with no dark matter (as in Section 4.3), and with dark matter but no constraints from the H I (as in Section 4.4) are not relevant to this section, as we have identified the best constraints and match to the data are produced by our novel model which includes the H I information (see Section 4.5). In order to identify poor fits to the data, we labelled galaxies as successful fits, or unsuccessful fits based on the following criteria:

- Any galaxy which exhibited a $\chi^2_{IFU} > 5$ had to undergo a visual inspection in order to assess the quality of the IFU fit. The majority of these were rejected. We note we did not filter our sample based on the quality of the IFU data, and so expected this to be the point where these cases were removed. See Figure 4.23 for an example of this.

- The models remaining after this had their rotation curves visually inspected, and were rejected if they revealed a dark matter component which did not dominate the stellar potential at any radius. These specific failures are attributed to the shape of the kinematics in the IFU data being reproduced by the stellar kinematics, and then a flat contribution being added from the halo which can then be interchangeably swapped for a lower mass to light ratio. See Figure 4.24 for an example of this.

Once the sample was inspected for the issues explained above, we find 50 galaxies with good quality fits as per our criteria, and reject 34 galaxies. Examples of failed fits are shown below.

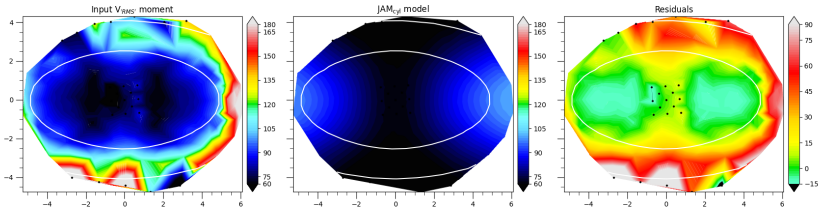

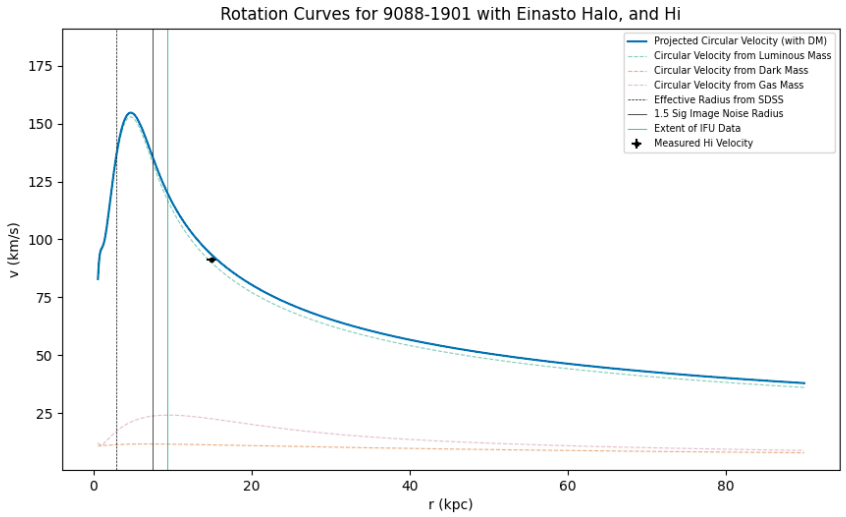

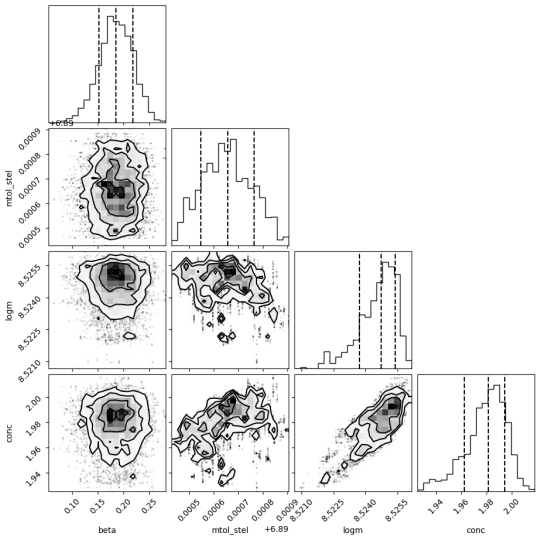

Figure 4.23: An example of a fit which has failed due to IFU data quality. Panels same as in Figure 4.19.

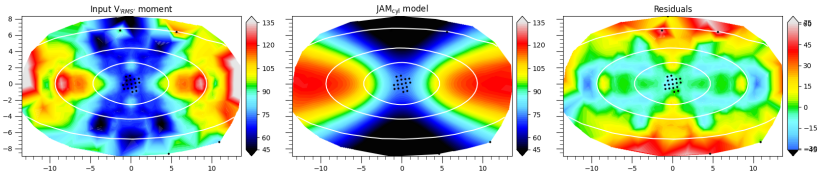

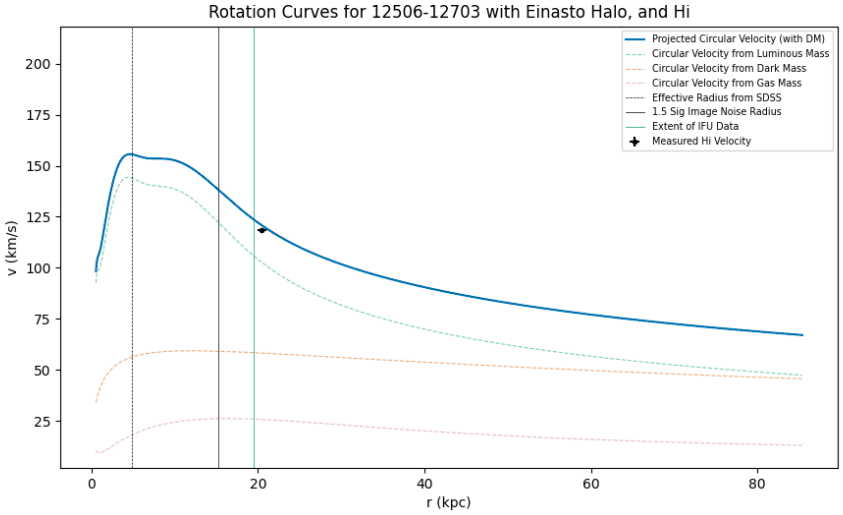

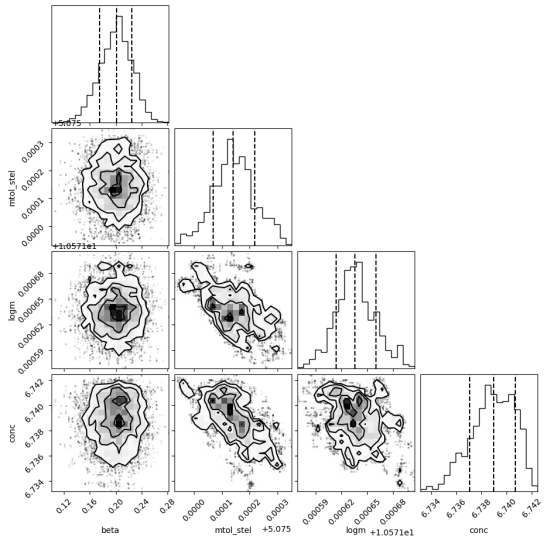

Figure 4.24: An example of a fit which has failed due to data being unable to distinguish between dark matter and higher mass to light ratio. Panels same as in Figure 4.19.

4.6.3 Evaluating Measurements

In order to evaluate how well our models have managed to accurately measure the parameters, we take a look at some quantities measured for the sample against other independent measurements for the sample.

First, we examine the properties of our sample compared to the galaxy population globally. In Figure 4.25 we present our sample highlighted on a colour-mass diagram for both $(g-r)$ and $(u-r)$. On this we differentiate between the galaxies which were classified as failed models and rejected. We note that, as expected based on our sample selection for galaxies detected in H I , the majority of our sample exists in the "blue cloud" region of the parameter space, with some extending into the "green valley". Some galaxies were selected from the "red sequence", however these failed to produce viable models. For discussion on what these regions mean for galaxy evolution, see Section 1.1 and Figure 1.2. We also see that the galaxies which failed are not confined to any specific part of the colour-mass plane.

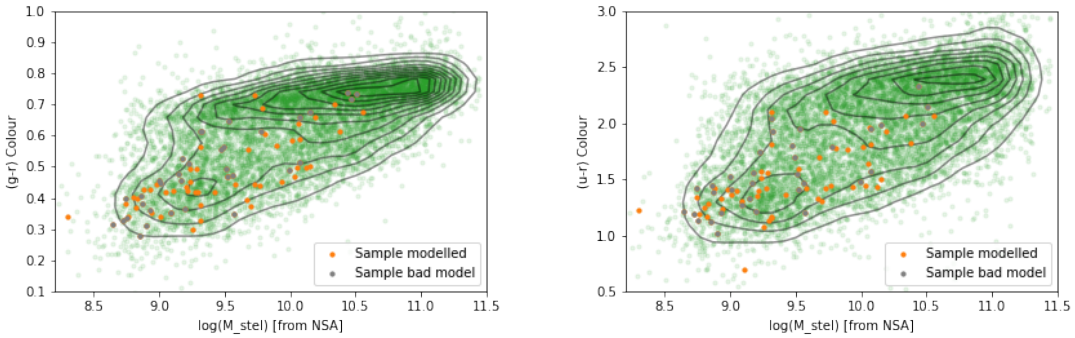

Figure 4.25: Distribution of the sample in colour (**Left:** $(g-r)$, **Right:** $(u-r)$) mass space. Green points and black contours show the full SDSS DR17 sample, orange points show the successfully modelled galaxies, and grey points show galaxies which were modelled but were rejected for the reasons detailed in the text.

Further, we situate our sample within the full sample of the H I -MaNGA survey DR3 in Figure 4.26. This shows that our sample spans the full range of parameter space explored by the H I -MaNGA survey, and hence is a suitable proof-of-concept study for use in other combined IFU-H I surveys.

In order to assess our measurements of the stellar component in the sample, we first compare the photometry recovered by the MGE parameterisations to catalogue values. Initially, we compared the apparent r-band magnitudes measured by the MGEs created from the Legacy

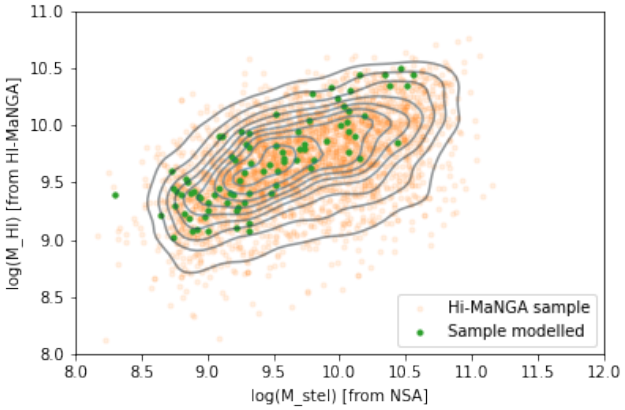

Figure 4.26: The modelled sample compared with the full H I -MaNGA DR3 sample in H I mass versus stellar mass. Orange points and black contours show the H I -MaNGA sample, green points show galaxies which were modelled.

survey imaging, to the published apparent r-band magnitudes from the NSA catalogue which uses elliptical petrosian apertures to quantify flux from SDSS imaging. However, this exhibited a large offset. Instead, we compared the MGEs made from Legacy imaging with the magnitudes published in the Legacy catalogue in order to see if this explained the discrepancy. These results are shown in Figure 4.27. We find that the photometry from the Legacy catalogue matches our MGE photometry, however the SDSS photometry does not match.

We consider this due to the differences between measurements of a petrosian flux which is defined within a set aperture, and the Legacy catalogue values which are generated from modelled photometry – therefore capturing light to greater depths than those observed. That this is a systematic offset is enough validation that we have correctly reproduced the surface brightness distribution for our models.

This discrepancy however reaches further than just photometry measurements. As our method of determining the stellar mass is hinged upon the luminosity – a simple multiplication of the luminosity by the fitted stellar mass-to-light ratio – we expect that our stellar masses will not match stellar masses in the NSA catalogue, as these are derived from SDSS imaging.

Derived separately from the fluxes, the Nasa-Sloan Atlas provides stellar mass-to-light ratios derived from scaling relations to colour differences from photometry. These should be independent of the depth issues, and so we can compare our measurements with these – which we do in Figure 4.28. We see a massive discrepancy between our values and those measured by our models. We compare the NSA values to our modelled values for the models with no dark matter (this would be expected to be higher as it is compensating for the dark compo-

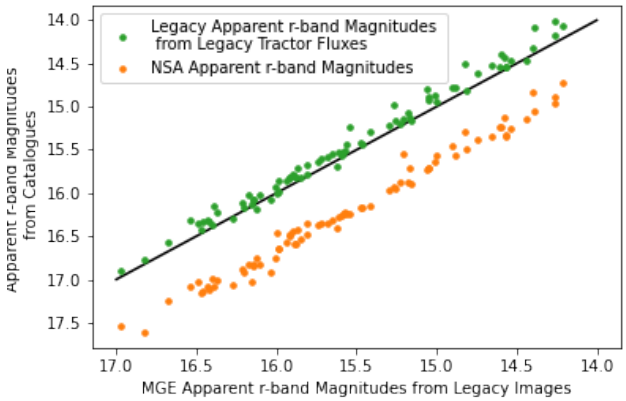

Figure 4.27: *r*-band magnitudes measured in our MGE models created from Legacy imaging, versus catalogue values for the NSA catalogue (orange) and Legacy catalogue (green). Black line shows one-to-one relation.

nent), the models with dark matter but no H I (which show large uncertainties due to the lack of constraints), and the full models which include the H I information. The full models provide mass-to-light ratios which are lower than those with no dark matter, which is expected as the dark component should correct for some of the missing mass. However, we still see far higher values from our models. To an extent, the NSA values are derived using a less accurate method and so may be failing to properly account for the properties of the galaxies, however this requires further investigation using other spectral fitting measures of the mass-to-light ratio.

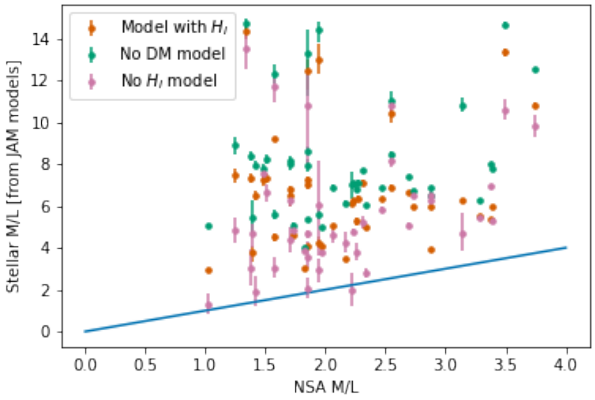

Figure 4.28: Mass-to-light ratios from the best fit JAM models compared to the NSA catalogue stellar r-band values derived from photometry. Red points show stellar M/L values from models which include dark matter and the H I . Green points show dynamical M/L values from models which contain no dark matter. Pink points show stellar M/L values from models which contain dark matter but do not include the H I . Blue line shows the one-to-one relation.

4.7 Discussion

4.7.1 The Need for Cold Gas

We have shown in Section 4.5 that the additional constraint of H I kinematics improves the fit of the rotation curve for our four example galaxies. Considering the full sample, Figure 4.29 compares the dark matter halo mass derived by the models with and without the inclusion of H I . This, strikingly, shows that there is little or no correlation between the halo masses found without using cold gas and those found using cold gas. Further, the errorbars on the models with no H I are extremely large, covering in some cases as much as 3 dex. Meanwhile, the uncertainties on the models which are constrained by the additional H I information are much smaller. In order to confirm that our full models do indeed derive more accurate values, in Section 4.7.3 we compare the values to those in literature, and find that our value reproduce the literature values. This confirms that the vast differences and lack of correlation found by the models without H I are real, and massively reinforces that without the inclusion of cold gas kinematics, we do not measure accurate values of dark matter mass.

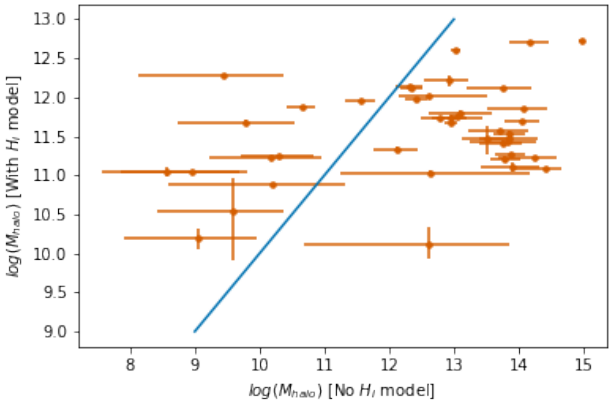

Figure 4.29: log halo mass values for models which include H I versus those which do not. Blue line shows one-to-one relation.

4.7.2 The Halo-Concentration Relation

Above we have validated that our models produce values in line with comparable catalogue values. As such, in this Section we proceed to look at how our measurements compare to published relations in the literature.

Here we consider the halo mass-concentration relation which we included in our model

through the prior on the concentration. As this was a part of the assumptions fed into the model, we expect some bias towards reproducing this relation, however we note that the prior was given wide scatter, so points were allowed to deviate from the relation where the data justified it. This is shown in Figure 4.30. Included in these plots is an alternative halo mass-concentration relation, also from Klypin et al. (2011), for subhalos – in contrast to the relation used in our prior which is for field haloes. This is included to investigate whether any of our galaxies have settled on this instead. Upon removing our failed fits, we see that overall our sample follows the relation, but we identify 7 notable outliers which warrant further investigation – as highlighted in Figure 4.30.

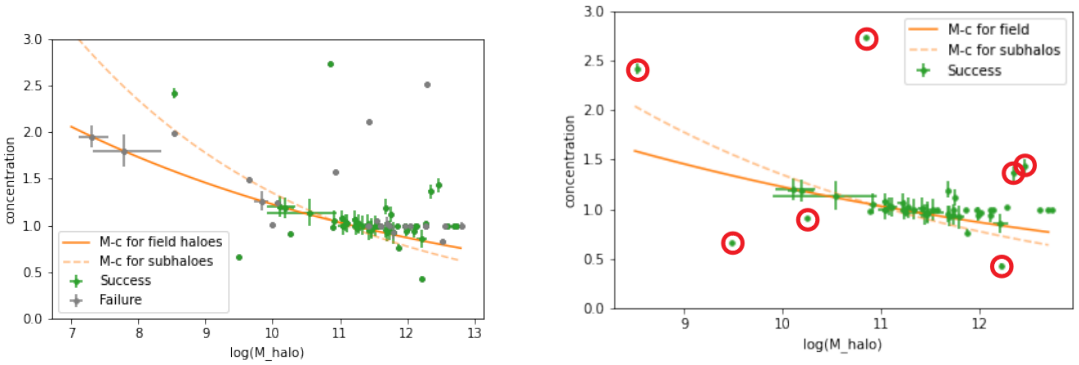

Figure 4.30: Halo mass - concentration relation (HMCR) for modelled galaxies. The solid orange line shows the literature relation from Klypin et al. (2011) which is used as the prior in our models, the dashed orange line shows an alternative relation also from Klypin et al. (2011), for subhaloes. **Left:** HMCR showing galaxies which were successfully modelled (green points) alongside those which failed (grey points). **Right:** HMCR for successfully modelled galaxies only, red circles highlighting those identified as outliers which are examined further in the text.

M-c Outliers

The outliers were visually re-inspected, and were found to deviate for a variety of reasons. Some, such as in Figure 4.31 clearly fail due to a lack of IFU data points, others show they were simply missed in the original visual inspection as the IFU χ^2 cut didn't flag up a need for inspection of the rotation curve (Figure 4.32), others defy explanation as to their fits (Figure 4.33). These are excluded from the following analysis.

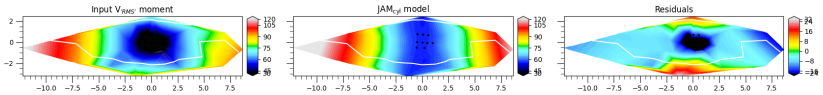

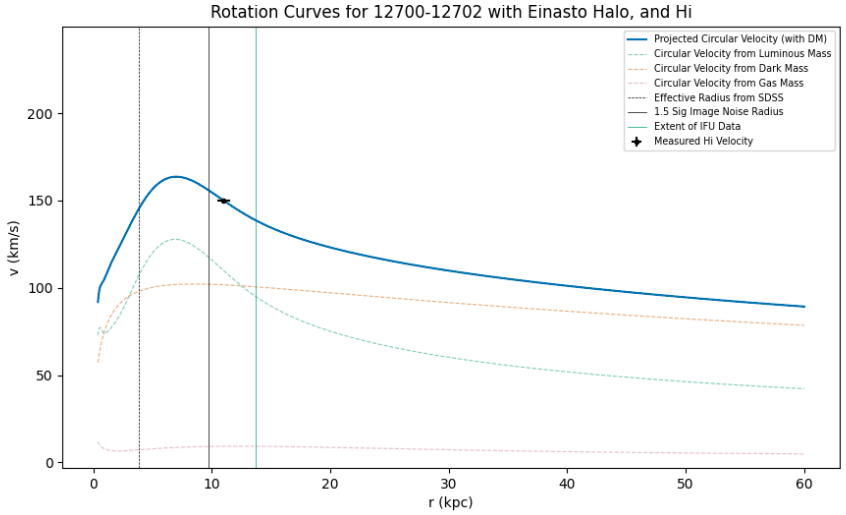

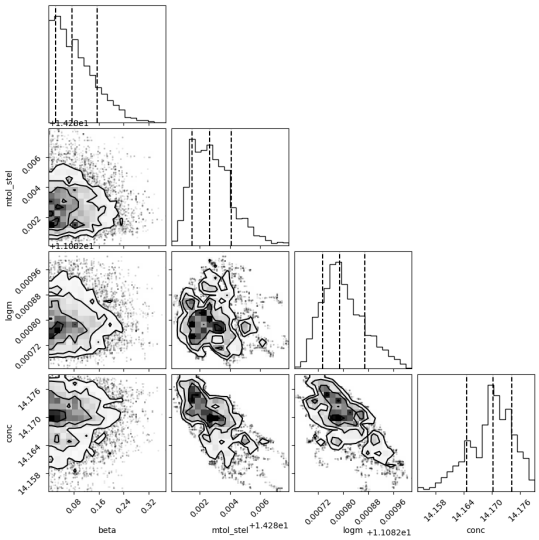

Figure 4.31: Evaluation of JAM modelling for 12700-12702, one of the outliers which illustrates those rejected for IFU issues. Panels the same as in Figure 4.19.

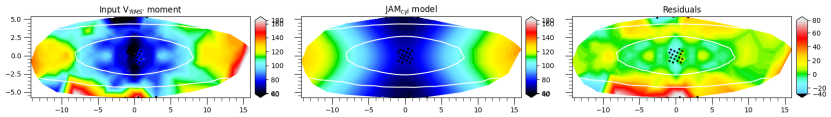

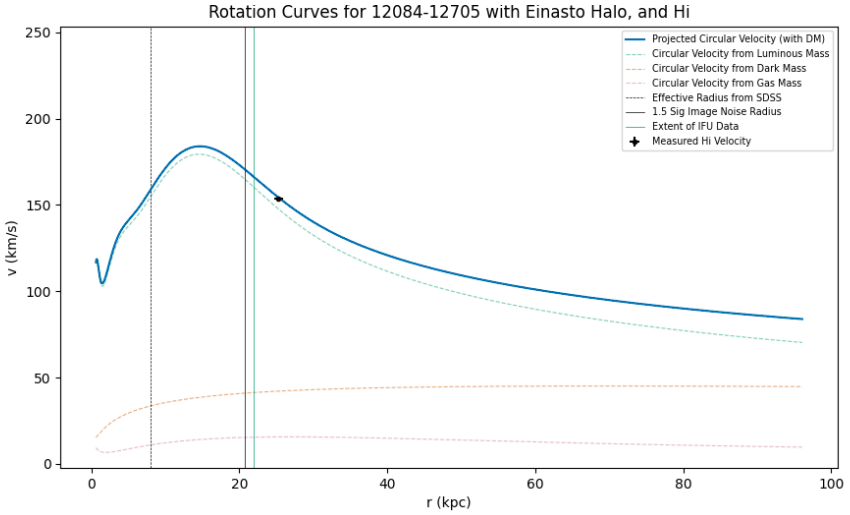

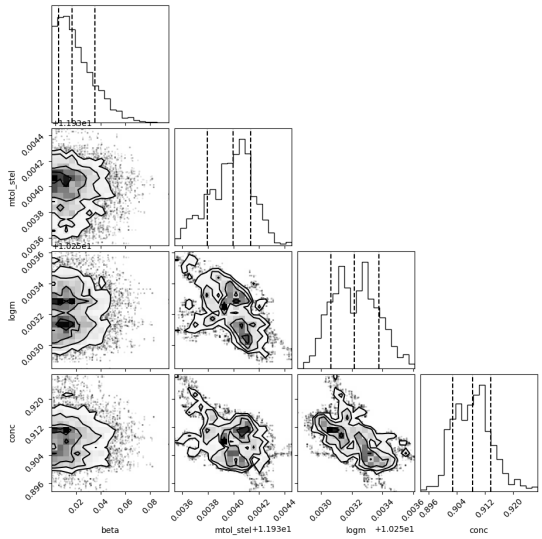

Figure 4.32: Evaluation of JAM modelling for 12084-12705, one of the outliers which illustrates those rejected dark matter component failing to become dominant. Panels the same as in Figure 4.19.

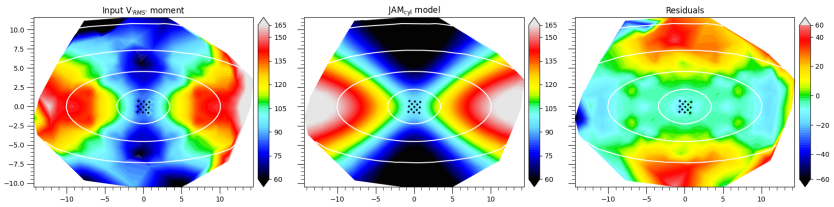

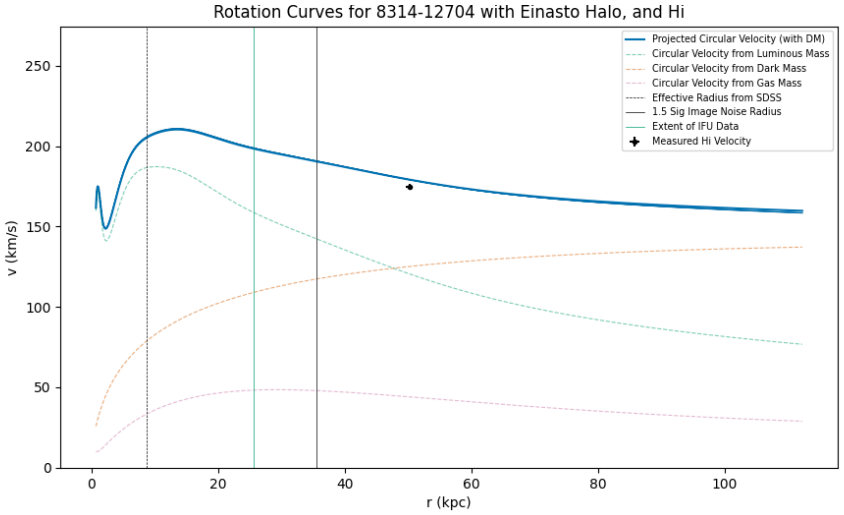

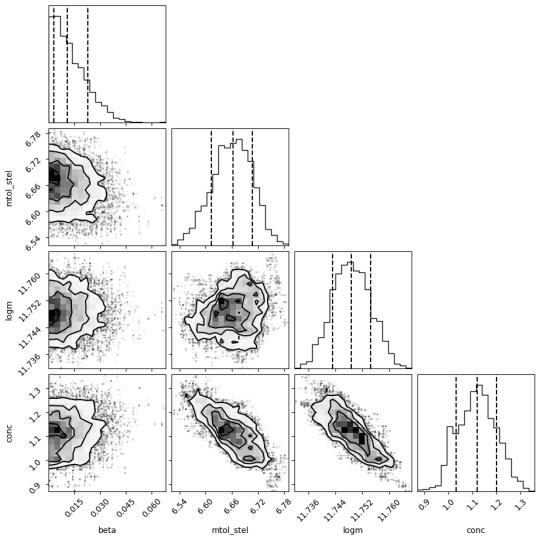

Figure 4.33: Evaluation of JAM modelling for 8314-12705, one of the outliers which illustrates those which were rejected for being outliers on the M-c relation, but not showing any discernible features otherwise. Panels the same as in Figure 4.19.

4.7.3 Comparison with Other Properties and Literature

The underlying dark matter properties of galaxies have been shown to be intimately linked to their evolution and so have correlations with the properties of the stellar component.

First we consider the split of the dynamical mass between the dark matter component and the stellar component (the stellar-halo mass relation, SHMR). This has been well studied in simulations and in literature, and is an indication of how efficient star formation is for different dark matter halo masses. Our results are shown in Figures 4.34, with both axes options for ease of comparison with literature. In Figure 4.35, we also show these results in the form of the ratio between stellar mass and halo mass against the halo mass.

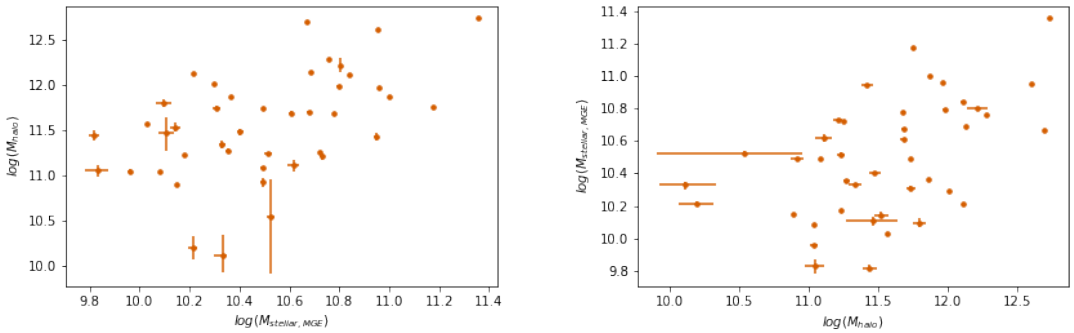

Figure 4.34: Stellar-halo mass relation (SHMR) for stellar and halo masses fit by the JAM models. Left and right panels show the same but with the axes swapped for ease of comparison with literature.

In Legrand et al. (2019), the authors use stellar halo abundance matching (considering the halo mass function and stellar mass functions, and matching the largest haloes to the largest stellar masses) to construct the form of the SHMR across different redshifts. Their results are shown in Figure 4.36, in both the SHMR relation and a version showing the ratio of stellar and halo mass vs the halo mass.

Comparing the lowest redshift results in Figure 4.36 (as MaNGA covers low redshift galaxies) with our results in Figures 4.34 and 4.35, we see that qualitatively the values are in the same region as the literature values, with the SHMR results in the left panel of Figure 4.34 tentatively suggesting a change of gradient for higher stellar masses as predicted in the literature results from Figure 4.36. However, looking at the relation displayed as a ratio of the stellar and halo masses, we fail to reproduce the turnover seen in the literature at halo masses around 10^{12}.

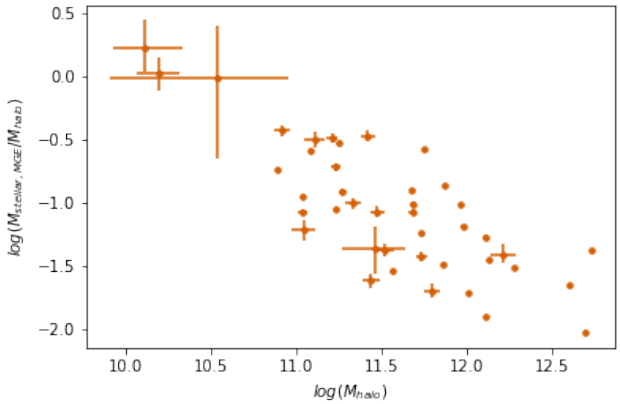

Figure 4.35: SHMR shown for our galaxies in the form of the ratio of the stellar to halo masses, versus the halo mass. This form is commonly used in literature.

These conclusions are also confirmed when comparing to the results of Girelli et al. (2020) shown in Figure 4.37, which uses a similar method to compare observed stellar masses with simulated halo masses through stellar halo abundance matching; and further by comparing the right hand panel of our results in Figure 4.34, with the upper panel of the results from Moster et al. (2010) (which uses a statistical comparison with simulated halo masses) shown in Figure 4.38, alongside comparing Figure 4.35 with the lower panel.

That our data doesn't reproduce the turnover when comparing the ratio of stellar to halo mass with halo mass is a concern, however we note the small sample size we are using, and also the bias in our sample. As shown in Figure 4.25, our sample is almost entirely late-type spiral galaxies. In Figures 4.39 and 4.40 results from Posti & Fall (2021) are shown. In this work, the authors use dynamical observations (H I in the case of spiral galaxies and globular clusters in the case of elliptical galaxies) to measure the SHMR observationally. They show that late-type spiral galaxies do not follow the relations seen through stellar halo abundance matching, which could explain our inability to reproduce this turnover. Specifically, comparing the right panel of Figure 4.34 with Figure 4.39 shows a much less pronounced downturn in gradient which is more feasible for our small sample. Also, comparing the right panel of Figure 4.40 with our results in Figure 4.35, we see a massive scatter in the lower mass end in the spiral galaxies, which would mean a much larger sample size would be needed in order to appropriately ascertain if we see the turnover.

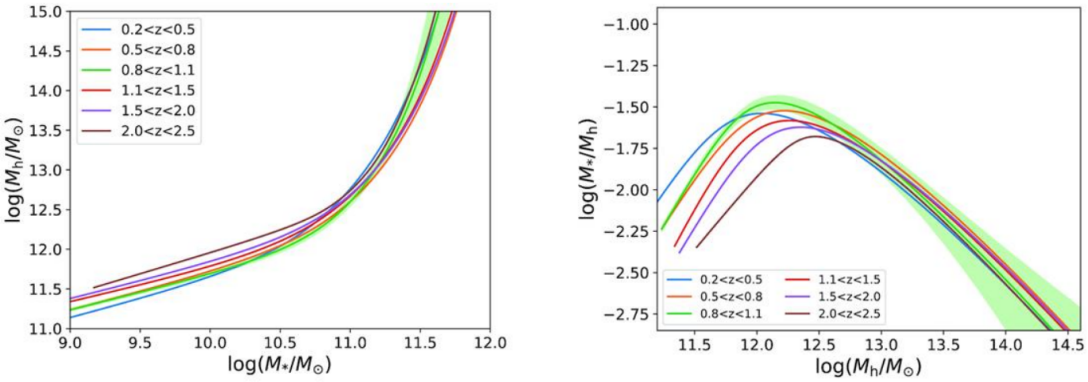

Figure 4.36: SHMR reproduced from Legrand et al. (2019) for different redshifts (colours, blue most relevant to our work). **Left:** SHMR shown in usual form, **Right:** SHMR shown in the form of the ratio.

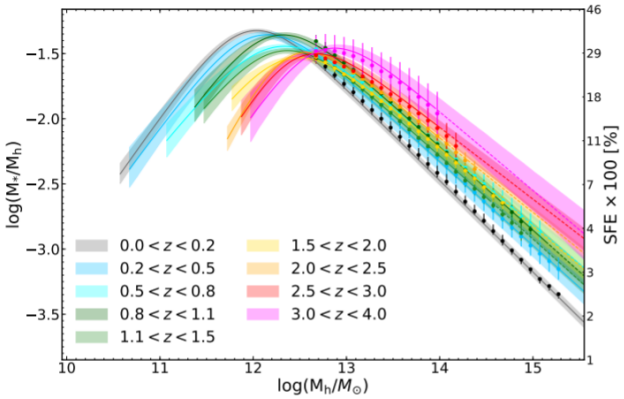

Figure 4.37: SHMR in ratio form, reproduced from Girelli et al. (2020) for different redshifts (colours, grey most relevant to our work).

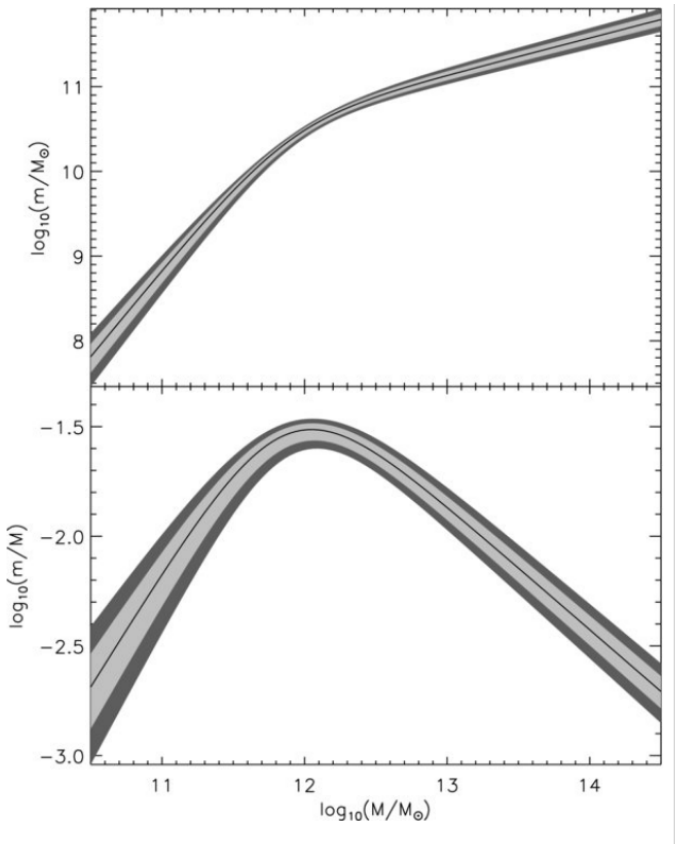

Figure 4.38: SHMR from simulations reproduced from Moster et al. (2010). M denotes the halo mass, while m refers to the stellar mass. **Upper:** SHMR shown in usual form, **Lower:** SHMR shown in the form of the ratio.

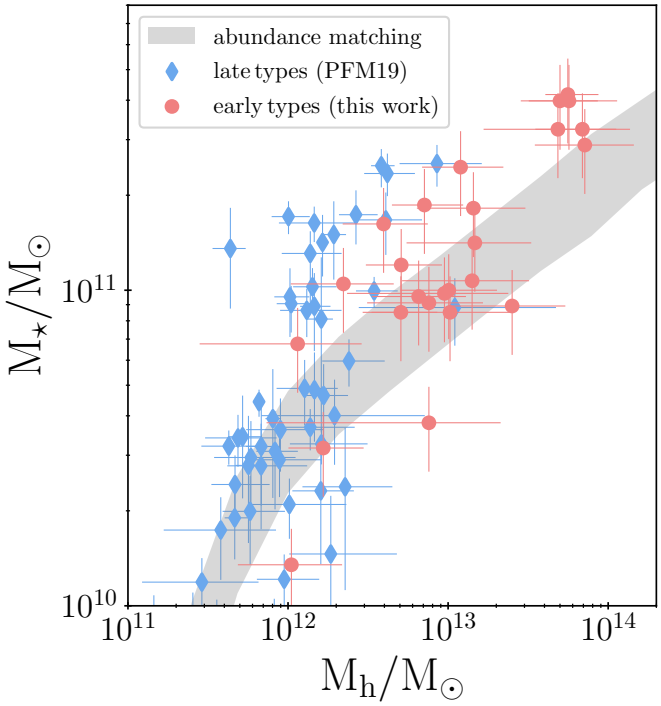

Figure 4.39: Observed SHMR from Posti & Fall (2021). Blue points show late type galaxies, from which halo masses are derived from H I dynamical observations; red points show early-type galaxies, which use globular cluster dynamics. The grey region shows the expected relation from abundance matching.

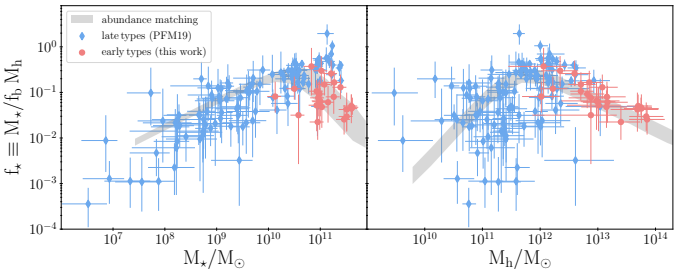

Figure 4.40: Observed SHMR from Posti & Fall (2021), in the form of the ratio against stellar mass (left), and the ratio against halo mass (right). Blue points show late type galaxies, from which halo masses are derived from H I dynamical observations; red points show early-type galaxies, which use globular cluster dynamics. The grey region shows the expected relation from abundance matching.

Following our understanding of galaxy formation, as set out in Section 1.4, a more massive dark matter halo leads to a deeper potential well and so the accretion of more cold gas to fuel star formation. Using our H I mass data from H I -MaNGA, Figure 4.41 shows the relation between gas mass and halo mass. This agrees qualitatively with the concept of more gas for higher mass haloes, and reinforces the theory that the turnover in the SHMR is not due to a lack of gas but due to effects which lower the efficiency of star formation from the gas reservoirs in higher mass haloes. We compare this to Figure 4.42 which is taken from Dutta et al. (2022). This paper used ALFALFA H I observations alongside a statistical scaling method to obtain halo masses from stellar masses (described in Moster et al., 2013). Comparing with our results, we see that again our values are qualitatively similar to those in the paper , but more importantly note the large scatter in the literature plot. This again highlights that our small sample size would make comparisons difficult.

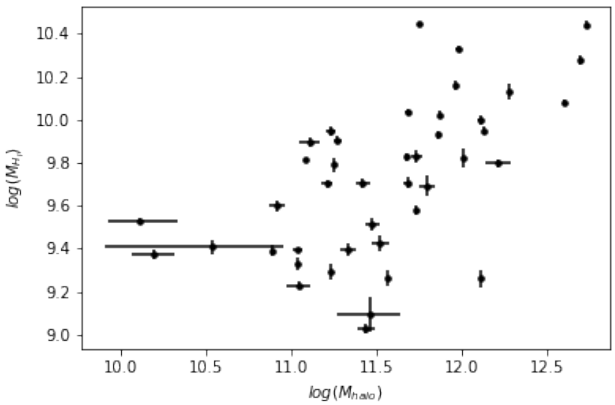

Figure 4.41: Halo mass against H I mass for modelled galaxies.

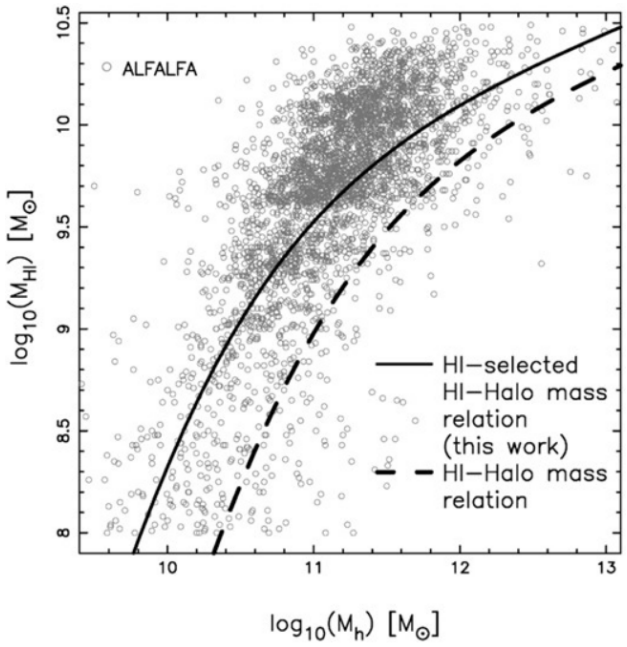

Figure 4.42: Halo mass against H I mass for the ALFALFA sample, reproduced from Dutta et al. (2022). The solid black line shows the H I -Halo mass relation derived from this work, while the dashed black line shows that derived from previous work.

The effect of the halo mass on the ability of a galaxy to accrete gas also has an effect on the star formation rate, however this is more complicated due to the effects of feedback and other baryonic processes. In Wang et al. (2013), the authors compare the observed star formation rate with halo masses which are obtained using a scaling relation between stellar and halo mass which is tuned on observations. Using data from the Pipe3D MaNGA Value-Added Catalogue (Sánchez et al., 2016b,a) which derives stellar population properties using stellar spectral fitting, we produce Figure 4.43 to see how halo mass affects SFR. Figure 4.44 shows the expected form of this relation for different redshifts. Comparing our results again with the lowest redshift as MaNGA galaxies are low redshift, we reproduce similar values qualitatively.

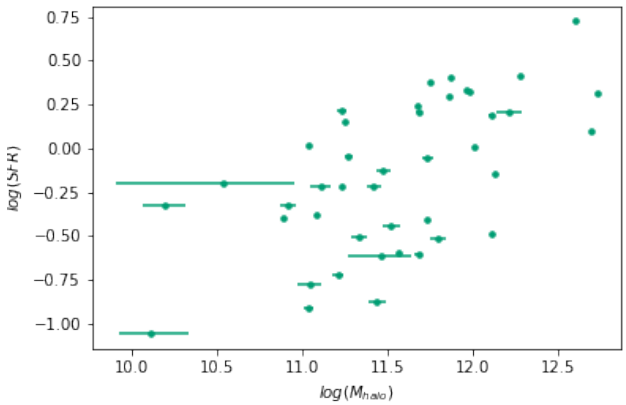

Figure 4.43: Star formation rate (SFR) versus halo mass for galaxies modelled in this work. SFR values come from the Pipe3D Value Added Catalogue as part of MaNGA, which derives this value using spectral fitting.

The qualitative reproduction of literature values across a range of properties is confirmation that our method is recovering the correct values for dark matter halo properties, but as Figure 4.29 highlighted this method recovers more precise and accurate values than without the use of H I information.

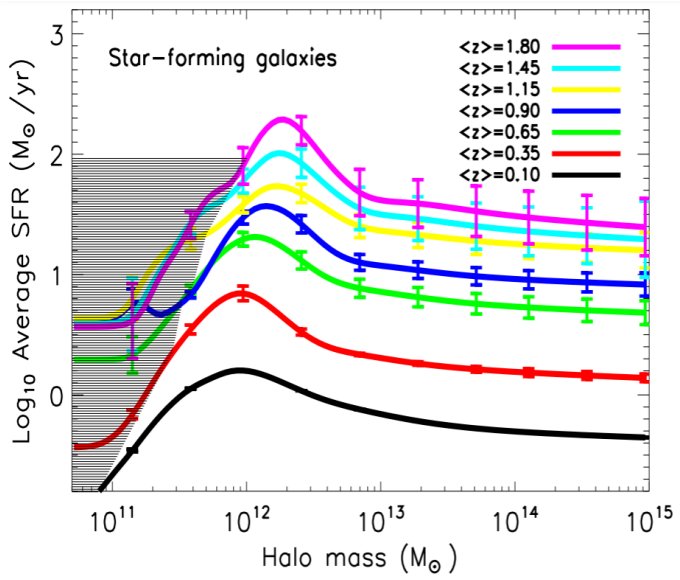

Figure 4.44: Reproduced from Wang et al. (2013), showing observed SFR against halo mass at different redshifts (coloured lines, black most relevant to this work). The halo masses are derived from a scaling relation which was tuned on observations. Black hashed region shows region lacking statistics.

4.8 Summary

In this chapter, I have described the work I have completed which developed a novel dynamical modelling method which combines stellar IFU data with single-dish H I radio observations in order to better constrain the dark matter halo properties of a sample of galaxies. The work in this chapter has acted as a pilot study on a modest sample in order to confirm that this combination of observations, and modified modelling method allows for an improvement on measurements. Importantly, through comparing models which contained only luminous matter with those which had a dark matter component added in, we found that the models lacking dark matter were not able to reproduce the kinematics in the outer regions measured by the H I observations – while the models which did include a dark matter component were able to match the stellar kinematics in the central regions **and** the H I kinematics in the outer regions. In order for the dark matter component to be adequately constrained, the inclusion of the H I measurement in the likelihood of the model was required. The quantities derived from this method aligned with those in the literature from previous studies, however the sample size was not large enough to directly compare quantitatively. To rigorously check this, we plan to expand the sample as best as possible, and consider applying the method to mock observations. The main restriction on this sample size was the ability to produce MGE models for spiral galaxies which contained asymmetric structures such as bars. Nonetheless, this is a crucial proof-of-concept study demonstrating the powerful role of cold gas kinematics in synergy with stellar IFU data for mass component modelling in galaxies. Moving forwards, the data output by the WEAVE-Apertif Survey (providing stellar kinematics deeper than MaNGA alongside resolved H I observations; Falcón-Barroso et al., 2019) will open a new window of opportunity to advance this method further, and apply to a rich sample.

5

Signatures of Current Ongoing Quenching in Jellyfish Galaxies

Suggested listening: Under the Sea by Jacob Collier

As explained in Section 1.6, stellar population modelling can be used to reveal the recent

Chapter image: Composite image of ESO 137-001 using imaging from the Hubble Space Telescope and X-Ray

evolution of a galaxy, and combined with IFS data this can be done in a resolved manner in order to study how different regions of a galaxy have changed. While this doesn't directly identify the process which has driven the evolution, spatial differences in evolution, situated in the context of the galaxy, can be used to infer the mechanism.

Some of the most obvious candidates for galaxies undergoing quenching in a spatially resolved manner are jellyfish galaxies. Introduced in Section 1.5, these galaxies exist in dense cluster environments and show evidence of undergoing extreme ram pressure stripping. Looking at the stellar properties of these galaxies in a resolved fashion can allow us to study the details of the processes taking place. In this Section, a sample of jellyfish galaxies in the MaNGA sample are studied in order to establish whether the post-starburst signatures seen are due to ram pressure stripping.

This Chapter presents work which is currently in progress towards a joint first author paper alongside Ho-Hin Leung. Much of the work has been done in collaboration, but in this Chapter the work done by me is emphasised, and any work completed by Hin is credited appropriately. The dataset used is taken from Roberts et al. (2021), which was the paper that inspired us to pursue this project.

5.1 Background

Quenching mechanisms can be split into two main groups: secular processes which result from processes within a galaxy, and environmental processes which are driven by effects from outside the galaxy – while their causes are distinct, their effects are often intertwined. These are discussed in more detail in Sections 1.4 and 1.5. Considering the timescale of quenching and the spatial progression of quenching, in tandem with the environment the galaxy is situated in, can allow us to disentangle which mechanisms have been involved. If a galaxy has quenched slowly, and with little spatial variation, this could be the result of simply gas depletion; if a galaxy has quenched rapidly, starting from the inside to the outside regions, this would point to nuclear activity as the culprit; and in cases where a galaxy has quenched from outside in, or in different patterns from side to side etc, then we have to consider the environment in which the galaxy resides. Environmental effects on galaxies are complex, varied, often non-linear, and act on many different scales. One clear trend we can see though is that

observations from Chandra, NASA/ESA/CXC

quenching increases in higher density environments. Indeed, the fraction of galaxies which have been quenched is significantly higher in more dense environments compared to those in isolation (only around 20% of field galaxies are quenched, which rises to 40% in the outer regions of clusters, to almost 100% in the central regions of massive clusters; Dressler, 1980), highlighting the importance of environmental processes in galaxy evolution.

The most extreme instances of ram pressure stripping (RPS) result in some of the most visually stunning types of galaxies – jellyfish galaxies. In these cases, the ram pressure has stripped gas out of the galaxies in such density that it can be detected in long streaming tails behind the path of the galaxy (see Chapter header image), even dense enough to allow star formation to occur in-situ away from the main disk of the galaxy (Gullieuszik et al., 2023). While the simple linear picture of how RPS can cause quenching appears intuitive – the gas is removed from the galaxy, so star formation cannot continue – the details of the process are more involved. RPS can remove gas, but also increase its density; can trigger star formation, but this heats gas making it easier to remove; RPS can disturb gas and remove it, but also funnel it to the central regions triggering AGN activity (we have evidence of higher rates of AGN in galaxies affected by RPS: Ricarte et al., 2020). IFS observations combined with multiwavelength observations have shown multiphase gas present in jellyfish galaxies, with wide ranges of densities and temperatures, with multiple different ionising sources alongside effects of shocks and turbulence. This, as noted in Poggianti et al. (2019a), makes jellyfish galaxies excellent "laboratories" for the physics of star formation and quenching in extreme conditions, and galaxy evolution more widely.

Indeed, in contrast to the simple linear quenching scenario, it has been found that simulated galaxies undergoing RPS in clusters can actually exhibit enhanced star formation in some regions, specifically the leading half as the galaxy infalls (Troncoso-Iribarren et al., 2020). Using the EAGLE simulation (Schaye et al., 2015), Troncoso-Iribarren et al. (2020) identified the leading half of the galaxy using the full 3-dimensional velocity vector, and found systematically higher star formation rates in this leading half. The extra information afforded by the simulation revealed increased gas pressure in the leading half, which supports the idea that the excess star formation seen in the leading half is caused by compression of the gas due to motion through the intracluster medium.

This effect has been seen observationally, in individual cases (Gavazzi et al., 2001; Vulcani

et al., 2018; Lee et al., 2020; Hess et al., 2022; Boselli et al., 2021), and with Roberts et al. (2022) presenting a sample of galaxies which show this enhancement systemically. In Roberts et al. (2022), a sample of jellyfish galaxies identified through radio observations are cross-matched with the MaNGA survey (described in Section 2.2.1). The method used in Troncoso-Iribarren et al. (2020) with full 3D velocity information is then repeated as best can be with just the 2D information given by the direction of the jellyfish tail, and the results showing enhanced star formation in the leading half are reproduced.

There have been connections showing that dense clusters are more likely to host galaxies which are globally classified as post-starburst galaxies (Chandar et al., 2021; Werle et al., 2022; Bellhouse et al., 2022), suggesting that ram pressure stripping can cause the star formation burst and rapid quenching which leads to these features (see Section 5.3.1) – which makes sense considering the extreme effects we see on the gas reservoirs of these galaxies.

A modest sample of jellyfish galaxies with readily available IFS data in MaNGA presents an excellent opportunity for resolved studies of how ram pressure stripping acts as a driver for galaxy evolution – both through triggering and quenching star formation – and considering whether this can generate post-starburst signatures in these galaxies.

5.2 Data

Studying the effects of ram pressure stripping on the internal processes of galaxies in a resolved manner requires a combination of data in order to identify jellyfish galaxies (those galaxies undergoing the most extreme ram pressure stripping), and resolved spectroscopic data to explore the properties of the stars and gas in the galaxy. Before now, observing capabilities suited to searching for and identifying jellyfish galaxies have been limited. Though signatures of RPS can be observed in molecular gas (Jáchym et al., 2019; Moretti et al., 2020), ultraviolet (George et al., 2018; Gullieuszik et al., 2023), and X-rays (Bartolini et al., 2022) , ideally H I (Oosterloo & van Gorkom, 2005) or Hα (Gavazzi et al., 2001) are preferred tracers – as these are diffuse components, they show stronger disturbance in cases of RPS. However, in order to survey a large number of galaxies for RPS signatures, observations are required which cover a large field of view and aren't limited by redshift range (as is the case for narrow-band Hα imaging). While optical morphologies from optical imaging can be used (Poggianti et al., 2016b; Roman-Oliveira et al., 2021), giving the benefit of wide fields of view and short exposures, the

stellar component is not as sensitive to RPS effects as H I or Hα. This means many galaxies undergoing less intense RPS effects will not exhibit disturbances in optical morphology and will be missed, and similarly there are other processes in a cluster environment which may result in a disturbed optical morphology (Moore et al., 1996; Kelkar et al., 2017). Thankfully, the Low Frequency Array (LOFAR; van Haarlem et al., 2013) has opened the door to efficient identification of jellyfish galaxies. Specifically the LOFAR Two-meter Sky Survey (LoTSS; Shimwell et al., 2017, 2019) will produce resolved imagery of the entire northern sky in 120-168 MHz with resolution of 6 arcsecs (see Section 2.4 for full description). This is ideal for finding jellyfish galaxies, as this bandwidth detects synchrotron emission which is produced by cosmic ray electrons, accelerated by supernovae, which are transported out of the galaxy by ram pressure – and so will trace the tails in jellyfish galaxies. The LoTSS survey is ongoing, however many jellyfish galaxies have already been identified from the initial data releases. In Roberts et al. (2021), they use the 144MHz observations to systematically survey 29 galaxy clusters for signs of jellyfish galaxies, by looking for galaxies which exhibit one-sided extended radio tails, and find around 100 candidates.

In order to explore the internal properties of these galaxies and how they are affected by RPS, Roberts et al. (2022) crossmatches this sample to the MaNGA survey (see Section 2.2.1) to present a sample of jellyfish galaxies which have resolved spectroscopic data. They find 29 galaxies which are in both surveys, and this is the sample which we use in this section of the paper.

The sample is published in Roberts et al. (2022) and Roberts et al. (2021), alongside other useful ancillary data relating to the galaxies and their host clusters. The sample of clusters used was taken from the SDSS-ROSAT All Sky Survey (RASS; Voges et al., 1999) cluster catalogue (Popesso et al., 2004) which measured X-ray luminosities of SDSS optical clusters.[1] They selected any cluster in this catalogue which had been observed by LoTSS and met the following criteria: redshifts below 0.05, RASS X-ray data with signal-to-noise ratio above 3, and cluster halo masses greater than $10^{14} M_{sun}$ as determined by abundance matching in Yang et al. (2007). From these, galaxies which are visually identified to have unidirectional tails in the LoTTS data are selected as jellyfish and assigned a "tail direction" which is considered to be 180° from the direction of motion in the cluster. They identify 100 jellyfish galaxies in these clusters, 29 of

[1]Author note: the Roberts paper cites a paper about H I profiles as the cluster catalogue. I believe this is wrong. The Popesso paper is for the ROSAT-SDSS cluster catalogue

which are observed by MaNGA.

Bringing all these data sources together, we have a rich dataset giving a wide array of information about our sample. This includes:

- The right ascension and declination of the galaxy, along with the right ascension and declination of the central host – these combine to give the projected distance to the cluster centre, and the projected direction to the cluster centre.
- The stellar mass and star formation rate of the galaxy as determined using SED fitting in Salim et al. (2016, 2018).
- Tail directions which give inferred projected direction of motion.
- 1D velocity dispersion of the host cluster, σ, virial mass, and the virial radius, R_{180}, determined using the method in Yang et al. (2007) and equations 1 and 2 in Roberts et al. (2021). These are used to give dimensionless scaled comparative values for the projected distance of the galaxy from the cluster centre (R/R_{180}) and the line-of-sight velocity-offset of the galaxy with respect to the cluster ($\Delta v/\sigma$).
- From Roberts et al. (2022), we use the values found for SFR and sSFR enhancement in the "leading edge" of the galaxy, derived using MaNGA observations as detailed therein.
- MaNGA emission line maps and velocity maps, see Section 2.2.1 for information on how these quantities are derived.
- PCA1 and PCA2 maps from the definition in Wild et al. (2009), and the classifications derived from these as per Rowlands et al. (2018).

This collection of data is used here to investigate the processes taking place in our sample.

5.3 Methods

5.3.1 Identifying Post-Starburst Spaxels

Post-starburst regions are defined by a burst of star formation in the recent past which has since been rapidly quenched. Traditionally, the spectral signature of this type of star formation history has been the presence of strong Balmer absorption which indicates the presence of

intermediate-aged stars, but an absence of emission lines which would indicate no ongoing star formation. In Chen et al. (2019b), a more refined method was used to identify PSB regions so as not to exclude areas where small amounts of star formation are still present. This method uses the absorption of $H\delta$ ($H\delta_A$) and the equivalent width of $H\alpha$ emission ($W(H\alpha)$), as per Section 2.8.1.

In Chen et al. (2019a), maps were produced for the whole DR17 MaNGA sample which classify the spaxels as either PSB or not. These are internally available to collaborators and so we visually inspected these for the sample introduced in Roberts et al. (2021), in order to ascertain if there are spatial correlations with the inferred direction of motion in the cluster.

5.3.2 Classifying PSB Morphologies

By visually inspecting the distribution of spaxels identified as PSB in our maps compared to the direction of motion inferred from direction of the tails, we assigned an index to the galaxy based on whether it exhibited PSB features on its leading edge (ie. the edge facing away from the tail). These indices are: 0 (no PSB spaxels were found), 1 (some PSB spaxels but not aligned with the leading edge), 2 (PSB spaxels aligned with the leading edge).

5.3.3 Projected Phase Space Information

From observations alone we cannot fully measure the 6D phase space information for the galaxies in our cluster. Ordinarily, for cluster galaxies we can access the line of sight velocity with respect to the cluster centre, and the projected radius from the cluster centre. This allows some understanding of the geometries involved, and has allowed studies looking at how quenching, gas content, and infall time correlates with position in this projected phase space (Oman et al., 2013; Jaffé et al., 2015; Oman & Hudson, 2016). In the case of our jellyfish galaxies, we also gain one more constraint – the direction of travel projected in the plane of the sky. This is inferred as the direction opposite to the direction of the tail detected in LoTSS, and while it adds information we still caution that it is a projected quantity. For example, a galaxy with a projected direction which is radially towards the centre of the cluster may in fact be moving away from the centre when the line of sight component is taken into account. However, galaxies which have tails that infer a direction which is moving radially away from the centre cannot be moving towards it, even in 3D.

In order to take this information into account, we use the coordinates for our galaxies and

the coordinates for the centre of their cluster in order to calculate a vector for the direction to the centre of the cluster in projected space. We use the dot product of this with the vector opposite that of the identified tail direction (i.e. the inferred direction of motion), in order to quantify how the galaxy is moving radially in its cluster according to projected information. We note again that a positive dot product, suggesting that the galaxy is moving towards the cluster centre, could be a false positive due to projection effects; however a negative dot product, suggesting the galaxy is moving away from the centre cannot be a false signal.

5.3.4 Control Sample

In order to ensure that the PSB regions we see when we reduce the SNR cut in the Chen selection method are not a result of noise, I construct a control sample which is matched to the jellyfish sample. To do this I select 10 galaxies for each jellyfish galaxy, which is matched within 0.1 on the NSA stellar mass, matched within 0.005 in redshift, has no quality flags in MaNGA data, has the same IFU size as the jellyfish galaxy, and is characterised as having less than 3 galaxies in the group measured by the Galaxy Environment for MaNGA value-added catalogue (GEMA; released with SDSS DR17, following the methods in Argudo-Fernández et al., 2015). This creates a sample of 290 galaxies with the same distribution as the jellyfish sample in mass, redshift, IFU size, but are not located in clusters.

Using a KS test to statistically quantify how similar the distributions are in mass and redshift, we find a p-value of 0.999 for the mass distributions, and a p-value of 0.951 for the distribution in redshift. These values indicate that the samples are drawn from the same distribution with 95% confidence.

5.3.5 Kinematic Asymmetries

As RPS is known to be an effect which impacts galaxies asymmetrically as they infall, it is valuable to quantify how this can manifest in our observations. The process is not known to be strong enough in most instances to disrupt the morphology of the stellar component, and so surface brightness should remain undisturbed. More sensitive than the morphology, the kinematics of the stellar and gaseous components in a galaxy rely on equilibrium in their orbits and so can be perturbed by the pressure of RPS. As such, we measure the asymmetry of the velocity of the stellar and gaseous components, along with the velocity dispersion of these components. This is motivated by signatures seen in the gas velocity dispersion maps

of the strongest RPS candidates. To do this, the MaNGA map for each of the four kinematics components (stellar velocity, stellar velocity dispersion, gas velocity, gas velocity dispersion) for our sample are masked to remove spaxels with SNR < 8 in order to ensure we are not measuring noisey spaxels in the outer regions. The maps are rotated 180 degrees, and then subtracted from the original maps. The maps are rotated around the centre defined by the MaNGA pointing – we note that this is not the most accurate way to do this, and may result in large issues in this measurement. A way to mitigate this in a future study would be through the use of kinematic modelling to locate the kinematics centre of the data. The absolute magnitude of the difference in each of the spaxels are then added to create one number which quantifies the asymmetry of the kinematic map. These values are used in our analysis.

5.4 Results and Discussion

5.4.1 Validity of PSB Regions at SNR>3

Comparing to the control sample we defined in Section 5.3.4, I consider the difference in fraction of spaxels defined as PSB using the Chen method with the differing SNR cuts of 8 and 3, for both the jellyfish sample and the control sample. The normalised distributions of this quantity for the two samples, are shown in Figure 5.1.

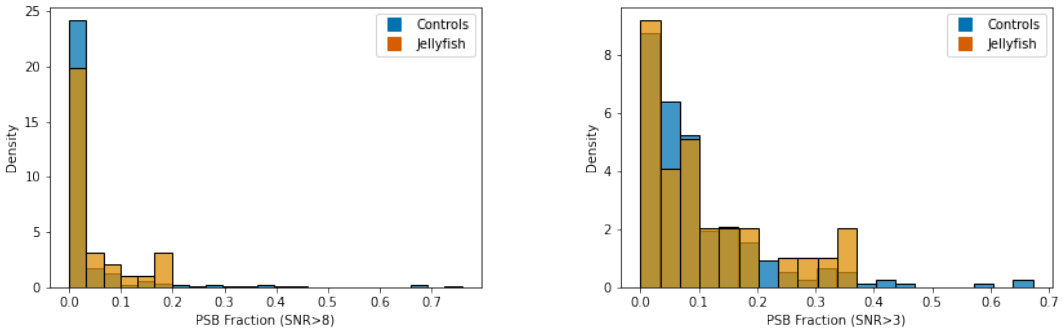

Figure 5.1: Normalised histograms showing the distribution of galaxies based on fraction of spaxels classified as PSB using the Chen method with SNR limited to > 8 (left) and > 3 (right) for our jellyfish sample (orange) and our control sample (blue).

We see that the control sample, containing galaxies matched on mass and redshift, but which are not members of clusters, shows a trail off as we get to higher PSB fractions in both SNR cut cases. The jellyfish galaxies also see a large number of galaxies with no signal, however in both SNR cut cases there is a second peak seen at greater fractions. We note that

the signal persists with the same form, which highlights that galaxies which have true PSB regions gain a higher fraction by the extension to lower SNR regions. Meanwhile, despite some galaxies which are classified as PSBs independent of their cluster membership (these have most likely quenched due to non-RPS effects), the control sample does not gain a secondary peak by the inclusion of noisier regions. Thus we conclude that this expansion is valid and we are not at risk of creating a false PSB signal due to noise. Further, we note that the analysis relies on the alignment of the PSB region with the implied leading edge of the galaxy, if PSB regions were an artifact of noise in our SNR > 3 sample, then this signal would appear independent of direction.

5.4.2 Post Starburst Regions at the Leading Edge

For our sample of jellyfish galaxies, we used the spatially resolved $H\alpha$ and $H\delta$ maps to create maps of spaxels categorised as PSB or not, as per the method from Chen et al. (2019b) outlined in Section 5.3.1. For this we used spaxels which had SNR > 3. This was a lower cut than used previously, however comparison to a control sample (see Section 5.4.1) shows that PSB signals in low SNR regions are not due to noise. In Figures 5.2 to 5.12, I show summary plots of data for our sample of jellyfish galaxies which are classified with index 2 – i.e. they exhibit PSB regions aligned with the leading edge. This includes a thumbnail image with the tail direction and direction to the centre of the cluster indicated, 2D maps from MaNGA which show emission line maps for lines relevant to our PSB selection (the Hα equivalent width, and Hδ absorption), the Chen PSB selection maps where yellow indicates a PSB spaxel classification (as described in Section 2.8.1), the D4000 break where higher values indicate older stellar populations, PCA1 and PCA2 index maps which correspond roughly to the D4000 break and Balmer absorption (these indices are described in Section 2.8.2), the PCA PSB selection maps which classify spaxels based on their PCA1 and PCA2 values (as shown in Section 2.8.2), and the stellar and gas velocities and velocity dispersion maps. The tail direction allows the inferred direction of motion of the galaxy to be compared to the distribution of the PSB spaxels. For the first 11 galaxies shown, the PSB regions align in a crescent shape along the leading edge with respect to the direction of motion. We also note that these regions are in front (with respect to the direction of motion) of bands of increased star formation rate, as identified in Roberts et al. (2022) as the regions contributing to the excess star formation they find in the leading half. These are seen through increased Hα equivalent width, and regions of decreased D4000.

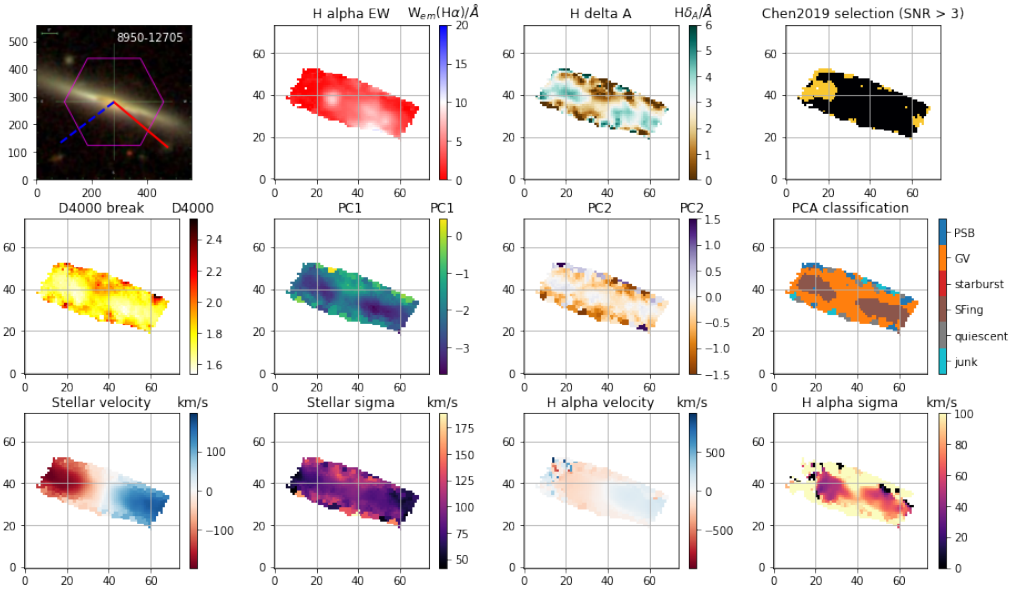

Figure 5.2: Summary of observations for 8950-12705, classified with index 2. Panels described in text. Chen PSB selection spaxels in yellow.

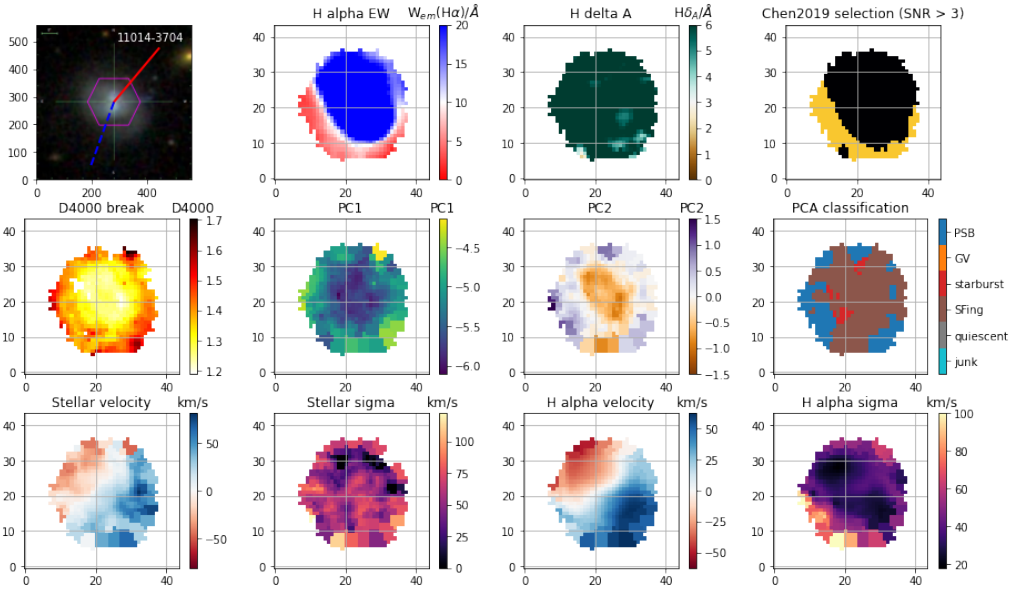

Figure 5.3: Summary of observations for 11014-3704, classified with index 2. Panels described in text. Chen PSB selection spaxels in yellow.

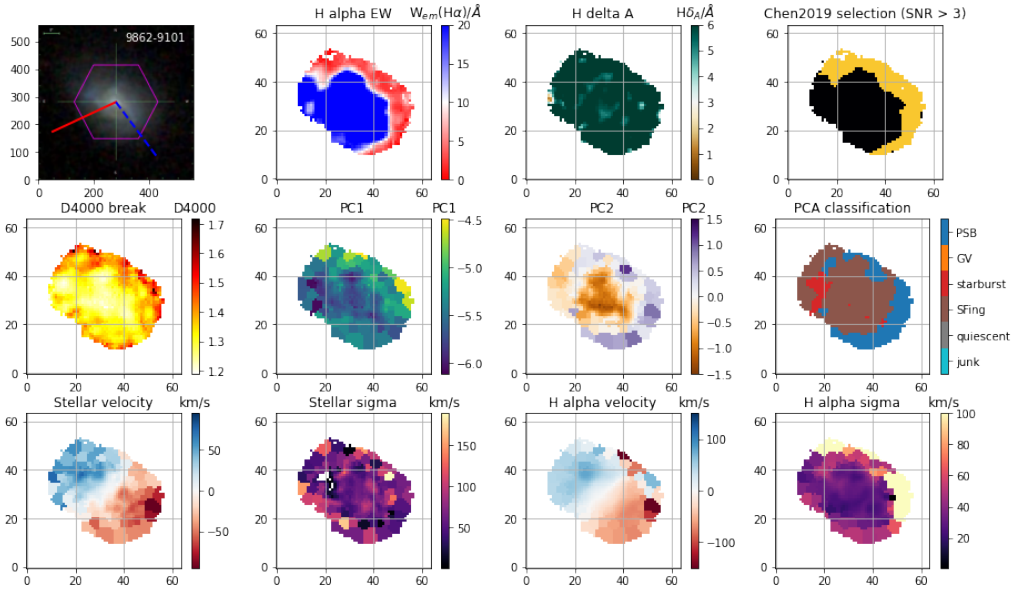

Figure 5.4: Summary of observations for 9862-9101, classified with index 2. Panels described in text. Chen PSB selection spaxels in yellow.

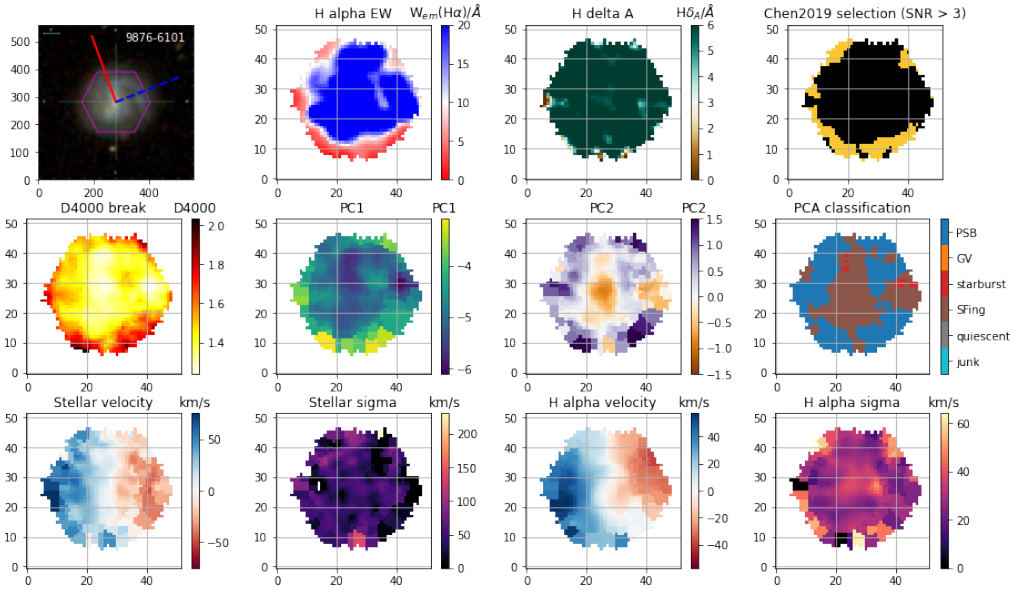

Figure 5.5: Summary of observations for 9876-6101, classified with index 2. Panels described in text. Chen PSB selection spaxels in yellow.

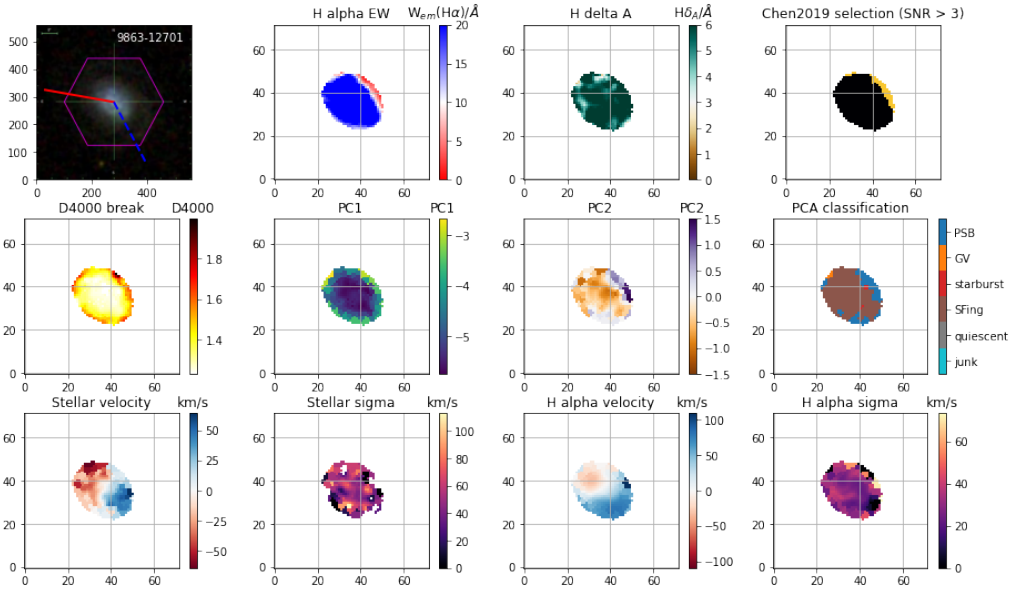

Figure 5.6: Summary of observations for 9863-12701, classified with index 2. Panels described in text. Chen PSB selection spaxels in yellow.

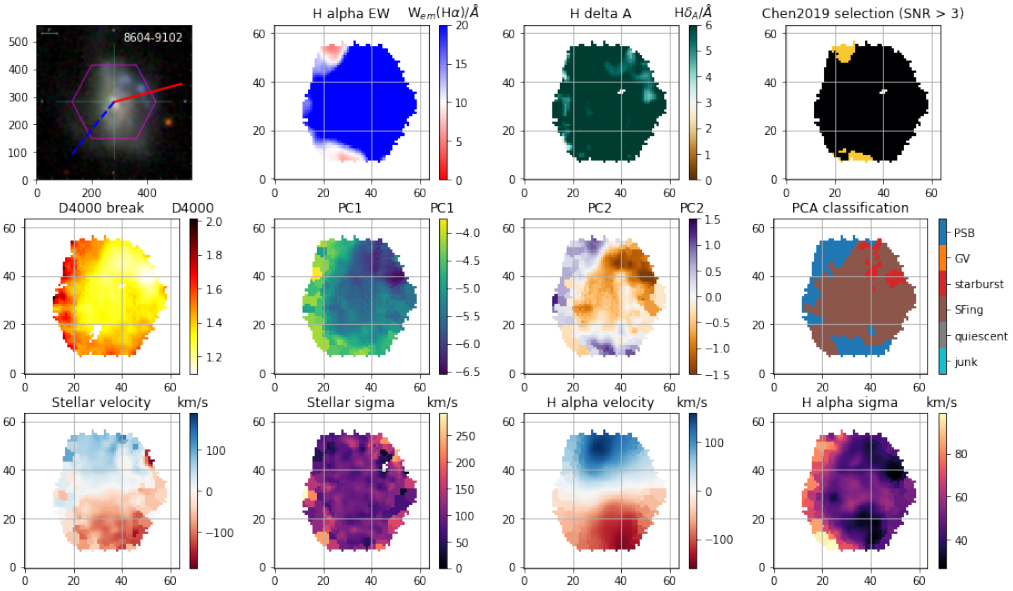

Figure 5.7: Summary of observations for 8604-9102, classified with index 2. Panels described in text. Chen PSB selection spaxels in yellow.

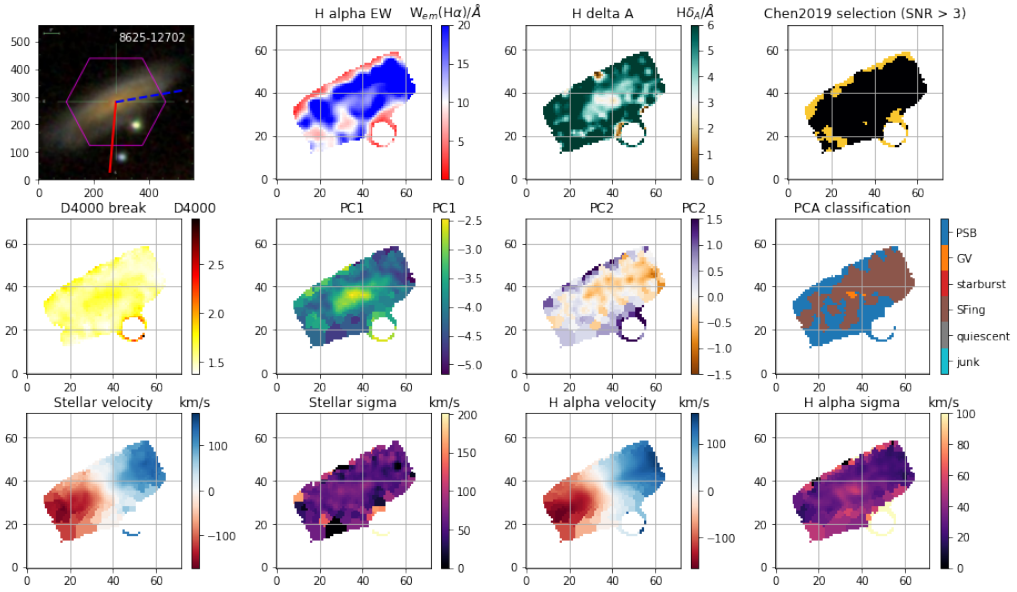

Figure 5.8: Summary of observations for 8625-12702, classified with index 2. Panels described in text. Chen PSB selection spaxels in yellow.

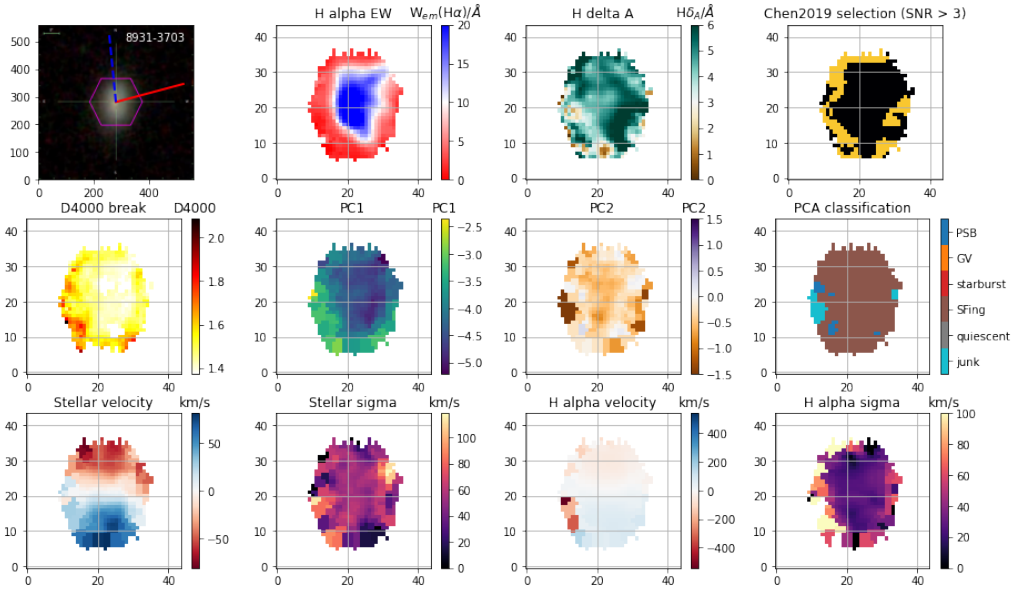

Figure 5.9: Summary of observations for 8931-3703, classified with index 2. Panels described in text. Chen PSB selection spaxels in yellow.

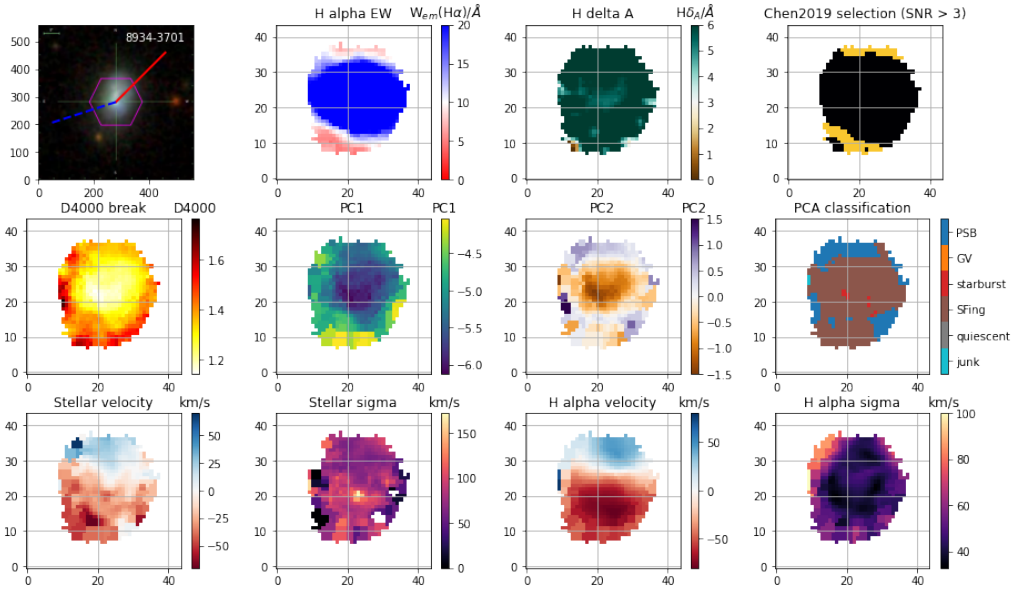

Figure 5.10: Summary of observations for 8934-3701, classified with index 2. Panels described in text. Chen PSB selection spaxels in yellow.

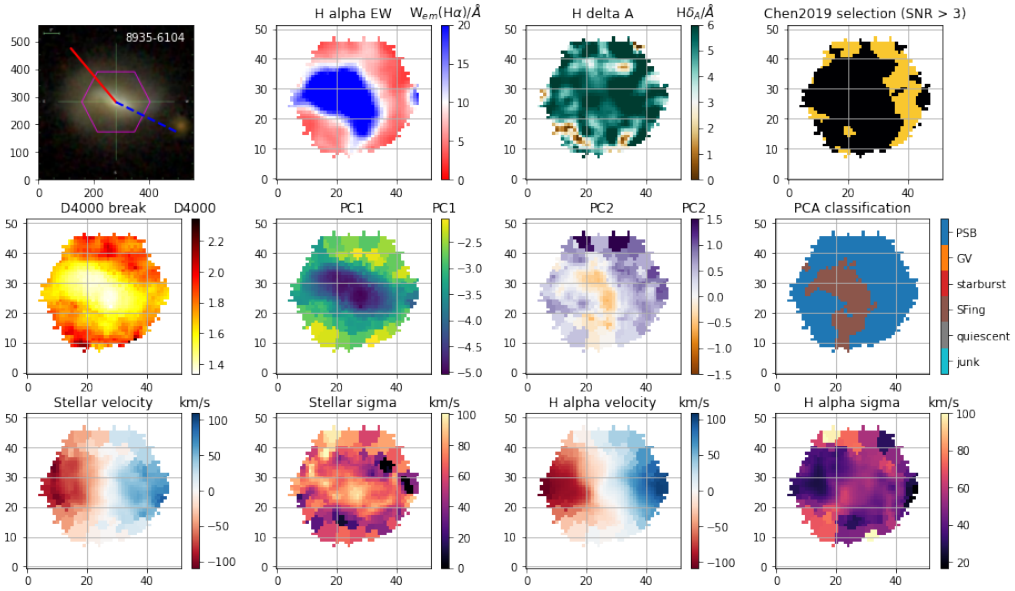

Figure 5.11: Summary of observations for 8935-6104 classified with index 2. Panels described in text. Chen PSB selection spaxels in yellow.

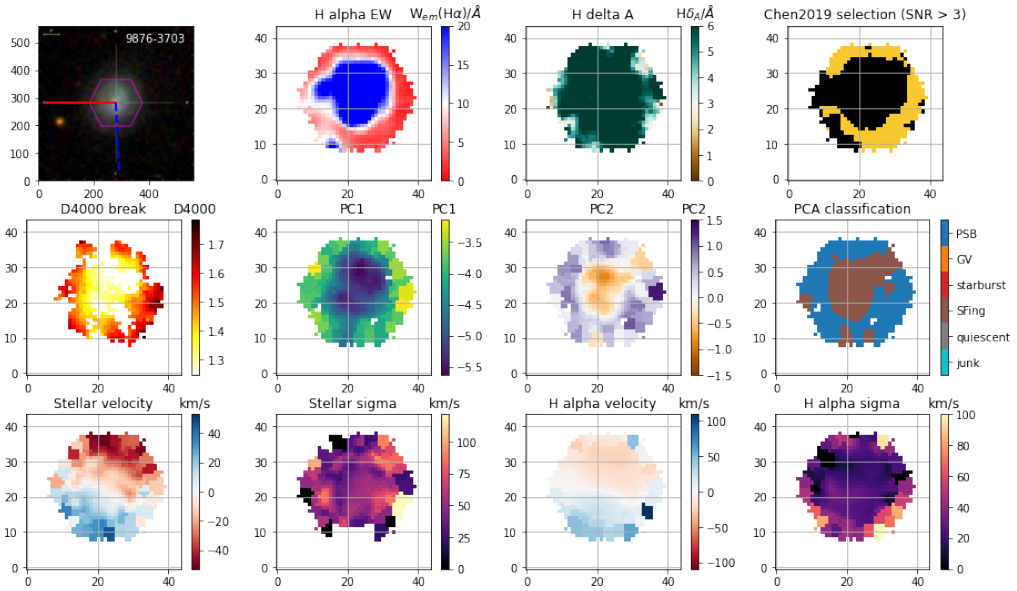

Figure 5.12: Summary of observations for 9876-3703, classified with index 2. Panels described in text. Chen PSB selection spaxels in yellow.

Figures 5.13 to 5.21 show the 9 galaxies classified with index 1 (i.e. those which show PSB regions but are not aligned with the leading edge), while those classified as index 0 (lacking PSB regions) are presented in Appendix A.

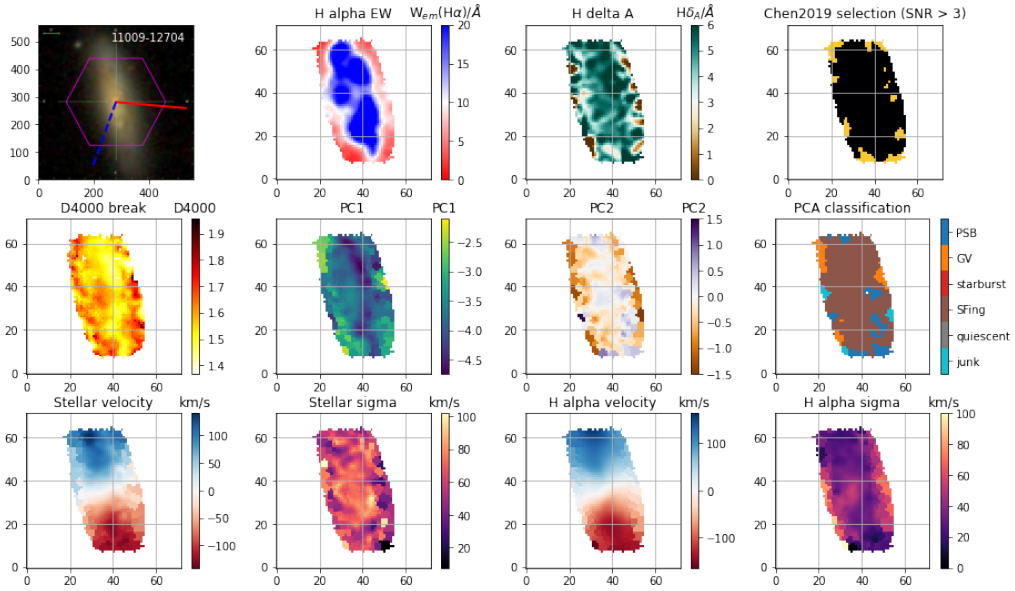

Figure 5.13: Summary of observations for 11009-12704, classified with index 1. Panels described in text. Chen PSB selection spaxels in yellow.

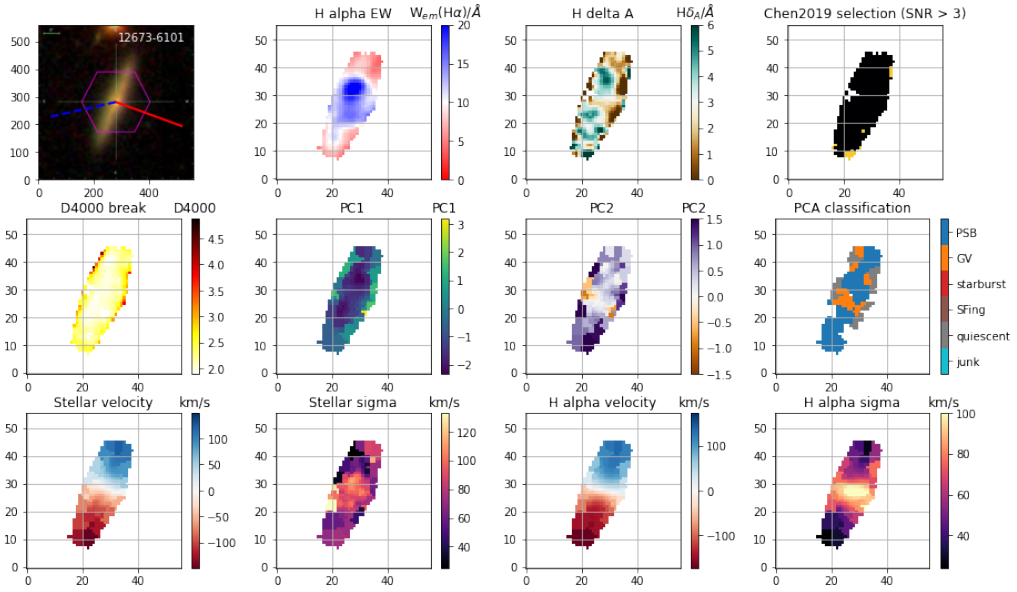

Figure 5.14: Summary of observations for 12673-6101, classified with index 1. Panels described in text. Chen PSB selection spaxels in yellow.

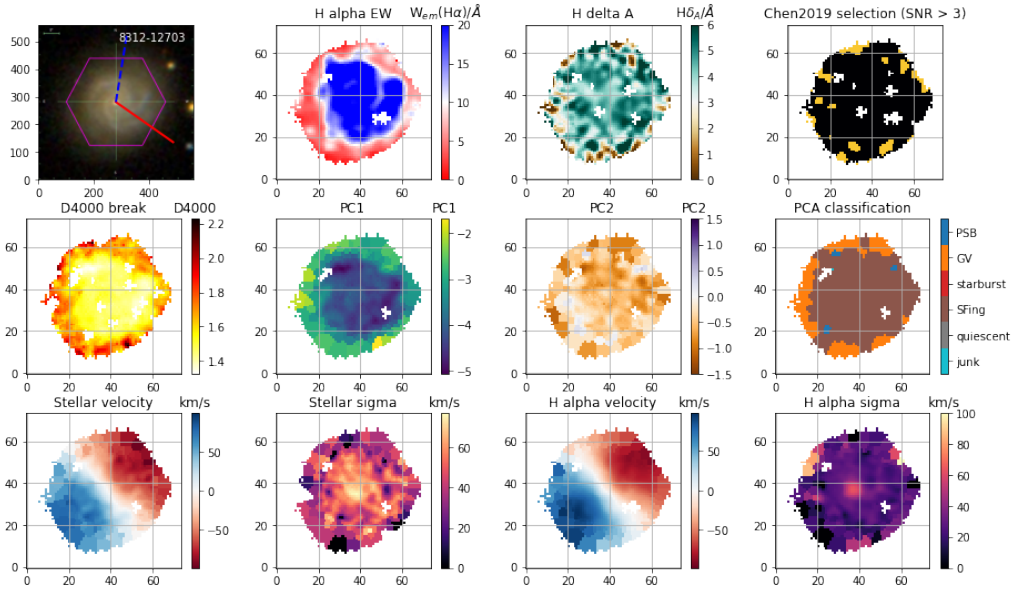

Figure 5.15: Summary of observations for 8312-12703, classified with index 1. Panels described in text. Chen PSB selection spaxels in yellow.

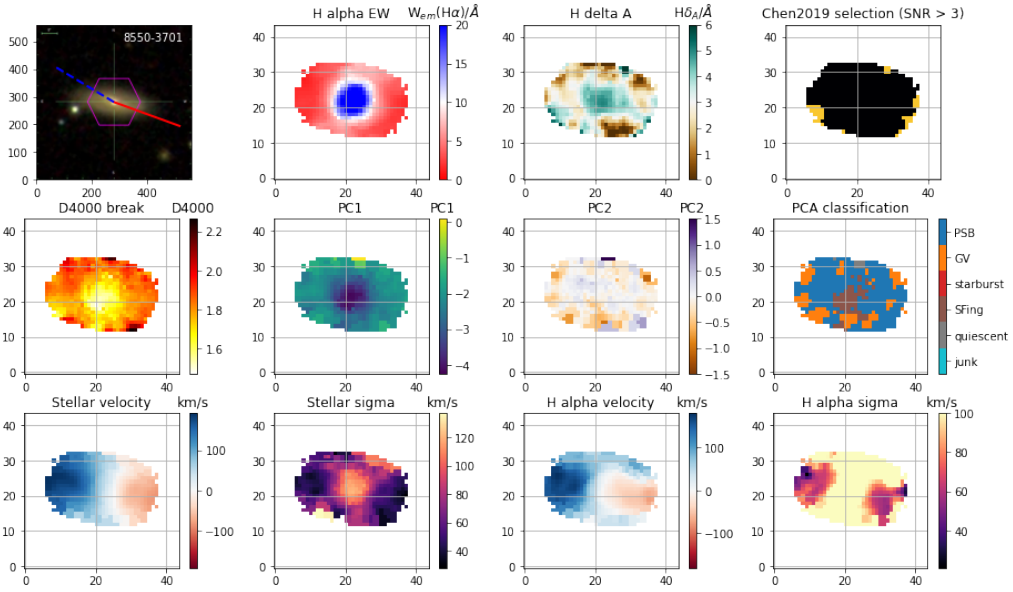

Figure 5.16: Summary of observations for 8550-3701, classified with index 1. Panels described in text. Chen PSB selection spaxels in yellow.

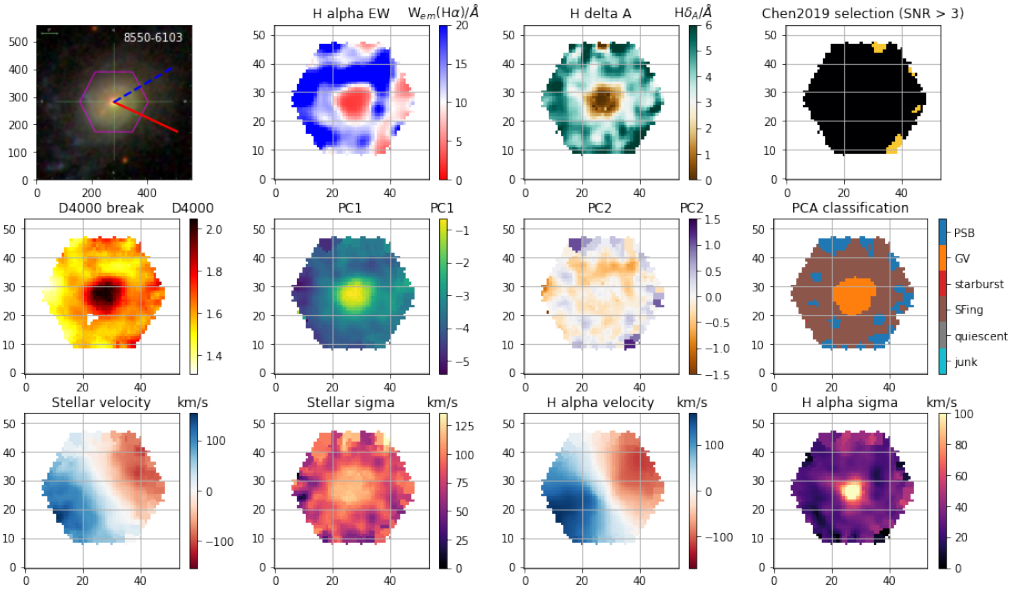

Figure 5.17: Summary of observations for 8550-6103, classified with index 1. Panels described in text. Chen PSB selection spaxels in yellow.

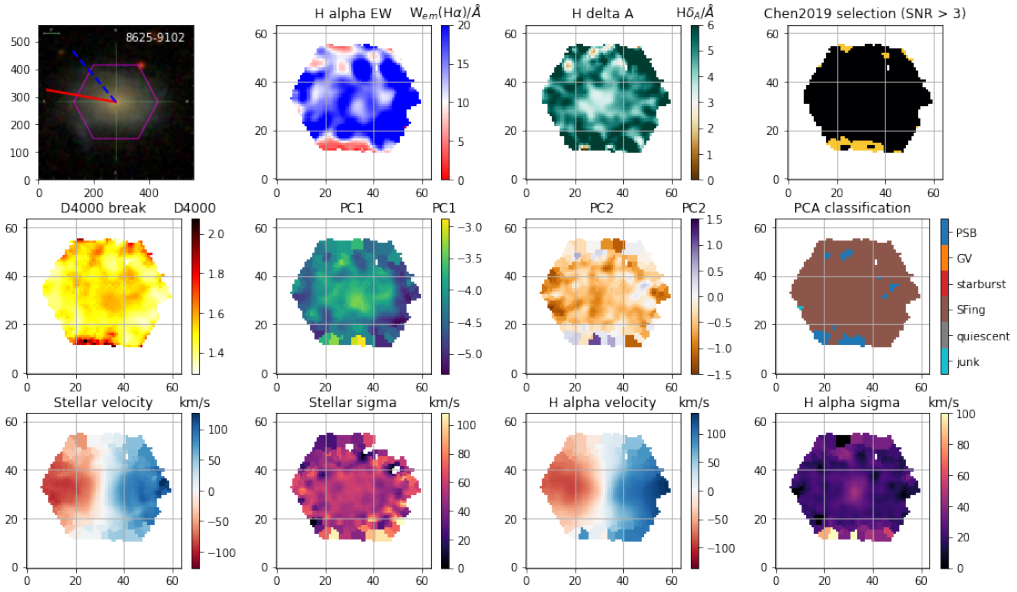

Figure 5.18: Summary of observations for 8625-9102, classified with index 1. Panels described in text. Chen PSB selection spaxels in yellow.

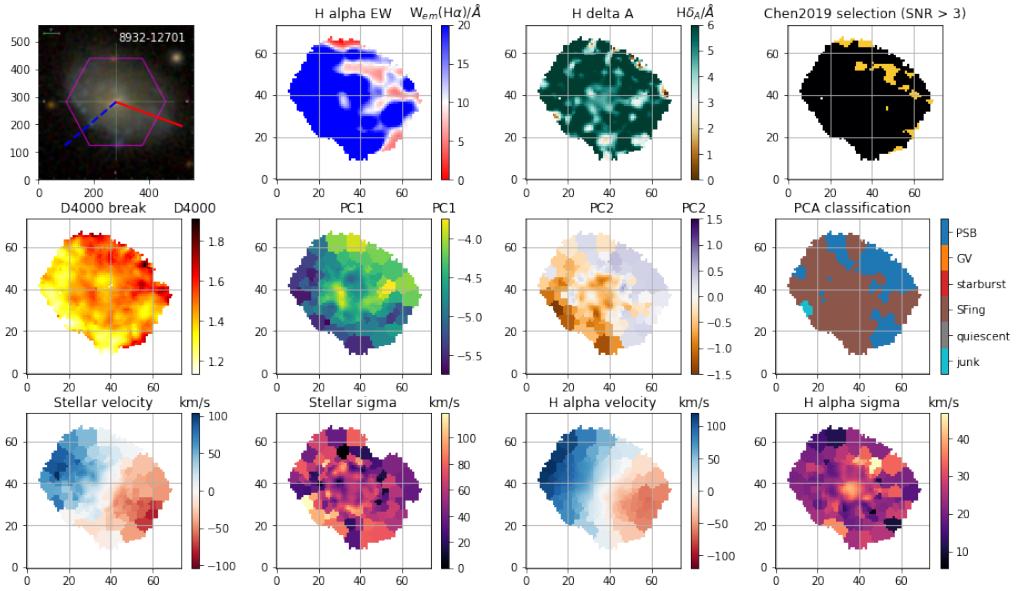

Figure 5.19: Summary of observations for 8932-12701, classified with index 1. Panels described in text. Chen PSB selection spaxels in yellow.

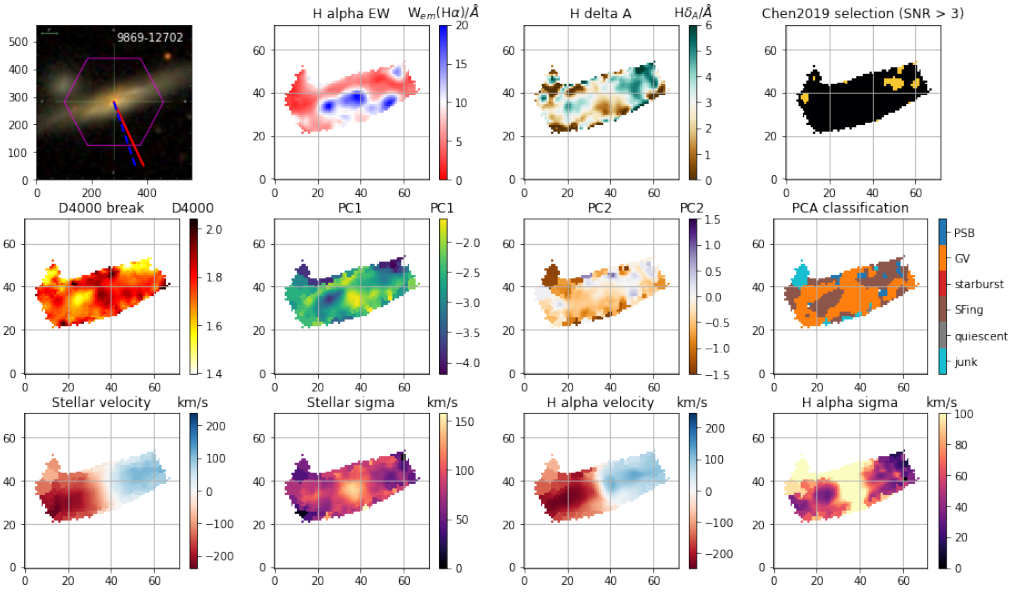

Figure 5.20: Summary of observations for 9869-12702, classified with index 1. Panels described in text. Chen PSB selection spaxels in yellow.

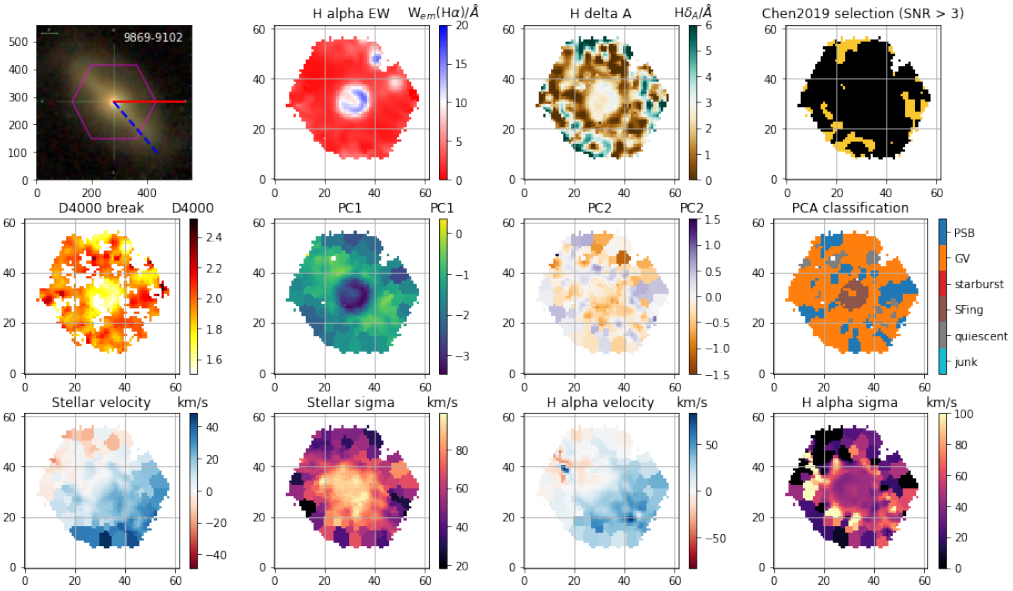

Figure 5.21: Summary of observations for 9869-9102, classified with index 1. Panels described in text. Chen PSB selection spaxels in yellow.

5.4.3 Phase Space Information

In order to ascertain that the PSB signals are due to ram pressure stripping, we would expect the position of the galaxy in projected phase space to correlate with the signatures. To do this, we use the projected cluster information given in Roberts et al. (2021), and add the information given by the tail direction through the dot product of the inferred direction of motion with the direction to the centre of the cluster.

Figure 5.22 shows the distribution of our different classifications in traditional projected phase space. We see that the galaxies which are classified with index 2 – i.e. those that show regions of PSB spaxels aligned with their leading edge– are found almost completely within 0.5 effective radii of the cluster. Meanwhile, those which exhibit some PSB regions but which are not aligned with the leading edge are seen across radii, along with those showing no PSB spaxels (though these are absent in the innermost 0.3 effective radii). Ram pressure stripping is expected to be strongest as galaxies pass through higher density intracluster medium, found in the central regions. As such, this is an expected effect, with the projection effects taken into account to explain the class 1 galaxies which appear to be at the closest radii to the centre. The velocity offset with respect to the cluster is also a driving factor, with a greater velocity offset creating greater RPS effects. This is not seen as a strong separator of the classes in our sample, however we note this could be attributed to the loss of three dimensions of the velocity vector due to only being able to observe the line of sight velocity offset, which is more susceptible to muddying by projection effects.

In Figure 5.23, we show how the different populations of classification compare in dot product values. The dot product is that between the vector of inferred direction of motion and the vector of direction to the centre of the cluster. As such, $+1$ dot product indicates the galaxy is heading directly towards the centre of the cluster (in projection), -1 indicates the galaxy is moving directly away from the cluster centre, and 0 indicates that the galaxy is moving tangential to the direction to cluster centre. We see that the index 2 galaxies – those which display PSB regions which are spatially correlated with their leading edge (as determined by the tail direction) – are those which are moving towards the centre of the cluster. This is expected in an RPS scenario as these galaxies would be moving into denser medium, and RPS effects increase with both velocity through the medium, and the density of the medium.

A comparison of the projected phase space information with the dot product information

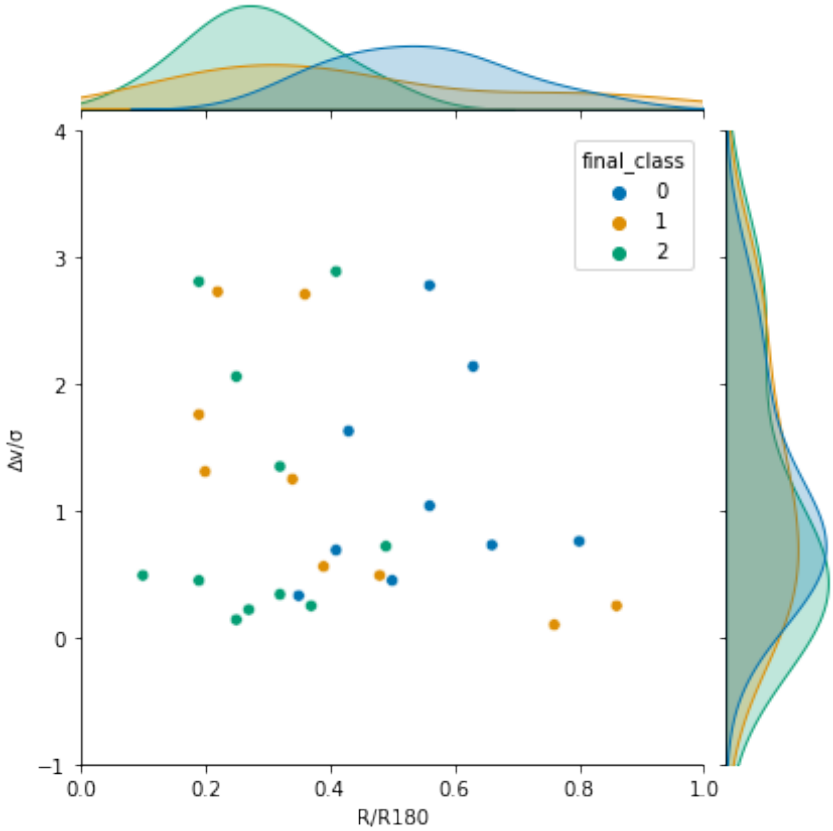

Figure 5.22: Distribution of galaxies by classification in projected phase space (PPS) – the projected radius of the galaxy in its the cluster (normalised by the virial radius of the cluster), versus the line of sight velocity with respect to that of the cluster centre (normalised by the velocity dispersion of the cluster). Green, yellow, and blue points show the 2, 1, and 0 classification groups respectively. The marginal distributions are shown as smoothed histograms on each axis.

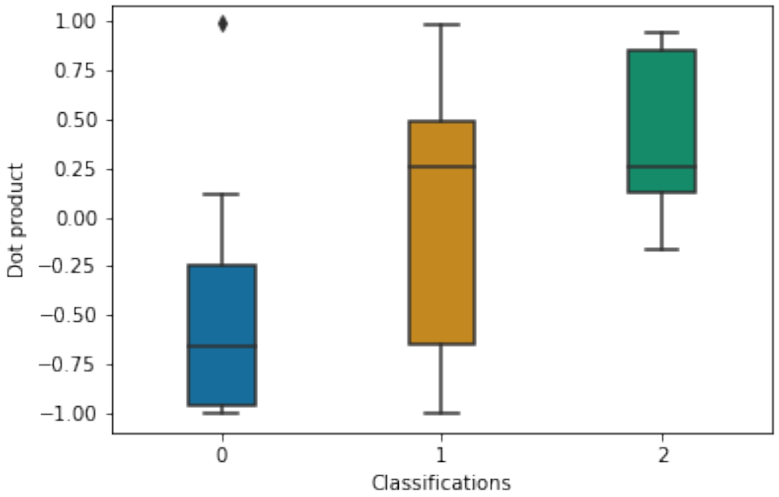

Figure 5.23: Box plot showing the values of dot product across the different classifications. The dot product is the scalar product between the direction of movement of the galaxy inferred from the tail, and the direction towards the centre of the cluster. Positive values denote the galaxy appears to be moving towards the centre of the cluster (allowing for projection effects), while a negative value means it is moving away.

for our classifications of PSBs is shown in Figure 5.24. This shows again that the line of sight velocity offset is not a strong predictor of our classifications, but that the three classes can almost be fully separated by diagonal lines in the plane of projected radius against dot product. Class 2 galaxies inhabit the lower right corner, class 0 galaxies are confined to the upper left corner, while class 1 galaxies exist in the region in between. This highlights that the galaxies which we see the strongest PSB leading edge signatures in are those which are falling in towards the cluster centre and are nearing their closest approach. This is a valuable observation which can be compared to literature and simulation expectations of RPS processes and potentially be used to constrain the process taking place. One final observation of note is that there are galaxies in our sample which are moving away from the cluster centre (i.e. have a negative dot product). Geometry of projection means these cannot be false signals (a projected tail implying motion towards the centre can be false, but a projected tail implying motion away from the centre cannot), and so this demonstrates backsplash galaxies which have already undergone their first pericentre but are still exhibiting observable RPS tails. This may challenge the findings of Oman et al. (2021) and Rohr et al. (2023), which found that simulated galaxies should lose the majority of their gas content during the first infall. This is discussed further in Section 5.4.6.

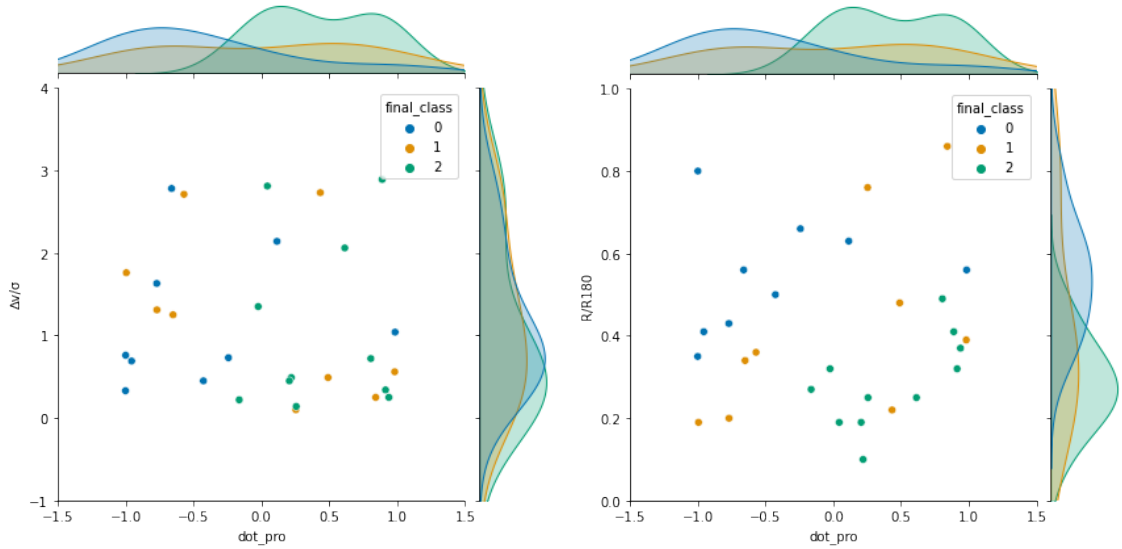

Figure 5.24: Distribution of galaxies by classification in PPS versus the dot product. **Left:** Dot product versus line of sight velocity with respect to that of the cluster centre (normalised by the velocity dispersion of the cluster). **Right:** Dot product versus the projected radius of the galaxy in its the cluster (normalised by the virial radius of the cluster).

5.4.4 Star Formation and Gas Content

Roberts et al. (2021) considered the star formation excesses in the front leading half of the galaxies compared to the other half. In many of our galaxies, we see a band of increased Hα emission behind the leading edge PSB signal, as discussed in Section 5.4.2. These are the regions which generate the enhancements studied in that paper. In Figure 5.25 we consider whether the star formation (and specific star formation) enhancements seen in this paper are related to our classification of PB morphology, and find no trend. While specific star formation excess and star formation excess are correlated as expected, our classifications are not confined to any part of this plane. Additionally, in Figure 5.26 we consider if the alignment with the cluster centre (through the dot product) effects the star formation excesses, but also see no trend. This indicates that despite the spatial correlation, the strength of these effects seems to be decoupled, which may suggest the effect is dominated by RPS removing gas as opposed to intense starbursts caused by pressure depleting the gas.

In order to consider this, we use data from the H I -MaNGA survey (see Section 2.3.1 for details). Of our 29 jellyfish galaxies, 8 galaxies are detected in the H I -MaNGA survey, while all have been observed. This means non-detections are due to lack of H I surface brightness. Figure 5.27 shows how the galaxies which show the strongest spatially correlated PSB regions are also those showing the least H I detections. To explore this further, we look at the gas mass

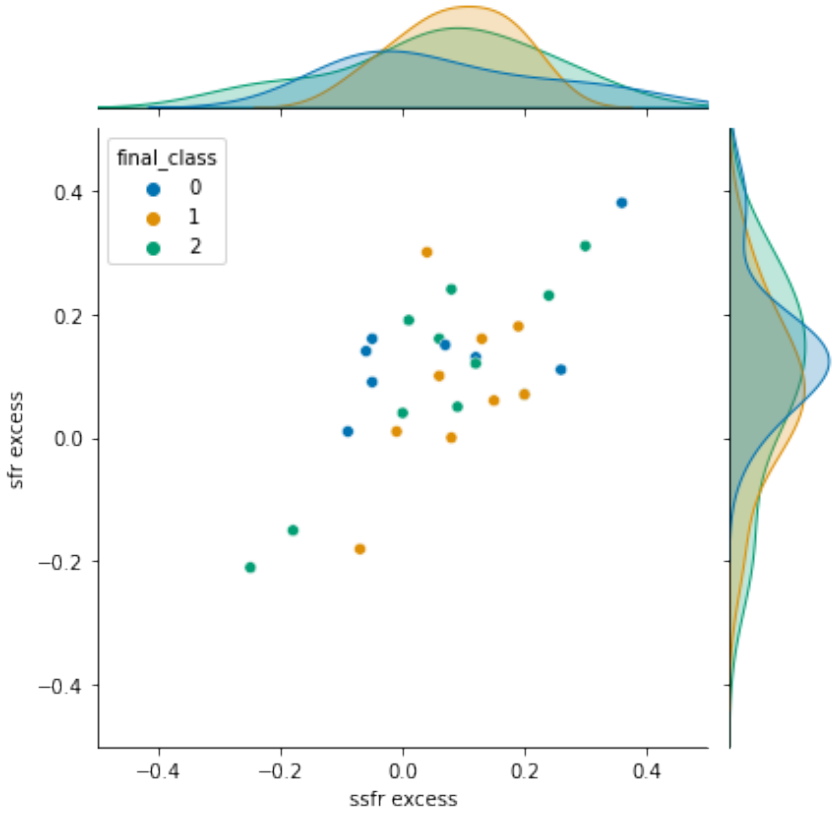

Figure 5.25: Distribution of galaxies by classification in star formation and specific star formation excess. The excess values were derived in Roberts et al. (2022) from Hα observations, and express the excess (specific) star formation seen in the leading half (i.e. the half opposite the tail direction, at the front of the direction of motion) compared to the trailing half.

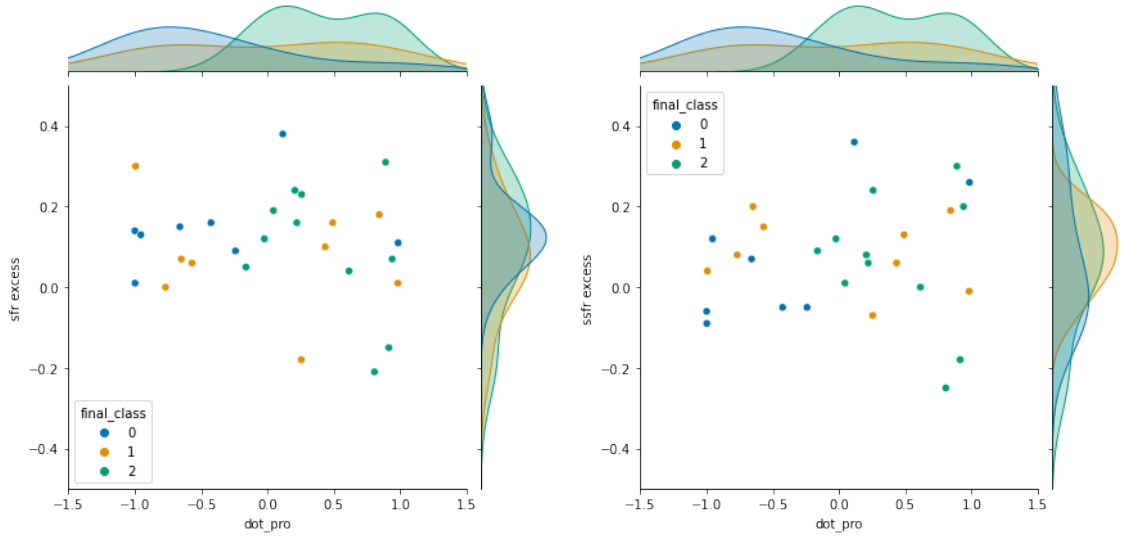

Figure 5.26: Distribution of galaxies by classification in star formation excess (left) and specific star formation excess (right) versus dot product.

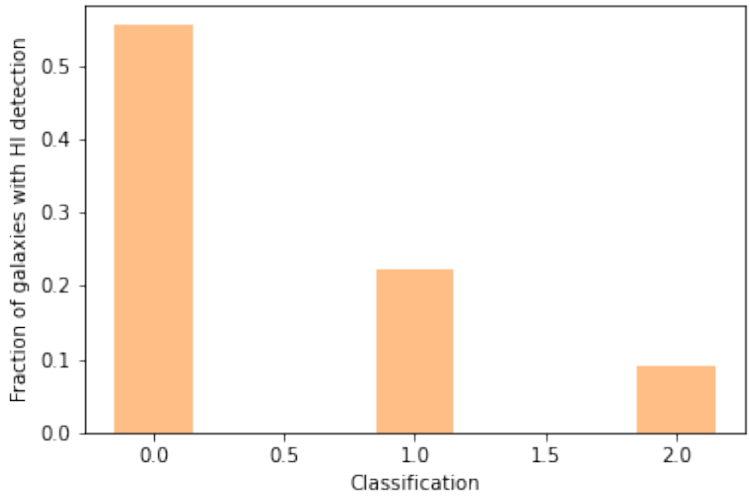

Figure 5.27: Histogram showing the fraction of galaxies with each classification which were detected by the H I -MaNGA survey. This is specifically the fraction with a positive detection over the number in each classification which was observed in H I -MaNGA

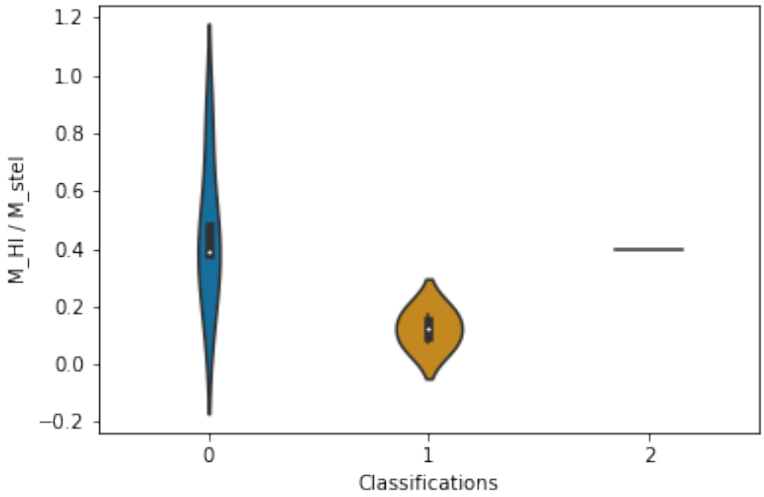

Figure 5.28: Violin plot highlighting the observed H I mass-stellar mass ratio for galaxies detected in H I -MaNGA in each classification group. Point in classification 2 group indicates only one galaxy with data here.

fraction in our sample for those with detections, and how this varies across the classifications. This is shown in Figure 5.28, tentatively indicating that lower gas mass fractions are found in galaxies showing the stronger PSB signal, however we do not have enough galaxies detected in H I to determine this for certain.

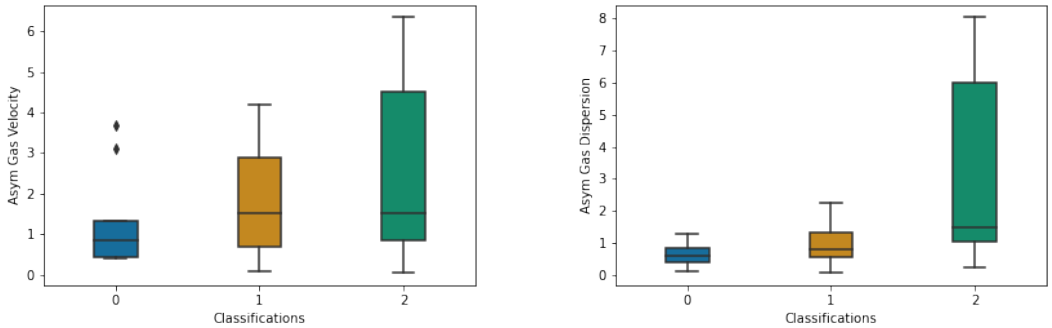

Figure 5.29: Box plots showing the distribution across classification groups for galaxies for asymmetries in the gas velocity (left) and velocity dispersion (right) maps.

5.4.5 Gas Asymmetries

The trends with HI content suggest the effects are due to gas removal. To see if this can be seen in action, we visually inspected the Hα velocity maps, and see some disturbances and deviations from rotation which are not seen in the stellar velocity fields. These are most pronounced in our classification 2 galaxies, for example, galaxies 8950-12705, 9863-12701, and 9876-6101 (see Figures 5.2, 5.6, and 5.5). Further, on visually inspecting the Hα velocity dispersion maps, we see strong correlations with the PSB regions to regions with heightened gas velocity dispersion (for example 8604-9102, 9862-9101, and 11014-3704 – Figures 5.7, 5.4, and 5.3). This suggests the gas has been disrupted and removed by the RPS effects. In order to quantify this, we determine the asymmetry of all four of the stellar and gas, velocity and velocity dispersion fields. This method is described in Section 5.3.5.

In Figures 5.29 and 5.30, we show how the kinematic asymmetry varies across the classifications for the velocity and the velocity dispersion, for both the stellar and gas components. RPS is not expected to exert enough pressure to disrupt the stellar component, so if this effect is due to RPS we would expect to see elevated asymmetry in the gas velocity and gas velocity dispersion, increasing for those showing the strongest RPS signal – ie those showing the strongest PSB signal. This is indeed what we see in the data and suggests that we are seeing PSB regions on the leading edge of our galaxies where RPS is removing and disrupting the gas and quenching these regions in real time.

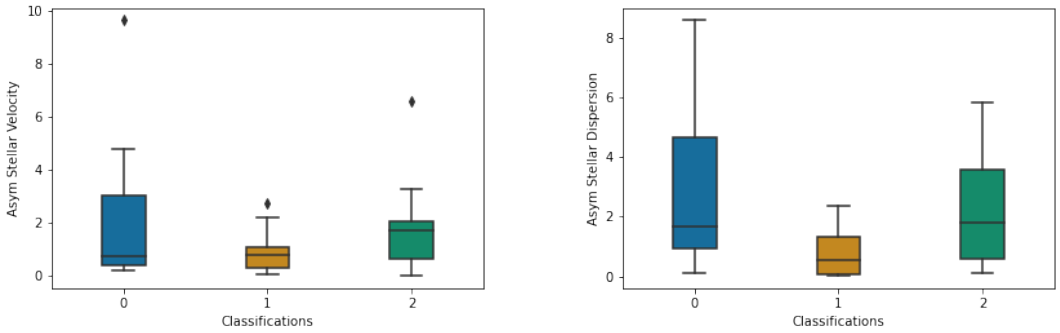

Figure 5.30: Box plots showing the distribution across classification groups for galaxies for asymmetries in the stellar velocity (left) and velocity dispersion (right) maps.

5.4.6 Comparison with Simulations

In Rohr et al. (2023), they find the main predictor of whether galaxies in clusters are classified as jellyfish galaxies is the ratio of the stellar mass of the galaxy to the mass of the cluster halo they are in. This makes sense intuitively, as a higher mass cluster halo will create a deeper potential well which will increase the infall velocity and also produce higher gas densities, while a lower galaxy stellar mass will mean the gas in the galaxy is less gravitationally bound and so easier to strip away. Rohr et al. (2023) classifies jellyfish galaxies using visual inspection of the gas particle densities from the simulation (Zinger et al., 2023), without considering whether these would be observable in the real universe. As such, these identifications will be sensitive to any RPS effects, regardless of strength, while our sample was visually selected based on visible tails in the LoTSS data, and so we expect to only identify the most extreme stripping examples. As we see in Figure 5.31, this is confirmed by comparing the distribution of our sample in $\log(M_{stel}/M_{halo})$ with the distribution of galaxies in the Rohr et al. (2023) sample that are identified as jellyfish.

As we see in Figure 5.32, despite the mass ratio being a strong predictor of identification as a jellyfish, our classifications based on PSB morphology do not have different values. This is indicative of our samples not showing different RPS signals in terms of tails (as we can only identify the most extreme cases here), but suggests our PSB signatures are only present in a select sample of galaxies, unrelated to the mass ratios. This could be due to timing, or position in the cluster. We have already seen that the strongest PSB signals are found in the inner regions of the clusters. Disentangling whether this is due to the timescales that RPS has been taking place, or simply the higher densities in the central regions, involves exploring the

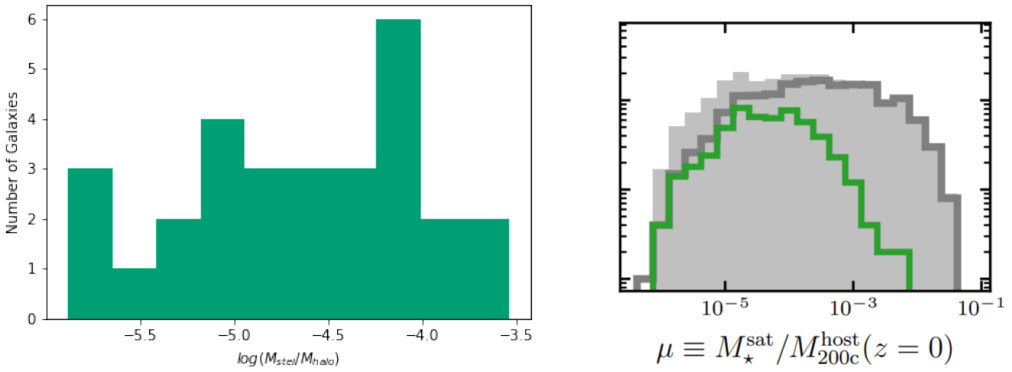

Figure 5.31: Distribution of galaxies by stellar-cluster halo mass ratio, for our sample (left) versus a simulated sample (right) from Rohr et al. (2023). On the right, the grey region indicates galaxies in clusters at z=0 in the Illustris sample, the dark grey line indicates those visually inspected in the sample, and the green line indicates those identified as jellyfish galaxies through visual inspection of the gas column density.

timescales in the cluster vs the timescales of the quenching.

The Chen PSB selection method is sensitive to quenching which has taken place rapidly in the past $\sim$ 1Gyr, which gives some indication of the timescales involved. Further, the PCA PSB selection method is sensitive to a different quenching scenario which does not take into account emission lines, and in some galaxies we see spatial trends where the Chen method identifies spaxels which are at a different region of the leading edge than those identified by the PCA method, while the gas velocity dispersion and D4000 break show disruption across the whole region (eg. 8604-9102, seen in Figure 5.7). This could indicate a time evolution occuring along the leading edge of the galaxy as the gas is stripped away, which is easiest to describe for this galaxy. As seen in Roberts et al. (2022), moving out from the centre of the galaxy towards the leading edge, we see a band of enhanced star formation which has been attributed to gas being compressed – seen in simulations (Troncoso-Iribarren et al., 2020) and observations (Roberts et al., 2021). Just outside this arc is where we find the PSB regions identified by the Chen method which is known to identify very recent quenching. Then outside this region is where we find the regions defined as PSB by the PCA method which probes slightly later quenching. Looking at this trend, we propose a scenario where the galaxy has experienced RPS during infall into the cluster, which has progressively compressed the gas at the leading edge producing enhanced star formation, before removing the gas from this region causing quenching, and that this progresses in a wave over time from the outer leading edge towards the centre. To understand this fully, comparisons with timescales and SFH are required.

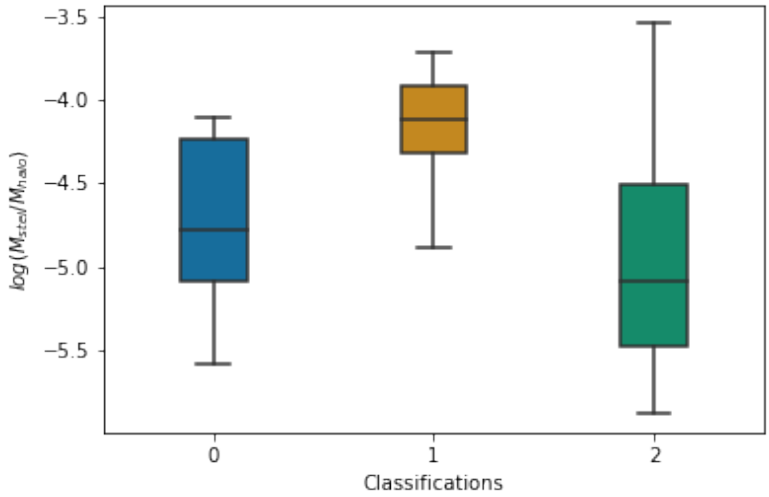

Figure 5.32: Distribution of values of stellar-cluster halo mass ratio for different classification groups.

In the simulated jellyfish studied in Rohr et al. (2023), they find that all of the cold gas in a jellyfish galaxy will be lost globally between initial infall and the galaxy beginning its second infall, and the galaxy quenches globally (falls 1dex below the main star forming sequence) shortly after pericentre. They also show that RPS can take a long time to fully remove the cold gas (ranging from 1 - 7 Gyrs), but that the majority of mass is lost during a short peak of RPS during the first infall which begins $\lesssim$ 1Gyr after infall and lasts $\lesssim$ 2 Gyr. While this considers complete gas loss and global quenching (the authors also note that galaxies continue forming stars until 99% of the cold gas content is lost), it suggests timescales similar to those probed by the PSB selections. Similarly, Oman et al. (2021) considers quenching timescales from infall into a cluster for simulated galaxies. In this case, they look at the H I gas content and find that H I is typically removed from a galaxy by the first pericentre, which is followed a few Gyr later by the disappearance of the Balmer lines, and then less than 1Gyr after this the galaxy begins to redden due to quenching. As the PSB selections rely on the Balmer lines, this may be the process we are seeing. Our observations of jellyfish galaxies which are implied to be moving out of the cluster by their tail directions may contradict these simulated findings – though we note these refer to cold gas content, while our LoTSS detections are from cosmic ray electrons. Following up these galaxies using resolved cold gas observations (for example with Apertif or SKA) would be illuminating in order to compare to these simulations.

In Oman et al. (2013), the authors use simulated orbits in clusters in order to correlate the infall time of a galaxy to the projected phase space coordinates. Their results are shown

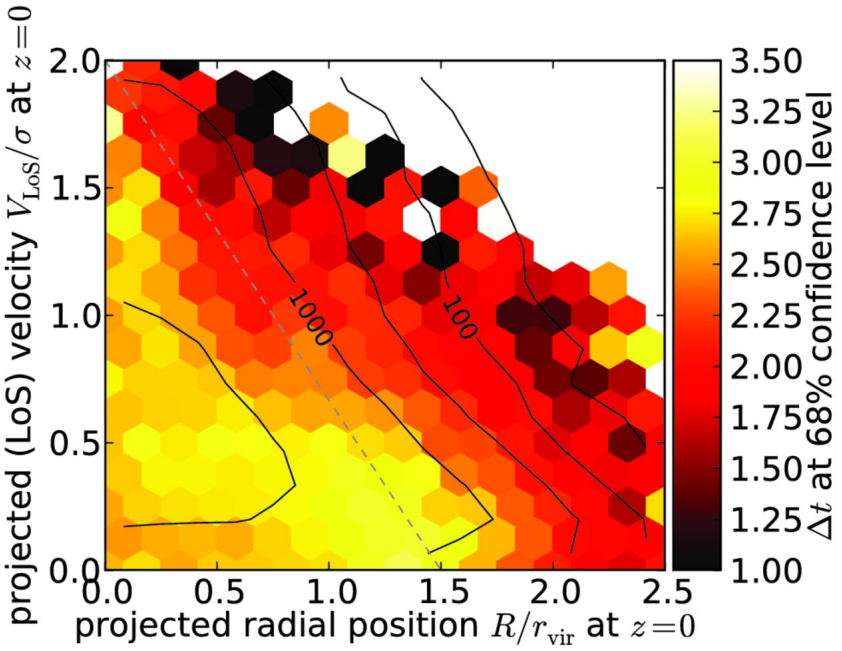

Figure 5.33: Reproduced from Oman et al. (2013). Distribution of time since infall (colours) within 68% confidence level within the projected phase space at z=0, for simulated galaxies. This demonstrates the potential for linking projected phase space values to infall times.

in Figure 5.33. As seen in Figure 5.22, our sample is found entirely at distances less than 1 virial radius, and with line of sight velocities spanning all the way from zero to 3 times the cluster velocity dispersion, with a high concentration of our classification 2 PSB galaxies found below 1. In this region of Figure 5.33, we expect time since initial infall to be higher than in other regions. Correlating the effects seen in simulations for global quenching with the effects seen in spatially resolved data is not straightforward, however this could suggest that we are seeing galaxies at the peak of the RPS mass loss, and just before a global quenching signature is detected in the simulated galaxies – i.e. we are seeing current quenching ongoing in these galaxies.

Pulling all of these findings together, we propose we are seeing current ongoing quenching on the leading edges of galaxies infalling into clusters and experiencing RPS. Our gas kinematic data indicates this is due to heating and disruption of the gas in these frontal regions, and removal of cold gas from the systems. We propose that this signal will propagate progressively along the axis from the centre towards the leading edge, beginning with a wave of enhanced star formation due to gas being compressed, before being quenched. In order to properly explore this, our future work will involve producing resolved stellar formation history maps in arced bins at increasing radii towards the leading edge. If our hypothesis is correct, we would

see a progressively longer ago quenching time as we moved inside-out. These quenching timescales can also be compared to projected phase space predictions of the time since infall, to see if these values show a tight correlation. While MaNGA has offered excellent data for many science cases, the spatial resolution of the bins combined with the PSF means that it is not possible to achieve the SNR required to perform this analysis. The MUSE instrument has produced high resolution IFU data for jellyfish galaxies as part of the GASP survey, and some resolved SFH maps have been produced for jellyfish galaxies, however these have not focused on the PSB features of these galaxies at the leading edge. Offering higher SNR and deeper observations, we hope that the WEAVE instrument will allow this analysis to be completed for a large sample of jellyfish galaxies. Further aiding in this area of research, the continuation of LoTSS will hopefully identify many more jellyfish candidates which can be targeted for IFU followup with WEAVE, while further in the future the SKA and Apertif surveys will enable us to examine vast numbers of galaxies to search for jellyfish signatures in resolved cold gas. This will also illuminate the disruption to the gas component more directly, and allow more detailed study of the cold gas content across samples.

5.5 Summary

In this Chapter I have described the study of a sample of jellyfish galaxies which have been identified through the LoTSS survey and observed by the MaNGA survey. In the widest scope, this research shows again the importance of synergy between different astronomical surveys and the value of multiwavelength programmes to study the processes of galactic evolution. The use of low frequency data allowed the identification of the RPS signatures in these galaxies and the inference of their direction of motion; the optical IFU observations from MaNGA allowed the PSB signatures on the leading edges to be found, the stellar populations to be examined, and the kinematics of both the stars and gas to be tied to the PSB regions; and the HI -MaNGA 21cm data allowed the cold gas content to be explored. This also pulled information from X-Ray catalogues and cluster observations which underpin quantities which were published in the Roberts et al. (2022) paper. Using these data, I have shown that the PSB regions are preferentially on the leading edge of jellyfish galaxies which are near the centre of their cluster and moving towards it, and are found beside regions of enhanced star formation (attributed to gas compression by ram pressure, as found in Roberts et al., 2021). There are indications that cold gas content is lower in those galaxies which show the aligned PSB

regions, though this is inconclusive due to the small sample size. Further, we propose a time evolution scenario spatially across these galaxies, quenching from the leading edge in (with an arc of enhanced star formation preceding this where the gas is compressed) which cannot be ruled out or confirmed by the data we currently have. We have outlined our hopes for future work towards testing this theory using upcoming facilities which will offer greater samples of jellyfish galaxies with deeper complimentary IFU observations to allow resolved SFHs to be produced in order to compare with infall timescales.

6

Summary and Future Work

Suggested listening: Thank You for the Music by ABBA

This thesis has charted my work, which has sought to use observations and modelling to

Chapter image: Arp-Madore 417-391 captured by Hubble, ESA/Hubble/NASA/NOIRLab/NSF/AURA/J Dalcanton

better understand galaxies, their structure, and their evolution. Galaxies are tumultuous and violent environments, despite appearing placid from where we observe them. They are, in an instant, moving at great speeds internally, while also undergoing massive global changes in their internal processes and appearance over their lifetimes. This overarching theme is woven through the Chapters of this work, which has considered this from multiple angles, and aimed to advance our knowledge of galaxies using the state-of-the-art observations available to us at this time. The work has also advanced the modelling techniques available to us, and acted as a proof of concept for the incredible work which will become feasible with the next generation of observatories. Here I summarise the work that I have done, and discuss how this work can be built upon in the future with the data soon to be available from new facilities.

6.1 JAM Modelling for Red Geysers

In Chapter 3, I introduced dynamical modelling and showcased its power in measuring physical properties of galaxies which are not easily obtained through using imaging alone. This was done through using Jeans models to advance our science case for the direct observation of large scale nuclear outflows in the red geyser population of galaxies. Important to galaxy evolution, there have been limited observations which have shown evidence for the outflows which are hypothesised to be required to keep galaxies quenched. In the red geyser population, the gas kinematics and ionisation we observe are proposed to be signatures of large scale outflows. In order to discern between this model and the alternative one of a rotating gas disk, Roy et al. (2021) used detailed spectroscopic observations to measure the changing shape of emission lines along the axis of these galaxies. These were then compared to the expected shapes from models of outflows or models of disks.

To create the predicted models, we required a measurement of the inclination of the galaxy with respect to the observer. As red geysers are predominantly elliptical galaxies, the inclination is difficult to constrain through imaging alone, and so I created dynamical models to measure this accurately using kinematic observations. These dynamical models used only stellar kinematics from the inner regions and lacked a dark matter component, however are able to constrain the inclination for these purposes.

Comparing the models to the observations, the results supported the hypothesis that the observations are the result of an outflow from the nuclear regions, helping to add to evidence

for this phenomenon.

6.2 JAM Modelling for Dark Matter Content

In Chapter 4, I expanded upon the modelling methods used in the previous Chapter by turning the focus to the dark matter component of galaxies. I developed a novel modelling method which extended the Jeans Modelling used in the previous Chapter, through the addition of cold H I gas observations.

First, I once more created models for the galaxies without including dark matter. While these are able to reproduce the observations in the inner regions, I wanted to assess how well they reproduced kinematics in the outer regions where dark matter is most dominant. To do this, I took advantage of data from the H I -MaNGA survey, which provided single dish H I observations of galaxies which already had IFS observations in MaNGA. Single dish observations lack spatial resolution, however contain kinematic information about the rotational velocity of the cold gas in the outer regions. Using this, I was able to compare the models without dark matter to the observations, and in doing so confirmed that the models are unable to reproduce observations with the luminous component alone. This result emphasises that galaxies must contain another matter component which we cannot detect directly.

Following from this, I added dark matter haloes into the models and constrained the content first using just the IFS data from the stellar kinematics, and then the additional constraint of the H I kinematics. I found that the dark matter halo cannot be well constrained by the stellar data alone, but by adding the H I kinematics to the likelihood of the model the halo parameters are constrained and allow measurement of the halo mass and concentration.

One key benefit of using single dish H I observations is that these are available for a significant sample of galaxies, and so this method is applicable to a large sample. As a proof of concept, I applied this method to a sample of galaxies and constrained the dark matter content. I then compared these measurements to values in the literature, and found that we qualitatively reproduce the values, but require a larger sample in order to compare fully.

In summary, this Chapter confirmed that dark matter is required in dynamical models, and highlighted the necessity of combining single dish cold gas observations with IFS data in order to properly constrain the dark matter content for a statistically significant sample. This proof-of-concept is an important precursor to highlight future work that will be possible as our

sample of galaxies which have both IFS and cold gas observations expands.

6.3 Exploring Quenching in Jellyfish Galaxies

In Chapter 5, I shifted my work to look at the more long term evolution of galaxies and their stellar component, and explore what we can learn about this from jellyfish galaxies – galaxies undergoing extreme environmental effects from infalling through dense medium in a cluster. This project again highlighted the value in combining many types of observations, as identifying jellyfish galaxies requires detection of diffuse material in their tails (whether directly through cold gas observations, or through cosmic ray electron synchrotron emission in this case), while understanding their stellar populations requires optical observations.

This work expanded upon the study of a sample of jellyfish galaxies identified by their tails in the LOFAR survey, which also had IFS observations in the MaNGA survey. The synergy between these observations alongside cluster information, and even H I -MaNGA 21cm observations allowed a holistic look at the effects of their extreme environments on their evolution.

Resolved spectral analysis of these galaxies allowed regions on the leading edge to be discovered which exhibit the signatures of post-starburst (PSB) regions, implying that they have recently quenched following a burst of star formation. Using the combination of IFS data, phase space information, and 21cm gas observations, I presented evidence which proposes this signature is due to ram pressure stripping first compressing the gas on the leading edge (causing a starburst), before removing the gas and causing fast quenching.

The results supported this concept, however a final analysis which would confirm this through resolved stellar formation histories is not possible with the MaNGA data, and I explained our plans to enact this analysis in the future.

6.4 Future Work

Here I would like to discuss my views for how the field will advance in the near future, building upon the work done in this thesis. As noted at the end of each Chapter, there is scope for future work related to each of these projects. The first, concerning outflows in red geysers, would involve further dynamical modelling in order to measure the escape velocities of these galaxies and determine if the gas we see is gravitationally bound. More widely, the red geyser population has continued to be studied through many wavelengths and again highlights the

essential need to observe and analyse astrophysical phenomena across the full spectrum of observations available. As these objects deal with nuclear activity, the combination of radio observations with stellar observations is critical.

This theme is carried on in the other projects in this work. Chapter 4 highlighted the benefits of including cold gas observations in dynamical models in order to measure dark matter properties. With the H I -MaNGA survey in the north providing a large sample of galaxies with both IFS and single dish hydrogen kinematics, along with the SAMI-H I survey providing the same synergy in the south, this is soon to provide an extremely rich dataset for this method to be applied widely, and developed further. Further ahead, WEAVE-Apertif will provide this synergy with higher signal to noise IFS observations, and the benefit of resolved H I observations. This will allow more advanced modelling methods which take advantage of fully resolved H I kinematics to be applied to a significant sample and further this field. This also sets the scene for the rich dataset which will be provided when the Square Kilometer Array (SKA) comes online, vastly expanding the number of galaxies observed with resolved H I , offering many more targets for IFU surveys to observe to achieve this synergy.

Similar to the field of dynamical modelling and dark matter mass studies, the study of stellar populations within jellyfish galaxies also requires the same synergy of IFS data and some observation which traces the tails. Here resolved 21cm observations also offer a massive benefit. Being able to identify more galaxies through the observation of tails of neutral hydrogen in wide field 21cm imaging will offer a massive increase in jellyfish galaxies identified when these observatories come online. This will also be added to by the full completion of the LoTSS survey, adding more jellyfish identified by cosmic ray electron synchrotron emission. Through the increased resolution and sensitivity offered by Apertif and SKA, we will be able to identify jellyfish undergoing more subtle environmental effects and begin to expand the RPS regime to include less extreme cases. This will then again benefit from the followup of IFS surveys to study and understand the effects on the stellar populations in the galaxies in a resolved manner. WEAVE-Apertif will be able to be exploited towards this scientific end. For even more detailed IFS observations, the candidates already identified and studied in this paper would benefit from deeper IFS data in order to perform resolved stellar formation history fitting on the spectra. This could be offered by WEAVE or by a potential followup using MUSE for any galaxies which are far enough south. By mosaicing MUSE pointings across the whole galaxy, similar to that being done for edge on galaxies in the GECKOS survey (van de Sande et al.,

2023), the SNR and spatial resolution required to study the SFHs of the stars in the leading edge would be available.

As discussed above, the future for astronomy must exploit the synergy between surveys in order to maximise the scientific ground we can cover. We are on the edge of the next generation of telescopes, and survey design should work to create this synergy wherever possible. Galaxies are complex systems made up of many different components. They contain some of the densest environments in the universe, emitting in high frequencies; while also relying upon vast reservoirs of diffuse cold gas which are observable in low frequencies. This vast range of emission, and the interconnectedness of the processes involved at all scales, necessitates the multiwavelength nature of the observation and study of these objects. Alongside multiwavelength observation, we must also develop and expand our modelling techniques in order to take advantage of the information available in all kinds of data – for dynamical modelling, and modelling of any sort. Galactic astronomy remains a ripe field, and will continue to be for a long time into the future. Our steps forward in these areas will address outstanding questions in our understanding for the Universe, for example the nature of dark matter and the cusp-core problem.

Finally, on a personal note, a lot of astronomical work discusses galaxies as distant and abstract objects, and often neglects the awe found in truly acknowledging that we are a part of our own galaxy, and a product of its own evolution. I strive to maintain this perspective in all the work I do, and hope the field continues this more widely.

A

Index Zero Jellyfish Galaxies

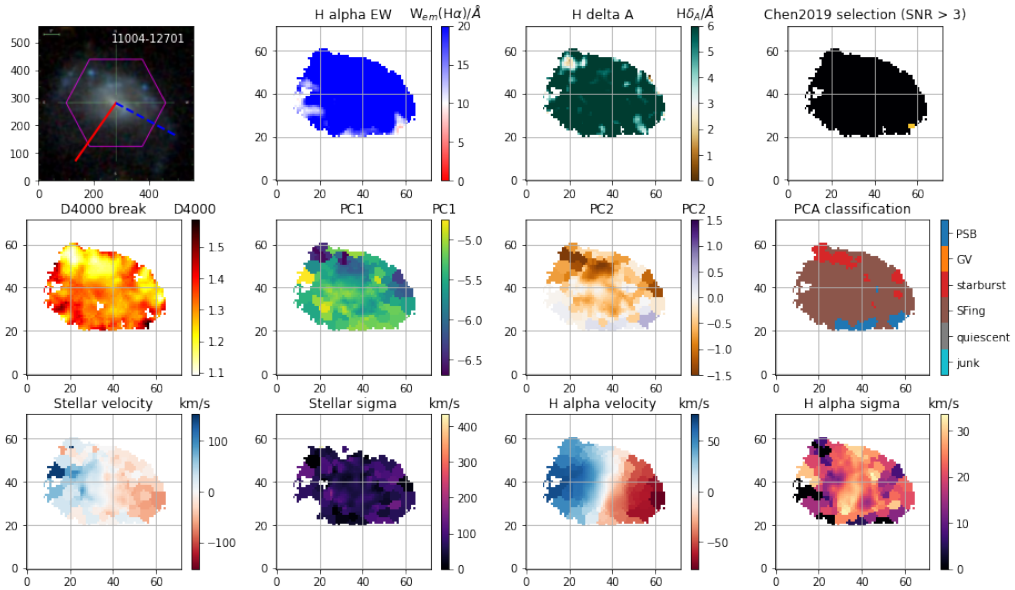

Figure A.1: Summary of observations for 11004-12701, classified with index 0. Panels described in text.

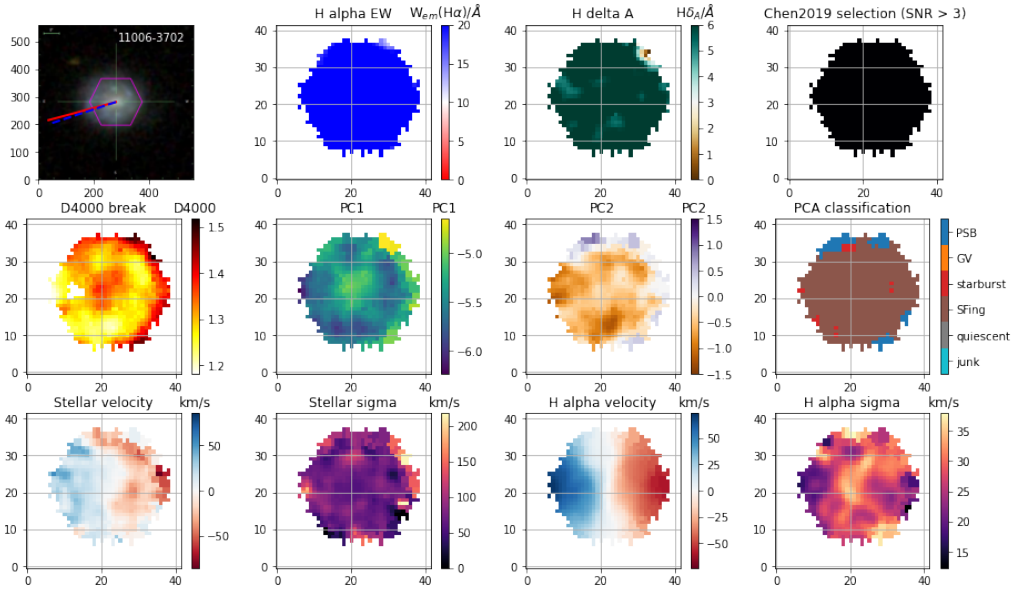

Figure A.2: Summary of observations for 11006-3702, classified with index 0. Panels described in text.

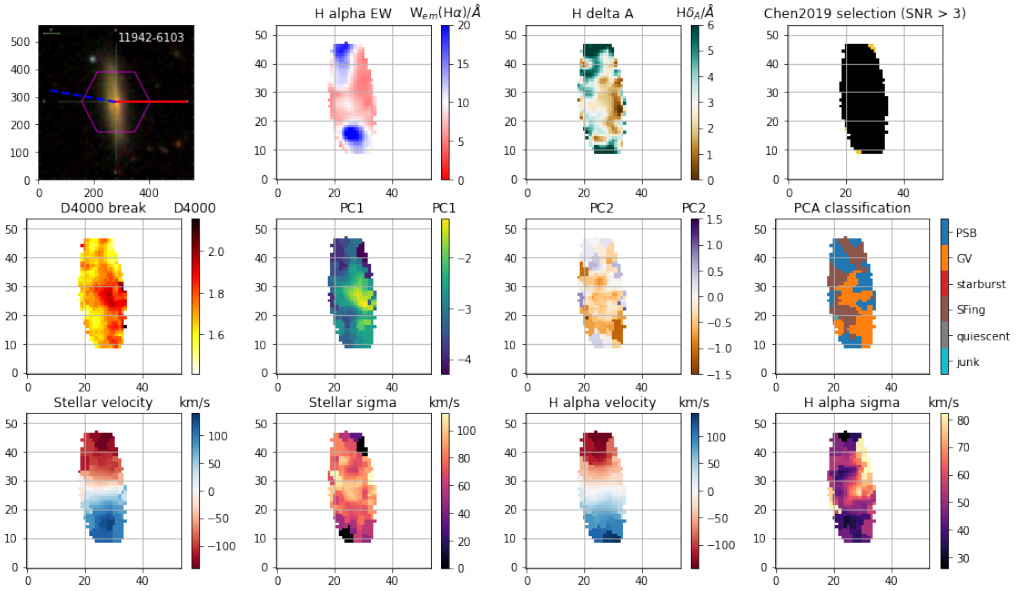

Figure A.3: Summary of observations for 11942-6103, classified with index 0. Panels described in text.

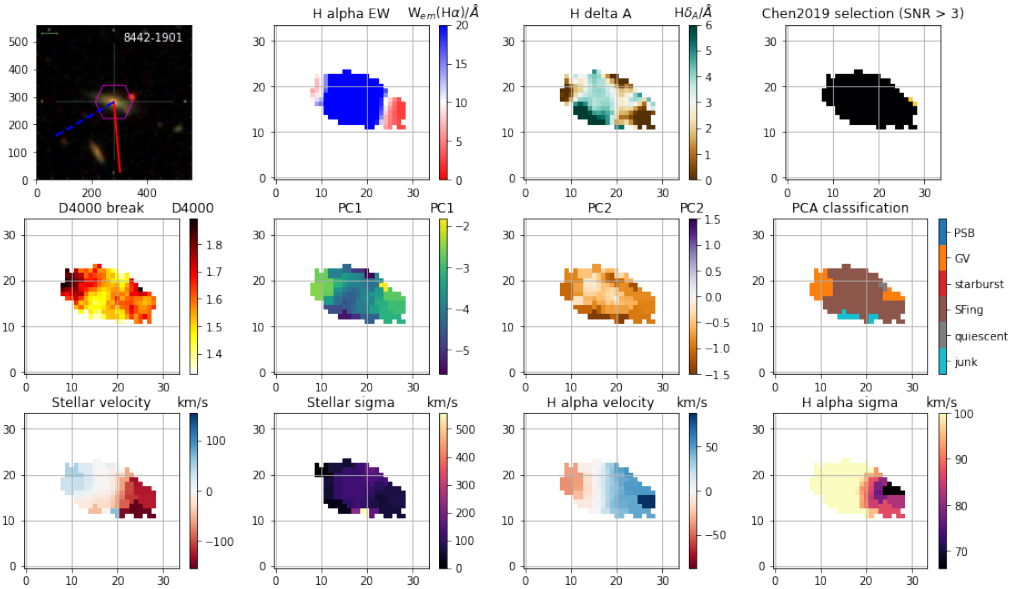

Figure A.4: Summary of observations for 8442-1901, classified with index 0. Panels described in text.

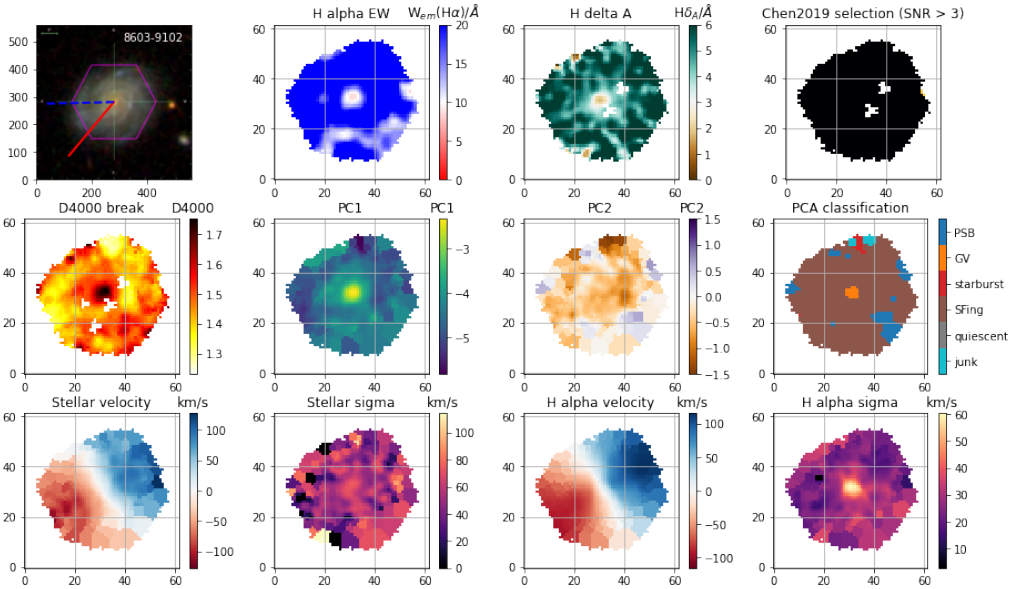

Figure A.5: Summary of observations for 8603-9102, classified with index 0. Panels described in text.

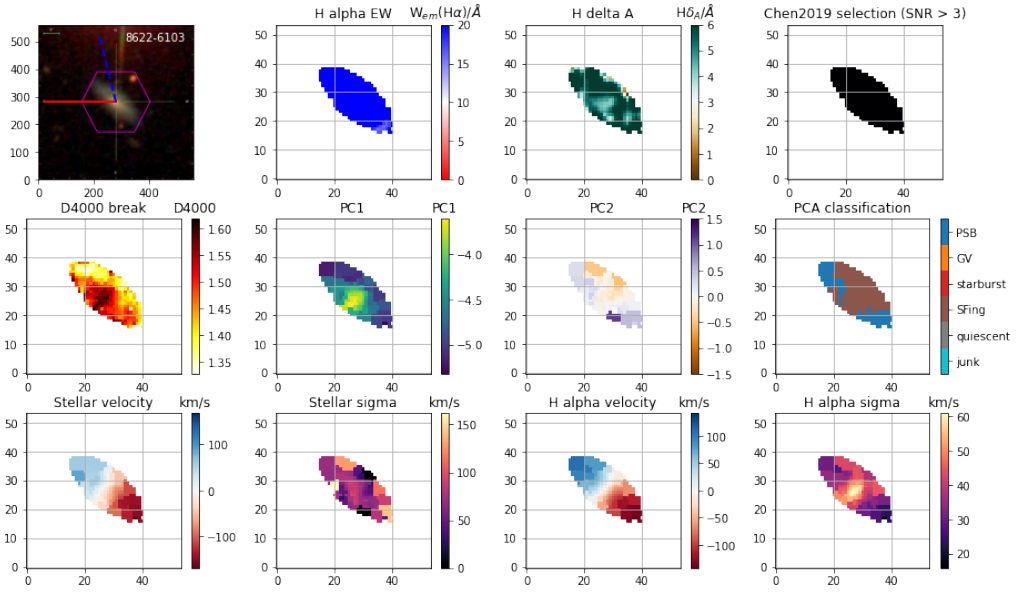

Figure A.6: Summary of observations for 8622-6103, classified with index 0. Panels described in text.

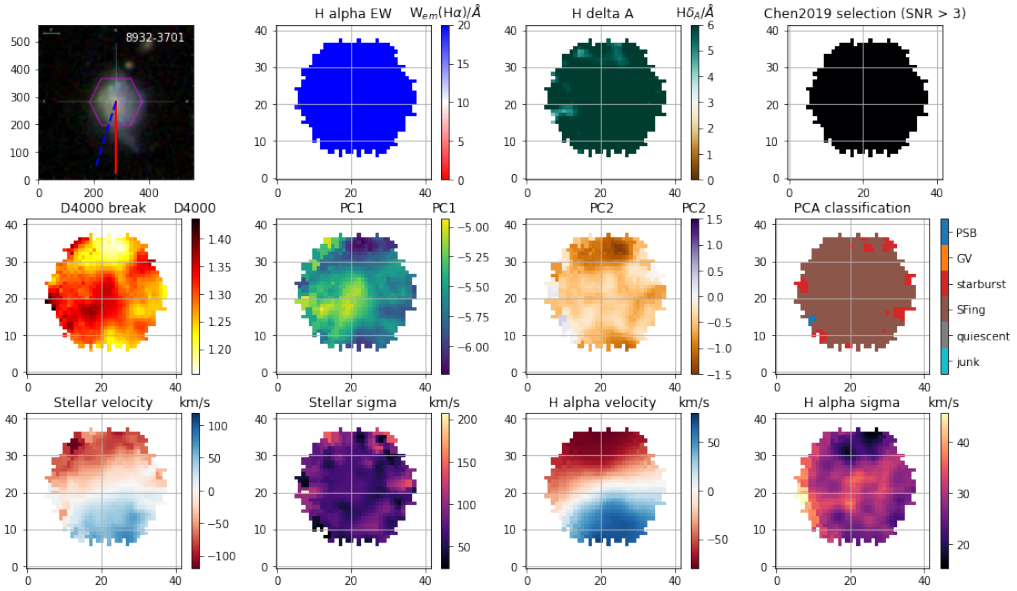

Figure A.7: Summary of observations for 8932-3701, classified with index 0. Panels described in text.

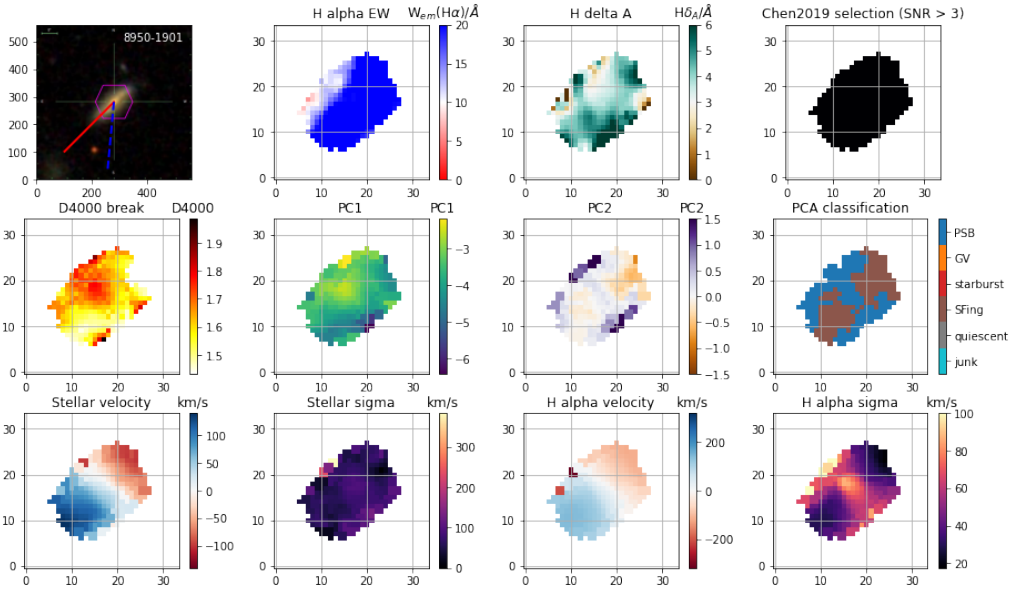

Figure A.8: Summary of observations for 8950-1901, classified with index 0. Panels described in text.

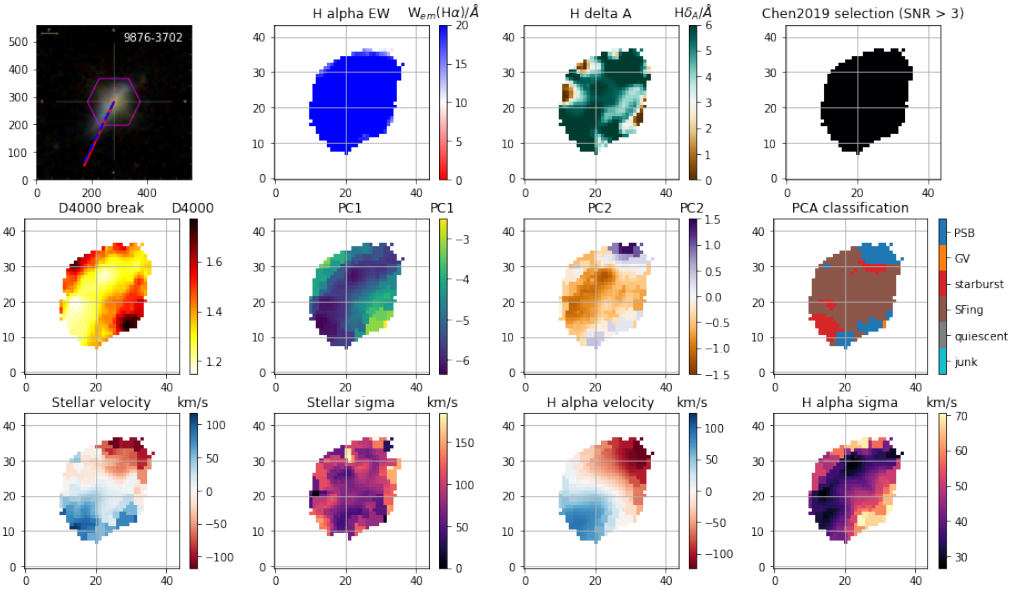

Figure A.9: Summary of observations for 9876-3702, classified with index 0. Panels described in text.

Bibliography

Abazajian, K. N. et al. 2009, ApJS, 182, 543, 0812.0649

Abdurro'uf et al. 2022, ApJS, 259, 35, 2112.02026

Ade, P. A. R. et al. 2016, Astronomy & Astrophysics, 594, A13

Aghamousa, A. et al. 2016, The DESI Experiment Part I: Science,Targeting, and Survey Design, 1611.00036

Allen, J. T. et al. 2015, MNRAS, 451, 2780, 1505.03872

Andernach, H. 2017, English and Spanish Translation of Zwicky's (1933) The Redshift of Extragalactic Nebulae, 1711.01693

Aragon Calvo, M. A., Neyrinck, M. C., & Silk, J. 2019, The Open Journal of Astrophysics, 2, 7, 1607.07881

Argudo-Fernández, M. et al. 2015, A&A, 578, A110, 1504.00117

Bacon, R., Accardo, M., Adjali, L., Anwand, H., Bauer, S., Biswas, I., & Blaizot, J. 2010, in Society of Photo-Optical Instrumentation Engineers (SPIE) Conference Series, Vol. 7735, Ground-based and Airborne Instrumentation for Astronomy III, ed. I. S. McLean, S. K. Ramsay, & H. Takami, 773508, 2211.16795

Bartolini, C. et al. 2022, ApJ, 936, 74, 2208.01425

Beccari, G., & Carraro, G. 2015, in Astrophysics and Space Science Library, Vol. 413, Astrophysics and Space Science Library, ed. H. M. J. Boffin, G. Carraro, & G. Beccari, 1, 1406.3462

Beckman, J. E., Zurita, A., & Vega Beltrán, J. C. 2004, in Lecture Notes and Essays in Astrophysics, ed. A. Ulla & M. Manteiga, Vol. 1, 43–62

Bellhouse, C. et al. 2022, ApJ, 937, 18, 2208.10524

Benson, A. J., Bower, R. G., Frenk, C. S., Lacey, C. G., Baugh, C. M., & Cole, S. 2003, ApJ, 599, 38, astro-ph/0302450

Bialas, D., Lisker, T., Olczak, C., Spurzem, R., & Kotulla, R. 2015, A&A, 576, A103, 1503.01965

Bigiel, F., & Blitz, L. 2012, ApJ, 756, 183, 1208.1505

Binette, L., Magris, C. G., Stasińska, G., & Bruzual, A. G. 1994, A&A, 292, 13

Binney, J., & Tremaine, S. 2008, Galactic Dynamics: Second Edition

Blanc, G. A. et al. 2010, in Astronomical Society of the Pacific Conference Series, Vol. 432, New Horizons in Astronomy: Frank N. Bash Symposium 2009, ed. L. M. Stanford, J. D. Green, L. Hao, & Y. Mao, 180, 1001.5035

Bland-Hawthorn, J. 1997, ApJ, 490, 143–155

Blanton, M. R. et al. 2017, AJ, 154, 28, 1703.00052

Blumenthal, G. R., Pagels, H., & Primack, J. R. 1982, Nature, 299, 37

Bodenheimer, P. 2003, in Encyclopedia of Physical Science and Technology (Third Edition), third edition edn., ed. R. A. Meyers (New York: Academic Press), 45–78

Boomsma, R., Oosterloo, T. A., Fraternali, F., van der Hulst, J. M., & Sancisi, R. 2008, A&A, 490, 555, 0807.3339

Boselli, A. et al. 2021, A&A, 646, A139, 2012.07377

Bourne, M. A., Nayakshin, S., & Hobbs, A. 2014, MNRAS, 441, 3055, 1405.5647

Bradt, H. 2004, Astronomy Methods: A Physical Approach to Astronomical Observations

Brammer, G. B. et al. 2009, ApJL, 706, L173, 0910.2227

Broeils, A. H., & Rhee, M. H. 1997, A&A, 324, 877

Bryant, J. J. et al. 2015, MNRAS, 447, 2857, 1407.7335

Bull, P. et al. 2016, Physics of the Dark Universe, 12, 56, 1512.05356

Bundy, K. et al. 2015, ApJ, 798, 7, 1412.1482

——. 2006, ApJ, 651, 120, astro-ph/0512465

Cappellari, M. 2002, MNRAS, 333, 400, astro-ph/0201430

——. 2008, MNRAS, 390, 71, 0806.0042

Cappellari, M. 2015, in IAU Symposium, Vol. 311, Galaxy Masses as Constraints of Formation Models, ed. M. Cappellari & S. Courteau, 20–30, 1410.7329

——. 2017, MNRAS, 466, 798, 1607.08538

Cappellari, M., & Copin, Y. 2003, MNRAS, 342, 345, astro-ph/0302262

Cappellari, M., & Emsellem, E. 2004, PASP, 116, 138, astro-ph/0312201

Cappellari, M. et al. 2007, MNRAS, 379, 418, astro-ph/0703533

——. 2011, MNRAS, 413, 813, 1012.1551

——. 2013, MNRAS, 432, 1709, 1208.3522

Carolina Sparavigna, A. 2013, International Journal of Sciences, -1, 52–60

Catinella, B. et al. 2023, MNRAS, 519, 1098, 2212.04728

——. 2018, MNRAS, 476, 875, 1802.02373

Chambers, K. C. et al. 2016, arXiv e-prints, arXiv:1612.05560, 1612.05560

Chandar, R., Mok, A., French, K. D., Smercina, A., & Smith, J.-D. T. 2021, ApJ, 920, 105, 2106.14883

Chen, Y.-C. et al. 2017, MNRAS, 466, 1880, 1509.06376

Chen, Y.-M. et al. 2019a, MNRAS, 489, 5709, 1909.01658

——. 2019b, MNRAS, 489, 5709, 1909.01658

Cheung, E. et al. 2016, Nature, 533, 504, 1605.07626

Ciotti, L., & Ostriker, J. P. 1997, ApJ, 487, L105, astro-ph/9706281

Clarke, P. A. 2016, Journal of Ethnobiology, 36, 277, https://doi.org/10.2993/0278-0771-36.2.277

Coenda, V., Martínez, H. J., & Muriel, H. 2018, MNRAS, 473, 5617, 1710.05928

Condon, J. J. 1992, ARA&A, 30, 575

Conroy, C. 2013, ARA&A, 51, 393, 1301.7095

Conroy, C., van Dokkum, P. G., & Kravtsov, A. 2015, ApJ, 803, 77, 1406.3026

Conselice, C. J., Wilkinson, A., Duncan, K., & Mortlock, A. 2016, The Astrophysical Journal, 830, 83

Cramer, W. J., Kenney, J. D. P., Sun, M., Crowl, H., Yagi, M., Jáchym, P., Roediger, E., & Waldron, W. 2019, ApJ, 870, 63, 1811.04916

Cuillandre, J.-C. J. et al. 2012, in Society of Photo-Optical Instrumentation Engineers (SPIE) Conference Series, Vol. 8448, Observatory Operations: Strategies, Processes, and Systems IV, ed. A. B. Peck, R. L. Seaman, & F. Comeron, 84480M

Danezis, E., Theodossiou, E., Dimitrijević, M. S., Dacanalis, A., & Katsavrias, C. 2010, Bulgarian Astronomical Journal, 13, 140

Darvish, B., Sobral, D., Mobasher, B., Scoville, N. Z., Best, P., Sales, L. V., & Smail, I. 2014, ApJ, 796, 51, 1409.7695

Davis, M., Efstathiou, G., Frenk, C. S., & White, S. D. M. 1985, ApJ, 292, 371

de Blok, W. J. G. 2010, Advances in Astronomy, 2010, 1–14

de Lapparent, V., Geller, M. J., & Huchra, J. P. 1986, ApJL, 302, L1

de Zeeuw, P. T. et al. 2002, MNRAS, 329, 513, astro-ph/0109511

Demoulin-Ulrich, M. H., Butcher, H. R., & Boksenberg, A. 1984, ApJ, 285, 527

Dewdney, P. E., Hall, P. J., Schilizzi, R. T., & Lazio, T. J. L. W. 2009, IEEE Proceedings, 97, 1482

Dey, A. et al. 2016, in Society of Photo-Optical Instrumentation Engineers (SPIE) Conference Series, Vol. 9908, Ground-based and Airborne Instrumentation for Astronomy VI, ed. C. J. Evans, L. Simard, & H. Takami, 99082C

Dey, A. et al. 2019, The Astronomical Journal, 157, 168

Diemer, B. 2018, ApJS, 239, 35, 1712.04512

Dressler, A. 1980, ApJ, 236, 351

Dressler, A., & Gunn, J. E. 1983, ApJ, 270, 7

Dressler, A., Oemler, Augustus, J., Poggianti, B. M., Smail, I., Trager, S., Shectman, S. A., Couch, W. J., & Ellis, R. S. 2004, ApJ, 617, 867, astro-ph/0408490

Drory, N. et al. 2015, AJ, 149, 77, 1412.1535

Dubois, Y., Pichon, C., Devriendt, J., Silk, J., Haehnelt, M., Kimm, T., & Slyz, A. 2013, MNRAS, 428, 2885, 1206.5838

Duffy, A. R., Meyer, M. J., Staveley-Smith, L., Bernyk, M., Croton, D. J., Koribalski, B. S., Gerstmann, D., & Westerlund, S. 2012, MNRAS, 426, 3385, 1208.5592

Dutta, R. 2019, Journal of Astrophysics and Astronomy, 40, 41, 1910.06334

Dutta, S., Khandai, N., & Rana, S. 2022, MNRAS, 511, 2585, 2108.03253

Egana-Ugrinovic, D., Essig, R., Gift, D., & LoVerde, M. 2021, J. Cosmology Astropart. Phys., 2021, 013, 2102.06215

Eibensteiner, C. et al. 2023, A&A, 675, A37, 2304.02037

Einasto, J. 1965, Trudy Astrofizicheskogo Instituta Alma-Ata, 5, 87

Einasto, J. 2009, Dark Matter, 0901.0632

Eisenstein, D. J. et al. 2023, arXiv e-prints, arXiv:2306.02465, 2306.02465

Ellison, S. 2019, in Linking Galaxies from the Epoch of Initial Star Formation to Today, 37

Emsellem, E., Monnet, G., & Bacon, R. 1994, AAp, 285, 723

Faber, S. M. et al. 2007, ApJ, 665, 265, astro-ph/0506044

Fabian, A. C. 2012a, ARA&A, 50, 455, 1204.4114

——. 2012b, ARA&A, 50, 455, 1204.4114

Fabian, A. C., Sanders, J. S., Taylor, G. B., Allen, S. W., Crawford, C. S., Johnstone, R. M., & Iwasawa, K. 2006, MNRAS, 366, 417, astro-ph/0510476

Falcón-Barroso, J., Sánchez-Blázquez, P., Vazdekis, A., Ricciardelli, E., Cardiel, N., Cenarro, A. J., Gorgas, J., & Peletier, R. F. 2011, A&A, 532, A95, 1107.2303

Falcón-Barroso, J. et al. 2019, WEAVE-Apertif Survey Plan, Internal

Filipovic, M. D., White, G. L., Jones, P. A., Haynes, R. F., Pietsch, W. N., Wielebinski, R., & Klein, U. 1996, in Astronomical Society of the Pacific Conference Series, Vol. 112, The History of the Milky Way and Its Satellite System, ed. A. Burkert, D. H. Hartmann, & S. A. Majewski, 91

Flaugher, B. et al. 2015, AJ, 150, 150, 1504.02900

Foreman-Mackey, D., Hogg, D. W., Lang, D., & Goodman, J. 2013, PASP, 125, 306, 1202.3665

Franx, M., van Gorkom, J. H., & de Zeeuw, T. 1994, ApJ, 436, 642

French, K. D. 2021, PASP, 133, 072001, 2106.05982

Frenk, C. S., & White, S. D. M. 2012, Annalen der Physik, 524, 507, 1210.0544

Gabor, J. M., Davé, R., Finlator, K., & Oppenheimer, B. D. 2010, MNRAS, 407, 749, 1001.1734

Gadotti, D. A. 2009, in Astrophysics and Space Science Proceedings, Vol. 8, Chaos in Astronomy, 159, 0802.0495

Gadotti, D. A. 2011, MNRAS, 415, 3308, 1003.1719

Gao, L., Navarro, J. F., Cole, S., Frenk, C. S., White, S. D. M., Springel, V., Jenkins, A., & Neto, A. F. 2008a, MNRAS, 387, 536, 0711.0746

——. 2008b, MNRAS, 387, 536, 0711.0746

Gavazzi, G., Boselli, A., Mayer, L., Iglesias-Paramo, J., Vílchez, J. M., & Carrasco, L. 2001, ApJ, 563, L23, astro-ph/0111085

George, K. et al. 2018, MNRAS, 479, 4126, 1803.06193

Giovanelli, R., & Haynes, M. P. 1988, in Galactic and Extragalactic Radio Astronomy, ed. K. I. Kellermann & G. L. Verschuur, 522–562

Giovanelli, R., Haynes, M. P., Herter, T., Vogt, N. P., Wegner, G., Salzer, J. J., da Costa, L. N., & Freudling, W. 1997, AJ, 113, 22, astro-ph/9610117

Girelli, G., Pozzetti, L., Bolzonella, M., Giocoli, C., Marulli, F., & Baldi, M. 2020, A&A, 634, A135, 2001.02230

Giunchi, E. et al. 2023, ApJ, 949, 72, 2302.10615

Gomes, J. M. et al. 2016, A&A, 588, A68, 1511.02191

Goodman, J., & Weare, J. 2010, Communications in Applied Mathematics and Computational Science, 5, 65

Grossi, M. et al. 2009, A&A, 498, 407–417

Gullieuszik, M. et al. 2023, ApJ, 945, 54, 2301.08279

Gunn, J. E. et al. 2006, AJ, 131, 2332, astro-ph/0602326

Hafez, I., Stephenson, R., & Orchiston, W. 2011, Abdul-Rahman al-Sufi and his Book of the Fixed Stars, 121–138

Hahn, C. et al. 2023, AJ, 165, 253, 2208.08512

Hamacher, D. W. 2018, The Australian Journal of Anthropology, 29, 89, https://onlinelibrary.wiley.com/doi/pdf/10.1111/taja.12257

Haynes, M. P. et al. 2018, ApJ, 861, 49, 1805.11499

——. 2011, AJ, 142, 170, 1109.0027

Haynes, M. P., Hogg, D. E., Maddalena, R. J., Roberts, M. S., & van Zee, L. 1998, AJ, 115, 62

Heckman, T. M., & Best, P. N. 2014, ARA&A, 52, 589, 1403.4620

Hensler, G. 2014, in Supernova Environmental Impacts, ed. A. Ray & R. A. McCray, Vol. 296, 265–272, 1402.0117

Hess, K. M., Kotulla, R., Chen, H., Carignan, C., Gallagher, J. S., Jarrett, T. H., & Kraan-Korteweg, R. C. 2022, A&A, 668, A184, 2209.05605

Hubble, E. P. 1926, ApJ, 64, 321

Huchra, J., Davis, M., Latham, D., & Tonry, J. 1983, ApJS, 52, 89

Huchra, J. P., & Geller, M. J. 1991, in Astronomical Society of the Pacific Conference Series, Vol. 15, Large-scale Structures and Peculiar Motions in the Universe, ed. D. W. Latham & L. A. N. da Costa, 143

Hunt, J. A. S., Bovy, J., & Carlberg, R. G. 2016, ApJ, 832, L25, 1610.02030

Ilbert, O. et al. 2010, ApJ, 709, 644, 0903.0102

Iwanus, N., Elahi, P. J., & Lewis, G. F. 2017, MNRAS, 472, 1214, 1707.06770

Jáchym, P. et al. 2019, ApJ, 883, 145, 1905.13249

Jaffé, Y. L., Smith, R., Candlish, G. N., Poggianti, B. M., Sheen, Y.-K., & Verheijen, M. A. W. 2015, MNRAS, 448, 1715, 1501.03819

Jeans, J. H. 1915, MNRAS, 76, 70

——. 1922, MNRAS, 82, 122

Jeffreys, H. 1939, Theory of Probability

Jin, S.-W., Gu, Q., Huang, S., Shi, Y., & Feng, L.-L. 2014, ApJ, 787, 63, 1404.2398

Jonas, J., & MeerKAT Team. 2016, in MeerKAT Science: On the Pathway to the SKA, 1

Kalinova, V., van de Ven, G., Lyubenova, M., Falcón-Barroso, J., Colombo, D., & Rosolowsky, E. 2017, MNRAS, 464, 1903, 1609.08700

Kapteyn, J. C. 1922, ApJ, 55, 302

Kauffmann, G., Heckman, T. M., De Lucia, G., Brinchmann, J., Charlot, S., Tremonti, C., White, S. D. M., & Brinkmann, J. 2006, MNRAS, 367, 1394, astro-ph/0510405

Kaviraj, S., Kirkby, L. A., Silk, J., & Sarzi, M. 2007, MNRAS, 382, 960, 0707.3570

Kehrig, C. et al. 2012, A&A, 540, A11, 1202.0511

Kelkar, K., Gray, M. E., Aragón-Salamanca, A., Rudnick, G., Milvang-Jensen, B., Jablonka, P., & Schrabback, T. 2017, MNRAS, 469, 4551, 1705.03402

Kenney, J. D. P., & Koopmann, R. A. 1999, AJ, 117, 181, astro-ph/9812363

Klypin, A., Kravtsov, A. V., Valenzuela, O., & Prada, F. 1999, The Astrophysical Journal, 522, 82–92

Klypin, A. A., Trujillo-Gomez, S., & Primack, J. 2011, ApJ, 740, 102, 1002.3660

Koribalski, B. S. et al. 2020, Ap&SS, 365, 118, 2002.07311

Kormendy, J. 2013, in Secular Evolution of Galaxies, ed. J. Falcón-Barroso & J. H. Knapen, 1

Kormendy, J. 2016, in Astrophysics and Space Science Library, Vol. 418, Galactic Bulges, ed. E. Laurikainen, R. Peletier, & D. Gadotti, 431, 1504.03330

Kormendy, J., & Ho, L. C. 2013, ARA&A, 51, 511, 1304.7762

Kraljic, K. et al. 2018, MNRAS, 474, 547, 1710.02676

Kravtsov, A. V. 2013, ApJ, 764, L31, 1212.2980

Kunitzsch, P. 1987, The Messenger, 49, 42

Lagos, C. d. P., Padilla, N. D., Davis, T. A., Lacey, C. G., Baugh, C. M., Gonzalez-Perez, V., Zwaan, M. A., & Contreras, S. 2015, MNRAS, 448, 1271, 1410.5437

Laine, S., & Gottesman, S. T. 1998, MNRAS, 297, 1041

Lambas, D. G., Alonso, S., Mesa, V., & O'Mill, A. L. 2012, A&A, 539, A45, 1111.2291

Larson, R. B. 2003, in Astronomical Society of the Pacific Conference Series, Vol. 287, Galactic Star Formation Across the Stellar Mass Spectrum, ed. J. M. De Buizer & N. S. van der Bliek, 65–80, astro-ph/0205466

Le Borgne, D. et al. 2006, ApJ, 642, 48, astro-ph/0503401

Lee, J., Kimm, T., Katz, H., Rosdahl, J., Devriendt, J., & Slyz, A. 2020, ApJ, 905, 31, 2010.11028

Lee, Y., Kim, S., Rey, S.-C., & Chung, J. 2021, ApJ, 906, 68, 2011.11169

Legrand, L. et al. 2019, MNRAS, 486, 5468, 1810.10557

Levin, B. W., Sasorova, E. V., Steblov, G. M., Domanski, A. V., Prytkov, A. S., & Tsyba, E. N. 2017, Geodesy and Geodynamics, 8, 206

Li, H. et al. 2017, ApJ, 838, 77, 1703.04894

Li, W. et al. 2023, MNRAS, 523, 720, 2305.07474

Lund, J. M., & Dixon, R. S. 1973, PASP, 85, 230

Maraston, C. 2013, in The Intriguing Life of Massive Galaxies, ed. D. Thomas, A. Pasquali, & I. Ferreras, Vol. 295, 272–281

Martinsson, T. P. K., Verheijen, M. A. W., Westfall, K. B., Bershady, M. A., Andersen, D. R., & Swaters, R. A. 2013, A&A, 557, A131, 1308.0336

Masters, K. L., Crook, A., Hong, T., Jarrett, T. H., Koribalski, B. S., Macri, L., Springob, C. M., & Staveley-Smith, L. 2014, MNRAS, 443, 1044, 1406.5924

Masters, K. L. et al. 2010, MNRAS, 405, 783, 0910.4113

Masters, K. L. et al. 2019, Monthly Notices of the Royal Astronomical Society

Mathews, W. G., & Brighenti, F. 2003, Annual Review of Astronomy and Astrophysics, 41, 191, https://doi.org/10.1146/annurev.astro.41.090401.094542

McClure-Griffiths, N. M., Stanimirovic, S., & Rybarczyk, D. R. 2023, arXiv e-prints, arXiv:2307.08464, 2307.08464

McKee, C. F. 1995, in Astronomical Society of the Pacific Conference Series, Vol. 80, The Physics of the Interstellar Medium and Intergalactic Medium, ed. A. Ferrara, C. F. McKee, C. Heiles, & P. R. Shapiro, 292

McMullin, J. et al. 2022, in Society of Photo-Optical Instrumentation Engineers (SPIE) Conference Series, Vol. 12182, Ground-based and Airborne Telescopes IX, ed. H. K. Marshall, J. Spyromilio, & T. Usuda, 121820Q

Medupe, T. R. 2015, Indigenous Astronomy in Southern Africa, ed. C. L. Ruggles (New York, NY: Springer New York), 1031–1036

Mitzkus, M., Cappellari, M., & Walcher, C. J. 2017, MNRAS, 464, 4789, 1610.04516

Moazzenzadeh, M., & Firouzjaee, J. T. 2021, arXiv e-prints, arXiv:2108.00115, 2108.00115

Monnet, G., Bacon, R., & Emsellem, E. 1992, AAp, 253, 366

Moore, B., Katz, N., Lake, G., Dressler, A., & Oemler, A. 1996, Nature, 379, 613, astro-ph/9510034

Moretti, A. et al. 2020, ApJ, 889, 9, 1912.06565

Morganti, R. et al. 2006a, MNRAS, 371, 157, astro-ph/0606261

——. 2006b, MNRAS, 371, 157, astro-ph/0606261

Moster, B. P., Naab, T., & White, S. D. M. 2013, MNRAS, 428, 3121, 1205.5807

Moster, B. P., Somerville, R. S., Maulbetsch, C., van den Bosch, F. C., Macciò, A. V., Naab, T., & Oser, L. 2010, ApJ, 710, 903, 0903.4682

Moustakas, J. et al. 2013, ApJ, 767, 50, 1301.1688

Murphy, E. J., Kenney, J. D. P., Helou, G., Chung, A., & Howell, J. H. 2009, ApJ, 694, 1435, 0812.2922

Murray, S. D., White, S. D. M., Blondin, J. M., & Lin, D. N. C. 1993, ApJ, 407, 588

Napolitano, N. R., Pota, V., Romanowsky, A. J., Forbes, D. A., Brodie, J. P., & Foster, C. 2014, MNRAS, 439, 659, 1401.1501

Navarro, J. F., Frenk, C. S., & White, S. D. M. 1996, ApJ, 462, 563, astro-ph/9508025

Nelson, E. 2009, Pomona Senior Theses

Nogueira-Cavalcante, J. P. et al. 2019, A&A, 630, A88, 1907.11244

Noordermeer, E., Merrifield, M. R., & Aragón-Salamanca, A. 2008, MNRAS, 388, 1381, 0805.3230

O'Dell, C. R. 2001, ARA&A, 39, 99

Oman, K. A., Bahé, Y. M., Healy, J., Hess, K. M., Hudson, M. J., & Verheijen, M. A. W. 2021, MNRAS, 501, 5073, 2009.00667

Oman, K. A., & Hudson, M. J. 2016, MNRAS, 463, 3083, 1607.07934

Oman, K. A., Hudson, M. J., & Behroozi, P. S. 2013, MNRAS, 431, 2307, 1301.6757

Oosterloo, T. et al. 2010, MNRAS, 409, 500, 1007.2059

Oosterloo, T., & van Gorkom, J. 2005, A&A, 437, L19, astro-ph/0505397

Oosterloo, T., Verheijen, M., van Cappellen, W., Bakker, L., Heald, G., & Ivashina, M. 2009, Apertif - the focal-plane array system for the WSRT, 0912.0093

Ouchi, M., Ono, Y., & Shibuya, T. 2020, ARA&A, 58, 617, 2012.07960

Padoan, P., & Nordlund, Å. 2002, ApJ, 576, 870, astro-ph/0011465

Paduroiu, S., Revaz, Y., & Pfenniger, D. 2015, arXiv e-prints, arXiv:1506.03789, 1506.03789

Parker, E. N. 1966, ApJ, 145, 811

Poggianti, B. M. et al. 2020, The role of environment on quenching, star formation and AGN activity, 2005.03735

Poggianti, B. M. et al. 2016a, AJ, 151, 78, 1504.07105

——. 2016b, AJ, 151, 78, 1504.07105

——. 2019a, ApJ, 887, 155, 1910.11622

——. 2019b, ApJ, 887, 155, 1910.11622

——. 2017, ApJ, 844, 48, 1704.05086

Poggianti, B. M., Smail, I., Dressler, A., Couch, W. J., Barger, A. J., Butcher, H., Ellis, R. S., & Oemler, Augustus, J. 1999, ApJ, 518, 576, astro-ph/9901264

Pontzen, A., & Governato, F. 2012, MNRAS, 421, 3464, 1106.0499

Pontzen, A., Tremmel, M., Roth, N., Peiris, H. V., Saintonge, A., Volonteri, M., Quinn, T., & Governato, F. 2017, MNRAS, 465, 547, 1607.02507

Popesso, P., Böhringer, H., Brinkmann, J., Voges, W., & York, D. G. 2004, A&A, 423, 449, astro-ph/0403354

Posti, L., & Fall, S. M. 2021, A&A, 649, A119, 2102.11282

Quintero, A. D. et al. 2004, ApJ, 602, 190, astro-ph/0307074

Rafferty, D. A., McNamara, B. R., & Nulsen, P. E. J. 2008, ApJ, 687, 899, 0802.1864

Ricarte, A., Tremmel, M., Natarajan, P., & Quinn, T. 2020, ApJ, 895, L8, 2003.05950

Richter, O. G., & Sancisi, R. 1994, A&A, 290, L9

Roberts, I. D. et al. 2022, ApJ, 941, 77, 2210.16013

——. 2021, A&A, 650, A111, 2104.05383

Roberts, M. S. 1966, ApJ, 144, 639

——. 1978, AJ, 83, 1026

Roediger, E. 2009, Astronomische Nachrichten, 330, 888, 0909.2638

Rohr, E., Pillepich, A., Nelson, D., Zinger, E., Joshi, G. D., & Ayromlou, M. 2023, MNRAS, 524, 3502, 2304.09196

Roman-Oliveira, F., Chies-Santos, A. L., Ferrari, F., Lucatelli, G., & Rodríguez Del Pino, B. 2021, MNRAS, 500, 40

Rowlands, K. et al. 2018, MNRAS, 480, 2544, 1807.06066

Roy, N. et al. 2018, ApJ, 869, 117, 1811.04072

——. 2021, ApJ, 913, 33, 2103.14928

Rubin, V. C. 1983, Science, 220, 1339, https://science.sciencemag.org/content/220/4604/1339.full.pdf

Rubin, V. C., Ford, W. K., J., & Thonnard, N. 1978, ApJL, 225, L107

——. 1980, ApJ, 238, 471

Rubin, V. C., & Ford, W. Kent, J. 1970, ApJ, 159, 379

Saintonge, A. 2007, AJ, 133, 2087, astro-ph/0702178

Salim, S. 2014, Serbian Astronomical Journal, 1–14

Salim, S., Boquien, M., & Lee, J. C. 2018, ApJ, 859, 11, 1804.05850

Salim, S. et al. 2016, ApJS, 227, 2, 1610.00712

Sánchez, S. F. et al. 2012, A&A, 538, A8, 1111.0962

——. 2016a, Rev. Mexicana Astron. Astrofis., 52, 171, 1602.01830

——. 2016b, Rev. Mexicana Astron. Astrofis., 52, 21, 1509.08552

Sánchez-Blázquez, P. et al. 2006, MNRAS, 371, 703, astro-ph/0607009

Santucci, G. et al. 2022, ApJ, 930, 153, 2203.03648

Sarazin, C. L. 1986, Reviews of Modern Physics, 58, 1

Sarzi, M. et al. 2010, MNRAS, 402, 2187, 0912.0275

Schawinski, K. et al. 2009, MNRAS, 396, 818, 0903.3415

Schawinski, K. et al. 2014, MNRAS, 440, 889–907

Schaye, J. et al. 2015, MNRAS, 446, 521, 1407.7040

Schoenmakers, R. H. M., Franx, M., & de Zeeuw, P. T. 1997, MNRAS, 292, 349, astro-ph/9707332

Schwarzschild, M. 1979, ApJ, 232, 236

Scott, N. et al. 2013, MNRAS, 432, 1894, 1211.4615

Serra, P. et al. 2012, MNRAS, 422, 1835, 1111.4241

Sharma, S. 2017, ARA&A, 55, 213, 1706.01629

Shimwell, T. W. et al. 2022, A&A, 659, A1, 2202.11733

——. 2017, A&A, 598, A104, 1611.02700

——. 2019, A&A, 622, A1, 1811.07926

Skrutskie, M. F. et al. 2006, AJ, 131, 1163

Smee, S. A. et al. 2013, AJ, 146, 32, 1208.2233

Somerville, R. S. et al. 2018, MNRAS, 473, 2714, 1701.03526

Springel, V., Frenk, C. S., & White, S. D. M. 2006, Nature, 440, 1137, astro-ph/0604561

Springob, C. M., Haynes, M. P., Giovanelli, R., & Kent, B. R. 2005, ApJS, 160, 149, astro-ph/0505025

Stark, D. V. et al. 2021, MNRAS, 503, 1345, 2101.12680

Stewart, I. M., Blyth, S. L., & de Blok, W. J. G. 2014, A&A, 567, A61, 1405.1838

Struck, C. 1999, Phys. Rep., 321, 1, astro-ph/9908269

Thean, A. H. C., Mundell, C. G., Pedlar, A., & Nicholson, R. A. 1997, MNRAS, 290, 15

Thomas, J. 2010, Reviews in Modern Astronomy, 22, 143, 1007.3591

Toomre, A. 1964, ApJ, 139, 1217

Tran, K.-V. H., Franx, M., Illingworth, G. D., van Dokkum, P., Kelson, D. D., & Magee, D. 2004, ApJ, 609, 683, astro-ph/0403484

Tremblay, B., Merritt, D., & Williams, T. B. 1995, ApJ, 443, L5, astro-ph/9510098

Troncoso-Iribarren, P., Padilla, N., Santander, C., Lagos, C. D. P., García-Lambas, D., Rodríguez, S., & Contreras, S. 2020, MNRAS, 497, 4145, 2001.06501

Trujillo, I., Chamba, N., & Knapen, J. H. 2020, MNRAS, 493, 87, 2001.02689

Tsukui, T., Iguchi, S., & Onishi, K. 2020, in Galactic Dynamics in the Era of Large Surveys, ed. M. Valluri & J. A. Sellwood, Vol. 353, 248–252

Tumlinson, J., Peeples, M. S., & Werk, J. K. 2017, ARA&A, 55, 389, 1709.09180

van de Sande, J., Fraser-McKelvie, A., Fisher, D. B., Martig, M., Hayden, M. R., & the GECKOS Survey collaboration. 2023, arXiv e-prints, arXiv:2306.00059, 2306.00059

van de Ven, G., de Zeeuw, P. T., & van den Bosch, R. C. E. 2008, MNRAS, 385, 614, 0712.0309

van den Bosch, R. C. E., van de Ven, G., Verolme, E. K., Cappellari, M., & de Zeeuw, P. T. 2008, MNRAS, 385, 647, 0712.0113

van Haarlem, M. P. et al. 2013, A&A, 556, A2, 1305.3550

Voges, W. et al. 1999, A&A, 349, 389, astro-ph/9909315

Vollmer, B., Soida, M., Beck, R., Chung, A., Urbanik, M., Chyży, K. T., Otmianowska-Mazur, K., & Kenney, J. D. P. 2013, A&A, 553, A116, 1304.1279

Vulcani, B. et al. 2018, ApJ, 866, L25, 1810.05164

Wake, D. A. et al. 2017, AJ, 154, 86, 1707.02989

Waldron, W. et al. 2023, MNRAS, 522, 173, 2302.07270

Wang, J., Koribalski, B. S., Serra, P., van der Hulst, T., Roychowdhury, S., Kamphuis, P., & Chengalur, J. N. 2016, MNRAS, 460, 2143, 1605.01489

Wang, L. et al. 2013, MNRAS, 431, 648, 1203.5828

Weijmans, A.-M., Krajnović, D., van de Ven, G., Oosterloo, T. A., Morganti, R., & de Zeeuw, P. T. 2008, MNRAS, 383, 1343, 0711.1775

Weinberg, D. H., Bullock, J. S., Governato, F., Kuzio de Naray, R., & Peter, A. H. G. 2015, Proceedings of the National Academy of Science, 112, 12249, 1306.0913

Werle, A. et al. 2022, ApJ, 930, 43, 2203.08862

Westfall, K. B. et al. 2019, AJ, 158, 231, 1901.00856

White, S. D. M., & Rees, M. J. 1978, MNRAS, 183, 341

Wild, V., Kauffmann, G., Heckman, T., Charlot, S., Lemson, G., Brinchmann, J., Reichard, T., & Pasquali, A. 2007, MNRAS, 381, 543, 0706.3113

Wild, V., Walcher, C. J., Johansson, P. H., Tresse, L., Charlot, S., Pollo, A., Le Fèvre, O., & de Ravel, L. 2009, MNRAS, 395, 144, 0810.5122

Wilkinson, D. M. et al. 2015, MNRAS, 449, 328, 1503.01124

Williams, C. C. et al. 2023, arXiv e-prints, arXiv:2301.09780, 2301.09780

Winkel, N., Pasquali, A., Kraljic, K., Smith, R., Gallazzi, A., & Jackson, T. M. 2021, MNRAS, 505, 4920, 2105.13368

Wong, T., Blitz, L., & Bosma, A. 2004, ApJ, 605, 183, astro-ph/0401187

Yang, M., Zhu, L., Weijmans, A.-M., van de Ven, G., Boardman, N., Morganti, R., & Oosterloo, T. 2019, Monthly Notices of the Royal Astronomical Society, 491, 4221–4231

Yang, X., Mo, H. J., van den Bosch, F. C., Pasquali, A., Li, C., & Barden, M. 2007, ApJ, 671, 153, 0707.4640

Zhu, K., Lu, S., Cappellari, M., Li, R., Mao, S., & Gao, L. 2023, MNRAS, 522, 6326, 2304.11711

Zhu, L. et al. 2014, ApJ, 792, 59, 1407.2263

——. 2016, MNRAS, 462, 4001, 1608.08238

Zinger, E., Joshi, G., Pillepich, A., Rohr, E., & Nelson, D. 2023, arXiv e-prints, arXiv:2304.09202, 2304.09202

Zou, H. et al. 2017, PASP, 129, 064101, 1702.03653

Zwicky, F. 1933, Helvetica Physica Acta, 6, 110